JOURNAL OF THE AERONAUTICAL SCIENCES

VOLUME 24 FEBRUARY, 1957 NUMBER 2

ST. LOUIS
FEB 11 1957
PUBLIC LIBRARY

CONTENTS

A Two-Dimensional Approximation to the Unsteady Aerodynamics of Rotary Wings. ROBERT G. LOEWY 81

Visualization of Low-Density Flows by Means of Oxygen Absorption of Ultraviolet Radiation PAULINE M. SHERMAN 93

An Introduction to Second-Order Wing Theory D. C. M. LESLIE 99

Supersonic Flutter of a Cylindrical Shell JOHN W. MILES 107

Tables and Curves for Deformations and Stresses in Circular Cylindrical Shells Under Localized Loadings JOSEPH KEMPNER, JAMES SHENG, AND FREDERICK V. POHLE 119

Dynamic Considerations Relating to the Behavior of Inertial Space-Stabilized Platforms EDMUND GORCZYCKI 130

The Calculation of Thermoelastic Beam Deflections by the Principle of Virtual Work. BRUNO A. BOLEY 139

Optimum Thickness and Lift Distribution for a Fuselage in the Presence of a Prescribed Wing System M. E. GRAHAM 142

Readers' Forum 145

Published by

INSTITUTE OF THE AERONAUTICAL SCIENCES, INC.

JOURNAL OF THE AERONAUTICAL SCIENCES

Editor: W. R. SEARS

Director, Graduate School of Aeronautical Engineering, Cornell University

Associate Editor: ROBERT R. DEXTER *Managing Editor:* RITA J. TURINO

Editorial Assistant: CAROLINE TAYLOR

Editorial Committee

Aerodynamics and Fluid Mechanics

Holt Ashley
H. Julian Allen
Dean R. Chapman
Francis H. Clauser
Hugh L. Dryden
John C. Evvard
Antonio Ferri
Alexander Flax
Wallace D. Hayes
R. T. Jones
Carl Kaplan
H. W. Liepmann
C. C. Lin
H. F. Ludloff
Harold Luskin
Clark B. Millikan
C. D. Perkins
H. J. E. Reid
George S. Schairer
G. B. Schubauer
John Stack
Theodore Theodorsen
Arthur N. Tifford
Th. von Kármán

Flight Testing

R. R. Gilruth
Melvin N. Gough
W. L. Howland
W. F. Milliken, Jr.

Rotating Wing Aircraft

F. B. Gustafson
K. H. Hohenemser
Bartram Kelley
R. B. Maloy
Ralph McClarren
R. H. Miller
R. H. Prewitt
Igor I. Sikorsky

Structures

John E. Duberg
N. J. Hoff
Samuel Levy
J. F. McBrearty
W. Ramberg
E. E. Sechler
F. R. Shanley
C. R. Strang
S. Timoshenko

Meteorology

C. F. Brooks
D. M. Little
F. W. Reichelderfer
K. C. Spengler

Vibration and Flutter

Lee Arnold
M. A. Biot
R. L. Bisplinghoff
Harold A. Cheilek
I. E. Garrick
Martin Goland

Aircraft Design

W. E. Beall
E. H. Heinemann
Hall L. Hibbard
Richard Hutton
C. L. Johnson
A. A. Kartveli
E. G. Stout
F. K. Teichmann

Electronics

Welcome W. Bender
K. C. Black
M. V. Kiebert, Jr.
David S. Little
S. B. Rogers
Paul Rosenberg
L. M. Sherer

Physiologic Problems

H. G. Armstrong
Louis H. Bauer
Robert J. Benford
W. Randolph Lovelace, II
Ross A. MacFarland

Flight Propulsion

William Bollay
George W. Brady
R. P. Kroon
Frank E. Marble
Abe Silverstein
Martin Summerfield
E. S. Taylor

Instruments

Alan G. Binnie
Charles H. Colvin
Frank R. Cook
C. S. Draper
S. G. Eskin
C. F. Savage
R. C. Sylvander

SUBSCRIPTION RATES

JOURNAL OF THE AERONAUTICAL SCIENCES, Published Monthly. United States and Possessions: 1 Year, $15.00; Single Copies, $1.50. Foreign Countries Including Canada (American Currency Rates): 1 Year, $16.00; Single Copies, $1.50.

AERONAUTICAL ENGINEERING REVIEW, Published Monthly. United States and Possessions: 1 Year, $3.00; Single Copies, $0.50. Foreign Countries Including Canada (American Currency Rates): 1 Year, $3.50; Single Copies, $0.50.

Notices of change of address should be sent to the Institute at least 30 days prior to actual change of address.

Manuscripts for publication, proofs, and all correspondence should be addressed to the Editorial Office of the JOURNAL.

Publication Office, 20th and Northampton Sts., Easton, Pa. Correspondence regarding subscriptions may be addressed to the Editorial Office of the JOURNAL OF THE AERONAUTICAL SCIENCES, 2 East 64th Street, New York 21, N.Y.

© *Copyright, 1957, by the Institute of the Aeronautical Sciences, Inc.*

Entered as Second-Class Matter at the Post Office, Easton, Pa., May 1, 1937. Acceptance for mailing at a special rate of Postage provided for in the Act of August 24, 1912. Authorized April 29, 1937.

JOURNAL OF THE AERONAUTICAL SCIENCES

VOLUME 24 FEBRUARY, 1957 NUMBER 2

A Two-Dimensional Approximation to the Unsteady Aerodynamics of Rotary Wings

ROBERT G. LOEWY*

Vertol Aircraft Corporation

SUMMARY

A two-dimensionalized model is postulated for the representation of the aerodynamics of an oscillating rotary wing airfoil operating at low inflow; forward speed effects are neglected. The resulting unsteady integral downwash equation leads to an equation for pressure distribution identical in form to that of classical fixed-wing flutter, but with a modified lift deficiency function. As a consequence, lift and moment expressions used in the fixed-wing flutter theory may be used directly for the rotary wing airfoil in harmonic motion, except that Theodorsen's function of reduced frequency, $C(k)$, is modified to include the effects of the number of blades in the rotor, the ratio of oscillatory frequency to rotational frequency, and the inflow ratio. It is shown that the effects due to the vorticity shed by previous blades and/or in previous revolutions diminish as the product of reduced frequency and inflow ratio increases. Curves of aerodynamic damping coefficient for flapping and pitching motions are presented, showing that these effects (1) reduce the flap damping significantly at integer values of the ratio of oscillatory frequency to rotational frequency, and (2) make single degree of freedom pitch instability possible at certain values of this parameter depending upon the location of the center of rotation. Application of these new coefficients to classical flutter analysis and other rotor problems is discussed.

SYMBOLS

a = pitch axis location (measured from midchord, positive aft)
b = blade semichord (dimensional quantity)
C = $F + iG$ = Theodorsen's lift deficiency function
C' = $F' + iG'$ = modified lift deficiency function for rotors
h = vertical distance between successive rows of vorticity = $2\pi u/bQ\Omega$
k = reduced frequency = $b\omega/V = (\omega/\Omega)(b/r') = m/r$
m = frequency ratio = ω/Ω
n = rotor revolution index
p = pressure
Q = number of blades in the rotor
r = blade section radius
t = time
u = inflow velocity (steady, normal to rotor disc)
v = vertical component of induced flow ("downwash")
V = steady resultant velocity $\approx \Omega r'$
W = wake weighting function
x = ordinate in stream direction along the airfoil (positive aft)
y = displacement of airfoil perpendicular to rotor disc
Γ = total circulation around the airfoil
γ = line strength of continuously distributed vorticity
ξ = ordinate in stream direction (positive aft)
ω = oscillatory frequency
Ω = rotational speed
ϕ = potential function
ρ = mass density of air
θ = blade pitch (torsion) angle
ψ_q = phase angle by which motion of qth blade leads that of the reference blade
η, λ, τ = dummy variables

Superscripts

$'$ = dimensional quantities
$\cdot$ = time derivatives
$\bar{\ }$ = functions independent of time

Subscripts

a = quantity associated with reference airfoil
n = rotor revolution index
q = multibladed-rotor blade index
U = refers to upper airfoil surface
L = refers to lower airfoil surface

INTRODUCTION

THE HELICOPTER ROTOR is subject to unsteady flow phenomena in many phases of its operation. Unlike fixed-wing aircraft, the rotor experiences oscillatory aerodynamic effects even in steady, gustless forward flight. This is fundamental for rotary wings since variations in relative airspeed occur at a blade section as the blade traverses the azimuth. In addition, flapping and blade pitch angles are made to vary with azi-

Presented at the Aerodynamics—II Session, Twenty-Fourth Annual Meeting, IAS, New York, January 23–26, 1956.

* Chief Dynamics Engineer. The work leading to this paper was performed while the author was employed at Cornell Aeronautical Laboratory.

The writer is indebted to Dr. T. Goodman for his valuable assistance in overcoming some of the mathematical hurdles encountered, T. T. Chang for his careful review of the manuscript, and D. Feign for his help in expediting the numerical calculations.

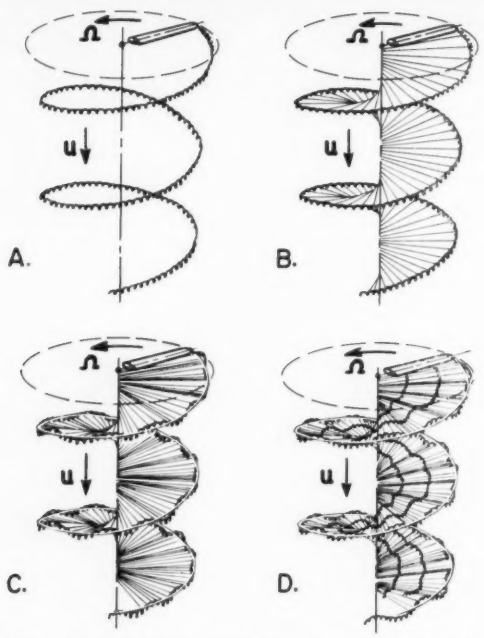

FIG. 1. Schematic elements of unsteady rotor flow field.

muth in order to tilt the thrust vector in the desired direction and eliminate overturning moments. Rotor blades, furthermore, have elastic, inertial, and aerodynamic properties in proportions which suggest susceptibility to instabilities analogous to fixed-wing flutter; cases of classical rotor flutter have, in fact, been encountered, although it has not generally been a major problem largely because of the practice of mass-balancing blades to reduce control forces.

Still another problem should be considered in discussing unsteady effects because of its widespread importance—namely, vibratory rotor blade bending. Azimuthal variations in the steady downwash distribution over the rotor disc in forward flight have been shown[1] to induce blade bending vibrations whose associated fatigue stresses are often high enough to design the blades structurally. Similar downwash distributions are possible in hovering with certain multirotor configurations. Since this effect involves resonances between the harmonics of steady air load distribution and the natural bending frequencies of the rotating blades, the magnitude of unsteady aerodynamic damping is most important in determining these stress levels.

Oscillatory airfoil coefficients have become a standard part of the fixed-wing aircraft engineer's equipment because of their importance in such problems as flutter, gust loads, and, under certain conditions, flight stability. Despite the indicated influence of analogous unsteady rotor aerodynamic effects on rotor instabilities, blade stresses, and helicopter fuselage vibration levels, unsteady aerodynamic coefficients are not generally available for rotating wings. Isaacs[2, 3] evaluated the lift and moment on a two-dimensional airfoil in a flow with sinusoidally varying air speed, for application to helicopter problems. The complex nature of the wake behind and below the rotor, however, was ignored in order to make the analysis tractable; using typical helicopter parameters in a numerical example showed that the results of the theory gave small differences from what is obtained by quasi-static means. Reference 4 presents a closed-form solution to the same problem.

Considerable research into the rotor flutter phenomenon has been conducted, prompted in some instances by specific cases of rotor instability, and more often by the possibility of gaining insight into the complexities of rotor dynamics and aerodynamics afforded by such studies. As a result of both experimental and theoretical programs (for example, see references 5 and 6), it appears that more specialized treatment of rotor aerodynamic coefficients must be made than has been done heretofore. Better representation of the troublesome induced effects could proceed in two directions, which for convenience can be considered independently; (1) accounting for three-dimensional effects *in the plane of the rotor*, such as the vorticity which results from the variation of circulation along the blade span and trails with circular form behind the blades, and (2) taking into consideration the influence of vorticity which has been shed and *blown below the rotor disc* and which must be passed over by succeeding blades and/or in succeeding revolutions. Cases of so-called "wake-excited flutter," reported in 1945 (see reference 7) and more recently encountered in tests at Cornell Aeronautical Laboratory and the NACA (see references 6 and 8, respectively), strongly hint that the effect of vorticity shed by previous blades and in previous revolutions is of importance, at least for low inflows, since "wake-excited flutter" could not exist without them.

Accordingly, the approach taken in this paper has been to account for the vorticity which lies below the plane of the rotor in a two-dimensional analysis. After a brief description of the unsteady rotor flow field and discussion of the two-dimensionalizing assumptions, a new set of unsteady aerodynamic coefficients is derived for application to rotor dynamics problems. It should be stated that this attempt is intended only as the first step in the development of a more satisfactory oscillating airfoil theory for rotors. Components of airspeed in the plane of the rotor, for example, as experienced by a helicopter in forward flight, have been neglected. It is also appreciated that the range of helicopter, propeller, and fan parameters is such that the three-dimensional effects mentioned above are undeniably significant for many cases. The results of the theory presented herein are expected to be useful, however, in studying unsteady effects on rotors operating at low inflows as well as vibratory phenomenon at larger inflows in which the oscillatory frequency is significantly higher than the rotational speed. Limitations resulting from basic assumptions are discussed further in the text.

(1) Rotor Unsteady Flow Field

A rotor in hovering or vertical flight trails a tip vortex which is blown axially downward so that, if otherwise

undisturbed, it would form a contracting helix as shown in Fig. 1A. If the inflow over the rotor disc, u, is assumed to be constant (an assumption which is generally satisfactory for performance calculations, but not satisfactory for computing blade stresses), then the fluid that comes off the trailing edge of the blades makes a helical surface with horizontal radial elements (see Fig. 1B). Now, if there is an oscillation in blade effective angle of attack, blade lift will alternate also, and as a result of these changes in lift, vortices will be shed continuously at the blade trailing edge. These vortices fall along the horizontal radial elements of the helical surface shown in Fig. 1B, so long as the oscillations in angle of attack are small. Fig. 1C illustrates this helical sheet of shed vorticity. It should be noted that vorticity is considered to be *on* the helical surface shown in Fig. 1B; the vertical displacements from that surface shown in Fig. 1C represent the strength of the vorticity at a particular azimuthal and radial position. The variation in this vertical displacement (hence vortex strength) around the azimuth corresponds to the history of the motion of a given blade element at a fixed radius; the variation of shed vortex strength in the radial direction at any fixed azimuth angle is a function of the variation with blade span of (1) blade chord, (2) amplitude of the oscillation in effective angle of attack, and (3) relative air velocity. Since (from the Hemholtz theorem) vorticity cannot begin or end in space, a variation of shed vorticity in the radial direction implies that there are trailing vortices at constant radii similar to and inboard of the tip vortex. These trailing vortices have been included in Fig. 1D.

The schematic drawings of Figs. 1A through 1D indicate pictorially the complexities of attempting to obtain a complete representation of unsteady rotor aerodynamics. One means of simplifying the problem is to consider extreme "pitch" values for the helix. Consider, for example, the case of very high u in relation to Ω, and the opposite, where u is very low compared to Ω. When $2\pi u/Q\Omega$ (the vertical spacing between adjacent helical surfaces of shed vorticity) is very large, then one would expect that all shed vorticity beyond a small fraction of a revolution would be too far below the blade in question to have an effect. Under these conditions, it would be sufficient to account for only the attached vortex sheet within that fraction of a revolution, as in Fig. 2A. On the other hand, when $2\pi u/Q\Omega$ is very small, all the sheets of shed vorticity tend to pile up on each other, and the effect of that vorticity close to the blade in question (shed by the several previous blades and/or in the several previous revolutions) is of more importance than that which exists beyond a still smaller azimuth angle on either side of the blade. This situation is depicted in Fig. 2B.

The first condition is one which would exist at high rotor thrust coefficients; in this respect it may be of consequence in the phenomena of rotor stall flutter with high disc loadings. The second condition certainly occurs at blade pitch angles near zero and is of prime importance in "wake-flutter." Vorticity shed

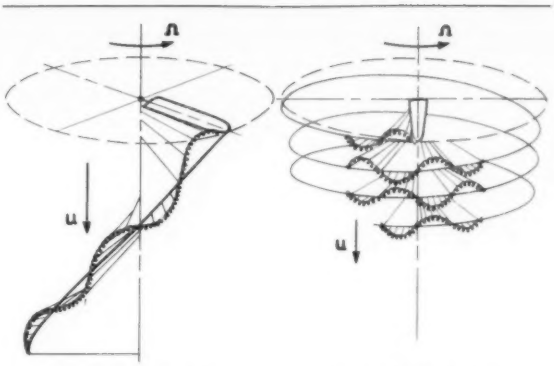

FIG. 2. Schematic representation of unsteady rotor flow fields.

by previous blades and in previous revolutions, as shown in Fig. 2B, may also be of substantial influence in improving other rotor calculations involving unsteady aerodynamics where the spacing between rows of vorticity is not too large. This case—that of low inflow—is considered in this paper, and one of the results which the analysis is intended to obtain is a *definition* of "low inflow" in this regard—i.e., to determine under what conditions the vorticity beneath the rotor disc is important.

(2) Formulation of the Aerodynamic Model

In arriving at a model which is mathematically tractable, the assumption has been made that for the case of low inflows, only the vorticity contained within a small double azimuth angle straddling the blade is of real consequence. In addition, it is assumed that the chord, amplitude of the oscillation in effective angle of attack, and relative air speed vary slowly enough with span or in a compensatory way so that what occurs aerodynamically at one blade radius station is essentially duplicated on either side of it. As a result of the first assumption, the azimuthal angularity of shed vorticity with respect to the blade may be ignored, as well as the horizontal distance that a spanwise element of shed vorticity is moved out of the vertical plane of a blade section at fixed radius as a result of azimuthal rotation. The second assumption is tantamount to saying that the flow problem at a given blade radius is two-dimensional. Thus, the portion of the circular cylindrical surface which is determined by (1) a particular blade radius, (2) the azimuth angle on either side of the blade section (within which the shed vorticity is of importance), and (3) the vertical distance spanned by a given number of rows of vorticity, can be regarded as a plane—one in which the two-dimensional unsteady aerodynamic problem may be attacked. This is shown in Fig. 3a, with an arrow indicating that the rows of vorticity under the rotor disc extend to infinity. From the original postulation of small inflow, it is clear that the vertical angularity of the wake with respect to the plane of the rotor blade, δ, is negligibly small. Furthermore, consistent with the idea that only the vorticity near the blade section has an important effect, one may

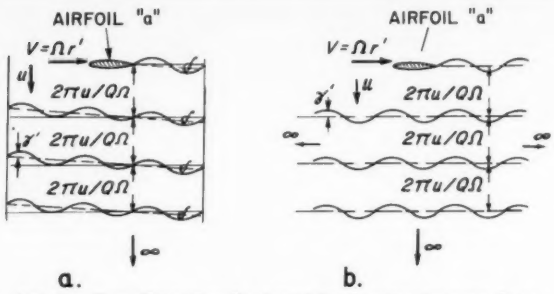

FIG. 3. Two-dimensionalized models of unsteady rotor flow.

allow the planar rows of vorticity to extend to infinity in the horizontal direction in order to achieve mathematical simplification. These final modifications are shown in Fig. 3b, which is a two-dimensional model of unsteady rotor aerodynamics for a single-bladed rotor operating at low inflows.

(3) Derivation of the Unsteady Aerodynamic Coefficients

The general approach used here is the same as that of Schwarz.[9] Only the effects resulting from oscillatory motion of a thin airfoil are considered, and the airfoil itself is represented by continuous vorticity, γ_a, distributed along a straight line. Fig. 4 is a repetition of the aerodynamic model presented in Fig. 3b, but showing the case of a multibladed rotor and the notation adopted for the mathematical analysis.

Since not all the vorticity has been shed by one blade, the vortex rows must be identified by two indices; n indicates which revolution a given row is associated with, while q reveals which blade has shed the vorticity.

If the airfoil motion is sinusoidal, the downwash over the reference airfoil, v_a, and its vorticity (either bound or shed) may be written, respectively, as

$$v_a = \bar{v}_a e^{i\omega t}$$

$$\gamma_a = \bar{\gamma}_a e^{i\omega t}$$

where the barred quantities are complex and independent of t. The vorticity along the reference airfoil, γ_a, and that in the wake are differentiated from each other by writing wake vorticity as γ_{00} for the attached sheet, and γ_{nq} for the sheet shed by the qth blade in the nth preceding rotor revolution.*

The induced velocity at a point x' on the airfoil, resulting from an element of vorticity of strength, γ_{nq}, at a general point in the wake is given by the Biot-Savart Theorem as

$$dv_a(x', t) = \frac{\gamma_{nq}(x' - \xi')d\xi}{2\pi\{(x' - \xi')^2 + (nQ + q)^2(h')^2\}}$$

where Q is the total number of blades and h' is the vertical distance between successive rows of vorticity. The total downwash over the airfoil can be expressed conveniently by writing the integrals involving the bound vorticity and the row of vorticity attached to the reference blade separately from those for the rows of vortices below the plane of the rotor, as follows:

$$v_a(x', t) = -\frac{1}{2\pi}\left[\int_{-b}^{b} \frac{\gamma_a(\xi', t)d\xi'}{x' - \xi'} + \int_{b}^{\infty} \frac{\gamma_{00}(\xi', t)d\xi'}{x' - \xi'} + \sum_{q=1}^{Q-1}\sum_{n=0}^{\infty}\int_{-\infty}^{\infty} \frac{\gamma_{nq}(\xi', t)(x' - \xi')d\xi'}{(x' - \xi')^2 + (nQ + q)^2(h')^2} + \sum_{n=1}^{\infty}\int_{-\infty}^{\infty} \frac{\gamma_{n0}(\xi', t)(x' - \xi')d\xi'}{(x' - \xi')^2 + n^2Q^2(h')^2}\right]$$

The first two terms on the right-hand side of this integral equation are those that arise in classical fixed-wing flutter; the third and fourth terms contribute the influence of all the vorticity below the plane of the rotor disc.

It should be stated that this is a first-order theory, so that such effects as that of the wake upon itself have been neglected. The oscillatory flow induced at the airfoil in the free-stream direction, for example, will affect the airfoil lift and moment as well as the vorticity shed at the trailing edge. Since the shed vorticity is being accounted for as perturbations in the main flow, however, this component of induced velocity will be small compared to the free-stream velocity (except when the spacing approaches zero) and must react with small, first-order airfoil displacements. Because of the physical unrealities associated with the standard mathematical representation of the problem (such as zero thickness of wake and airfoil, zero displacement of the wake from horizontal planes, and infinite velocities at the core of a vortex), the accuracy of the results as $h' \to 0$ is questionable. The effect of the horizontal component of induced flow, therefore, has been neglected in this analysis.

It may also be noted that the effects of viscosity in damping the shed vorticity could be accounted for by considering only a finite number of rows beneath the reference airfoil, or by multiplying the vortex strength, γ', by an experimental "decay" function related to "time" through the rotational speed and the number of rotational cycles corresponding to a particular vortex row. This has been omitted since vortex decay time is long compared to the rotational periods of most rotors.

The vorticity shed by the qth blade n revolutions

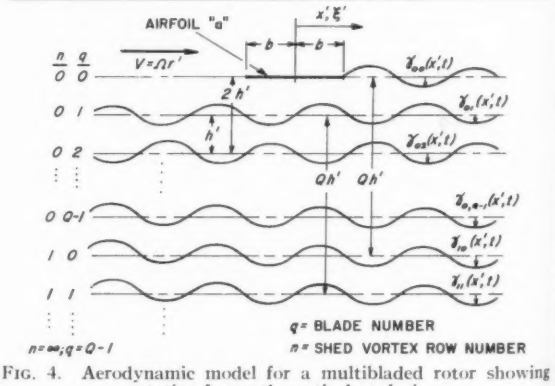

FIG. 4. Aerodynamic model for a multibladed rotor showing notation for mathematical analysis.

* Note that 0 for the blade index is associated with the reference airfoil (see Fig. 4).

ago can be related to that of the reference revolution as follows:

$$\gamma_{nq} = \bar{\gamma}_{0q} e^{i\omega[t-(2\pi n/\Omega)]} = \bar{\gamma}_{0q} e^{-i2\pi n(\omega/\Omega)} e^{i\omega t}$$

therefore $$\bar{\gamma}_{nq} = \bar{\gamma}_{0q} e^{-i2\pi(\omega/\Omega)n} \quad (1)$$

Since a vortex is shed at the trailing edge of an airfoil with each change in total airfoil circulation, Γ', the following may be written for the reference airfoil:

$$\gamma_{00}(b, t)dx' = -\frac{d\Gamma_a'(t)dt}{dt} = -i\omega\bar{\Gamma}_a' e^{i\omega t} dt$$

In addition, a vortex shed from the trailing edge of the qth airfoil is related to the change in circulation of that airfoil by

$$\gamma_{0q}\left(b - \frac{2\pi r' q}{Q}, t\right)d\xi' = -\frac{d\Gamma_q'(t)dt}{dt} = -i\omega\bar{\Gamma}_q' e^{i\omega t} dt$$

If the amplitude of the circulation of the qth airfoil is equal to that of the reference airfoil but leading it in time by the phase angle ψ_q,

$$\gamma_{0q}\left(b - \frac{2\pi r' q}{Q}, t\right)d\xi' = -i\omega\bar{\Gamma}_a' e^{i(\omega t+\psi_q)} dt$$

What is shed at the trailing edge of the qth airfoil at time, t, will be at a point in the wake described by ξ', n some time, Δt, later; where

$$\Delta t = (2\pi/\Omega)(q/Q) + [(\xi' - b)/\Omega r'] + (2\pi n/\Omega)$$

Thus,

$$\gamma_{0q}\left(b - \frac{2\pi r' q}{Q}, t\right)d\xi' = -i\omega\bar{\Gamma}_a' e^{i\omega t} e^{i\psi_q} dt = \bar{\gamma}_{nq}(\xi') e^{i\omega\{t+[(\xi'-b)/\Omega r']+(2\pi n/\Omega)+(2\pi/\Omega)(q/Q)\}} d\xi'$$

using Eq. (1) and the expression for Δt. Solving for $\bar{\gamma}_{nq}$,

$$\bar{\gamma}_{nq}(\xi') = -i\omega\bar{\Gamma}_0' e^{i\psi_q} e^{-i\omega\{[(\xi'-b)/\Omega r']+(2\pi n/\Omega)+(2\pi/\Omega)(q/Q)\}}(dt/d\xi') \quad (2)$$

and for the special case where $q = 0$; $n = 0$

$$\bar{\gamma}_{00}(\xi') = -i\omega\bar{\Gamma}_0' e^{-i\omega[(\xi'-b)/\Omega r']}(dt/d\xi') \quad (3)$$

Substituting Eq. (3) into Eq. (2), yields

$$\bar{\gamma}_{nq}(\xi') = \bar{\gamma}_{00}(\xi') e^{i\psi_q} e^{-i\omega[(2\pi n/\Omega)+(2\pi q/\Omega Q)]} \quad (4)$$

Eq. (4) is the phase relation between the strength of a vortex element at a general point in the wake and that in the plane of and shed by the reference airfoil. Recalling that $d\xi'/dt = \Omega r'$, Eq. (2) may be written

$$\bar{\gamma}_{nq}(\xi') = -(i\omega\bar{\Gamma}_0'/\Omega r') e^{i\psi_q} e^{-i2\pi(\omega/\Omega)(q/Q)} e^{-i2\pi(\omega/\Omega)n} e^{-i\omega[(\xi'-b)/\Omega r']}$$

Then defining the quantities,

$$m \triangleq \omega/\Omega; \quad k \triangleq (\omega/\Omega)(b/r') \triangleq m/r; \quad \bar{\Gamma} \triangleq (\bar{\Gamma}_0'/b)e^{ik}$$

one obtains

$$\bar{\gamma}_{nq}(\xi') = -ik\bar{\Gamma} e^{i\psi_q} e^{-i(m\xi'/r')} e^{-i2\pi(q/Q)m} e^{-i2\pi nm} \quad (5)$$

Substituting Eq. (5) into the integral downwash equation above Eq. (1) gives [since $v_a(x', t) = \bar{v}_a(x')e^{i\omega t}$]

$$\bar{v}_a(x') = -\frac{1}{2\pi}\left[\int_{-b}^{b} \frac{\bar{\gamma}_a(\xi')d\xi'}{x' - \xi'} - ik\bar{\Gamma} \times \int_{b}^{\infty} \frac{e^{-i(m\xi'/r')}d\xi'}{x' - \xi'} - ik\bar{\Gamma}\sum_{q=1}^{Q-1}\sum_{n=0}^{\infty} e^{-i\{i2\pi m[n+(q/Q)]-\psi_q\}} \times \int_{-\infty}^{\infty} \frac{e^{-i(m\xi'/r')}(x' - \xi')d\xi'}{(x' - \xi')^2 + (nQ + q)^2 h'^2} - ik\bar{\Gamma}\sum_{n=1}^{\infty} e^{-i2\pi mn} \times \int_{-\infty}^{\infty} \frac{e^{-(im\xi'/r')}(x' - \xi')d\xi'}{(x' - \xi')^2 + n^2Q^2h'^2}\right]$$

Nondimensionalizing—by dividing by b, and dropping the primes to indicate nondimensionalized quantities—one obtains

$$\bar{v}_a(x) = -\frac{1}{2\pi}\left[\int_{-1}^{1} \frac{\bar{\gamma}_a(\xi)d\xi}{x - \xi} - ik\bar{\Gamma}\int_{1}^{\infty} \frac{e^{-ik\xi}d\xi}{x - \xi} - ik\bar{\Gamma}\sum_{q=1}^{Q-1} e^{i[\psi_q - 2\pi m(q/Q)]}\sum_{n=0}^{\infty} e^{-i2\pi mn} \times \int_{-\infty}^{\infty} \frac{e^{-ik\xi}(x - \xi)d\xi}{(x - \xi)^2 + (nQ + q)^2h^2} - ik\bar{\Gamma}\sum_{n=1}^{\infty} e^{-i2\pi mn} \times \int_{-\infty}^{\infty} \frac{e^{-ik\xi}(x - \xi)d\xi}{(x - \xi)^2 + n^2Q^2h^2}\right] \quad (6)$$

The last two integrals are of the form,

$$\int_{-\infty}^{\infty} \frac{e^{-ik\xi}(x - \xi)d\xi}{(x - \xi)^2 + A^2}$$

and may be evaluated by the substitution $x - \xi = -A\lambda$, and use of tabulated definite integrals (for example, #11 of Table 103 in reference 10). Thus,

$$\int_{-\infty}^{\infty} \frac{e^{-ik\xi}(x - \xi)d\xi}{(x - \xi)^2 + A^2} = i\pi e^{-k(ix+A)}$$

The summations in Eq. (6) may then be written

$$\sum_{q=1}^{Q-1} e^{i[\psi_q - 2\pi m(q/Q)]}\sum_{n=0}^{\infty} e^{-2\pi mni}\cdot i\pi e^{-k\{ix+[nQ+q]h\}} \triangleq \sum_1$$

$$\sum_{n=1}^{\infty} e^{-i2\pi mn}\cdot i\pi e^{-k(ix+nQh)} \triangleq \sum_2$$

or

$$\sum_1 = i\pi e^{-ikx}\sum_{q=1}^{Q-1} e^{i\psi_q - (q/Q)[2\pi mi + khQ]}\sum_{n=0}^{\infty} e^{-n(i2\pi m + kQh)}$$

$$\sum_2 = i\pi e^{-ikx}\sum_{n=1}^{\infty} e^{-n(2\pi mi + kQh)}$$

Since kQh is always positive, the summations over n are convergent geometric series which may be written as

$$\sum_1 = i\pi e^{-ikx}\frac{\sum_{q=1}^{Q-1} e^{i\psi_q - (q/Q)[2\pi mi + khQ]}}{1 - e^{-(2\pi mi + kQh)}}$$

$$\sum_2 = i\pi e^{-ikx}\frac{e^{-(2\pi mi + kQh)}}{1 - e^{-(2\pi mi + kQh)}}$$

It should be noted that the closed form of the series has the restriction that $\left|e^{-(kQh+2\pi m)}\right| < 1$. Cases where $kh = 0$ are thus mathematically inadmissible; however, all singularities disappear in the final result, and numerical values corresponding to $kh = 0$ are in-

cluded in the results for completeness. Eq. (6) may now be rewritten

$$\left.\begin{aligned}\bar{v}_a(x) = \frac{-1}{2\pi}\left[\int_{-1}^{1}\frac{\bar{\gamma}_a(\xi)d\xi}{x-\xi} - ik\bar{\Gamma}\int_1^{\infty}\frac{e^{-ik\xi}d\xi}{x-\xi} + \pi k\bar{\Gamma}e^{-ikx}W\right]\\ \text{where}\qquad W = W(kh, m, Q, \psi_q) = \frac{1+\sum_{q=1}^{Q-1}\left\{e^{khQ}e^{i2\pi m}\right\}^{(Q-q)/Q}e^{i\psi_q}}{e^{hkQ}e^{i2\pi m}-1}\end{aligned}\right\} \quad (7)$$

Note that the total effect of the infinite number of vortex sheets below the plane of the reference airfoil is contained in the third term on the right-hand side of this equation. The function, W, may be thought of as a weighting function for the vorticity shed by preceding blades and/or in previous revolutions.

The form of the integral downwash equation given in Eq. (7) may be solved directly by applying Söhngen's inversion formula,[11] as in the derivation of fixed-wing flutter coefficients. Söhngen shows the solution of an equation of the form

$$g(x) = (1/2\pi)\int_{-1}^{1}\frac{f(\xi)d\xi}{x-\xi}$$

to be

$$f(x) = -\frac{2}{\pi}\sqrt{\frac{1-x}{1+x}}\int_{-1}^{1}\sqrt{\frac{1+\xi}{1-\xi}}\frac{g(\xi)}{(x-\xi)}d\xi$$

if $f(1)$ is finite. Satisfaction of $f(1)$-finite is tantamount to employing the Kutta condition in this case, where γ_a at the trailing edge must be finite. Hence,

$$\bar{\gamma}_a(x) = \frac{2}{\pi}\sqrt{\frac{1-x}{1+x}}\left[\int_{-1}^{1}\sqrt{\frac{1+\xi}{1-\xi}}\frac{\bar{v}_a(\xi)d\xi}{x-\xi} - \frac{ik\bar{\Gamma}}{2\pi}\int_{-1}^{1}\sqrt{\frac{1+\xi}{1-\xi}}\frac{1}{x-\xi}\int_1^{\infty}\frac{e^{-ik\eta}d\eta}{\xi-\eta}d\xi + \frac{k\bar{\Gamma}}{2}W\int_{-1}^{1}\sqrt{\frac{1+\xi}{1-\xi}}\frac{e^{-ik\xi}}{x-\xi}d\xi\right] \quad (8)$$

Performing the second integration on the right-hand side of the above equation, and then evaluating the circulation over the airfoil, $\bar{\Gamma}$, from

$$\bar{\Gamma} = e^{ik}\int_{-1}^{1}\bar{\gamma}_a(x)dx$$

yields†

$$\bar{\Gamma} = \frac{2\int_{-1}^{1}\sqrt{\frac{1+\xi}{1-\xi}}\bar{v}_a(\xi)d\xi}{i\pi k\left\{\frac{1}{2}[H_1^{(2)}(k) + iH_0^{(2)}(k)] + [J_1(k) + iJ_0(k)]W\right\}} \quad (9)$$

where $J_\nu(k)$ and $H_\nu^{(2)}(k)$ are Bessel functions of the first kind and Hankel functions, respectively.

Bernoulli's equation for unsteady motion using nondimensional lengths is

$$(\partial\phi/\partial t) + (V/b)(\partial\phi/\partial x) + (p/\rho) = f(t)$$

where ϕ is the velocity potential and p the pressure. Since the airfoil has been replaced by a vortex sheet, the difference between the velocity on the upper and lower surfaces is $\gamma_a(x, t)$. Thus, for any point on the airfoil,

$$(\partial\phi_U/\partial x) - (\partial\phi_L/\partial x) = b\gamma_a(x, t)$$

$$\phi_U - \phi_L = b\int_{-1}^{x}\gamma_a(\xi, t)d\xi$$

Combining the above with Bernoulli's equation gives

$$p_U - p_L \triangleq \Delta p = -\rho\left[V\gamma_a(x, t) + b\frac{\partial}{\partial t}\int_{-1}^{x}\gamma_a(\xi, t)d\xi\right]$$

For sinusoidal oscillatory motion, then

$$\frac{\Delta\bar{p}(x^*)}{\rho V} = -\bar{\gamma}_a(x^*) - ik\int_{-1}^{x^*}\gamma_a(\xi^*)d\xi^* \quad (10)$$

This equation can be evaluated in terms of downwash on the airfoil, $\bar{v}_a(\xi)$, by substituting Eqs. (8) and (9) in the appropriate form. It can be shown thus that the equation for the unsteady pressure distribution becomes

$$\frac{-\Delta\bar{p}(x^*)}{\rho r'\Omega} = \frac{(2i/\pi)[H_0^{(2)}(k) + 2J_0(k)W]}{H_1^{(2)}(k) + iH_0^{(2)}(k) + 2[J_1(k) + iJ_0(k)]W}\times\int_{-1}^{1}\sqrt{\frac{1-x^*}{1+x^*}}\sqrt{\frac{1+\xi}{1-\xi}}\bar{v}_a(\xi)d\xi + \frac{2}{\pi}\int_{-1}^{1}\left[\sqrt{\frac{1-x^*}{1+x^*}}\sqrt{\frac{1+\xi}{1-\xi}}\frac{1}{x^*-\xi} - ik\Omega_1(x^*, \xi)\right]\bar{v}_a(\xi)d\xi \quad (11)$$

where

$$\Omega_1(x^*, \xi) = \frac{1}{2}\ln\left[\frac{1-x^*\xi+\sqrt{1-\xi^2}\sqrt{1-x^{*2}}}{1-x^*\xi-\sqrt{1-\xi^2}\sqrt{1-x^{*2}}}\right]$$

Eq. (11) may be recognized as being in the same form as the corresponding equation for the two-dimensional fixed-wing oscillating in incompressible flow. If the factor multiplying the first integral is written as

$$(2/\pi)\ [1 - C'(k, m, h)]$$

† A more complete derivation is presented in Cornell Aeronautical Laboratory Report No. 75. The fact that a solution for the unsteady pressure distribution can be effected using published results for an airfoil entering a generalized gust was suggested by Dr. N. Rott from the floor during the January, 1956, Annual IAS Meeting. This latter method, following the original approach of Sears (in the Journal of the Aeronautical Sciences, Vol. 8, No. 3, p. 104, January, 1941), was developed completely by Dr. N. Kemp in subsequent correspondence with the author and provides an alternate means of development.

the function $C'(k, m, h)$ is directly analogous to Theodorsen's well-known lift deficiency function, $C(k)$, given in reference 12. Since the integrals required to solve for lift and moment remain unchanged, all the previous derivations of two-dimensional lift and moment on oscillating airfoils (for example, see reference 13) apply for the case considered here.

The function $C'(k, m, h)$ is obtained from the definition,

$$\frac{2}{\pi}[1 - C') = \frac{2i}{\pi}\frac{[H_0^{(2)}(k) + 2J_0(k)W(kh, m)]}{[H_1^{(2)}(k) + iH_0^{(2)}(k)] + 2[J_1(k) + iJ_0(k)]W(kh, m)}$$

so that

$$C'(k, m, h) = \frac{H_1^{(2)}(k) + 2J_1(k)W(kh, m)}{H_1^{(2)}(k) + iH_0^{(2)}(k) + 2[J_1(k) + iJ_0(k)]W(kh, m)} \tag{12}$$

This modified deficiency function can, of course, be separated into real and imaginary parts, as is done in the classical flutter case,

$$C'(k, m, h) = F'(k, m, h) + iG'(k, m, h)$$

and the oscillatory lift and moment for a helicopter rotor at low inflows can be calculated by the following familiar expressions, using the notation of reference 13, where F' and G', functions of k, m, and h (or of k, m, h, Q, and ψ_q in the case of multibladed rotors), have been substituted for F and G, Theodorsen's functions of k.

$$\left.\begin{aligned} L_h &= 1 - j2(1/k)(F' + jG') \\ L_\alpha &= (1/2) - j(1/k)\{1 + 2(F' + jG')\} - 2(1/k)^2(F' + jG') \\ M_h &= 1/2 \\ M_\alpha &= (3/8) - j\left(\frac{1}{k}\right) \end{aligned}\right\} \tag{13}$$

It will be noted that the moment expressions are unaffected by the wake since in reference 13 the moments are taken about the quarter chord.

(4) The Equivalent Single-Bladed Rotor

A number of general observations are pertinent regarding the new lift-deficiency function given by Eq. (12). It is clear that $C'(k, h, m, Q, \psi_q)$ approaches the Theodorsen function, $C(k)$, as W approaches zero. From Eq. (7) it may be seen that this limit, which expresses the negligible effect of vorticity below the rotor plane, occurs as would be expected, as the spacing between the rows, h, becomes infinite. It should be further noted from Eq. (7) that, although the parameters k and m are related through the expression $k = m/r$, the actual value of m is important in the expression for k, whereas when it appears as a phase angle, only the noninteger portion is of consequence.

For the case of a single-bladed rotor, one may write

$$W = 1/(e^{kh}e^{i2\pi m} - 1) \tag{14}$$

Now, the following facts are pertinent regarding a particular multi-bladed rotor whose blades are moving with prescribed relative phase, ψ_q. The parameter k expresses the number of oscillations in vortex strength which occur within a semichord length behind the reference airfoil. Thus, the value of k is directly tied to the motion of the reference airfoil and (since it is assumed that all blades are oscillating at the same frequency) is uninfluenced by the number of blades in the rotor. Because of the form of the aerodynamic model, however, the reference airfoil cannot differentiate between vortices shed by preceding blades and those which it shed in previous revolutions.

Thus, the fact that there are two additional parameters associated with the unattached wake—namely, h and m—and that W is a complex number (with two independent components) suggests that for a multibladed rotor under any condition of inflow and with arbitrary frequency ratio, m, there is a single-bladed rotor with equivalent values of h and m that has the same value of W.

Consider a two-bladed rotor:

$$W_{q=2} = (1 + e^{kh_2}e^{i\pi m_2}e^{i\psi})/(e^{2kh_2}e^{i2\pi m_2} - 1)$$

For the special case where $\psi = 0$,

$$W_{\substack{Q=2\\ \psi=0}} = (1 + e^{kh_2}e^{i\pi m_2})/(e^{2kh_2}e^{i2\pi m_2} - 1) = 1/(e^{kh_2}e^{i\pi m_2} - 1)$$

which can be equated to the function W, for a single-bladed rotor under equivalent conditions, thus,

$$W_{\substack{Q=2\\ \psi=0}} = W_{Q=1} = 1/(e^{kh_2}e^{i\pi m_2} - 1) = 1/(e^{kh_e}e^{i2\pi m_e} - 1)$$

so that $h_e = h_2$, which can be written as $u_e = u_2/2$ and $m_e = m_2/2$. Likewise, if $\psi = \pi$, then

$$h_e = h_2 \qquad \text{or} \qquad u_e = u_2/2$$

and

$$m_e = (m_2/2) + (1/2)$$

Likewise, for a three-bladed rotor,

$$W_{Q=3} = \frac{1 + e^{2kh_3}e^{i(4/3)\pi m_3}e^{i\psi_1} + e^{kh_3}e^{i\psi_2}}{e^{kh_3}e^{i2\pi m_3} - 1}$$

and, for $\psi_1 = \psi_2 = 0$,

$$W_{\substack{Q=3\\ \psi_q=0}} = \frac{e^{2kh_3}e^{i(4/3)\pi m_3} + e^{kh_3}e^{i(2/3)\pi m_3} + 1}{[e^{kh_3}e^{i(2/3)\pi m_3} - 1][e^{2kh_3}e^{i(4/3)\pi m_3} + e^{kh_3}e^{i(2/3)\pi m_3} + 1]} = \frac{1}{e^{kh_e}e^{i2\pi m_e} - 1}$$

so that

$$h_e = h_3 \qquad (\text{or } u_e = u_3/3)$$

and

$$m_e = m_3/3$$

In general, for "collective pitch" type disturbances—i.e., where $\psi_q = 0$,

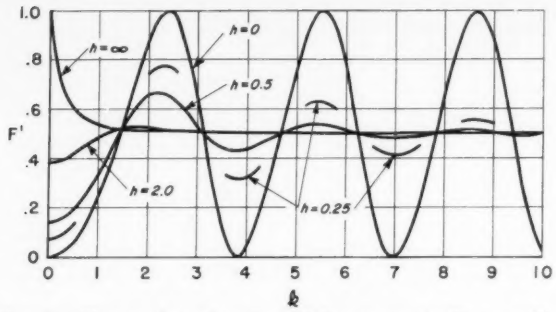

FIG. 5. F' versus k as a function of inflow parameter (for $m = 0$)

$$W_{\text{collective}} = \frac{1 + \sum_{q=1}^{Q-1} \left\{ e^{khQ} e^{i2\pi m} \right\}^{(Q-q)/Q}}{e^{khQ} e^{i2\pi m} - 1} \qquad (15)$$

which always results in $h_c = h_Q$ and $m_c = m_Q/Q$. For "cyclic pitch" type disturbances, $\psi_q = 2\pi(q/Q)(\omega/\Omega)$,

$$W_{\text{cyclic}} = \frac{1 + e^{khQ} e^{i2\pi m} \sum_{q=1}^{Q-1} e^{-khq}}{e^{khQ} e^{i2\pi m} - 1} \qquad (16)$$

The latter expression for ψ_q expresses the fact that each blade is experiencing the same disturbance as it passes a fixed point in space.

Since the unsteady air forces on a blade of an arbitrary rotor can be expressed in terms of those of a single-bladed rotor through the equivalent W function, as discussed above, the remaining general discussion shall be concerned with the case of a single-bladed rotor.

For this case, the real and imaginary parts of the lift deficiency function are given by

$$F'(k, m, h) = \frac{J_1\alpha A - (Y_1 + \beta J_1)B}{A^2 + B^2}$$

$$-G'(k, m, h) = \frac{(Y_1 + \beta J_1)A + J_1\alpha B}{A^2 + B^2}$$

where

$$A = J_1\alpha + Y_0 + J_0\beta$$
$$-B = Y_1 + J_1\beta - J_0\alpha$$

and

$$\alpha = \frac{e^{kh} - e^{-kh}}{e^{kh} - 2\cos 2\pi m + e^{-kh}}$$

$$\beta = \frac{2\sin 2\pi m}{e^{kh} - 2\cos 2\pi m + e^{-kh}}$$

Here again it is clear that as the spacing between rows of vorticity, h, becomes infinite, $F' \to F$ and $G' \to G$. On the other hand, since k and h appear as a product in the same terms resulting from the additional vorticity, $C'(k, m, h) \to C(k) \to 0.5$ as $k \to \infty$. This is physically interpretable as due to the fact that as the number of oscillations in vorticity within a given length becomes infinite, the distribution of vorticity below the rotor plane approaches symmetry about any point on the airfoil, so that the contributions of this vorticity to the net downwash at any point on the airfoil approaches zero.

Other limiting cases of interest occur when k and/or h approach zero. When h is zero, all the vorticity lies in the plane of the airfoil; if, in addition, m is integer,

$$C'(k, \text{integer}, 0) = \frac{J_1(k)}{J_1(k) + iJ_0(k)}$$

If $h \to 0$, $m \neq$ integer, and $k \to 0$ (by virtue of $r \to \infty$), then $C'(0, m, 0) \to C(0) \to 1$. Finally, if $k \to 0$ and $m \to 0$ or integer,

$$C'(0, \text{integer}, h) \to h/(h + \pi)$$

When $h = 0$, the meaning of any of these results, physically speaking, is not clear. The assumptions of zero thickness for both airfoil and wakes, and that the wakes are undisplaced from their trailing planes are all, of course, unrealistic.

Fig. 5 shows the real part of the lift deficiency function, F', plotted versus the reduced frequency for various values of the spacing and zero phase between successive rows of vorticity. Beyond a certain value of k, the function looks very much like a damped sinusoid which oscillates about the curve for infinite spacing—i.e., Theodorsen's function. The "damping" of these curves depends on the inflow ratio, or spacing, and the curve for $h = 0$ oscillates undiminished between 0 and +1. Fig. 6 is a similar plot of the imaginary part of the lift deficiency function, and displays similar characteristics. Beyond a certain value of k, $-G'$ oscillates about Theodorsen's function $-G$ like a damped sinusoid, apparently with the same period as the oscillation in F', but between the limits ± 0.5.

Both F' and $-G'$ oscillate with the same "period" beyond the critical value of k for all values of the phase parameter, m; as m changes, however, the critical value of k and the psuedo-sinusoids are shifted along the k-axis. Because of this periodicity and since the values of k of practical interest are in the lower range, Figs. 7 through 14 are plotted for values of k from 0 to 2.0. Both phase and inflow ratio are seen to affect markedly the lift deficiency function in general; it is of interest that below about $k = 0.5$ and for m near 0.75 the real part of Theodorsen's function represents F' rather well for all values of h. When the spacing between successive rows of vorticity exceeds about 5 chord lengths ($h = 10$), C' does not differ very much from C except near $k = 0$, $m = 0$.

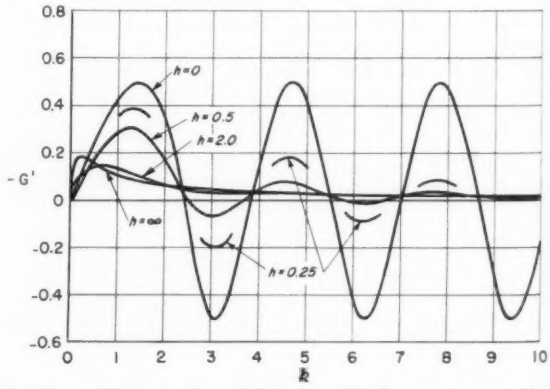

FIG. 6. $-G'$ versus k as a function of inflow parameter (for $m = 0$).

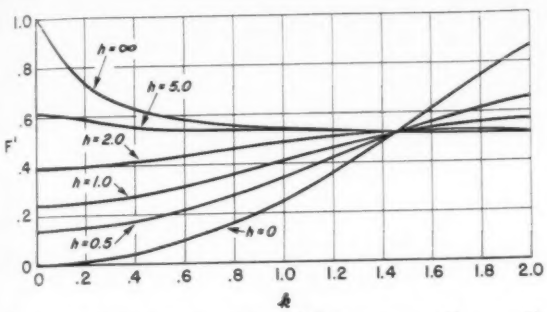

FIG. 7. F' versus k as a function of inflow parameter (for $m = 0$).

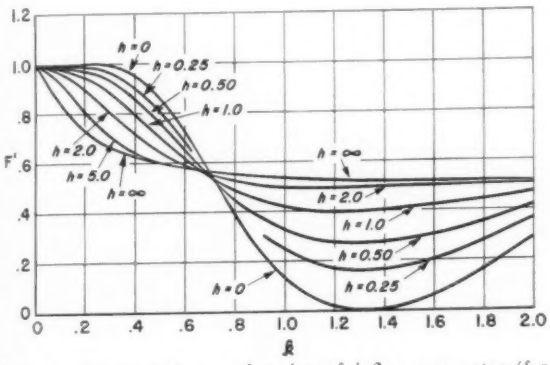

FIG. 8. F' versus k as a function of inflow parameter (for $m = 1/4$).

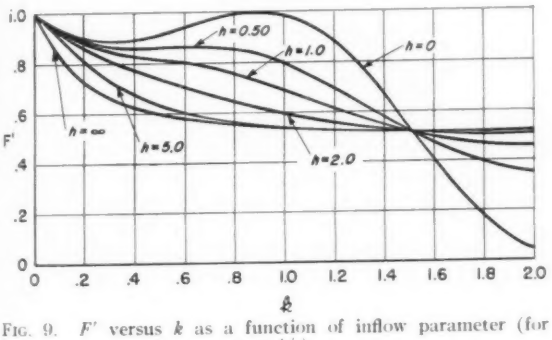

FIG. 9. F' versus k as a function of inflow parameter (for $m = 1/2$).

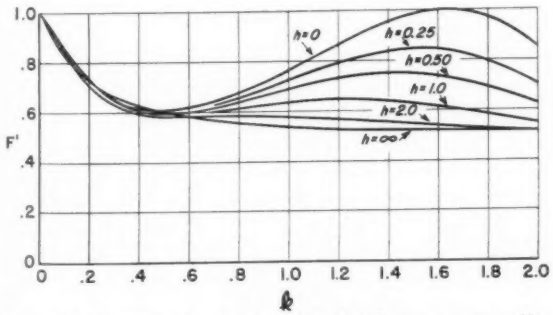

FIG. 10. F' versus k as a function of inflow parameter (for $m = 3/4$).

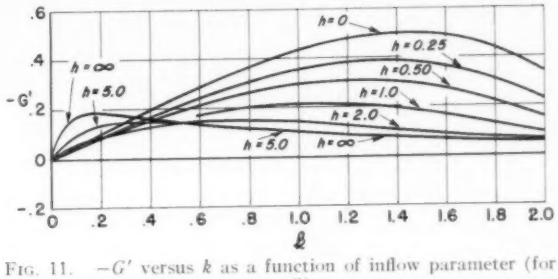

FIG. 11. $-G'$ versus k as a function of inflow parameter (for $m = 0$).

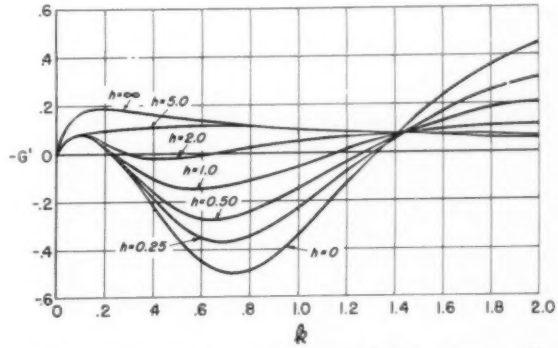

FIG. 12. $-G'$ versus k as a function of inflow parameter (for $m = 1/4$).

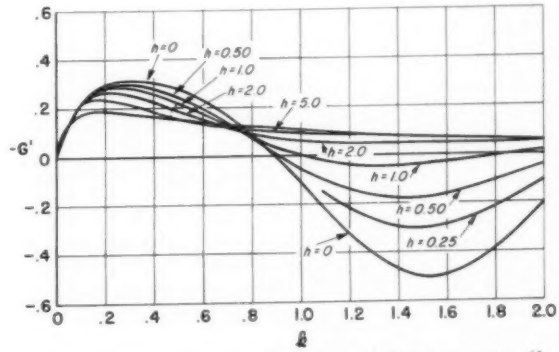

FIG. 13. $-G'$ versus k as a function of inflow parameter (for $m = 1/2$).

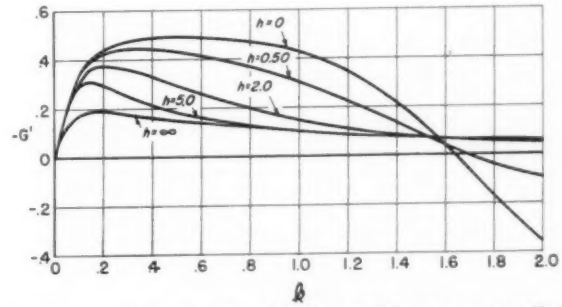

FIG. 14. $-G'$ versus k as a function of inflow parameter (for $m = 3/4$).

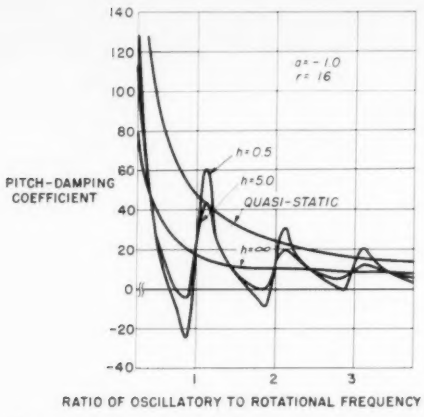

FIG. 15. Pitch-damping coefficient versus frequency ratio as a function of inflow parameter.

For use in dynamic rotary wing calculations, tables of F' and G' as well as the real and imaginary parts of the corresponding values of L_h and L_a are given in reference 14. These results are presented for all combinations of the parameter values listed below:

m	0, 1/8, 1/4, 3/8, 1/2, 5/8, 3/4, 7/8
h	0, 1/4, 1/2, 1, 2, 5, 10, ∞
k	0, 0.1, 0.2, 0.3, 0.4, 0.5, 0.6, 0.7, 0.8, 0.9, 1.0, 1.2, 1.4, 1.6, 1.8, 2.0, 2.5, 3.0, 3.5, 4.0, 4.5, 5.0, 5.5, 6.0, 6.5, 7.0, 7.5, 8.0, 8.5, 9.0, 9.5, 10.0

Note that values for $h = \infty$ (fixed-wing flutter case) and $h = 0$ are included for completeness.

(5) Applications to Rotor Analysis Problems

While the analytical attack employed in this development is two-dimensional, the coefficients derived herein may be used as a "strip theory" as well as in "typical section" analyses. For example, if the rotor geometry is given, and inflow as a function of radius and the rotational speed are known as operating conditions, then the parameter h is known for as many radial stations as desired. If, further, the oscillatory frequency, ω, is assumed, the remaining parameters m and k are defined. It will be noted that m is constant with blade span, but k varies as the semichord divided by the radius. It is thus apparent that the values of k and h may vary markedly over the blade span, and also that k, h, and m will have widely different values depending on the operating conditions and the phenomenon being investigated.

From review of the basic simplifying assumptions, it may be concluded that the new coefficients provide a good approximation (1) for low inflows, where deviations from fixed wing theory are greatest, and (2) where $k > 1$. The latter stipulation is analogous to cases where finite span corrections are unnecessary in fixed-wing flutter theory. It is clear from the proportions of the usual helicopter and propeller blades, however, that, for $k > 1$ near the blade tips, ω/Ω must be a large number.

Any of the standard methods of flutter analysis can be used to solve the equations of motion arrived at using the present coefficients. Their application appears to involve the least error for the phenomenon first reported in reference 7 as "wake-excited flutter" which occurs at low inflows with ω to Ω ratios as high as 20.0. The oscillatory frequency in these cases seemed nearly equal to that of the fundamental torsion mode; one might have therefore expected a forced excitation at resonant frequency where there is low damping, or a single degree of freedom instability. The former is implied in reference 7, whereas the tests reported in reference 6 revealed a region of instability. Figs. 15 through 19 were plotted to investigate the possibility of pitch instability. They show curves of the coefficient for damping in pitch for particular blade stations and pitch axis locations and various values of inflow. The form of this coefficient is the same as that given in reference 15—namely,

$$(1/k)\{[(1/2) - a] - [(1/2) + a](2G'/k) - [(1/4) - a^2]2F'\}$$

where a is the pitch axis location measured aft of the mid-chord in semichords. The damping moment per unit span is obtained from the coefficient for an airfoil oscillating in harmonic motion with frequency ω, through an angle θ, by multiplying by $\pi\rho b^4\omega^2\theta$. These curves reveal that negative damping can exist when the oscillatory frequencies are certain close-to-integer multiples of the rotor speed. The possibility of single degree of freedom flutter is, therefore, shown to exist using the new coefficients.

Fig. 17 is presented to emphasize the fact that, with the rotational axis on the quarter chord, the wake can have no influence on the airfoil moments. It is thus clear from these figures that as the pitching axis is moved aft from the leading edge, the "peak" values of negative damping become more stable, until there is no possibility of instability with the pitch axis on the quarter chord. As the pitch axis moves aft of the quarter chord to the midchord, negative damping appears again.

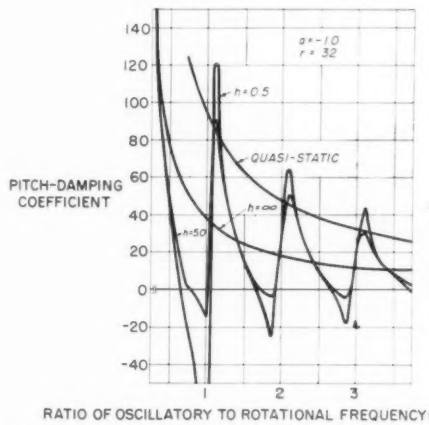

FIG. 16. Pitch-damping coefficient versus frequency ratio as a function of inflow parameter.

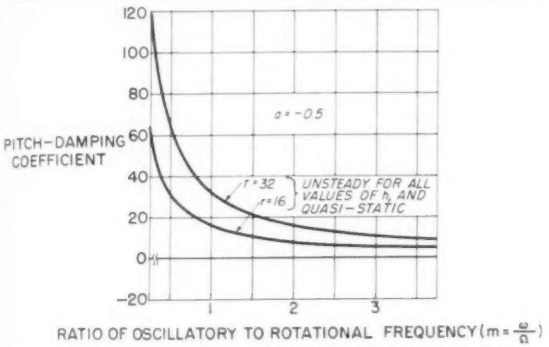
PITCH-DAMPING COEFFICIENT
a = -0.5
r = 32
r = 16
UNSTEADY FOR ALL VALUES OF h AND QUASI-STATIC
RATIO OF OSCILLATORY TO ROTATIONAL FREQUENCY (m = ω/Ω)

FIG. 17. Pitch-damping coefficient versus frequency ratio.

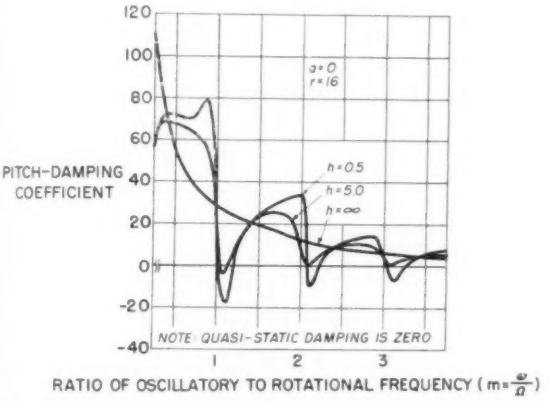

FIG. 18. Pitch-damping coefficient versus frequency ratio as a function of inflow parameter.

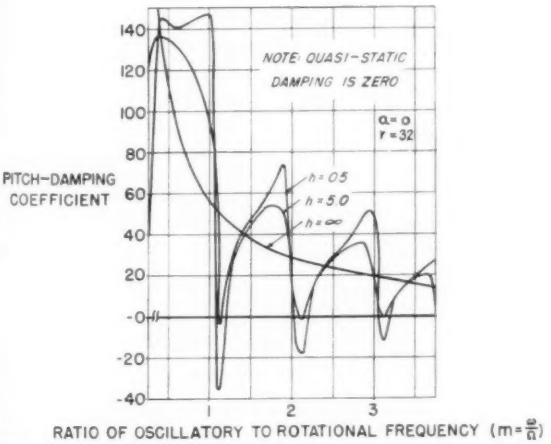

FIG. 19. Pitch-damping coefficient versus frequency ratio as a function of inflow parameter.

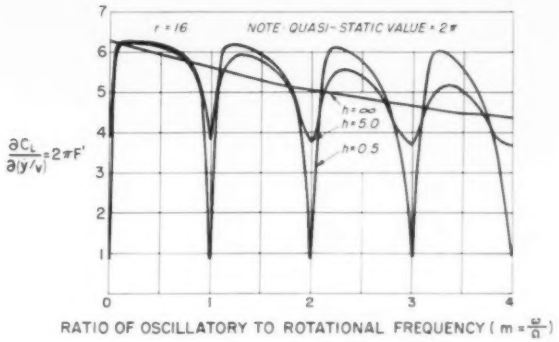

FIG. 20. Flap-damping coefficient versus frequency ratio as a function of inflow parameter.

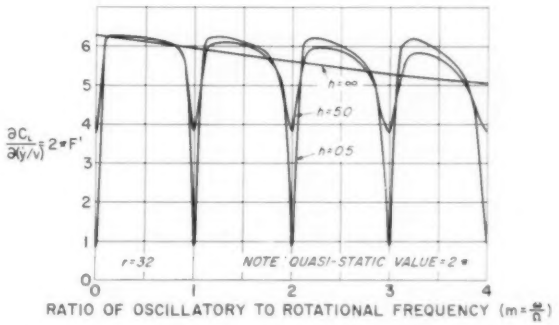

FIG. 21. Flap-damping coefficient versus frequency ratio as a function of inflow parameter.

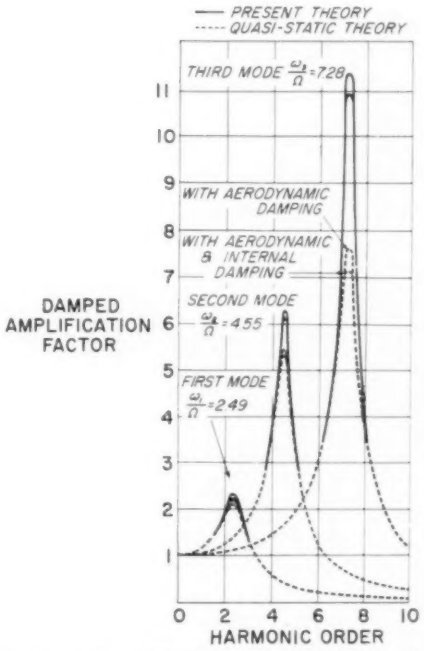

FIG. 22. Damped amplification factor versus harmonic order.

Since "wake-excited flutter" has been encountered with blades which have pitch axes essentially on the quarter chord, it appears that such cases cannot be interpreted merely as single degree of freedom flutter in pitch. A more likely explanation is suggested in Figs. 20 and 21, which show that flap-damping can go to very low (but positive) values at integer values of the frequency ratio. It thus seems likely that "wake excited flutter" is actually a classical type of flutter in which at least some of the aerodynamic derivatives are greatly modified due to the vorticity shed by preceding blades and/or in previous revolutions. This large change in the unsteady aerodynamic coefficients with frequency ratio at low inflow suggests itself as the mechanism by which it is possible to obtain two distinct types of classical flutter with one blade configuration which has only two degrees of freedom, as reported in reference 6.

Damped amplification factors have been applied to the problem of predicting rotor blade stresses by Goland and Flax[16] and others, using quasi-static aerodynamics to determine the value of damping. Fig. 22 is a comparison of the amplification factor curves computed for an existing helicopter blade using quasi-static aerodynamics and the coefficients of the present theory for a single-bladed rotor. The quasi-static curves are those calculated by Daughaday and Kline and presented in reference 1. This example is typical of good blade design, since the first three natural bending frequencies are removed from integer orders of rotor speed. The significant fact illustrated by these curves is that the aerodynamic damping, and hence the peak amplification factor, is critically dependent upon how close the frequency ratio, $m = \omega/\Omega$, is to an integer number. From Figs. 20 and 21, it is clear that the peaks of the curves obtained with the present theory could be higher still if m were closer to an integer number. The inflow ratio chosen for this calculation is roughly that of presently operational helicopters in hovering flight at maximum gross weight and was assumed constant over the blade radius. The effect of inflow can be to raise or lower these peaks, depending on the frequency ratio. In using the coefficients for a single bladed rotor directly, it is tacitly assumed that only one blade has been disturbed. Actually, the blade bending moment problem, being closely associated with the azimuthal distribution of downwash over the rotor disc, falls into the classification of "cyclic" disturbances described in Eq. (16). It is intuitively obvious and can be easily shown, using Eq. (16), that the spacing, h, between rows of vorticity for a Q-bladed rotor oscillating at integer multiples of rotor speed is effectively $1/Q$ that of a one-bladed rotor with the same value of inflow. From this it is clear that, when m is near integer, the more blades in a rotor producing a given force, the higher will be the amplification factor peaks. It should be noted that this effect is in addition to the reduction in flap damping resulting from the decrease in blade chord which often accompanies an increase in the number of blades in a rotor and which is compensated for, since the generalized exciting force is also proportional to the chord.

(6) Conclusions

Expressions for two-dimensional oscillatory airfoil coefficients have been derived for rotary wings, taking into account the shed vorticity beneath the plane of the rotor disc. The influence of these modifications to the fixed-wing theory appears only in a modified lift deficiency function. The effects of inflow ratio, number of blades in the rotor, phasing between the motion of adjacent blades, and ratio of oscillatory to rotational frequency have been included and appear as parameters along with the basic "reduced frequency" of fixed-wing unsteady aerodynamics. The results all approach those for fixed wings as the product of inflow ratio and reduced frequency increases. For values of the frequency ratio whose noninteger parts are between, roughly, 1/10 and 9/10, the effects of the out of plane vorticity are significant until the spacing between adjacent rows exceeds about five chord lengths. When the frequency ratio is closer to integer values, the present theory indicates the differences between rotary-wing coefficients and those for fixed wings to be substantial to somewhat higher values of inflow.

Attention has been drawn to the fact that the lift and moment on a blade in a rotor with an arbitrary number of blades (whose motions are in arbitrary phase) can be obtained from the coefficients for an equivalent single-bladed rotor.

From limited calculations, it is concluded that single degree of freedom flutter is possible in pitching motions for rotors operating a low inflow, when the pitch axis location and frequency ratio take on certain values. Similar calculations for flap-damping coefficients reveal that the aerodynamic damping of rotor blades in motion perpendicular to the plane of rotation falls off abruptly as the frequency ratio approaches integer values. Furthermore, in general, the lower the value of inflow, the lower the minimum value of both pitch-damping and flap-damping coefficients.

From these considerations, it is concluded that the quasi-static aerodynamic theory is inadequate for rotor dynamics problems such as calculating critical flutter speeds and/or damped amplification factors. The current trend toward increasing the number of blades per rotor, magnifies the importance of these effects, since an increase in the number of blades acts in general as a reduction in inflow.

Correlative calculations using these coefficients are needed to determine their accuracy and the limits of their practical usefulness; data are available from rotor flutter and response tests which can be used for this purpose. Furthermore, this first and simplified approach to the problem should be extended to include some of the important three-dimensional effects and an attempt made to account for forward speed.

(*Continued on page 144*)

Visualization of Low-Density Flows by Means of Oxygen Absorption of Ultraviolet Radiation†

PAULINE M. SHERMAN*
University of California at Berkeley

SUMMARY

The high absorption of ultraviolet radiation (1,400 Å.–1,500 Å.) by oxygen has been employed to obtain photographs of several flow configurations. A vacuum spectrograph-monochromator-camera with a 1,470 Å. radiation source was adapted for installation in the low-density wind tunnel of the University of California at Berkeley. The photographs taken were of shock waves formed by flow over a sphere, a cone-cylinder, wedges, and a cylinder with axis aligned parallel to the direction of the flow. All photographs were taken at a free-stream Mach Number of ~3.9, with a uniform jet area approximately two in. in diameter at the nozzle exit plane, and a tunnel test chamber static pressure of ~114μ Hg. An analytical method of determining stream density in axially symmetric flow from the absorption of radiation as indicated by the photographs is presented. Limitations of the method are discussed.

SYMBOLS

C = coefficient of absorption divided by gas density
C_1 = constant in linear emulsion response equation
D = density of photographic negative
E = calibration factor $(\ln 10)/\Gamma\rho_1 CL$
F = defined in Eq. (A-4), Appendix
f = defined in Eq. (A-5), Appendix
G = defined in Eq. (A-5), Appendix
I = intensity of radiation
I_0 = intensity of incident radiation
I_i = intensity of radiation incident on developed negative
I_f = intensity of radiation transmitted through developed negative
K_1 = constant in microphotometer-recorder response equation
K_2 = constant in microphotometer-recorder response equation
L = length of radiation path in test chamber, see Fig. A1
p = pressure
R = outside radius of the nonuniform axially symmetric region of flow, see Fig. A1
R_r = gas constant
r = distance from axis of symmetry, see Fig. A1
S = $R^2 - r^2$
t = $R^2 - y^2$
T = absolute temperature
W = reading on Brown recorder of microphotometer signal
x = horizontal coordinate, $x = \sqrt{r^2 - y^2}$, see Fig. A1
$\bar{x}$ = $\sqrt{R^2 - y^2}$, see Fig. A1
y = distance from horizontal plane through axis of symmetry, see Fig. A1
β = $(dW/dy)/(100 - W)\sqrt{y^2 - r^2}$
Γ = slope of negative density, D, vs. energy curve
$\gamma(S)$ = $\rho(r)$
ρ = gas density

Subscripts

1 = values in uniform jet upstream of flow disturbance
2, 3 = values for conditions without flow through the nozzle

Received February 7, 1956.
† Sponsored by Wright Air Development Center.
* Research Engineer, Low Pressure Project.

INTRODUCTION

THE USUAL METHODS of flow visualization (shadowgraph, schlieren interferometer) are not feasible for low gas densities (pressures < 1 mm. Hg). There has been considerable interest, therefore, in developing a new technique which may be used in low-density wind tunnels. One new method is that based on the absorption of ultraviolet radiation by oxygen. The absorption of the ultraviolet is a function of the density of the oxygen. Therefore, the intensity of radiation passing through a region of high density will be less than that passing through a region of low density, and shadows will be formed indicating the flow configuration.

Oxygen has a radiation absorption peak in the ultraviolet region at a wave length of 1,400 Å. to 1,500 Å. In order to make use of this property for flow visualization, it is necessary to produce a collimated, uniform, and high intensity beam of proper wave length which is stable and has a minimum of scattered light or light of other wave lengths in it. Since ultraviolet light is absorbed by most materials, even in thin films, the optical

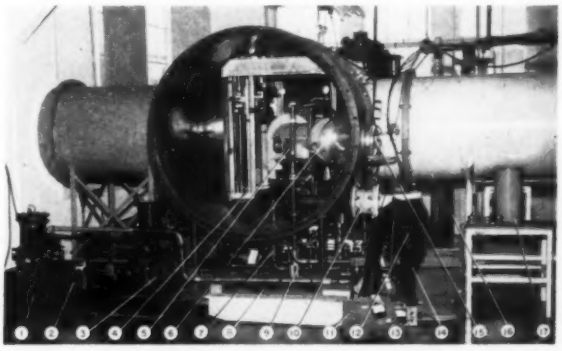

FIG. 1. Arrangement of Spectrograph-Monochromator in tunnel showing auxiliary equipment. (1) 1/2 hp. Kinney mechanical pump. (2) Refrigeration system condenser. (3) 1/2 hp. Kinney mechanical pump. (4) Tunnel traverse mechanism frame. (5) Spectrograph chamber. (6) Lamp chamber. (7) Water cooled vacuum roughing line trap. (8) Lamp cooling oil circulation pump. (9) Heat exchanger for lamp cooling oil. (10) Remotely controlled 1/4 swing valve. (11) Alphatron. (12) Insulated refrigerated trap. (13) Alphatron. (14) Diffusion pump. (15) Lamp access port with window. (16) Tunnel settling chamber. (17) Lamp cooling oil storage tank.

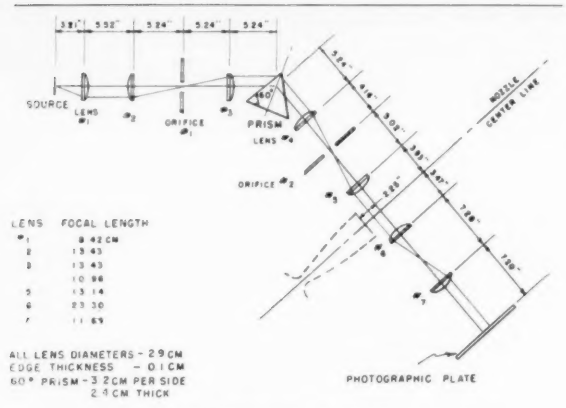

FIG. 2. Calcium fluoride optical system—schematic.

elements must be made of material which absorbs very little of the radiation, yet has the other qualities necessary for making good lenses. A vacuum system is necessary which is clean and tight. A sensitive method of recording the radiation beam attenuation due to the oxygen absorption is also necessary.

R. A. Evans[1] did the pioneer work on the development of a system which meets the aforementioned requirements. He developed a xenon gas discharge lamp (xenon has a resonance line at 1,470 Å.), a vacuum spectrograph-monochromator to isolate the 1,470 Å. wave-length radiation, and a camera for use with the ultraviolet radiation. He obtained some pictures of shock waves formed by transverse cylinders in a small two-dimensional flow field.

The present program was undertaken to investigate the feasibility of the method for use in a large wind tunnel and its capability in yielding quantitative density measurements.

Experimental Apparatus and Procedures

The studies were made in the No. 4 wind tunnel of the University of California Low Pressures Project. The tunnel is an open jet, nonreturn type, operated continuously by a five-stage steam ejector system.[2] Interchangeable axially symmetric nozzles are used to produce flows over a range of Mach Numbers. A Mach 4 nozzle[3] was used for the tests described here. The tunnel facility includes pressure manometers; thermometers; flowrators; thermocouples with recorders, necessary to measure flow properties; and a manifold equipped to handle bottled gas so that the tunnel can be operated on gases other than air. A traverse mechanism inside the test chamber provides for remotely controlled, counter monitored motion in three mutually perpendicular directions.

The radiation source, spectrograph-monochromator, and camera described in reference 1 were modified for the present tunnel installation. The radiation source, an oil-cooled xenon discharge lamp with hot thoriated tungsten electrodes and a quartz envelope, was filled with a 90 per cent neon and 10 per cent xenon mixture to a pressure of 20 mm. Hg. It was operated at 220 volts a.c. with a nominal current of 1 amp. The spectrograph-monochromator, supported rigidly in the wind-tunnel test section (see Figs. 1, 3, and 4,), consisted of a vacuum chamber for the lamp with adjustable lamp support and a vacuum chamber with optical benches on which were mounted adjustable optical element supports. The optical system, of calcium fluoride (CaF_2), is shown schematically in Fig. 2. The spectrograph-monochromator and the camera had a separate vacuum system, shown schematically in Fig. 3.

Five models were chosen for the flow pictures—a $1\frac{3}{8}$ in. diameter sphere, a 90° cone-cylinder of 1-in. diameter base, a 1-in. diameter cylinder with axis parallel to direction of flow; and two 72° wedges, one $1\frac{3}{4}$ in. long and one 4 in. long. All models were made of aluminum, and were supported by long stings attached to the tunnel traverse mechanism. All photographs with flow were made at a flow through the nozzle of 18 lbs./hr. or at a Mach Number of ~3.9 and a test chamber static pressure of ~114 μ Hg.

A photographic emulsion, sensitive to 1,470 Å. radiation, which had good uniformity, high contrast, and low background density was required. Kodak Spectrum Analysis #1 U.V. and Kodak S W R (experimental) were chosen. The exposure time for flow photographs had to be such that for the photographic emulsion used, all portions of the negative were in the region of negative density, D, where the emulsion had a linear response. For the same flow configurations and emulsion a much longer exposure time is necessary for pure oxygen than is required for air. Since the Kodak Spectrum Analysis #1 plates were much less sensitive but were more uniform and of higher contrast than the Kodak S W R plates, they were used for all the pictures taken with air flow. The Kodak S W R plates were used with pure oxygen flow where too long an exposure time would be necessary for Spectrum Analysis #1 plates. The S W R plates were exposed 90 sec. The Spectrum Analysis #1 plates were exposed 50 to 60 sec. Calibration exposures were made on each plate at appropriate pressures without flow through the nozzle.

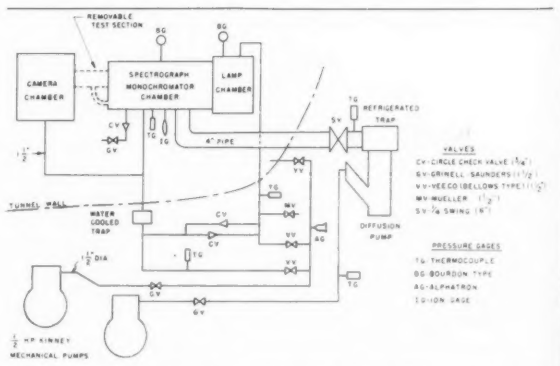

FIG. 3. Schematic of Spectrograph-Monochromator-camera vacuum system.

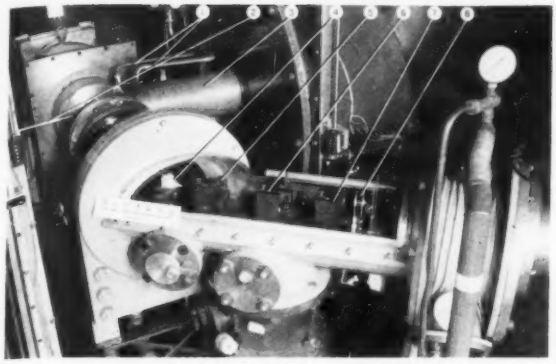

FIG. 4. Spectrograph-Monochromator with covers off in tunnel. (1) Pressure tap lead tubes for jet-test chamber pressure balancing. (2) Model sting. (3) Nozzle. (4) Prism. (5) Lens #3 mounting. (6) Orifice #1 mounting. (7) Lens #2 mounting. (8) Shutter.

The photographic negatives were studied by means of a Zeiss microphotometer modified to record on a Brown Function Plotter an indication of negative density as a function of position on the negative. The microphotometer photocell output was fed into an electrometer and the amplified signal fed to the Brown. The recording roll was driven by a selsyn, with reversing switch, geared to the traversing drive of the microphotometer.

ANALYTICAL PROCEDURES

Mack[4] derived a theoretical expression relating the density of a gas in axially symmetrical flow (with zero density at the outer boundary of the flow) to the absorption of a beam of radiation perpendicular to the axis of flow. In the Appendix a similar expression is derived which is appropriate for an actual density measurement of a flow having a finite density, ρ_1, at the boundary. From the Appendix, for a parallel beam of radiation of constant intensity,

$$\frac{\rho(r)}{\rho_1} - 1 = E\frac{L}{\pi}\int_r^R \beta[W(y), r]\, dy \qquad (1)$$

where

$$E \equiv \frac{(\rho_3 - \rho_2)/\rho_1}{\log\,[(100 - W_3)/(100 - W_2)]} = \frac{1}{\rho_1}\,\frac{\partial\rho_2}{\partial[\log\,(100 - W_2)]}$$

$$\beta \equiv \frac{dW/dy}{(100 - W)\sqrt{y^2 - r^2}}$$

ρ is the gas density in the axially symmetric flow region and is, therefore, a function of r, the distance from the axis of symmetry (see Fig. A1). R is the value of r at which the gas density becomes ρ_1. ρ_1 is the value of the gas density in the uniform stream upstream of the flow disturbance. Subscripts 2 and 3 pertain to calibration values obtained under conditions of no-flow. L is the length of the radiation path in the test section, that is, the distance between the outside lenses #5 and #6. y is the distance from the horizontal plane through the axis of symmetry (see Fig. A1). W is the reading on the Brown recorder in arbitrary units of divisions of the recorder chart paper. W is, therefore, a function [see Eq. (A-14)] of the radiation intensity striking the photographic plate. E is a function [see Eq. (A-18)] of film characteristics.

E is determined by means of two or more calibration exposures where the pressure and temperature or density ratios are known and the corresponding readings W_2 and W_3 are taken with the microdensitometer. W and dW/dy are determined for a series of values of y from the trace on the Brown recorder. For a chosen r, β is plotted as a function of y and the integration is performed graphically.

The analysis of the Appendix is possible only if the traverse, which is made perpendicular to the body axis, can extend into the region of known flow conditions. The flow picture must therefore include a region of known undisturbed flow in the plane perpendicular to the axis of symmetry through the region of unknown flow properties to be analyzed. Thus, there are limitations on the geometries of flow regions which can be analyzed with a radiation beam of given cross-sectional area.

EXPERIMENTAL RESULTS

Some of the shock-wave photographs obtained are shown in Fig. 5. Figs. 5(a), (b), and (c) are photographs taken in pure oxygen of shock waves formed in front of a cone-cylinder. Most of the local variation in photograph density is due to the photographic process rather than to the flow configuration, although the body was moved to a somewhat different position in each case so that a different part of the shock wave could be seen. The effect of radiation path length is particularly noticeable in this case where the shock wave change in density becomes more apparent as the effective path length increases with distance from the cone vertex. Fig. 5(d) was taken in air, and the result of a relatively long effective radiation path ($\sim 1\frac{3}{4}$ in.) is readily seen in the high contrast of the region before the shock with that in back of the shock. Fig. 5(e) is

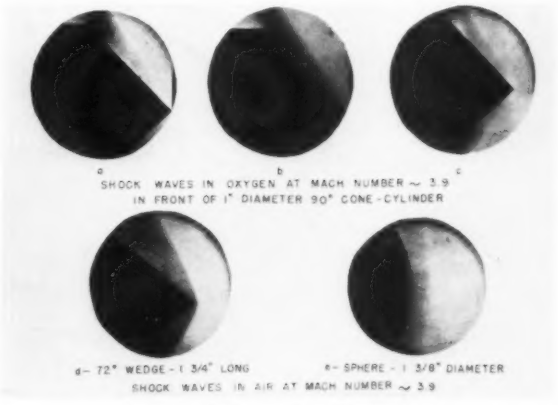
a
b
c
SHOCK WAVES IN OXYGEN AT MACH NUMBER ~ 3.9
IN FRONT OF 1" DIAMETER 90° CONE-CYLINDER
d- 72° WEDGE - 1 3/4" LONG
e- SPHERE - 1 3/8" DIAMETER
SHOCK WAVES IN AIR AT MACH NUMBER ~ 3.9

FIG. 5. Shock wave photographs.

a similar photograph but of an axially symmetrical configuration.

Fig. 6 shows a typical shock-wave trace with three calibration traces. The shock-wave trace was taken perpendicular to the axis of symmetry, at a location approximately 1/4 of the distance from cone vertex to shoulder. It was obtained from the same negative as Fig. 5(a). Ideally, for a uniform radiation beam, the calibration traces should be perfectly straight lines. Similar slopes at different absolute values would simply indicate a nonuniformity in the radiation beam. However, the somewhat strange emulsion response shown is difficult to explain with the limited quantity of data taken. Unfortunately, this response was not detectable either by the naked eye or a Weston Model #877 densitometer and, therefore, was not anticipated. The limited emulsion response data made the inaccuracy too large for any density analysis to be significant.

Discussion of Limiting Conditions on the Method

In order to examine the effects of the physical parameters more easily, a simple two dimensional configuration will be considered. Consider Eq. (A-2) of the Appendix for $\rho = \rho_1 =$ constant, $(2\bar{x} = L)$, for each of two values of density ρ_2 and ρ_3. The difference may be written

$$\ln (I_2/I_3) = (\rho_3 - \rho_2)CL = [(\rho_3/\rho_2) - 1](CL\, p_2/R_c T_2) \quad (2)$$

where R_c is the gas constant and I_2, I_3 are the radiation intensities after passing a distance L through oxygen of densities ρ_2, ρ_3, respectively. $C\rho$ is $\simeq 350$ cm.$^{-1}$ (see reference 5) for pure oxygen at N T P and 1,470 Å. radiation. Therefore, C/R_c is ~ 125 [°K./(cm.-mm. Hg)] and

$$\ln (I_2/I_3) = 125[(\rho_3/\rho_2) - 1](p_2/T_2)L \quad (3)$$

Fig. 7 is a plot of this equation.

It can be seen that there are practical limitations in the detection of resultant radiation. For a limited path length, if the density is low, $\ln (I_2/I_3)$ may be too close to the noise level of the system for good results. If the density is high, the signal may be too small to detect. This would mean a prohibitive exposure time if the photographic technique is employed. In the latter case, however, a gas mixture of a small quantity of oxygen and a large quantity of a gas with a low absorption coefficient, might be used; so that even though the overall gas density is high, the density effecting the radiation attenuation, the density of the oxygen, remains low.

For the S W R emulsion of Figs. 5(a), (b), and (c), a negative density difference $D_2 - D_3 \simeq 0.2$ corre-

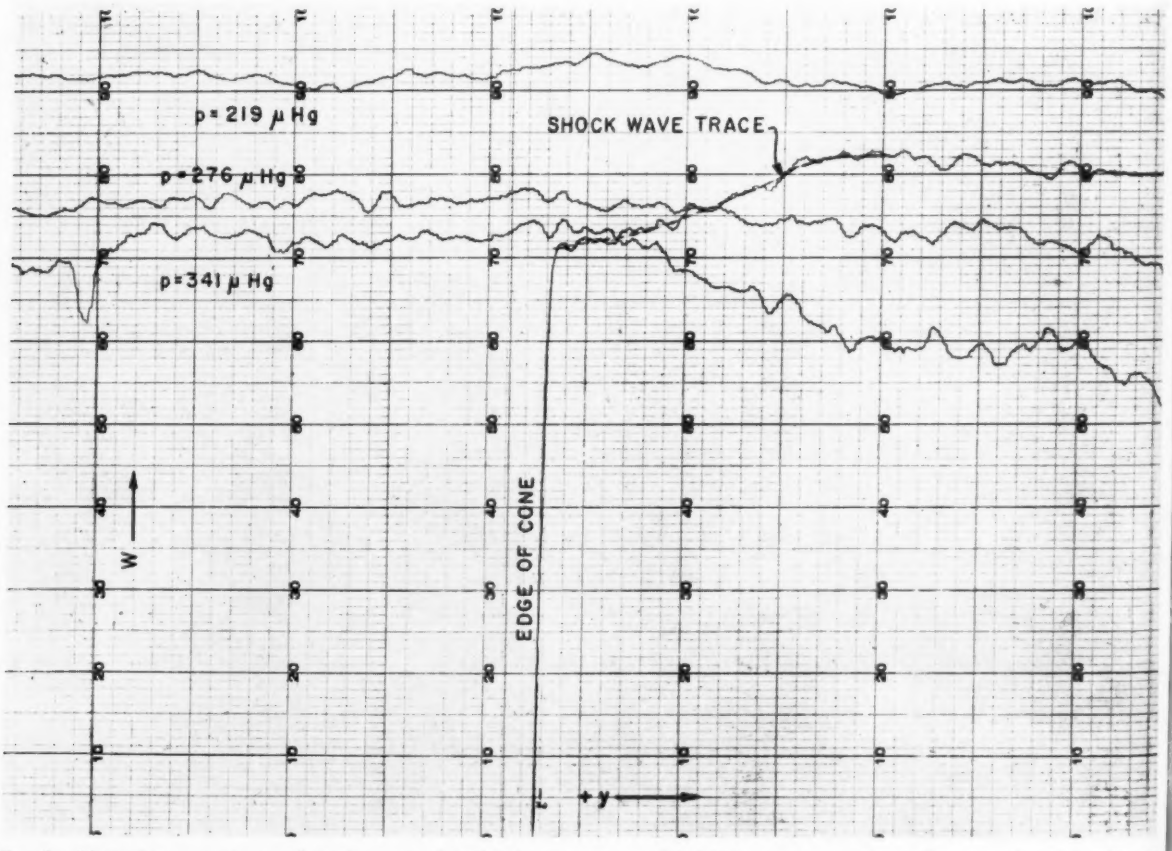

Fig. 6. Microphotometer traces of shock wave and calibration traverses, ~5.9 divisions per mm. of negative, scanning spot 150μ × 150μ.

sponds to $\ln (I_2 / I_3) \simeq 0.5$. This is a minimum level for a good measurement with the S W R emulsion. This means that, for conditions described by the area below $\ln (I_2 / I_3) \simeq 0.5$ in Fig. 7, the present photographic process cannot be used.

Conclusions

Density measurements are possible by the ultraviolet radiation absorption method. The main limitations on the method may be summarized as follows: (1) Long effective radiation paths are necessary through density fields of small gradients. (2) With a radiation source of finite intensity, the exposure time necessary in high density regions with long radiation paths is prohibitive. (3) The photographic detection of the transmitted radiation with present day commercial ultraviolet sensitive emulsions requires that a large number of calibration and flow photographs be taken to provide sufficient data for a statistical analysis. The statistical analysis is necessary because of variations in emulsion response. This may not be a limitation when better emulsions are developed.

In order to achieve a system possessing the simplicity and reliability necessary in a practical wind-tunnel instrument, modifications of the apparatus employed in the present tests are essential. It is recommended that, before other studies are made, the following be investigated: (a) Use of a phototube instead of a camera for detection purposes. With a phototube detector a lamp of greater intensity may be required. (b) Development of a fluorescent screen to facilitate optical alignment and focusing. (c) Construction of remotely controlled positive positioning mountings for the lenses, orifices, and prism, with verniers to permit optical adjustment under vacuum conditions. (d) Design of a simplified optical system having fewer optical elements. (The optical system constructed included a spectrograph test section for lamp development purposes which is not necessary for the present application of the equipment.)

Appendix

Determination of Gas Density in Axially Symmetric Flow by the Absorption of a Beam of Radiation

If a beam of radiation is directed in the positive x direction (see Fig. A1), the radiation intensity $I(x, y)$ decays according to the well known law which may be expressed as

$$\partial I / \partial x = -C\rho I \qquad \text{(A-1)}$$

where C is a known positive constant, ρ the gas density, and x the horizontal coordinate. When the gas flow is axisymmetric, the gas density is a function of r, the radial distance. If radiation of intensity $I_0(y)$ is incident on the region considered, parallel to x axis, then $I(y)$ will emerge and, from Fig. A1,

$$\ln I(y) - \ln I_0(y) = -2C\int_0^{\bar{x}} \rho dx - C\rho_1(L - 2\bar{x}) \equiv F(y) \qquad \text{(A-2)}$$

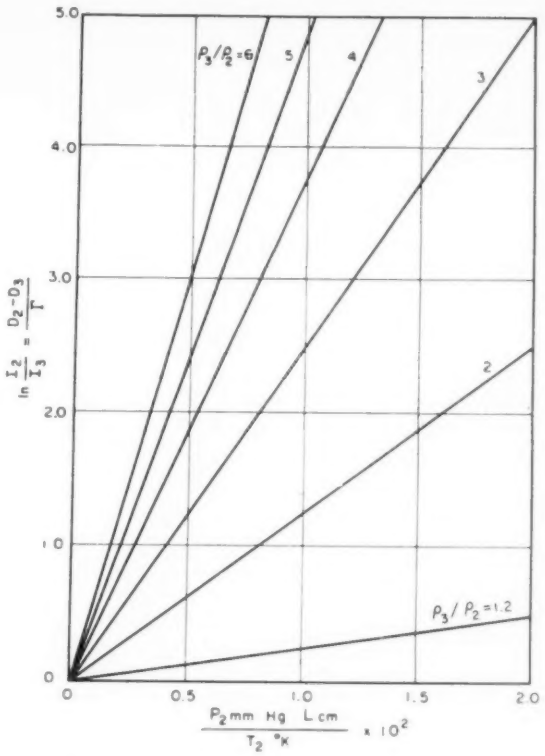

FIG. 7. Flow parameters vs. radiation intensity ratio for oxygen.

where $\bar{x} = \sqrt{R^2 - y^2}$ and where ρ_1 is the known density in the region outside $(r > R)$ the axially symmetric region. Of course, this assumes the radiation beam is parallel to the x axis and that the refraction is negligible.

Since $r^2 = x^2 + y^2$, it follows that for y constant $r\,dr = x\,dx = \sqrt{r^2 - y^2}\,dx$. When $x = 0$, $r = y$, and when $x = \bar{x}$, $r = R$, so

$$F(y) = -2C\int_y^R \frac{r\rho(r)\,dr}{\sqrt{r^2 - y^2}} - C\rho_1(L - 2\sqrt{R^2 - y^2}) \qquad \text{(A-3)}$$

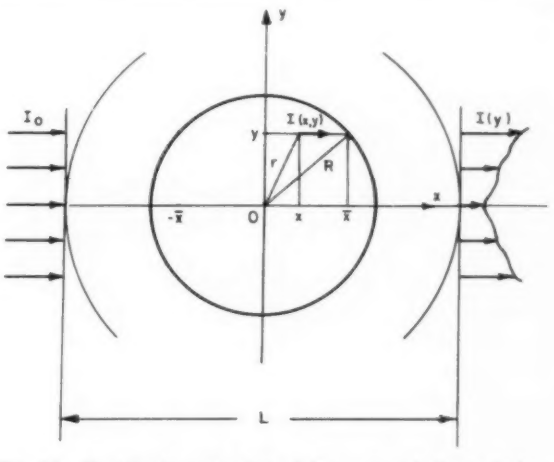

FIG. A1. Coordinate system for axially symmetric flow solution.

A second change of variable may be made by putting $S = R^2 - r^2$ and $\gamma(S) = \rho(r)$. Then $dS = -2r\,dr$, $S = R^2 - y^2$ at $r = y$, and $S = 0$ at $r = R$. Then

$$F(y) = C\int_{R^2-y^2}^{0} \frac{\gamma(S)\,dS}{\sqrt{R^2 - y^2 - S}} - C\rho_1(L - 2\sqrt{R^2 - y^2}) \quad \text{(A-4)}$$

which may be simplified by substituting $t = R^2 - y^2$. Then

$$f(y) = F(y) + C\rho_1(L - 2\sqrt{R^2 - y^2}) = -C\int_0^t \frac{\gamma(S)\,t\,dS}{\sqrt{t - S}} \equiv G(t) \quad \text{(A-5)}$$

Eq. (A-5) is of the Abel type[6] with unknown $\gamma(S)$ and has the solution

$$\gamma(S) = -\frac{1}{\pi C}\frac{d}{dS}\int_0^S \frac{G(t)\,dt}{\sqrt{S - t}} \quad \text{(A-6)}$$

or, after integration by parts,

$$\gamma(S) = -\frac{1}{\pi C}\frac{G(0)}{\sqrt{S}} - \frac{1}{\pi C}\int_0^S \frac{G'(t)\,dt}{\sqrt{S - t}} \quad \text{(A-7)}$$

where $G'(t) = (d/dt)G(t)$ $\quad G(0) = f(R) = 0$

Now $G'(t)\,dt = f'(y)\,dy$ and $y = R$ when $t = 0$; $y = \sqrt{R^2 - S^2} = r$ when $t = S$ or

$$\rho(r) = \frac{1}{\pi C}\int_r^R \frac{f'(y)\,dy}{\sqrt{y^2 - r^2}} \quad \text{(A-8)}$$

From Eq. (A-5) for I_0 a constant,

$$\rho(r) = \frac{1}{\pi C}\int_r^R \frac{d}{dy}\ln I \frac{dy}{\sqrt{y^2 - r^2}} + \frac{1}{\pi C}\int_r^R \frac{C\rho_1 y\,dy}{\sqrt{y^2 - r^2}\sqrt{R^2 - y^2}} \quad \text{(A-9)}$$

After integration of the second term in Eq. (A-9),

$$\rho(r) - \rho_1 = \frac{1}{\pi C}\int_r^R \frac{d}{dy}\ln I \frac{dy}{\sqrt{y^2 - r^2}} \quad \text{(A-10)}$$

Intensity $I(y)$ was recorded by means of a photographic emulsion whose density after development was measured by means of a microphotometer and Brown function plotter. The density of the negative, D, is defined by $D \equiv \log(I_i/I_f)$ where I_i is the intensity of light impinging on the developed negative and I_f is intensity of light transmitted through the developed negative. For an emulsion with linear response $D = \Gamma \log I + C_1 = \log I_i - \log I_f$ (for a given exposure time). For linear plotter response $W = -K_1 I_f + K_2$ where W is the signal from the microphotometer as read on the Brown function plotter, and K_1 and K_2 are constants. At infinite D, W was set at 100, so $100 - W = K_1 I_f$ or

$$\log(100 - W) = \log I_f + \log K_1 = \log I_i - \Gamma \log I - C_1 + \log K_1 \quad \text{(A-11)}$$

then

$$(d/dy)\ln I = [(\ln 10)/\Gamma]\,[(dW/dy)/(100 - W)] \quad \text{(A-12)}$$

Substituting Eq. (A-12) into Eq. (A-10)

$$\rho(r) - \rho_1 = \frac{\ln 10}{\pi C\Gamma}\int_r^R \frac{dW/dy}{(100 - W)\sqrt{y^2 - r^2}}\,dy \quad \text{(A-13)}$$

From Eq. (A-11)

$$\log(100 - W) = -\Gamma \log I + \text{constant} \quad \text{(A-14)}$$

since in analyzing the negatives the incident light I_i was kept constant. But from Eq. (A-2), for ρ constant,

$$\ln I - \ln I_0 = -CL\rho \quad \text{(A-15)}$$

Then, with $\ln I_0$ also absorbed in the constant term,

$$\log(100 - W_2) = (LC\Gamma \ln 10)\rho_2 + \text{constant} \quad \text{(A-16)}$$

$$\log(100 - W_3) = (LC\Gamma \ln 10)\rho_3 + \text{constant} \quad \text{(A-17)}$$

Subtracting Eq. (A-16) from Eq. (A-17) and transposing

$$(\ln 10)\,C\Gamma = \frac{\rho_3 - \rho_2}{\log[(100 - W_3)/(100 - W_2)]}\frac{1}{L} = \frac{d\rho_2}{d[\log(100 - W_2)]}\frac{1}{L} \quad \text{(A-18)}$$

Now if both sides of Eq. (A-13) are divided by ρ_1

$$\frac{\rho(r)}{\rho_1} - 1 = \frac{[(\rho_2 - \rho_2)/\rho_1]}{\log[(100 - W_3)/(100 - W_2)]} \times \frac{L}{\pi}\int_r^R \frac{dW/dy}{(100 - W)\sqrt{y^2 - r^2}}\,dy \quad \text{(A-19)}$$

For I_0 not equal to a constant Eq. (A-10) becomes

$$\rho(r) - \rho_1 = \frac{1}{\pi C}\int_r^R \frac{d}{dy}(\ln I - \ln I_0)\frac{dy}{\sqrt{y^2 - r^2}} \quad \text{(A-20)}$$

and Eq. (A-19) above becomes

$$\frac{\rho(r)}{\rho_1} - 1 = \frac{[(\rho_2 - \rho_2)/\rho_1]}{\log[(100 - W_3)/(100 - W_2)]} \times \frac{L}{\pi}\int_r^R \left[\frac{dW/dy}{100 - W} - \frac{dW_2/dy}{100 - W_2}\right]\frac{dy}{\sqrt{y^2 - r^2}} \quad \text{(A-21)}$$

where $(dW_2/dy)/(100 - W_2)$ is the derivative of the logarithm of $100 - W$ for ρ equal a constant.

References

[1] Evans, R. A., *A New Method of Flow Visualization for Low Density Wind Tunnels*, University of California, Institute of Engineering Research Project Report HE-150-119, 1954.

(*Continued on page 106*)

An Introduction to Second-Order Wing Theory

D. C. M. LESLIE*

Sir W. G. Armstrong Whitworth Aircraft, Ltd.

SUMMARY

In this paper the particular integral for the second-order iteration equation of inviscid supersonic flow, discovered by Fell and the author,[1] is applied to wing theory. This enables us to calculate second-order derivatives for wings of finite aspect ratio, and thence to determine how far the second-order strip theory of Busemann is in error for such wings. Remarking that the most interesting effect in second-order wing theory is the influence of thickness on lifting derivatives, and that corrections to strip theory will be largest on a wing with subsonic edges, we choose as our example the lift coefficient of a rectangular wing with a simple thickness distribution.

Some details are given of the calculation, which is fairly complex; use of the ζ method introduced by Perry and the author[2,3] is found to reduce the labor involved very considerably.

INTRODUCTION

THE SECOND-ORDER strip theory of Busemann has been known for many years. If we apply this second-order theory either to an infinitesimally thin wing at incidence, or to a wing of finite thickness at zero incidence, we get a small contribution to the drag, but none to the lifting derivatives. To get a second-order contribution to these derivatives, we have to consider a wing of finite thickness at incidence. Second-order lift is found to be zero, but, for wings of practical thickness, the second-order correction to the first-order pitching moment may be very large.

It would be of great interest to know whether the predictions of second-order strip theory are any guide to the behavior of wings of low aspect ratio, but this requires a full solution of the second-order problem, which has not previously been available. Martin and Gerber[4] have calculated the damping in roll of an infinite sweptback wing, and Clarkson[5] has made a preliminary study of the general problem, but no second-order derivatives for wings of finite aspect ratio have been published hitherto.

The rectangular wing has been chosen as an example, since on a wing of simple planform, the "aspect-ratio" corrections to the second-order strip theory lift will probably be small (the corresponding first-order correction is zero). The thickness distribution chosen seems to be the simplest which gives zero thickness on all the edges (the theory would not be applicable to wings with thick edges).

Received March 1, 1956.

*Senior Aerodynamicist, Armaments Division. Now at the Royal Aircraft Establishment, Farnborough, Hants, England.

FORMULATION OF THE SECOND-ORDER PROBLEM

The systematic development of second-order theory is due to Van Dyke,[6] and this section should be read as a sequel to his paper. Our notation is similar to his, but differs from it at one or two points. Equations given in Van Dyke's paper are quoted here without proof.

Ward[7] has shown that, in first-order theory, the problem of a lifting wing of finite thickness can be separated into an antisymmetric or lifting problem in which the thickness of the wing may be ignored, together with a symmetric or drag problem in which the wing may be treated as being at zero incidence. Let $Y(x, y)$ denote the height of the wing surface above the midplane, while $Z(x, y)$ denotes the distance between the midplane, and $z = 0$, which is taken as the "plane of the wing" (the supersonic free stream being in the x direction). Then

$$\xi = \partial Y / \partial x \tag{1}$$

is the thickness incidence, while

$$\alpha = \partial Z / \partial x \tag{2}$$

is the lifting incidence. The overall height of the wing surface above the plane $z = 0$ is

$$z_w = (Y \mp Z)$$

depending upon whether we are on the upper or lower surface of the wing. Let the potential of the antisymmetric problem be ϕ and that of the symmetric problem be θ. The overall linearized potential will be

$$\Phi_l = \theta + \phi \tag{3}$$

on the lower surface, and

$$\Phi_u = \theta - \phi \tag{4}$$

on the upper surface, the functions θ, ϕ being defined initially in $z < 0$, and being extended to $z > 0$ by their symmetry properties. The second-order potential will be of the general form

$$\varphi = (\theta \mp \phi)^2$$

(this is not an equation for φ). The antisymmetric (or lifting) portion of φ is of the form $\theta \times \phi$, the terms θ^2, ϕ^2 merely contributing to the drag.

It is convenient to evaluate the potentials and their derivatives on $z = 0$ rather than on the wing surface. If we follow this convention, the second-order pressure

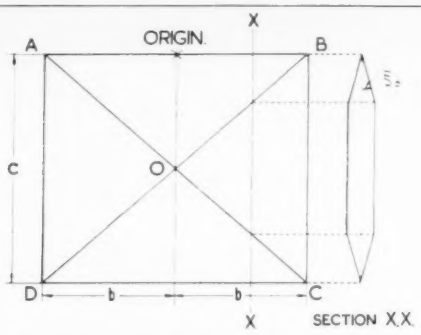

FIG 1. The thickness distribution and dimensions of the wing studied in this paper.

coefficient is given by

$$C_p^{(2)} = -2\varphi_x - 2z_u\Phi_{xz} - \Phi_y^2 - \Phi_z^2 + \beta^2\Phi_x^2 \quad (5)$$

where Φ denotes Φ_l or Φ_u and φ is the second-order potential, which is given by

$$\varphi = M^2\Phi\Phi_x + \psi + \tilde{\omega} \quad (6)$$

Here ψ, the "irreducible part" of φ, is a particular integral of

$$\Box^2\psi \equiv \psi_{yy} + \psi_{zz} - \beta^2\psi_{xx} = 2M^2\beta^2 N\Phi_x\Phi_{xx} \quad (7)$$

and the complementary function $\tilde{\omega}$ is a solution of the linearized equation. $\tilde{\omega}$ is, of course, determined by the boundary conditions, which are

$$\tilde{\omega}_z = (\partial/\partial y)(z_w\Phi_y) - \beta^2(\partial/\partial x)(z_w\Phi_x) - M^2\Phi(\partial^2 z_w/\partial x^2) - \ldots_z \quad \text{on the wing} \quad (8a)$$

$$\tilde{\omega} = 0 \quad \text{off the wing,} \quad (8b)$$

As in the corresponding first-order problem, Eq. (8b) is a consequence of the antisymmetry of the potentials. It follows from Eq. (8) that as long as the subsonic edges of the wing are independent—i.e., as long as

$$A' = 2\beta b/c \geq 1$$

$\tilde{\omega}$ is given by Evvard's theorem (see reference 7); the dimensions b, c of the wing are defined on Fig. 1.

The explicit calculation of $\tilde{\omega}(x, y)$ from Evvard's theorem would be a formidable matter, and, fortunately, it is not necessary. The quantities we actually want to calculate are integrated derivatives of the form

$$Q = 2\iint_{wing} f(x, y)C_p^{(2)}(x, y)\,dxdy$$

where the distribution function f is 1 for lift, x for leading-edge pitching moment, and so on. We shall confine ourselves to the case of lift ($f = 1$), but the generalization to more complex forms of f will be obvious. Thus in dealing with the complementary function, we wish to evaluate integrals of the type

$$\iint_{wing} \tilde{\omega}_z(x, y)\,dxdy \quad (9)$$

Now $\tilde{\omega}$ satisfies the first-order equation and, therefore, obeys the standard reciprocity theorem

$$\iint_{wing} \tilde{\omega}_z(x, y)\,dxdy = \iint_{wing} \tilde{\omega}_z(x, y)\phi_x^{(R)}(x, y)\,dxdy \quad \text{if} \quad A' \geq 1 \quad (9a)$$

where $\phi^{(R)}$ is the linearized potential induced by a reversed flow over the wing at constant unit incidence. Since $\tilde{\omega}_z$ is given on the wing by Eq. (8a), Eq. (9a) enables us to evaluate integrals of the form (9) without recourse to Evvard's theorem.

We now substitute Eqs. (3) and (4) into Eqs. (5), (6), and (8a) and separate out the antisymmetric part of the second-order pressure coefficient: we also change our notation slightly, introducing reference incidences α_0, ξ_0, and writing

$$\alpha(\text{old}) = \alpha_0 \times \alpha(\text{new})$$

and similarly for ξ; the new functions α, ξ are nondimensional functions of order 1.

The quantity we are actually going to calculate is

$$C_{L,\,\alpha_0\xi_0} = \partial^2 C_L/\partial\alpha_0\partial\xi_0 = 2\Gamma\iint_{wing} C_p^{(2)}(x, y)\,dxdy \quad (10)$$

where C_L is the lift coefficient, and

$$\Gamma = 1/\alpha_0\xi_0 \cdot S$$

S being the wing area. Using the first-order boundary conditions,

$$\theta_z = \xi_0\xi \qquad \phi_z = \alpha_0\alpha$$

we may show that

$$C_{L,\,\alpha_j\xi_k} = \sum_{r=1}^{3} II_r + \sum_{r=1}^{6} I_r + \sum_{r=1}^{8} J_r \quad (11)$$

In this equation

$$II_r = \frac{1}{S}\iint_{wing} h_r(x, y)\,dxdy \quad (12)$$

where

$$h_1 = -4\alpha\xi, \qquad h_2 = -4\Gamma(\partial\alpha/\partial x), \qquad h_3 = -4Z(\partial\xi/\partial x) \quad (12a)$$

$$I_r = \Gamma\iint_{wing} i_r(x, y)\,dxdy \quad (13)$$

where

$$\left.\begin{aligned} i_1 &= 4\beta^2\phi_x\theta_x, \qquad i_2 = -4\theta_y\phi_y, \qquad i_3 = -4M^2(\partial/\partial x)(\theta_x\phi) \\ i_4 &= -4M^2(\partial/\partial x)(\theta\phi_x), \qquad i_5 = -4\psi_{1x}, \qquad i_6 = -4\psi_{2x} \end{aligned}\right\} \quad (13a)$$

and

$$J_r = \Gamma\iint_{wing} \phi_x^{(R)}(x, y)j_r(x, y)\,dxdy \quad (14)$$

where

$$\left.\begin{aligned} j_1 &= -4\alpha_0(\partial/\partial y)\,(Z\theta_y), & j_2 &= -4\xi_0(\partial/\partial y)\,(Y\phi_y),\\ j_3 &= 4\beta^2\alpha_0(\partial/\partial x)\,(Z\theta_x), & j_4 &= 4\beta^2\xi_0(\partial/\partial x)\,(Y\phi_x),\\ j_5 &= 4M^2\alpha_0\cdot\theta(\partial\alpha/\partial x), & j_6 &= 4M^2\xi_0\cdot\phi(\partial\xi/\partial x),\\ j_7 &= 4\psi_{1z}, & j_8 &= 4\psi_{2z} \end{aligned}\right\} \quad (14a)$$

In Eqs. (13a) and (14a), ψ_1 and ψ_2 are particular integrals of the equations

$$\Box^2\psi_1 = 2M^2\beta^2 N\theta_{xx}\phi_x \quad (15a)$$

$$\Box^2\psi_2 = 2M^2\beta^2 N\theta_x\phi_{xx} \quad (15b)$$

Eqs. (11) to (15) constitute a closed formulation of the second-order antisymmetric problem. In our present problem, we have

$$\alpha = 1, \qquad S = 2bc$$

and therefore, since Y is zero on all the edges,

$$H_1 = H_2 = 0 \qquad H_3 = 4$$

Description of the ζ Method

The terms I_r and J_r can, in principle, be calculated directly, but such a calculation would be extremely long and tedious. The ζ method, which was introduced in references 2 and 3, simplifies this work very greatly.

The first-order drag potential is given by

$$\theta(x, y, 0) = -\frac{\xi_0}{\pi}\iint \xi(x', y')\,\frac{dx'dy'}{\sqrt{(x-x')^2 - \beta^2(y-y')^2}} \quad (11)$$

the integration being over the forecone of (x, y): we are not interested in the values of the potentials off the plane $z = 0$. In this equation, we make the ζ substitution

$$y' = y - \zeta(x - x') \quad (12)$$

and we then find that the potential is given by

$$\theta(x, y, 0) = -\frac{\xi_0}{\pi}\int_{-1/\beta}^{1/\beta} \Xi_1(\zeta; x, y)\,\frac{d\zeta}{\sqrt{1-\beta^2\zeta^2}} \quad (12a)$$

where

$$\Xi_1(\zeta; x, y) = \int_{-\infty}^{x} \xi[x', y - \zeta(x - x')]\,dx' \quad (13)$$

In this definition, ξ is to be understood to be zero off the wing. These expressions may be differentiated freely under the integral sign—for example,

$$\theta_x(x, y, 0) = -\frac{\xi_0}{\pi}\int_{-1/\beta}^{1/\beta} \xi_1(\zeta; x, y)\,\frac{d\zeta}{\sqrt{1-\beta^2\zeta^2}} \quad (13a)$$

where

$$\xi_1(\zeta; x, y) = \frac{\partial}{\partial x}\Xi_1(\zeta; x, y) = \int_{-\infty}^{x} \frac{\partial\xi}{\partial x'}[x', y - \zeta(x - x')]\,dx' \quad (14)$$

From Fig. 1 we see that on the wing

$$\xi = 1 - H(mx - y - b) - H(mx + y - b) \quad (14a)$$

m being the slope of the bend lines AC, BD ($\beta' = \beta m$): the origin is taken at the midpoint of the leading edge.* Substituting this into Eq. (18), we find

$$\Xi_1 = xH(b + y - \zeta x) - [(mx + y - b)/(m + \zeta)]\,H(mx + y - b) - [(mx - y - b)/(m - \zeta)]\,\{H(mx - y - b) - H(\zeta x - y - b)\}\cdot\zeta > 0 \quad (15)$$

a formula which will be used repeatedly in subsequent work.

The case of the lifting potential is slightly more complicated. The general formula

$$\phi(x, y, 0) = -\frac{1}{\pi}\iint \phi_z(x', y', 0)\,\frac{dx'dy'}{\sqrt{(x-x')^2 - \beta^2(y-y')^2}}$$

is still valid, and ϕ_z is still equal to $\alpha_0\alpha$ on the wing: however, outboard of the wing, but inside the Mach cones of the points A, B, ϕ_z has a non-zero value which is initially unknown. This value can be determined by conical flow methods, for example, and if we then define

$$A_1(\zeta; x, y) = \int_{-\infty}^{x} \phi_z[x', y - \zeta(x - x')]\,dx' \quad (16)$$

we shall have

$$\phi(x, y) = -\frac{1}{\pi}\int_{-1/\beta}^{1/\beta} A_1(\zeta; x, y)\,\frac{d\zeta}{\sqrt{1-\beta^2\zeta^2}} \quad (17)$$

The matter is discussed at greater length by Leslie,[3] who shows that

$$A_1 = x - \tfrac{1}{2}x - [(b + y)/\zeta]\}^{\frac{1}{2}} \times H\{\tfrac{1}{2}x - [(b + y)/\zeta]\}^{\frac{1}{2}}\sqrt{(1 + \beta\zeta)/\beta\zeta} \quad (16a)$$

for $\zeta > 0$; there is a similar formula for $\zeta < 0$.

Calculation of I_1 to I_4

The calculation of these items is quite straightforward; we shall take I_3 as an example, since some of the work will be useful later on. Now

$$I_3 = -4M^2\Gamma\int_{-b}^{b} \theta_x(c, y)\phi(c, y)\,dy$$

and we therefore define

$$S_3(\zeta, \kappa) = \frac{1}{2bc}\int_{-b}^{b} A_1(\zeta; c, y)\xi_1(\kappa; c, y)\,dy \quad (17)$$

* Here $H(x)$ is the unit function, defined by

$H(x) = 0$ if $x < 0$
$H(x) = 1$ if $x > 0$

I_3 is then given by

$$I_3 = -\frac{4M^2}{\pi^2\beta^2}\int\int_{-1/\beta}^{1/\beta} S_3(\zeta,\kappa)\,\frac{\beta d\zeta}{\sqrt{1-\beta^2\zeta^2}}\,\frac{\beta d\kappa}{\sqrt{1-\beta^2\kappa^2}} \tag{23}$$

Since α and ξ are both symmetric functions of y, we have

$$S_3(-\zeta,-\kappa) = S_3(\zeta,\kappa) \qquad S_3(\zeta,-\kappa) = S_3(-\zeta,\kappa)$$

from which it follows that

$$I_3 = -\frac{8M^2}{\pi^2\beta^2}\int_0^{1/\beta}\frac{\beta d\kappa}{\sqrt{1-\beta^2\kappa^2}}\times \int_{-1/\beta}^{1/\beta} S_3(\zeta,\kappa)\,\frac{\beta d\zeta}{\sqrt{1-\beta^2\zeta^2}} \tag{23a}$$

We therefore only need to know Ξ_1 for $\kappa > 0$ [cf. Eq. (19)].

Regarded as a function of ζ for fixed positive κ, S_3 changes analytical form at

$$\zeta = -(m-\kappa) \qquad \zeta = 0 \qquad \zeta = \kappa$$

If $A' < 1$, there are further changes of form at $\zeta = \pm m$, but our theory depends on Evvard's theorem, and is therefore only valid for $A' \geq 1$. The change of form at $\zeta = -(m-\kappa)$ occurs when the line of ζ discontinuity

$$y = b - |\zeta|x$$

meets the line of κ discontinuity

$$y = -b + \kappa x$$

This can only occur for $A' < 2$, and I_3 must therefore have a change of analytical form at $A' = 2$. If we confine ourselves to $A' \geq 2$, as we shall do in the present paper, S_3 has differing analytical forms in the three regions

$$-(1/\beta) < \zeta < 0 \qquad 0 < \zeta < \kappa \qquad \kappa < \zeta < (1/\beta)$$

The calculation of these three forms is quite straightforward: substituting them into Eq. (23a), we find

$$\beta^2 I_3/M^2 = 4[(2A'/\sqrt{A'^2-1}) - 1]\times [1-(1/2A')] - (4/\pi^2 A')\,(4K_2 - K_1 + L_1 + 2L_3) \tag{24}$$

where

$$K_n \equiv K_n(A') = \int_0^1 \frac{u^n}{A'-u}\sin^{-1}\sqrt{u}\,\frac{du}{\sqrt{1-u^2}} \tag{25a}$$

and

$$L_n \equiv L_n(A') = \int_0^1 \frac{u^n}{A'-u}\,\frac{du}{\sqrt{u(1+u)}} \tag{25b}$$

These quantities satisfy the recurrence relations

$$K_n = A'K_{n-1} - \lambda_{n-1}$$

$$L_n = A'L_{n-1} - D_{n-1}$$

where

$$\lambda_n = \int_0^1 u^n \sin^{-1}\sqrt{u}\,\frac{du}{\sqrt{1-u^2}} = \frac{n-1}{n}\lambda_{n-2} + \frac{1}{2n}(D_n + D_{n-1})$$

and

$$D_n = \int_0^1 \frac{u^n\,du}{\sqrt{u(1+u)}} = \frac{\sqrt{2}}{n} - \frac{2n-1}{2n}D_{n-1}$$

The K_n and L_n have been computed by using the recurrence relations, the "down-ladder" process being started at values of n high enough for the asymptotic formulas

$$K_n \sim \frac{\pi}{2(A'-1)}\int_0^{\pi/2}\sin^n\theta\,d\theta$$

$$L_n \sim 1/[(n+1)(A'-1)\sqrt{2}]$$

to be sufficiently accurate (for example, a 25 per cent change in L_8 (15) only affects L_5 (15) to one unit in the fifth place). The auxiliary quantities λ_n, D_n can be obtained by an "up-ladder" process from

$$D_0 = 2\ln(1+\sqrt{2}), \qquad \lambda_0 = 1.53196,$$
$$\lambda_1 = (1/2)(D_0 + D_1)$$

(λ_0 has been calculated by numerical integration). Values of K_n and L_n for suitable ranges of n and A' have been computed by the above process; with these values, we can calculate $\beta^2 I_3/M^2$ as a function of A'. It should be noted that Eq. (24) is only valid for $A' \geq 2$. Tables have been prepared giving the values of K_n, L_n, λ_n, and D_n, $S_r(\zeta,\kappa)$, $R_r(\zeta,\kappa)$ (these quantities are introduced later) and the I_r and J_r. Lack of space in the JOURNAL has prevented the inclusion of these tables, but the author has a few copies available for distribution.

I_1, I_2, and I_4 can be calculated in exactly the same way. We define

$$S_1(\zeta,\kappa) = \frac{1}{2bc}\int\int_{wing}\alpha_1(\zeta;x,y)\xi_1(\kappa;x,y)\,dxdy$$

$$S_2(\zeta,\kappa) = \frac{1}{2bc}\int\int_{wing}\frac{\partial A_1}{\partial y}(\zeta;x,y)\,\frac{\partial \Xi_1}{\partial y}(\kappa;x,y)\,dxdy$$

and

$$S_4(\zeta,\kappa) = \frac{1}{2bc}\int_{-b}^{b}\alpha_1(\zeta;c,y)\Xi_1(\kappa;c,y)\,dy$$

where

$$\alpha_1 = \partial A_1/\partial x$$

We then have

$$I_r = \frac{8f_r}{\pi^2}\int_0^{1/\beta}\frac{\beta d\kappa}{\sqrt{1-\beta^2\kappa^2}}\int_{-1/\beta}^{1/\beta}S_r(\zeta,\kappa)\,\frac{\beta\,d\zeta}{\sqrt{1-\beta^2\zeta^2}}$$

where

$$f_1 = 1 \qquad f_2 = -(1/\beta^2) \qquad f_3 = f_4 = -(M^2/\beta^2)$$

Calculation of I_5 and I_6

In this group, we shall take as our example

$$I_5 = -4\Gamma \int_{-b}^{b} \psi_1(c, y)\, dy$$

It follows from the results of Fell and Leslie[1] that

$$\psi_1(x, y, z) = (M^2N/2\pi^2) \iiiint (\partial\alpha/\partial x_1) \times (x_1, y_1)\, (\partial^2\xi/\partial x_2^2)\, (x_2, y_2) \times \sigma_r(x, y, z; x_1, y_1; x_2, y_2)\, dx_1 dx_2 dy_1 dy_2 \quad (26)$$

where

$$\sigma_r = \log \frac{(\boldsymbol{R} - \boldsymbol{R}_1)\cdot(\boldsymbol{R} - \boldsymbol{R}_2) - |\boldsymbol{R} - \boldsymbol{R}_1||\boldsymbol{R} - \boldsymbol{R}_2|}{(\boldsymbol{R} - \boldsymbol{R}_1)\cdot(\boldsymbol{R} - \boldsymbol{R}_2) + |\boldsymbol{R} - \boldsymbol{R}_1||\boldsymbol{R} - \boldsymbol{R}_2|} = 4\beta^2\lambda_r \quad (26a)$$

λ_r being the quantity introduced in reference 1. We substitute into Eq. (26) the standard ζ relations

$$y_1 = y - \zeta(x - x_1) \qquad \text{and} \qquad y_2 = y - \kappa(x - x_2)$$

and that equation becomes on $z = 0$ (we are not interested in the value of ψ_1 elsewhere)

$$\psi_1 = \frac{M^2N}{2\pi^2} \iint_{-1/\beta}^{1/\beta} \sigma_r(\zeta, \kappa)\, d\zeta d\kappa \times \int_{-\infty}^{x} (x - x_1) \frac{\partial\alpha}{\partial x_1} [x_1, y - \zeta(x - x_1)]\, dx_1 \times \int_{-\infty}^{x} (x - x_2) \frac{\partial^2\xi}{\partial x_2^2} [x_2, y - \kappa(x - x_2)]\, dx_2 \quad (27)$$

where, from Eq. (26a)

$$\sigma_r(\zeta, \kappa) = \log \frac{(1 - \beta^2\zeta\kappa) - \sqrt{1 - \beta^2\zeta^2}\sqrt{1 - \beta^2\kappa^2}}{(1 - \beta^2\zeta\kappa) + \sqrt{1 - \beta^2\zeta^2}\sqrt{1 - \beta^2\kappa^2}}$$

We may readily show that Eq. (27) is equivalent to

$$\psi_1(x, y) = \frac{M^2N}{2\pi^2} \iint_{-1/\beta}^{1/\beta} \sigma_r(\zeta, \kappa) \frac{\partial^2}{\partial\zeta\partial\kappa} \times [\zeta\kappa I_1(\zeta; x, y)\xi_1(\kappa; x, y)]\, d\zeta d\kappa$$

and, therefore, that

$$I_5 = -\frac{2M^2N}{\pi^2} \iint_{-1/\beta}^{1/\beta} \sigma_r(\zeta, \kappa) \frac{\partial^2}{\partial\zeta\partial\kappa} \times [\zeta\kappa S_3(\zeta, \kappa)]\, d\zeta d\kappa \quad (28)$$

S_3 being the quantity defined in Eq. (22). Integrating Eq. (28) by parts, and using the symmetry properties of S_3, we find

$$I_5 = I_{5a} + I_{5b} \quad (29)$$

where

$$I_{5a} = \frac{8M^2N}{\pi^2\beta^2} \int_0^{1/\beta} \frac{\beta^2\kappa^2 \cdot \beta\, d\kappa}{\sqrt{1 - \beta^2\kappa^2}} \times \int_{-1/\beta}^{1/\beta} S_3(\zeta, \kappa) \frac{\beta\, d\zeta}{\sqrt{1 - \beta^2\zeta^2}} \quad (29a)$$

$$I_{5b} = \frac{8M^2N}{\pi^2\beta^2} \int_0^{1/\beta} \beta\kappa \sqrt{1 - \beta^2\kappa^2}\, \beta\, d\kappa \times \int_{-1/\beta}^{1/\beta} \frac{q_3(\zeta, \kappa) - q_3(\kappa, \kappa)}{\zeta - \kappa} \frac{\beta d\zeta}{\sqrt{1 - \beta^2\zeta^2}} \quad (29b)$$

In this last equation

$$q_3(\zeta, \kappa) = S_3(\zeta, \kappa) + \kappa(\partial/\partial\kappa)S_3(\zeta, \kappa)$$

Evaluating the integrals of Eq. (29), we find that I_5 can be expressed in terms of the K_n and L_n. I_6 may be treated in the same way; its relationship to S_4 is the same as that of I_5 to S_3.

Calculation of the Terms J_1 to J_6

This group of terms is quite straightforward, and as an example we shall consider

$$J_1 = -4\Gamma\alpha_0 \iint_{wing} \phi_x^{(R)}(x, y) \frac{\partial}{\partial y} (Z\theta_y)\, dxdy$$

In reference 3, it is shown that

$$\phi_x^{(R)} = -\frac{1}{\pi} \int_{-1/\beta}^{1/\beta} \Gamma(\zeta; x, y) \frac{d\zeta}{\sqrt{1 - \beta^2\zeta^2}} \quad (30)$$

where

$$\left.\begin{aligned} \Gamma(\zeta; x, y) &= 1 \qquad \text{if} \qquad -b + \tfrac{1}{2}[(1 + \beta\zeta) \times (c - x)]/2\beta^2 < y < b - \tfrac{1}{2}[(1 - \beta\zeta)\,(c - x)]/2\beta^2 \\ &= 0 \qquad \text{otherwise} \end{aligned}\right\} \quad (30a)$$

Then if we define

$$R_1(\zeta, \kappa) = \frac{1}{2bc} \iint_{wing} \Gamma(\zeta; x, y) \frac{\partial}{\partial y} \times \left\{Z(x, y) \frac{\partial\Xi_1}{\partial y}(\kappa; x, y)\right\} dxdy \quad (31)$$

we have

$$J_1 = -\frac{8}{\pi^2} \int_0^{1/\beta} \frac{d\kappa}{\sqrt{1 - \beta^2\kappa^2}} \times \int_{-1/\beta}^{1/\beta} R_1(\zeta, \kappa) \frac{d\zeta}{\sqrt{1 - \beta^2\zeta^2}} \quad (32)$$

(R_1 has the same symmetry properties as S_3). In our particular case, $Z = x$ and using Eq. (30a) we have

$$R_1 = \frac{1}{2bc} \iint_{\text{DMNC}} x \frac{\partial^2\Xi_1}{\partial y^2} dxdy = \frac{1}{2bc} \left(\int_{\text{NC}} - \int_{\text{MD}}\right) x \frac{\partial\Xi_1}{\partial y}\, dx$$

(the lines MD, NC are shown on Fig. 2). These in-

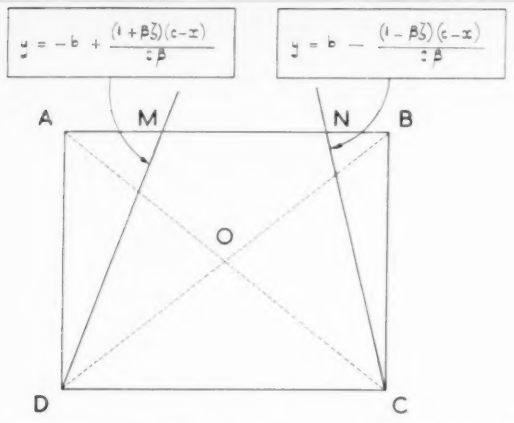

FIG. 2. Diagram illustrating the area of integration for R_7.

tegrals may be evaluated without difficulty. [From Eq. (32), it will be seen that a change in the sign of ζ in any of the terms comprising R_1 leaves J_1 unaltered: this property can be used to simplify the formulas for R_1 and the other R_r defined below.] Substituting the resulting formula into Eq. (32), we find

$$J_1 = [(7A' + 11)\sqrt{2}]/[A'(A' + 1)^2]$$

a formula which is valid for $A' \geq 1$.

The terms J_2 to J_6 can be dealt with in the same way. We define

$$R_s(\zeta, \kappa) = \frac{1}{2bc} \iint_{wing} V(\zeta; x, y) r_s(\kappa; x, y)\, dxdy$$

where

$$r_2 = (\partial/\partial y)[V(\partial\xi_1/\partial y)], \qquad r_3 = (\partial/\partial x)(Z\xi_1),$$
$$r_4 = (\partial/\partial x)(V\alpha_1),$$
$$r_5 = \Xi_1(\partial\alpha/\partial x), \qquad r_6 = A_1(\partial\xi/\partial x)$$

The required terms are then given by

$$J_r = \frac{8g_r}{\pi^2} \int_0^{1/\beta} \frac{\beta\, d\kappa}{\sqrt{1 - \beta^2\kappa^2}} \int_{-1/\beta}^{1/\beta} R_r(\zeta, \kappa) \frac{\beta\, d\zeta}{\sqrt{1 - \beta^2\zeta^2}}$$

where

$$g_1 = g_2 = -(1/\beta^2), \qquad g_3 = g_4 = 1,$$
$$g_5 = g_6 = M^2/\beta^2$$

CALCULATION OF J_7 AND J_8

In this group, we shall take as our example

$$J_7 = 4\Gamma \iint_{wing} \phi_x^{(R)}(x, y)\psi_{1z}(x, y, 0)\, dxdy$$

ψ_{1z} can be obtained by differentiating Eq. (26) under the integral sign, to give

$$\psi_{1z} = (M^2N/2\pi^2) \iiiint (\partial\alpha/\partial x_1)(x_1, y_1) \times (\partial^2\xi/\partial x_2^2)(x_2, y_2)(\partial\sigma_r/\partial z)(x, y, 0; x_1, y_1; x_2, y_2) \times dx_1dx_2dy_1dy_2 \quad (33)$$

Differentiating Eq. (26a), we find

$$\frac{\partial\sigma_r}{\partial z}(z = 0) = \frac{2\pi|x_1 - x_2|}{(x - x_1)(x - x_2)} \times \delta\left(\frac{y - y_1}{x - x_1} - \frac{y - y_2}{x - x_2}\right) \sqrt{1 - \frac{\beta^2(y - y_1)^2}{(x - x_1)^2}} \quad (33a)$$

the Dirac delta function $\delta(x)$ being the derivative of the unit function $H(x)$. We now substitute from Eq. (33a) into Eq. (33), and, in the resulting equation, we set

$$y_1 = y - \kappa(x - x_1) \qquad y_2 = y - \nu(x - x_2)$$

The delta factor of Eq. (33a) then becomes $\delta(\kappa - \nu)$, which shows very clearly how suitable the ζ method is for this type of work. Carrying out the γ integration, we have, finally,

$$\psi_{1z}(x, y, 0) = \frac{M^2N}{\pi} \int_{-1/\beta}^{1/\beta} \mu(\kappa; x, y) \sqrt{1 - \beta^2\kappa^2}\, d\kappa \quad (34)$$

where

$$\mu(\kappa; x, y) = \iint_{-\infty}^{x} |x_1 - x_2| \frac{\partial\alpha}{\partial x_1}[x_1, y - \kappa(x - x_1)] \times \frac{\partial^2\xi}{\partial x_2^2}[x_2, y - \kappa(x - x_2)]\, dx_1dx_2 \quad (35)$$

We then define

$$R_7(\zeta, \kappa) = \frac{1}{2bc} \iint_{wing} V(\zeta; x, y)\mu(\kappa; x, y)\, dxdy \quad (36a)$$

and J_7 is then given by

$$J_7 = -\frac{8M^2N}{\pi^2\beta^2} \int_0^{1/\beta} \beta\sqrt{1 - \beta^2\kappa^2}\, d\kappa \times \int_{-1/\beta}^{1/\beta} R_7(\zeta, \kappa) \frac{\beta\, d\zeta}{\sqrt{1 - \beta^2\zeta^2}} \quad (36b)$$

The evaluation of μ requires a certain amount of care. Substituting from Eq. (18b) into Eq. (35), we find

$$\mu = H(y + b - \kappa x) \iint_{-\infty}^{x} |x_1 - x_2| \frac{\partial\alpha}{\partial x_1} \times [x_1, y - \kappa(x - x_1)]\delta'(x_2)\, dx_1dx_2 -$$
$$\left(\frac{m}{m - \kappa}\right)^2 H(y + b - \kappa x) \iint_{-\infty}^{x} |x_1 - x_2| \frac{\partial\alpha}{\partial x_1} \times [x_1, y - \kappa(x - x_1)]\delta'\left(x_2 - \frac{y + b - \kappa x}{m - \kappa}\right) dx_1dx_2 -$$
$$\left(\frac{m}{m + \kappa}\right)^2 \iint_{-\infty}^{x} |x_1 - x_2| \frac{\partial\alpha}{\partial x_1} \times [x_1, y - \kappa(x - x_1)]\,\delta'\left(x_2 - \frac{\kappa x - y + b}{m + \kappa}\right) dx_1dx_2 \quad (37)$$

In the region of $y + b > \kappa x$, we have

$$\alpha = H(x_1)$$

so that the first term is equal to

$$\operatorname{sgn} 0 = 0 \tag{37a}$$

and the second to

$$[m/(m-\kappa)]^2\, H(y+b-\kappa x)\,\{H(mx-y-b) - x\delta[(mx-y-b)/(m-\kappa)]\} \tag{37b}$$

The third term needs more formal treatment: we find that its value is

$$-[m^2/(m+\kappa)]\,\delta(y+mx-b)\,(\partial/\partial\kappa)\,(\kappa A_1) + [m/(m+\kappa)]^2\, H(y+mx-b)\cdot\alpha_1 \tag{37c}$$

Adding together Eqs. (37a), (37b), and (37c), and substituting into Eq. (36), we obtain formulas for R_7 and thence J_7, which is found to be zero; we have not found any basic explanation for this.

J_8 may be treated in exactly the same way; we find

$$J_8 = -\frac{8M^2N}{\pi^2\beta^2}\int_0^{1/\beta}\sqrt{1-\beta^2\kappa^2}\,\beta\,d\kappa\,\times \int_{-1/\beta}^{1/\beta} R_8(\zeta,\kappa)\,\frac{\beta\,d\zeta}{\sqrt{1-\beta^2\zeta^2}}$$

where

$$R_8 = \frac{1}{2bc}\iint_{wing} \Gamma(\zeta;x,y)\,\nu(\kappa;x,y)\,dxdy$$

and

$$\nu(\kappa;x,y) = \int_{-\infty}^{x}\int |x_1-x_2|\,\frac{\partial^2\alpha}{\partial x_1^2}\,[x_1,\ y-\kappa(x-x_1)]\,\times \frac{\partial\xi}{\partial x_2}\,[x_2,\ y-\kappa(x-x_2)]\,dx_1dx_2$$

By methods similar to those used for the analysis of μ, we may show that

$$\nu = -[m/(m-\kappa)]H(b+y-\kappa x)H(mx-y-b) - [m/(m+\kappa)]\,H(y+mx-b)\,\{(\partial/\partial\kappa)\,(\kappa\alpha_1) - [(y+mx-b)/(m+\kappa)]\,(\partial\alpha_1/\partial x)\}$$

from which formulas for R_9 and J_8 follow at once.

The formulas for J_r obtained in this way are all valid for $A' \geq 1$.

Discussion of the Results

Combining Eqs. (12), (13), and (14), and substituting into Eq. (11), we see that the second-order lift coefficient may be written in the form

$$\beta^2 C_{L.\,\alpha_0\xi_0} = M^2N l_1(A') + M^2 l_2(A') + \beta^2 l_3(A') \tag{38}$$

where l_1, l_2, and l_3 are functions of A' only, defined by

$$l_1 = (\beta^2/M^2N)\,(I_5+I_6+J_7+J_8) \tag{39a}$$

$$l_2 = (\beta^2/M^2)\,(I_3+I_4+J_5+J_6) \tag{39b}$$

and

$$l_3 = 4 + I_1 + I_2 + J_1 + J_2 + J_3 + J_4 \tag{39c}$$
$$= I_1 + I_2 + J_2 + J_4$$

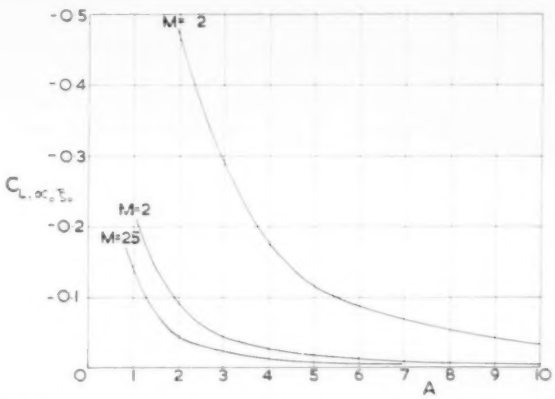

Fig. 3. Graph of $C_{L.\,\alpha_0\xi}$ against A for $M = \sqrt{2}$, 2, and 2.5

since

$$J_1 + J_3 = -4$$

Tables of l_1, l_2, and l_3 for a selection of values of $A' \geq 2$ have been prepared by the author.* Using these tables, $C_{L.\,\alpha_0\xi_0}$ can be computed for any value of A and M. In Fig. 3 we show graphs of $C_{L.\,\alpha_0\xi_0}$ as a function of A for $M = \sqrt{2}$, $M = 2$, and $M = 2.5$ (we take $\gamma = 1.4$).

From these graphs, we see that $C_{L.\,\alpha_0\xi_0}$ is always negative, and that it tends to zero as A' tends to infinity, in accordance with strip theory. The maximum absolute value recorded is 0.47 at $M = \sqrt{2}$ and $A = 2$, but since the strip theory value of $C_{L.\,\alpha_0\xi_0}$ is zero, it is rather difficult to say what this means in terms of departure from strip theory. In this connection, we may note that, according to strip theory, the second-order lift of the panels AOB, COD (see Fig. 1) is

$$\Delta C_{L.\,\alpha_0\xi_0} = \pm(M^2N-2)/\beta^2 = \pm 2.8$$

at $M = \sqrt{2}$: the maximum absolute value recorded above is about one-sixth of this.

Rather larger values of $C_{L.\,\alpha_0\xi_0}$ may be expected in the range $1 \leq A' \leq 2$, and the extension of our results to this range is now in hand. Further work is needed only on the I_r terms, the formulas given for the J_r being valid for $A' \geq 1$: the main work involved is the calculation of the S_r for $\zeta < -(m-\kappa)$.

The method of Bonney[8] can readily be applied to the wing under study. It gives

$$\beta^2 C_{L.\,\alpha_0\xi_0} = (M^2N-2)\,\{[A'/\sqrt{A'(A'+1)}] - 1 + (1/2A')\}$$

According to this formula, $C_{L.\,\alpha_0\xi_0}$ is small and positive, its value at $A = 2$ and $M = \sqrt{2}$ being 0.186: Bonney's method is therefore not satisfactory for wings with sloping bend lines.

Concluding Remarks

Although the strip theory prediction that second-order lift is zero is not correct at low aspect ratios, it

*Because of space considerations, these tables have been omitted from this publication. However, copies may be obtained from the author.

does seem that the second-order correction to the first-order lift is unimportant for practical wing shapes. This remark does not apply to pitching moments, and it would therefore be of the greatest interest to know whether the strip theory value of the second-order pitching moment is seriously in error at low aspect ratios. The calculations reported above suggest that this may be so, but to check the point it is necessary to calculate the accurate pitching moment coefficient about some suitable axis.

It will be noted that these methods could be applied to the calculation of accurate quasi-static damping derivatives; the corresponding strip theory is due to Van Dyke.[9]

Acknowledgments

This work forms part of the research program of the Armaments Division of Sir W. G. Armstrong Whitworth Aircraft Ltd. and is published by permission of the firm. The author is deeply indebted to Mr. A. Lightbody for his interest and encouragement, and to T. W. Groom for his careful work in checking the heavy algebra involved.

References

[1] Fell, J., and Leslie, D. C. M., *Second-Order Methods in Inviscid Supersonic Theory*, Journal of the Aeronautical Sciences, Vol. 21, No. 12, p. 851, December, 1954.

[2] Leslie, D. C. M., and Perry, J., *Wave Drag of Wings at Supersonic Speeds*, Proceedings of the Royal Society, Series A, Vol. 225, p. 213, 1954.

[3] Leslie, D. C. M., *The ξ Method for Lifting Wings* (to be published).

[4] Martin, John C., and Gerber, Nathan, *The Second-Order Lifting Pressure and Damping in Roll of Sweptback Rolling Airfoils at Supersonic Speeds*, Journal of the Aeronautical Sciences, Vol. 20, No. 10, p. 699, October, 1953.

[5] Clarkson, M. H., *A Second-Order Theory for Three-Dimensional Wings in Supersonic Flow*, Quarterly Journal of Mechanics and Applied Mathematics, Vol VII, Part 2, p. 203, June, 1954.

[6] Van Dyke, M. D., *A Study of Supersonic Second-Order Flow Theory*, NACA TN 2200, January, 1951.

[7] Ward, G. N., *Supersonic Flow Past Thin Wings. I. General Theory*, Quarterly Journal of Mechanics and Applied Mathematics, Vol. II, Part 2, p. 136, June, 1949.

[8] Bonney, E. A., *Aerodynamic Characteristics of Rectangular Wings at Supersonic Speeds*, Journal of the Aeronautical Sciences, Vol. 14, No. 2, p. 110, February, 1947.

[9] Van Dyke, M. D., *Supersonic Flow Past Oscillating Airfoils Including Nonlinear Thickness Effects*, NACA TN 2982, July, 1953.

Appendix

We shall now show that when the incidence is independent of y, our Eqs. (26) and (33) lead to the standard strip theory result. We shall use a one-incidence one-potential formulation to simplify the work. In this formulation, the irreducible part of the potential is given by

$$\psi = \frac{M^2N}{2\pi^2} \int_{-\infty}^{x-\beta z}\int \frac{d\alpha}{dx_1}\,\frac{d^2\alpha}{dx_2^2} \times dx_1dx_2 \int\int_{Cones}^{Mach} \sigma_r(x, y, z; x_1, y_1; x_2, y_2)\, dy_1dy_2$$

Integrating by parts, we have

$$\psi = \frac{M^2N}{4\pi^2} \int_{-\infty}^{x-\beta z}\int \frac{d\alpha}{dx_1}\,\frac{d\alpha}{dx_2}\, \tilde{f}(x, y, z; x_1; x_2)\, dx_1dx_2$$

where

$$\tilde{f} = -\int\int_{Cones}^{Mach} \left(\frac{\partial\sigma_r}{\partial x_1} + \frac{\partial\sigma_r}{\partial\sigma_r}\right) dy_1dy_2 = -\frac{\pi^2}{\beta^2}\,(2x - x_1 - x_2)$$

Thus we have

$$\psi = -(M^2N/2\beta^2)\,[\beta z\{\alpha(x - \beta z)\}^2 + \alpha(x - \beta z)Z(x - \beta z)] \quad (40)$$

$$= (1/2)M^2N\Phi_x[z\Phi_z - \Phi]$$

which is identical with the formula given by Van Dyke[6] for this case.

We can now go on to consider Eq. (35), which, for a one-potential two-dimensional problem, reads

$$\mu = \int_{-\infty}^{x}\int |x_1 - x_2|\,\frac{d\alpha}{dx_1}\,\frac{d^2\alpha}{dx_2^2}\, dx_1dx_2 = Z(x)\,\frac{d\alpha}{dx}$$

Substituting this into Eq. (34), we get

$$\psi_z(z = 0) = (M^2N/2\beta)Z(d\alpha/dx)$$

in agreement with Eq. (40).

Visualization of Low-Density Flows . . .

(*Continued from page 98*)

[2] Schaaf, S. A., Horning, D. O., and Kane, E. D., *Design and Initial Operation of a Low Density Supersonic Wind Tunnel*, University of California, Institute of Engineering Research Project Report HE-150-62, 1949.

[3] Owen, J. M., and Sherman, F. S., *Design and Testing of a Mach 4 Axially Symmetric Nozzle for Rarefied Gas Flows*, University of California, Institute of Engineering Research Project Report HE-150-104, 1952.

[4] Mack, S. F., *Determination of the Local Density of a Gas in Axially Symmetric Flow*, unpublished.

[5] Watanabe, K., Inn, C., and Zelikoff, M., *Absorption Coefficients of Gases in the Vacuum Ultraviolet*, J. Chem. Phys., Vol. 20, No. 12, pp. 1969–1970, December, 1952.

[6] Margenau and Murphy, *The Mathematics of Chemistry and Physics*, p. 507; D. Van Nostrand Company, Inc., New York, 1949.

Supersonic Flutter of a Cylindrical Shell†

JOHN W. MILES*

University of California, Los Angeles

(1) Summary

The aerodynamic instability of traveling waves on a cylindrical shell exposed to an external supersonic air stream and containing an internal fluid is examined on the hypothesis of short wave length (compared with the radius and length of the shell). The stability criterion for an empty isotropic shell and the negative damping ratio when this criteria is not met are determined. It is shown that the negative damping ratio calculated in the absence of structural damping decreases monotonically with an increase in structural damping, but structural damping cannot prevent instability and may render an otherwise stable motion weakly unstable.

(2) Introduction

The following analysis of the dynamic instability (*panel flutter*) of thin-walled cylindrical shells under the action of an exterior supersonic flow is presented as a sequel to an earlier formulation of the two-dimensional problem.[1] In that paper panel flutter was studied as a traveling wave phenomenon, following Kelvin's classical analysis of the surface waves produced by wind blowing over water. We remark at the outset that all of the essential features of this approach to panel flutter are elucidated by the two-dimensional analysis without recourse to any approximations beyond those implicit in the assumptions of small disturbances, a perfect fluid, and an infinite surface; however, further analysis and additional approximations are necessary in order to render the results applicable to practical configurations.‡

These principal conclusions of this two-dimensional analysis were as follows.

Waves traveling upstream *relative to the panel* are necessarily stable (this is significant in any attempt to extrapolate the results to *standing* waves).

The critical air speed, U_c, above which flutter is predicted, may be related to the speed of propagation of a given wave, V_0, the mass parameter, $(\rho_a\lambda/m)$, and the Mach Number, M, according to

$$U_c = V_0(\lambda)f[(\rho_a\lambda/m), M] \tag{2.1}$$

where λ is the wave length, ρ_a the air density, and m the areal mass density (f was determined implicitly and presented graphically in reference 1).

U_c exceeds V_0 for all values of the mass parameter $(\rho_a\lambda/m)$ and Mach Number M but is asymptotic to V_0 as either of these parameters approaches infinity.

If $\rho_a\lambda \ll m$ and $M < 1$, the instability approximates a simple (exponential) divergence, and the critical speed is given by (assuming air to flow over only one side of the panel)

$$(1 - M^2)^{-1/2}\rho_a U^2 = (2\pi m/\lambda)V_0^2 \tag{2.2}$$

If $\rho_a\lambda \ll m$ and $M > 1$, the instability takes the form of a slowly divergent oscillation, traveling upstream at the velocity of sound a with respect to a point fixed in space, and the critical speed is given by (*in two dimensions*)

$$U_c = V_0 + a \tag{2.3}$$

The foregoing criteria imply that planel flutter is critical in the (spectral) neighborhood of minimum wave speed (V_0). The mass parameter for cylindrical configurations usually would be sufficiently small in this neighborhood to render subsonic divergence, as governed by the critical condition (2.2), unlikely, and we shall consider further only supersonic flutter at small values of the mass ratio.

The most striking new aspect in the flutter analysis of a cylindrical shell, relative to that of a flat panel, is that, in virtue of the curvature of its surface, any deformation of the shell is necessarily accompanied by direct extensional stresses for which the variation of wave speed with wave length is opposite to that associated with flexural stresses; the result is a true minimum in the wave speed analogous to that found for water waves in consequence of the opposing effects of gravitational and capillary forces. This minimum wave speed occurs at a wave length that is of the order of the geometric mean of the radius and thickness of the shell, thereby justifying the approximation of an infinitely long shell. The smallness of the wave length compared with the radius of the cylinder suggests further that the aerodynamic forces are approximately independent of the curvature of the surface and essentially similar to those associated with a traveling wave on a flat panel, and that they may be calculated as perturbations on the *local* steady flow—i.e., the values of ρ_a, a, and U may be taken as those in the local flow rather than at infinity.[5]

A second, important difference between the two-dimensional flat panel and the three-dimensional cylindrical shell is the necessity of prescribing two parameters, say wave length and helix angle, to specify the three-dimensional wave forms. It follows from this consideration that the critical requirement that the wave move upstream with sonic velocity relative to a fixed point in

Received February 14, 1956.

† The material in this paper was condensed from The Ramo-Wooldridge Corporation Report GM-TR-32, May 25, 1956.

* Professor of Engineering; also, Consultant, The Ramo-Wooldridge Corporation.

‡ Many of the details of this further analysis, especially as regards justification of the approximations, are omitted in the present paper but may be found in references 2–5.

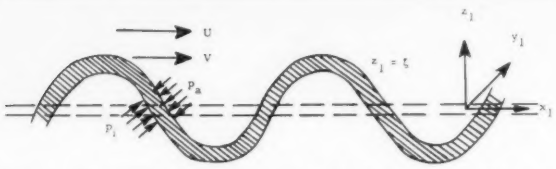

FIG. 1. The surface wave ζ and the relative air speed U in the local coordinate system (x_1, y_1, z_1, t_1) of the shell.

space may be met by a (finite) continuum of waves in the two-parameter spectrum, whereas the condition (2.3) defines a unique wave form in the two-dimensional problem. We emphasize that this follows from the increase in number of dimensions, rather than the change in shape of the panel; in particular, a two-parameter spectrum of waves also exists for a flat panel in three dimensions.

The effects of the fluid below the panel (and at rest relative thereto) were neglected in the two-dimensional analysis, but the fluid enclosed in a cylindrical shell, especially if under pressure, may assume a dominant role in respect to panel flutter. Pressurization leading to relatively large, static stresses will be important insofar as the membrane stresses associated with variations about these static stresses (and proportional to the curvature induced by the traveling wave) become comparable with the extensional and/or flexural stresses induced by the traveling wave. The importance of the inertial effects of the internal fluid will be proportional to the parameter $\rho_i\lambda/m$. This parameter usually would be sufficiently small for an internal gas to render its inertia negligible compared with that of the shell, while for a liquid it could be sufficiently large to render negligible the inertia of the shell—in the latter instance the flutter problem may be regarded as an extension of Rayleigh's analysis of the disintegration of a jet,[6, 7] with the elastic forces exerted by the shell being regarded as analogous to surface tension (the analogy being particularly apt for those stresses associated with the pressurization).

The compressibility of an internal liquid would be negligible insofar as the flight speed (and, therefore, the critical wave speed) were small compared with the velocity of sound in the liquid; the latter criterion might not be met by a gas, of course, but then the effect of the internal fluid probably would be negligible in virtue of the small value of $\rho_i\lambda/m$. The possibility that an internal gas might prove important if the frequency of panel flutter were to coincide with one of the resonant frequencies of the cylindrical cavity is ruled out for the more important cavity modes (for which the wave length is of the order of the radius) by the relatively small value of the wave length of minimum wave speed.

Structural hysteresis was neglected in the analysis of reference 1 and was not considered explicitly in references 2–4, although it was erroneously stated in reference 2 that small amounts of structural damping (expressed as per unit diminution of amplitude per cycle) could be directly superimposed on the negative damping ratios calculated in its absence. A more precise examination of the neighborhood of maximum instability reveals that, while structural damping is beneficial in this neighborhood, no finite amount thereof can prevent the instability predicted by *linearized* theory.

It might be thought that, in analogy with the action of oil on disturbed water, the viscous friction between either the external or internal fluid and the shell could provide appreciable damping of panel flutter. We find, however, that the damping *per cycle* on the assumption of *laminar flow* is negligible compared with that which might be expected from structural hysteresis. It is quite conceivable, on the other hand, that the amplitude of flutter might be limited by turbulent damping.

A more complete understanding of panel flutter—even in a linear approximation—demands an investigation of the *refractive* (as opposed to viscous) effect of the steady flow boundary layer. We may anticipate that the existence of a region having a thickness not small compared with the wave length and a steady flow velocity appreciably less than the flight velocity could alter the results obtained herein in a decisive way. This question is now under investigation.

(3) The Equations of Motion

We require the equations governing the propagation of a *transverse* wave over an infinite shell that contains fluid internally and moves with velocity U relative to the air external to it. We assume that the thickness of the shell wall is small and that the radius of curvature of its surface is everywhere large compared with the wave length. The latter hypothesis allows the shell to be approximated as plane in establishing the interaction of the surface wave with the external air, in consequence of which we may assume a *plane* wave propagating outward from the surface (this approximation is examined in Appendix A).

It is convenient to express the equation of motion of the shell in a coordinate system (x_1, y_1, z_1, t_1) moving with the flight velocity and that of the surrounding air in a system (x, y, z, t) that is at rest relative to the air at infinity. In the first system $z_1 = 0$ defines the undisturbed position of the shell, x_1 and y_1 are measured in the surface of the shell, and the flight velocity U is directed along the negative x_1-axis; the two systems then are connected by the Gallilean transformation (see Fig. 1)

$$x_1 = x + Ut \qquad y_1 = y \qquad z_1 = z \qquad t_1 = t \tag{3.1a}$$

$$x = x_1 - Ut \qquad y = y_1 \qquad z = z_1 \qquad t = t_1 \tag{3.1b}$$

We emphasize that partial differentiation with respect to time is not invariant under this transformation; on the other hand, y_1 and z_1 may be replaced by y and z throughout the subsequent analysis.

The linearized equation of motion for small displacements (ζ) of the shell relative to $z = 0$ may be posed in the form

$$L\zeta + m(\partial^2\zeta/\partial t^2) = p_i - p_a \tag{3.2}$$

where L is an operator (which may involve differentiation with respect to the space coordinates but not time)

such that $L\zeta$ is the transverse load associated with the deformation ζ, m is the mass per unit area, and p_i and p_a are the internal and external pressures, respectively. The question of how small ζ must be to justify the neglect of nonlinear terms in the operator L has been examined by Reissner.[8] He concludes that if bending is important $|\zeta|$ must be small compared with the wall thickness, but if pressurization effects dominate those of bending $|\zeta|$ need be small only relative to the static displacement of the shell. The neglect of nonlinear terms in the following treatment of wave motion in the external and internal fluids also requires that $|\zeta|$ be small compared with the wave length and that the changes in density and pressure be small.

A general form for a plane wave in the Cartesian coordinates x, y, z is given by (the real part of)[9]

$$n = A \exp\{(2\pi i/\lambda)(at - x\sin\theta\cos\alpha - y\sin\theta\sin\alpha - z\cos\theta)\} \quad (3.3)$$

where n denotes the displacement normal to the wavefront, A the complex amplitude, λ the wave length in the *fixed* (x, t) coordinate system, θ the (polar) angle between n and the z-axis, α the (azimuthal) angle between the x-axis and the projection of n on $z = 0$ (see Fig. 2), and a the speed of sound in air. The angle θ must be real and smaller than $\pi/2$ in magnitude insofar as n represents a wave propagating *outward* from $z = 0$; however, Eq. (3.3) also remains valid (as a solution to the wave equation) for properly chosen complex values of θ [see Eq. (3.9b)].

The formulation of our problem requires the matching of the transverse component of the plane wave defined by Eq. (3.3) with the transverse wave ζ and the calculation of the resulting acoustic pressure. This condition may be imposed at the plane $z = 0$ (rather than $z = \zeta$) in virtue of the assumption of small displacements, whence

$$\zeta = (n\cos\theta)_{z=0} = A\cos\theta\exp\{(2\pi i/\lambda)(at - x\sin\theta\cos\alpha - y\sin\theta\sin\alpha)\} \quad (3.4)$$

Alternatively, we may say that the *transverse wave* of Eq. (3.4) would produce the plane wave of Eq. (3.3) in $z > 0$. The amplitude (A_1), wave speed (c), and wave length (λ_1) of the transverse wave of Eq. (3.4) in the two-dimensional coordinate system (x, y, t) are given by

$$A_1 = A\cos\theta \quad (3.5)$$

$$c = a\csc\theta \quad (3.6)$$

$$\lambda_1 = \lambda\csc\theta = (c/a)\lambda \quad (3.7)$$

and, in terms of these parameters, we have

$$\zeta = A_1\exp\{(2\pi i/\lambda_1)(ct - x\cos\alpha - y\sin\alpha)\} \quad (3.8)$$

$$\cos\theta = \sqrt{1 - (a/c)^2} \quad (3.9a)$$

We note that λ_1 is, by hypothesis, a positive real number throughout the remainder of this analysis. This imposes no essential restrictions on the end results.

If $|c| < a$, the disturbance of Eq. (3.3) becomes a *surface wave*, similar to the refracted disturbance following total reflection at an interface;[10] it then follows that (in satisfaction of the requirement that n must be bounded throughout the half space $z > 0$)

$$\cos\theta = -i(a/c)\sqrt{1 - (c/a)^2} \qquad |c| < a \quad (3.9b)$$

Eqs. (3.9a) and (3.9b) define the principal value of the radical not only for real c but also as an analytic function of c in a complex plane cut from $c = \pm a$ to $\pm a + \infty\exp(i\pi/2)$.

The acoustic pressure associated with the plane wave n must be equal to the rate of change of momentum across the wave front and is given by (the linearized approximation)

$$p_a = \rho_a a(\partial n/\partial t) = (2\pi i/\lambda)\rho_a a^2 n \quad (3.10)$$

where ρ_a denotes the density of the undisturbed air. The pressure on $z = 0$, obtained by expressing n in terms of ζ from Eq. (3.4) and introducing c, λ_1, and $\cos\theta$ from Eqs. (3.6), (3.7), (3.9a), and (3.9b), then is given by

$$p_a = 2\pi i\rho_a ac\lambda_1^{-1}[1 - (a/c)^2]^{-1/2}\zeta \quad (3.11a)$$

$$= -2\pi\rho_a c^2\lambda_1^{-1}[1 - (c/a)^2]^{-1/2}\zeta \quad (3.11b)$$

We now return to the equation of motion, Eq. (3.2), in the local coordinate system moving with the shell. The surface wave ζ in *this* system, obtained by substituting x and t from Eq. (3.1b) in Eq. (3.8), is given by

$$\zeta = A_1\exp\{(2\pi i/\lambda_1)[(c + U\cos\alpha)t_1 - x_1\cos\alpha - y\sin\alpha]\} \quad (3.12)$$

We find it convenient, in the subsequent analysis, to focus attention on the *axial phase velocity* relative to the shell—that is, that speed at which an observer would have to move along the positive x_1-axis in order to view the disturbance ζ as a standing wave. Denoting this speed by V, we have from Eq. (3.12)

$$\zeta = A_1\exp\{-(2\pi i/\lambda_1)[(x_1 - Vt_1)\cos\alpha + y\sin\alpha]\} \quad (3.13)$$

$$c = (V - U)\cos\alpha \quad (3.14)$$

The transverse acceleration corresponding to Eq. (3.13) is then given by

$$\partial^2\zeta/\partial t_1^2 = -[(2\pi V\cos\alpha)/\lambda_1]^2\zeta \quad (3.15)$$

The pressure p_i resulting from the disturbance in the internal fluid may be determined by substituting c in Eq. (3.11) from Eq. (3.14), replacing ζ by $-\zeta$ (since $-\zeta$ is the motion *into* the internal fluid), and setting $U = 0$ (since the internal fluid is at rest relative to the shell in its equilibrium position). The result may be further simplified if the internal fluid is incompressible—i.e., $a = \infty$; since the effects of the internal fluid are not likely to be important unless it is a liquid, we incorporate this approximation. We then have from Eq. (3.11b)

$$p_i = 2\pi\rho_i(V\cos\alpha)^2\lambda_1^{-1}\zeta \quad (3.16)$$

We remark that p_i represents the *virtual inertia* force of the internal fluid.

The structural operator L may be related to the axial wave speed V_0 that the transverse wave ζ would have in

the absence of the aerodynamic forces. Substituting Eqs. (3.15) and (3.16) in Eq. (3.2) and setting $p_a = 0$, we obtain

$$L\zeta = [m + (\rho_a\lambda_1/2\pi)](2\pi V_0 \cos\alpha/\lambda_1)^2\zeta \quad (3.17)$$

We emphasize that V_0 is an eigenvalue of the partial differential equation [Eq. (3.17)] and will exhibit a dependence on λ_1 and α that must be determined by the requirement that Eq. (3.13) shall be a solution to Eq. (3.17) when $V = V_0$. We also note that V_0 will be real only in the absence of structural hysteresis.

Substituting Eq. (3.11b) and Eqs. (3.15) through (3.17) in Eq. (3.2), we obtain

$$[m + (\rho_a\lambda_1/2\pi)](2\pi \cos\alpha/\lambda_1)^2(V_0^2 - V^2) = 2\pi\rho_a c^2/\lambda_1\sqrt{1 - (c/a)^2} \quad (3.18)$$

Introducing the mass parameter (which differs from that of reference 1)

$$\mu = \rho_a\lambda_1/(\rho_s\lambda_1 + 2\pi m) \quad (3.19)$$

and substituting c from Eq. (3.14), we may rewrite Eq. (3.18) in the form

$$V^2 + \mu(V - U)^2\{1 - [(V - U)/a \sec\alpha]^2\}^{-1/2} = V_0^2 \quad (3.20)$$

It remains to determine V_0 as a function of λ_1 and α from Eq. (3.17) and to solve Eq. (3.20) explicitly for V, interpreting the radical as a single-valued function of V by drawing branch cuts from $V = U \pm a \sec\alpha$ to ∞ exp $(i\pi/2)$, in accordance with Eqs. (3.9a) and (3.9b). The nature of the panel motion then may be inferred from Eq. (3.13); in particular, the motion will be unstable if the imaginary part of V is negative.

The generalization of Eq. (3.20) for nonplane waves and its solution for *long* wave lengths (compared with the radius) is discussed in Appendix B.

(4) The Stability Equation

The stability equation [Eq. (3.20)] may be reduced to the corresponding two-dimensional equation of reference 1, of which a Cauchy-Nyquist analysis revealed that *for* V_0 *real* it had either zero or one root with negative imaginary part as U was less or greater than a critical speed U_c. The results of that analysis are directly applicable to the present problem if M is replaced by $M \cos\alpha$, but we now wish to include the effects of structural hysteresis (V_0 complex). We also shall impose the approximation $\mu \ll 1$ a priori, thereby greatly simplifying the analysis without appreciably limiting the practical application of the results.

We begin by noting that Eq. (3.20) may be rewritten in the form

$$(V - V_0)(V + V_0)\sqrt{V - (U - a\sec\alpha)} \times \sqrt{(U + a\sec\alpha) - V} + \mu a \sec\alpha(V - U)^2 = 0 \quad (4.1)$$

If we set $\mu = 0$ a priori, this equation has the *primitive* roots $V = \pm V_0$ and $V = U \pm a \sec\alpha$; the speeds $\pm V_0$ correspond to transverse waves on the shell alone while the speeds $U \pm a \sec\alpha$—equivalent to speeds $c = \pm a$ relative to the air at rest—correspond to plane waves of sound having normals parallel to the shell and not interacting therewith (we may imagine that $\mu = 0$ implies $m = \infty$, rather than $\rho_a = 0$, for these waves). If we make μ approach zero through positive values, however, we find that the cuts from $V = U \pm a \sec\alpha$ to ∞ exp $(i\pi/2)$ restrict the possible wave motions as follows.

The transverse wave that travels *upstream relative to the shell* with speed approximating $V_0 (V \simeq -|V_0|)$ is damped by radiation if $|V_0| > a \sec\alpha - U$ [see Fig. 3(a), (b), (d), (e), (f)]; if $|V_0| < a \sec\alpha - U$ [see Fig. 3(c)] no radiation occurs, and the only effect of the aerodynamic forces is a slight decrease in speed (access of inertia). Structural hysteresis always serves to damp this wave.

The transverse wave that travels *downstream relative to the shell* with speed approximating V_0 is damped by radiation if $|V_0| > U + a \sec\alpha$ [see Fig. 3(a), (d)], is undamped but slowed down by aerodynamic inertia if $U - a \sec\alpha < |V_0| < U + a \sec\alpha$ [see Fig. 3(b), (c), (e)], and acquires energy from the air stream if $|V_0| < U - a \sec\alpha$ [see Fig. 3(f)]. *This last possibility exists only for supersonic speeds.* Structural hysteresis also tends to damp this wave, but, as we shall see subsequently, it may not suffice to eliminate instability if V_0 approximates $U - a \sec\alpha$.

The wave that travels *downstream relative to the air at rest* with speed approximating a acquires the character of a surface wave ($\cos\theta$ imaginary) in the presence of the shell if $|V_0| > U + a \sec\alpha$ [see Fig. 3(a), (d)] and is damped by structural hysteresis; if $|V_0| < U + a \sec\alpha$ [see Fig. 3(b), (c), (e), (f)] this wave is no longer dynamically possible.

The wave that travels *upstream relative to the air at rest* with speed approximating a also acquires the character of a surface wave in the presence of the shell if $|V_0| > |U - a \sec\alpha|$ [see Fig. 3(a), (b), (d), (e)]; structural hysteresis tends to damp this wave only if $U < a \sec\alpha$ [see Fig. 3(a),(b)], however, and actually leads to a weak instability* if $U > a \sec\alpha$ [see Fig. 3(d), (e)]—again a possibility only in supersonic flow. This wave also is dynamically impossible if $|V_0| < |U - a \sec\alpha|$ [see Fig. 3(c), (f)].

These results are illustrated in Fig. 3(a)–(f) for the possible ordered sequences of the primitive roots; the positions of the roots for $\mu = 0+$ and real V_0 (no structural hysteresis) are shown as open circles, those for small positive μ and real V_0 as dotted circles, and those for small positive μ and small structural hysteresis $\{V_0^2 = |V_0|^2 \exp[ig \operatorname{sgn}(\mathrm{R}1\ V)]\}$ by solid circles.

We emphasize that these conclusions are predicated on the assumption of small μ and are not uniformly valid with respect to the proximity of either $\pm V_0$ with $U \pm a$

* The damping ratio for this instability is given by

$$\delta = -g\mu^2(|V_0| \cos\alpha/a)^2(M \cos\alpha - 1)^{-1}[(|V_0| \cos\alpha/a)^2 - (M \cos\alpha - 1)^2]^{-2} \quad (4.1')$$

This is quite small unless V_0 approximates $U - a \sec\alpha$, in which event the analysis of Eq. (4.2) *et seq.* is applicable.

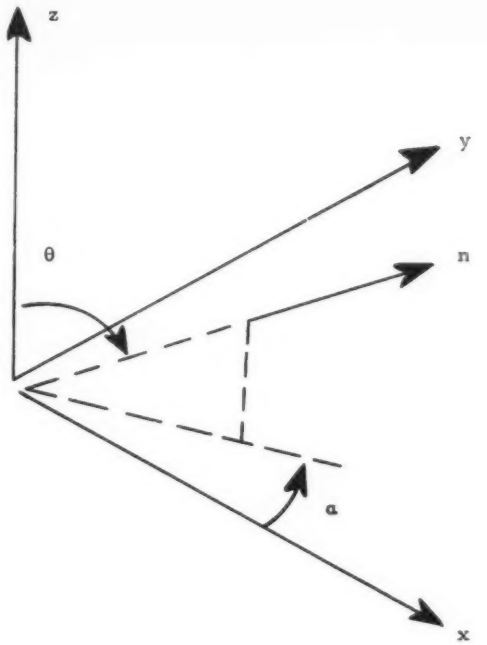

FIG. 2. The orientation of the wave normal n, assuming θ to be real.

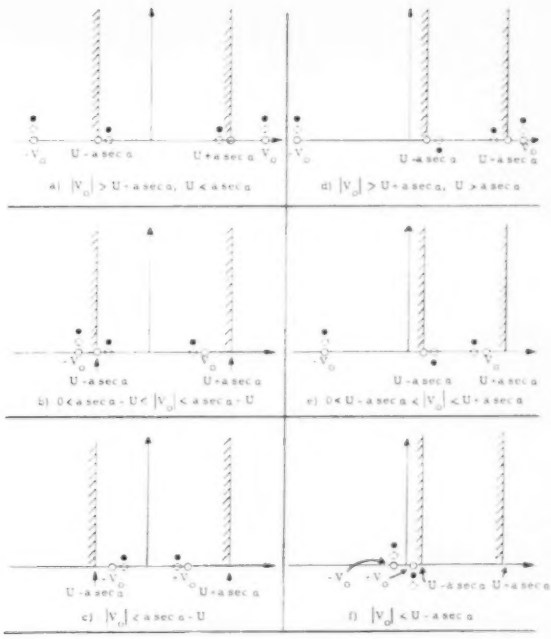
a) $|V_0| > U + a\sec\alpha$, $U < a\sec\alpha$
d) $|V_0| > U + a\sec\alpha$, $U > a\sec\alpha$
b) $0 < a\sec\alpha - U < |V_0| < a\sec\alpha - U$
e) $0 < U - a\sec\alpha < |V_0| < U + a\sec\alpha$
c) $|V_0| < a\sec\alpha - U$
f) $|V_0| < U - a\sec\alpha$

FIG. 3. Illustrating the relative position of the roots to Eq. (4.1) for various values of V_0; the open circles denote $\mu = 0+$, the broken circles small positive μ, and the solid circles small positive μ and g. The abscissa and ordinate in each diagram represent the real and imaginary parts of V, respectively.

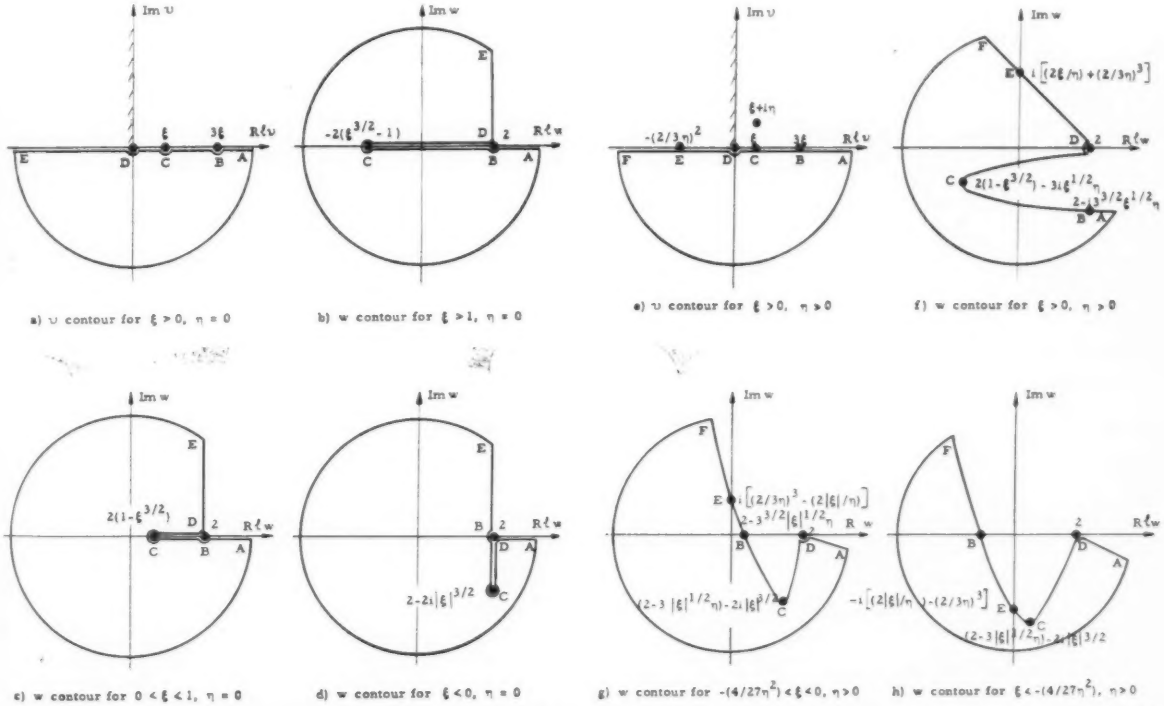
a) υ contour for ξ > 0, η = 0
b) w contour for ξ > 1, η = 0
e) υ contour for ξ > 0, η > 0
f) w contour for ξ > 0, η > 0
c) w contour for 0 < ξ < 1, η = 0
d) w contour for ξ < 0, η = 0
g) w contour for -(4/27η²) < ξ < 0, η > 0
h) w contour for ξ < -(4/27η²), η > 0

FIG. 4 (a)–(d). Cauchy-Nyquist diagrams mapping the lower half of the v plane on the plane $w = v^{3/2} - 3\xi v^{1/2} + 2$; an unstable root (Im $v < 0$ for $w = 0$) exists if the w contour encloses the origin, as in (c) and (d).
FIG. 4 (e)–(h). Cauchy-Nyquist diagrams for $w = v^{3/2} - 3(\xi + i\eta)v^{1/2} + 2$.

sec α. Nevertheless, they do indicate that the most serious instability for supersonic speeds will be associated with the confluence of the two primitive roots V_0 and $U - a$ sec α, and we therefore subject this neighborhood to a more refined analysis.

If both V_0 and V are assumed to approximate $U - a$ sec α, we may (approximately) factor out $(V + V_0)$ and $(U + a \sec \alpha - V)^{1/2}$ in Eq. (4.1) to obtain the approximation

$$(V - V_0)[V - (U - a \sec \alpha)]^{1/2} + 2^{-3/2}\mu(a \sec \alpha)^{5/2}(U - a \sec \alpha)^{-1} = 0 \quad (4.2)$$

We shall assume, in the remainder of this analysis, that V_0 can achieve the value $U - a$ sec α and that μ is sufficiently small to justify the neglect of $\mu^{4/3}(M \cos \alpha - 1)^{-10/3}$ relative to $\mu^{2/3}(M \cos \alpha - 1)^{-5/3}$ [cf. Eq. (4.3) below].

We now seek to establish more precisely the conditions under which Eq. (4.2) has a root (or roots) with negative imaginary part and to calculate the maximum magnitude of its phase angle—i.e., the maximum negative damping ratio. The analysis is expedited by the scale transformations

$$V = (U - a \sec \alpha)[1 + (1/2)v(\mu/2)^{2/3} \times (M \cos \alpha - 1)^{-5/3}], \quad -(3\pi/2) < \arg v \leq \pi/2 \quad (4.3a)$$

$$V_0 = (U - a \sec \alpha)[1 + (3/2)(\xi + i\eta)(\mu/2)^{2/3} \times (M \cos \alpha - 1)^{-5/3}] \quad (4.3b)$$

where v is a dimensionless complex variable that serves to expand the neighborhood of the branch point $V = U - a$ sec α, ξ measures the proximity of $|V_0|$ to this point, and η measures the structural hysteresis. If g denotes the usual structural damping ratio [such that $V_0^2 = |V_0^2|(1 + ig)$, $g \ll 1$], we have

$$\eta = (1/3)g(\mu/2)^{-2/3}(M \cos \alpha - 1)^{5/3} \quad (4.4)$$

Substituting Eqs. (4.3a) and (4.3b) in Eq. (4.2), we obtain

$$w(v) = v^{3/2} - 3(\xi + i\eta)v^{1/2} + 2 = 0, \quad -(3\pi/2) < \arg v \leq \pi/2 \quad (4.5)$$

where w is analytic in the cut v-plane.

A Cauchy-Nyquist analysis of Eq. (4.5) reveals that if $\eta = 0$, $w(v)$ has 0 or 1 zeros in Im $v < 0$ as $\xi > 1$ or $\xi < 1$, respectively, as shown in Fig. 4(a)–(d). We may compare this more refined approximation to the stability boundary in the absence of structural hysteresis—viz., $\xi = 1$—with the rough approximation $\xi = 0$ implied by the dotted circles in Fig. 3 [especially 3(e) and (f)].

The revision of the Cauchy-Nyquist diagrams required by structural hysteresis is shown in Fig. 4(e)–(h); this analysis leads to the conclusion that $w(v)$ has 0 or 1 zeros in Im $v < 0$ as $\xi < -(4/27\eta^2)$ or $\xi > -(4/27\eta^2)$, respectively. We infer from this result that structural hysteresis is capable of preventing instability in the neighborhood of $V = V_0$ only if V_0 is sufficiently small relative to $U - a$ sec α [cf. Fig. 3(f)]. If, on the other hand, V_0 is sufficiently close to $U - a$ sec α structural hysteresis cannot prevent instability, while if V_0 is sufficiently large compared with $U - a$ sec α ($\xi > 1$) instability actually must be charged to structural hysteresis in the sense that the motion would be stable in its absence [cf. Fig. 3(d) and (e)]. We remark that this rather striking result does not imply that energy can be produced by hysteresis per se, but rather that the phase shift associated with hysteresis may allow more energy per cycle to be extracted from the air stream than is dissipated in the structure.

Having established the conditions under which $w(v)$ has a root with negative imaginary part, we now seek to establish the maximum value of the latter quantity, corresponding to maximum growth *per cycle* of the unstable motion. We first separate the real and imaginary parts of v, say β and $-\gamma$, as functions of the independent variables ξ and η—viz.,

$$v = \beta(\xi, \eta) - i\gamma(\xi, \eta) \quad (4.6)$$

Substituting Eq. (4.6) in Eq. (4.5), differentiating partially with respect to ξ, and equating the real and imaginary parts of the result separately to zero yields*

$$\xi\gamma + \eta\beta = 0 \quad \text{if} \quad (\partial\gamma/\partial\xi)_\eta = 0 \quad (4.7)$$

This, together with the requirement that both η and γ be positive, requires the phases of $\xi + i\eta$ and $\beta - i\gamma$ to differ by $\pm\pi$; under this constraint Eq. (4.5) admits a solution in the cut plane only if the phases of these two complex numbers are taken as $\pi/3$ and $-2\pi/3$, respectively, and we write

$$\xi + i\eta = (2/\sqrt{3})\eta e^{i\pi/3} \quad (4.8a)$$

$$v = \beta - i\gamma = (2/\sqrt{3})\gamma e^{-2i\pi/3} \quad (4.8b)$$

Introducing these expressions in Eq. (4.5) yields

$$\gamma^{3/2} + 3\eta\gamma^{1/2} - 2^{-1/2} \cdot 3^{3/4} = 0 \quad (4.9)$$

The only *positive* root to Eq. (4.9) is found to be

$$\gamma = -2\eta + [(c^3 + \eta^3)^{1/2} + c^{3/2}]^{2/3} + [(c^3 + \eta^3)^{1/2} - c^{3/2}]^{2/3}, \quad c = \cos(\pi/6) = \sqrt{3}/2 \quad (4.10)$$

We now return to the original variables of Eq. (4.2). Imposing the constraint (4.8a) on Eq. (4.3b) and eliminating η through Eq. (4.4) yields

$$|V_0(\lambda, \alpha)| = (U - a \sec \alpha)[1 + O(g)] \quad (4.11)$$

while substituting v in Eq. (4.3a) from Eqs. (4.8b) and (4.10) and evaluating the damping ratio yields

* We recall that the original independent variables, with respect to which instability should be maximized, are the wave length λ_1 and the propagation angle α; within the approximation $\mu^{2/3}(M \cos \alpha - 1)^{-5/3} \ll 1$, the desired end may be accomplished by maximizing γ with respect to ξ and using the resulting value of ξ to establish a constraint between α and λ_1. The explicit representation of this constraint and the completion of the maximizing process require V_0 to be exhibited as a function of α and λ_1.

$$\delta = \text{Im } V/\text{Rl } V \tag{4.12a}$$

$$= -(1/2)\gamma(\mu/2)^{2/3}(M\cos\alpha - 1)^{-5/3} + O[\mu^{4/3}(M\cos\alpha - 1)^{-10/3}] \tag{4.12b}$$

$$= (g/3) - 2^{-2/3}[\sqrt{\delta_0^3 + (1/2)(g/3)^3} + \delta_0^{3/2}]^{2/3} - 2^{-2/3}[\sqrt{\delta_0^3 + (1/2)(g/3)^3} - \delta_0^{3/2}]^{2/3} \tag{4.12c}$$

where δ_0 is the negative damping ratio when $g = 0$, viz.,

$$\delta_0 = (\sqrt{3}/4)\mu^{2/3}(M\cos\alpha - 1)^{-5/3} \tag{4.13a}$$

$$= (\sqrt{3}/4)[\rho_a\lambda_1/(\rho_t\lambda_1 + 2\pi m)]^{2/3} \times (M\cos\alpha - 1)^{-5/3} \tag{4.13b}$$

It remains to maximize $-\delta$ with respect to λ_1 and α, subject to the constraint (4.11), but this cannot be done until the explicit dependence of V_0 on λ_1 and α is established. We remark that, for fixed δ_0, δ is a monotonically increasing function of g, so that it suffices to maximize δ_0, after which δ can be calculated from Eq. (4.12c).

The ratio δ/δ_0 is plotted in Fig. 5 as a function of g/δ_0—viz.,

$$\frac{\delta}{\delta_0} = \left(\frac{g}{3\delta_0}\right) - \left[\frac{\sqrt{1 + (1/2)(g/3\delta_0)^3} + 1}{2}\right]^{2/3} - \left[\frac{\sqrt{1 + (1/2)(g/3\delta_0)^3} - 1}{2}\right]^{2/3} \tag{4.14}$$

We note the following approximations:

$$\delta = -\delta_0 + (1/3)g + O(g^2/\delta_0) \tag{4.15}$$

$$\delta = -4g^{-2}\delta_0^3 + O(g^{-5}\delta_0^6) \tag{4.16a}$$

$$= -(3\sqrt{3}/16)(\mu/g)^2(M\cos\alpha - 1)^{-5} + O[\mu^4 g^{-5}(M\cos\alpha - 1)^{-10}] \tag{4.16b}$$

It follows from Eq. (4.15) that structural damping in sufficiently small amounts is two thirds effective (relative to the value $\delta = g/2$ that would result in the complete absence of aerodynamic forces); in large amounts Eq. (4.16) indicates the best that can be achieved is a weak instability of order g^{-2}. (By hypothesis g always must be small relative to unity, but it may be large relative to δ_0; if both g and δ_0 were sufficiently small, instability might be prevented by dissipative effects—viscous, thermal, or relaxation—in the air.) We also note that the condition $\xi < -(4/27\eta^2)$ implies that structural damping will stabilize the motion when

$$|V_0| < (U - a\sec\alpha)[1 - (1/2)\mu^2 g^{-2}(M\cos\alpha - 1)^{-5}] \tag{4.17}$$

The foregoing analysis could be extended to cover the neighborhood of the pseudosonic point $M\cos\alpha = 1$, where the transformation Eq. (4.3) requires modification. The first approximation to the stability boundary—i.e., the counterpart of $V_0 = U - a\sec\alpha$—is found to be[1]

$$V_0/U = (\sqrt{5}/2)\mu^{2/5} + O(|M\cos\alpha - 1|) \tag{4.18}$$

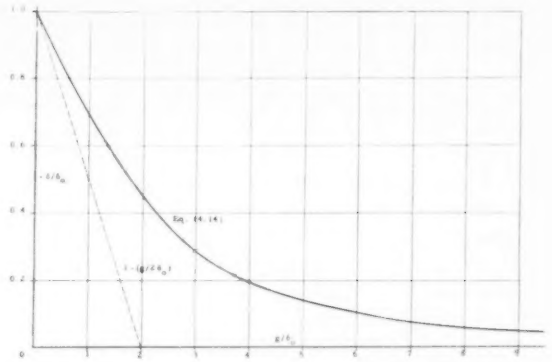

FIG. 5. The factor by which the negative damping ratio δ_0, calculated on the assumption of zero structural damping, is reduced by finite structural damping; the dashed line gives the reduction that would occur if the structural and aerodynamic damping factors could be calculated independently and then added directly.

The counterpart of Eq. (4.5) is a polynomial (in $v^{1/2}$) of fifth order, which would require numerical solution for the explicit calculation of the negative damping factor.

Again we emphasize that all of the results deduced from Eq. (4.2) *et seq.* assume that V_0 approximates $U - a\sec\alpha$ and that μ is small. If μ is small and the minimum value of V_0 exceeds $U - a$ by an appreciable amount, only the very weak instability of that primitive mode for which V approximates $U - a\sec\alpha$ [see Fig. 3(d) and (e) and footnote Eq. (4.1′)] can occur. If μ is large, on the other hand, the critical value of V_0 is U (see reference 1), but then the plane wave approximation may break down for a nonplane structure (see Appendixes A and B).

(5) Wave Speed for Cylindrical Shell

The types of waves that may be propagated along a cylindrical shell may be classified in a general way as longitudinal, tangential, or transverse as the dominant motion is axial, circumferential, or radial. The last class of waves is the one of principal interest in the present investigation, both because of the intrinsically smaller wave speeds and because only transverse motion gives rise to aerodynamic forces.

The equations governing transverse wave propagation might be deduced from the general equations of vibratory motion established by Rayleigh[11] and Love,[12] but we remark that, since frequency varies like $\lambda^{-1}V$, the wave lengths of minimum wave speed and minimum frequency must be expected to be quite different. For this reason, the anticipated deflection patterns resemble more closely those calculated (on small deflection theory) for axial buckling of a cylindrical shell, the axial load being analogous to the inertia force.* It is known[13] that such buckling characteristi-

* We note that observed buckling patterns usually differ markedly from those predicted on small deflection theory; however, we anticipate that nonlinear structural effects will be rather less important in the dynamical problem—see, e.g., Love's remarks, reference 12, p. 553—at least in the determination of stability criteria.

cally occurs with a wave length that is sufficiently small to make those extensional and flexural stresses associated with transverse deflections of approximately equal importance but sufficiently large to render extensional stresses dominant in the axial and circumferential directions. Motivated by this result, we shall include only direct extensional stresses in the axial and circumferential equations of motion, noting that the accuracy of the implied approximations may be established a posteriori. We also shall neglect the axial and circumferential accelerations (u_{tt} and v_{tt}) and the rotatory inertia of the shell wall.

The equations of equilibrium of a thin-walled, cylindrical shell are, on the basis of the foregoing approximations,[14]

$$u_{xx} + [(1 - \nu)/2]u_{yy} + [(1 + \nu)/2]v_{xy} - (\nu/R)w_x = 0 \quad (5.1a)$$

$$[(1 + \nu)/2]u_{xy} + [(1 - \nu)/2]v_{xx} + v_{yy} - (1/R)w_y = 0 \quad (5.1b)$$

$$[(Eh/R)/(1 - \nu^2)](-\nu u_x - v_y + R^{-1}w) - [N_x w_{xx} + N_y w_{yy}] + D\{w_{xxxx} + 2w_{xxyy} + w_{yyyy}\} = p \quad (5.1c)$$

where u, v, and w denote the axial, circumferential, and normal (radially inward) displacements of an element of the wall, x and y the axial and circumferential coordinates (x need not be distinguished from x_1 in determining V_0), R the radius of the cross section, h the wall thickness, ν Poisson's ratio, E Young's modulus, N_x and N_y the axial and circumferential preloads per unit length, p the normal load per unit area, and D the bending stiffness. The terms in parentheses, brackets, and braces on the left-hand side of Eq. (5.1c) represent the effects of extension, preload, and bending, respectively. We seek a reduction of Eqs. (5.1a, b, c) to [cf. Eq. (3.2)]

$$Lw = p \quad (5.2)$$

for deflections having the spacewise dependence [cf. Eq. (3.13)]

$$u, v, w \sim \exp\{-(2\pi i/\lambda_1)(x \cos\alpha + y \sin\alpha)\} \quad (5.3)$$

Substituting the displacements of Eq. (5.3) in Eqs. (5.1a, b, c) yields algebraic equations in u, v, and w; solving these for w and comparing the result to Eq. (5.2), we obtain

$$L = (Eh/R^2)\cos^4\alpha + (N_x\cos^2\alpha + N_y\sin^2\alpha) \times (2\pi/\lambda_1)^2 + D(2\pi/\lambda_1)^4 \quad (5.4)$$

The corresponding wave speed, as defined by Eq. (3.17), then is given by

$$V_0^2(\lambda_1, \alpha) = \frac{Eh(\lambda_1\cos\alpha/2\pi R)^2 + (N_x + N_y\tan^2\alpha) + D(2\pi/\lambda_1\cos\alpha)^2}{m + (\rho_i\lambda_1/2\pi)} \quad (5.5)$$

If we substitute

$$a_1^2 = Eh/m = E/\rho_1 \quad (5.6)$$

$$N_x = Eh\epsilon_x, \qquad N_y = Eh\epsilon_y \quad (5.7)$$

$$D = Eh^3/12(1 - \nu^2) \quad (5.8)$$

in Eq. (5.5), where a_1 is the velocity of sound *in* the shell material, ρ_1 its density, and ϵ_x and ϵ_y measures of the initial strains (ϵ_x and ϵ_y would be the true strains only if $\nu = 0$), we obtain the alternative expression

$$V_0^2(\lambda_1, \alpha) = a_1^2[1 + (\rho_i\lambda_1/2\pi\rho_1 h)]^{-1} \times \{(\lambda_1\cos\alpha/2\pi R)^2 + (\epsilon_x + \epsilon_y\tan^2\alpha) + [1/12(1 - \nu^2)](2\pi h/\lambda_1\cos\alpha)^2\} \quad (5.9)$$

which is especially appropriate when the shell inertia dominates that of the internal fluid ($\rho_i\lambda_1 \ll 2\pi\rho_1 h$).

The result of Eq. (5.5) may be generalized for application to an aeolotropic shell by introducing nonequal effective values of the wall thickness in axial extension (h_x), circumferential extension (h_y), and shear (h_{xy}) and of flexural and torsional rigidities for an axial element (I_x and I_{xy}) and a circumferential element (I_y and I_{yx}), all in the notation of Timoshenko.[15] The transverse wave speed, assuming the wave length to be *large* compared with the spacing of stiffening elements (so that their contributions to h_x, . . ., I_{yx} may be averaged over a wave length) but small compared with the radius and length of the shell, is given by[4]

$$V_0^2(\lambda_1, \alpha) = [m_1 + (\rho_i\lambda_1/2\pi)]^{-1}\{E[(\cos^4\alpha\, h_y) + (2\sin^2\alpha\cos^2\alpha\, h_{xy}) + (\sin^4\alpha\, h_x)]^{-1} \times (\lambda_1\cos\alpha\, 2\pi R)^2 + (N_x + N_y\tan^2\alpha) + E[I_x\cos^4\alpha + (I_{xy} + I_{yx})\sin^2\alpha\cos^2\alpha + I_y\sin^4\alpha](2\pi\lambda_1\cos\alpha)^2\} \quad (5.10)$$

We emphasize that the results just obtained for V_0 are valid only for wave lengths (λ_1) that are small compared with both the radius (R) and length (l) of the shell; the neglect of axial and circumferential bending and inertial forces is valid only if $\lambda_1 \ll R$, while the neglect of the end constraints requires $\lambda_1 \ll l$. It is perhaps well to recall, on the other hand, that we have implicitly assumed $\lambda_1 \gg h$, since the Eqs. (5.1) are valid only for *thin* shells and neglect rotatory inertia. We shall find that these inequalities usually will be satisfied in the neighborhood of minimum (with respect to λ_1 and α) wave speed, but they must be borne in mind in interpreting the limiting trends of the results for very large or very small wave lengths.

(6) Empty Isotropic Shell

We consider in this section the more specific configuration of an isotropic shell that is not prestressed. We also shall neglect the inertia of the internal fluid, on the assumption that

$$\rho_i\lambda_1 \ll 2\pi\rho_1 h \quad (6.1)$$

as usually would be true for a gas (but not a liquid). The wave speed given by Eq. (5.9) then reads

$$V_0^2(\lambda_1, \alpha) = a_1^2\{(\lambda_1\cos\alpha/2\pi R)^2 + [1/12(1 - \nu^2)](2\pi h/\lambda_1\cos\alpha)^2\} \quad (6.2)$$

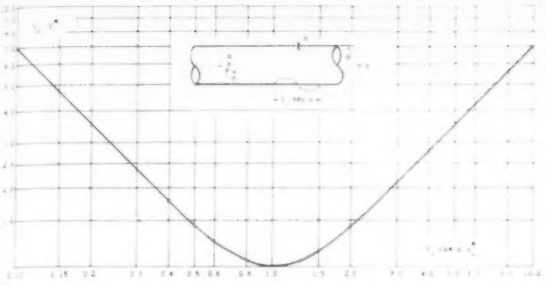

FIG. 6. The variation of axial wave speed for an empty isotropic cylindrical shell; α is the angle between the wave normal (n) and the x-axis, and λ_1 is the wave length in the direction of propagation—see Eqs. (6.3) to (6.5).

The wave speed of Eq. (6.2) depends on the single variable $\lambda_1 \cos \alpha$ (rather than λ_1 and α independently) in a very symmetrical way that may be emphasized by rewriting it in the form

$$V_0^2 = (1/2)V^{*2}[(\lambda_1 \cos \alpha/\lambda_1^*)^2 + (\lambda_1^*/\lambda_1 \cos \alpha)^2] \quad (6.3)$$

where V^*, the minimum value of V_0, is given by

$$V^* = [3(1 - \nu^2)]^{-1/4}(h/R)^{1/2}a_1 \quad (6.4)$$

and λ_1^*, the value of $\lambda_1 \cos \alpha$ at which this minimum occurs, by

$$\lambda_1^* = 2\pi[12(1 - \nu^2)]^{-1/4}(Rh)^{1/2} \quad (6.5)$$

This result is plotted in Fig. 6. We observe that extensional and flexural deformation make equal contributions to the wave speed at the minimum point; moreover, to any prescribed value of the wave speed greater than V^* there correspond two values of $\lambda_1 \cos \alpha$ having the geometric mean λ_1^*, with extension or flexure dominating as $\lambda_1 \cos \alpha$ exceeds or is inferior to λ_1^*. This behavior of the wave speed is analogous to that found for surface waves on water,[16] where gravity and surface tension appear as the counterparts of extension and flexure, respectively; however, in *that* problem the exponents of (λ/λ_1^*) would be ± 1, rather than ± 2 as in Eq. (6.3). We also remark that Eq. (6.5) implies that the wave length in the neighborhood of the minimum wave speed is of the order of the geometric mean of the radius and thickness of the shell, whence the hypotheses $\lambda_1 \ll R$ and $\lambda_1 \gg h$ both will be satisfied for thin shells ($h \ll R$).

The flutter speed—i.e., the minimum flight speed required to produce instability—is given in first approximation by the minimum value of $V_0(\lambda_1, \alpha) + a \sec \alpha$. Regarding $\lambda_1 \cos \alpha$ and α as independent variables, we find that this minimum occurs at $\alpha = 0$ and $\lambda_1 = \lambda_1^*$ and has the value

$$U^* = V^* + a \quad (6.6)$$

Eliminating V^* between Eqs. (6.4) and (6.6), we find that the shell wall thickness/radius ratio required to prevent flutter at a flight speed U is given by

$$(h^*/R) = \sqrt{3(1 - \nu^2)}[(U - a)/a_1]^2, \qquad U > a \quad (6.7)$$

This approximation is too crude near $U = a$, but it suffices if faired into the end point (at $U = a$) deduced from Eq. (4.18), which, in conjunction with Eqs. (6.4) and (6.5), yields

$$(h^*/R) = 1.29(1 - \nu^2)^{3/14}(a/a_1)^{10/7}(\rho_a/\rho_1)^{4/7} \quad \text{at } U = a \quad (6.8)$$

The numerical values of (h^*/R) given by Eqs. (6.7) and (6.8) are plotted vs. Mach Number in Fig. 7 for duralumin and steel at sea level or an altitude of 35,000 ft. We remark that Eq. (6.7), depending only on the sonic velocities a and a_1, is relatively insensitive to changes in altitude, especially in the troposphere (35,000–1,000,000 ft.), where a is approximately constant.

If the ratio h/R is inferior to the critical value (h^*/R), flutter is predicted by the analysis of Section 4, and we may determine the critical negative damping ratio by maximizing δ_0, as given by Eq. (4.13), with respect to λ_1 and α, subject to the constraint (4.11). The effect of structural hysteresis on the damping ratio then may be evaluated from Eq. (4.14) or Fig. 5.

If a factor $(\cos \alpha)^{2/3}$ is absorbed in the parameter μ in Eq. (4.13) and the remaining dependence on $\cos \alpha$ removed through the constraint [rewriting Eq. (4.11)]

$$\cos \alpha = [a/(U - V_0)] \quad (6.9)$$

we obtain

$$\delta_0 = (\sqrt{3}/4)(\rho_a\lambda_1 \cos \alpha/2\pi\rho_1 h)^{2/3}(V_0/a)^{-5/3} \times [(U - V_0)/a]^{7/3}, \qquad U > V_0 + a \quad (6.10)$$

which, referring to Eq. (6.2), is a function of the single variable $\lambda_1 \cos \alpha$. We find that a satisfactory approximation (less than 7 per cent error) to the maximum value of Eq. (6.10) as a function of $\lambda_1 \cos \alpha$ may be ob-

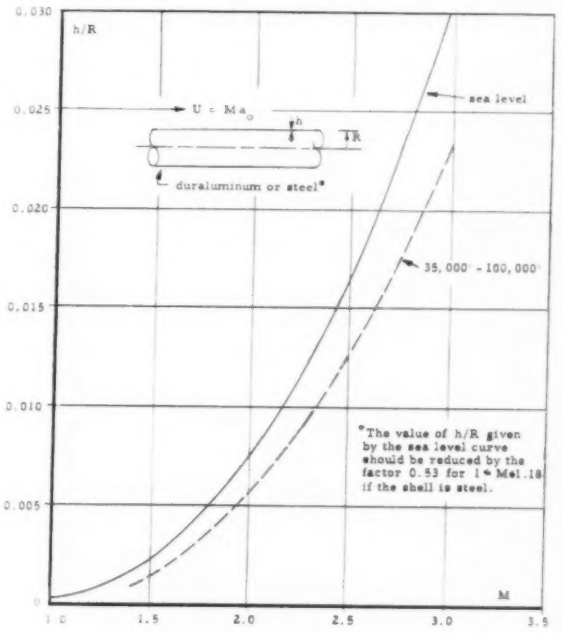

FIG. 7. The minimum thickness/radius ratio required to prevent flutter of an empty isotropic cylindrical shell in a supersonic air stream.

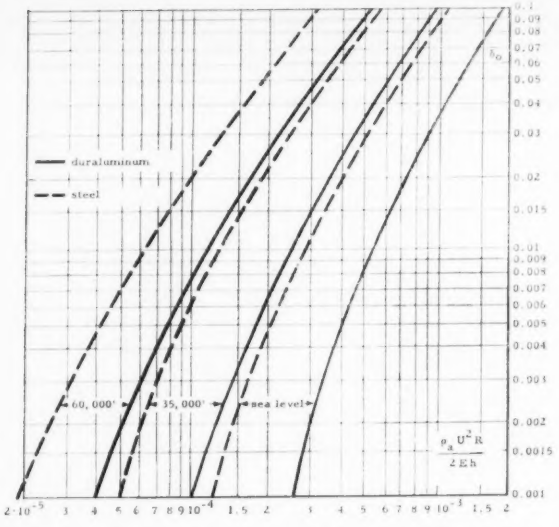

FIG. 8. The critical damping ratio δ_0 for an empty isotropic cylindrical shell; see Fig. 5 for the effect of structural damping.

tained by assuming it to coincide with the minimum of V_0; substituting $\lambda_1 \cos \alpha = \lambda_1^*$ and $V_0 = V^*$ from Eqs. (6.5) and (6.4) then yields

$$\delta_0^* = (3/4)^{3/4}(1 - \nu^2)^{1/4}(2a_1/a)^{2/3}(\rho_1/\rho_a)^{1/2} \times [(\rho_a U^2 R/2Eh)^{1/2} - (12)^{-1/4}(1 - \nu^2)^{-1/4} \times (\rho_a/\rho_1)^{1/2}]^{7/3} \qquad U > V^* + a \quad (6.11)$$

The corresponding numerical values are plotted in Fig. 8 for duralumin and steel at three altitudes.

The frequency at which flutter occurs is, by reference to Eq. (3.13),

$$f = \lambda_1^{-1} V \cos \alpha \qquad (6.12)$$

The frequency corresponding to Eq. (6.11) is obtained by letting $\lambda_1 = \lambda_1^* \sec \alpha$ and $V = V^*$ in Eq. (6.12) and substituting $\cos \alpha$ from Eq. (6.9), with the result

$$f^* = (\sqrt{2}a_1/2\pi R)[a/(U - V^*)]^2 > (\sqrt{2}a_1/2\pi R)M^{-2} \quad (6.13)$$

The frequency at the flutter speed ($U = V^* + a$) is, therefore, inversely proportional to the time that would be taken by sound to travel a distance equal to the circumference of the cylinder *in* the material itself and falls off approximately as the inverse square of the Mach Number at higher speeds. We find, for example, $f^* = 750$ cps for a steel or duralumin fuselage 10 ft in diameter at the flutter speed—viz., $U = V^* + a$.

APPENDIX A—AERODYNAMIC FORCES

We investigate here the accuracy of the plane wave approximation for a circular cylinder. The transverse wave motion along the surface of the cylinder given by Eq. (3.8) is, in cylindrical polar coordinates (x, r, φ),

$$\zeta = A_1 \exp\{(2\pi i/\lambda_1)[ct - x \cos \alpha - R\varphi \sin \alpha]\} \quad (A\text{-}1)$$

We require a solution to the wave equation

$$a^2 \nabla^2 \phi = \phi_{tt} \qquad (A\text{-}2)$$

subject to the boundary condition

$$\phi_r = \zeta_t = (2\pi i c/\lambda_1)\zeta \qquad r = R \quad (A\text{-}3)$$

together with the radiation and finiteness conditions at infinity.

We first remark that if ζ is to be continuous in φ, α and λ_1 must be constrained according to

$$2\pi R \sin \alpha/\lambda_1 = n \qquad (A\text{-}4)$$

where n is an integer; however, insofar as $\lambda_1 \ll R$ we may assume α and λ_1 to be distributed over a continuous spectrum. A solution to Eq. (A-1) that satisfies Eq. (A-3) and the conditions at infinity is given by

$$\phi = (2\pi i R c/\lambda_1)[K_n(zr/R)/zK_n'(z)]\zeta \qquad (A\text{-}5)$$

$$z = \frac{2\pi R}{\lambda_1}\sqrt{\cos^2 \alpha - (c/a)^2} \qquad (A\text{-}6)$$

provided that z is required to have a positive real part (*finiteness* condition) and a non-negative imaginary part (*radiation* condition); K_n is a modified Bessel function of the second kind.

The perturbation pressure on the cylinder is given by

$$p_a = -\rho_a \phi_t \qquad (A\text{-}7)$$

Substituting Eq. (A-5) in Eq. (A-7) and introducing the function

$$\psi_n(z) = -K_n(z)/zK_n'(z) \qquad (A\text{-}8a)$$

$$= 2^{z-1}[K_{n+1}(z) + K_{n-1}(z)]^{-1}K_n(z) \qquad (A\text{-}8b)$$

we obtain

$$p_a = -\rho_a(2\pi R c/\lambda_1)^2 \psi_n(z) \cdot (\zeta/R) \qquad (A\text{-}9)$$

We may show that the ψ_n functions have the asymptotic approximation (*vide infra*)

$$\psi_n(z) \sim (n^2 + z^2)^{-1/2} \qquad (A\text{-}10)$$

while for small z we find

$$\psi_0(z) = \ln(2/z) - 0.577 + O(z^2) \qquad (A\text{-}11a)$$

$$\psi_n(z) = (1/n) + O(z^2) \qquad n \geq 1 \quad (A\text{-}11b)$$

It follows that the approximation (A-10) is exact as z tends to either 0 or ∞ unless $n = 0$; if $n = 0$ there should be a logarithmic singularity at the origin rather than the z^{-1} singularity exhibited by Eq. (A-10). The corresponding approximation to the pressure, obtained by substituting Eq. (A-10) in Eq. (A-9) and evaluating n from Eq. (A-4), reads

$$p_a = -(2\pi \rho_a c^2/\lambda_1)[1 - (c/a)^2]^{-1/2}\zeta \qquad (A\text{-}12)$$

in agreement with Eq. (3.11b).

It remains to investigate the approximation (A-10) at the flutter point. We note first that the function ψ_n defined by Eq. (A-8a) satisfies the Riccati equation

$$z(d\psi_n/dz) = (n^2 + z^2)\psi_n^2 - 1 \qquad (A\text{-}13)$$

from which it may be inferred that the validity of Eq.

(A-10) demands

$$|n^2 + z^2|^{3/2} \gg n^2 + 1 \qquad \text{(A-14)}$$

We have, from Eq. (4.3a),

$$\epsilon = (V - U)\cos\alpha = -a[1 - (1/2)\nu(\mu/2)^{2/3} \times (M\cos\alpha - 1)^{-2/3}] \qquad \text{(A-15)}$$

which, in conjunction with Eqs. (A-4) and (A-6), yields

$$|n^2 + z^2|^{3/2} = |\nu/2|^{3/2}(2\pi R/\lambda_1)^2\{\rho_a R/[\rho_1 h + (\rho_i\lambda_1/2\pi)]\}\ (M\cos\alpha - 1)^{-1} \qquad \text{(A-16)}$$

We find, for example, that for the unpressurized shell of Section (6) the right-hand side of Eq. (A-16) is $0[(\rho_a a \div \rho_1 a_1)(R/h)^{5/2}\sec\alpha]$, whereas n^2 is $0[(R/h)\sin^2\alpha]$, where α is determined by the constraint Eq. (4.11). We conclude that the inequality Eq. (A-14) probably would be satisfied adequately at the minimum flutter speed ($\alpha = 0$) but might be violated for large α.

Appendix B—Long Wave-Length Instability

Leonard and Hedgepeth[17] recently have given a panel flutter analysis of a circular cylinder in which the plane wave approximation is not made; indeed, they imply that the most serious instabilities are to be anticipated at axial wave lengths—i.e., $\lambda_1 \sec\alpha$—comparable to or greater than the radius of the cylinder. This conclusion is, in our opinion, open to the following major objections:

(1) The waves corresponding to $n = 0$ (pure dilation of cross sections) and $n = 1$ (cross sections remain circular but execute translation) are rather arbitrarily excluded by Leonard and Hedgepeth, "because neither of these two motions involves panel action"; nevertheless, as we have shown in the preceding analysis, axially symmetric motion generally yields the minimum flutter speed for an isotropic shell and this at a wave length small compared with the radius.

(2) The comparative importance of the long and short wave-length stability boundaries for fixed $n \geq 2$ (resulting from the two minima of V_0 as a function of the axial wave length $\lambda_1 \sec\alpha$) depends, aside from the question of structural constraints such as rings, on the relative magnitudes of the respective negative damping factors. We shall calculate the long wave-length damping factor and show that it is likely to be much smaller in magnitude than the short wave-length factor of Eq. (4.13).

If the plane wave approximation to the aerodynamic pressure is not made, and $\rho_i = 0$, we may deduce from Eq. (A-9) that the required generalization of Eq. (3.20) is

$$V^2 + (\rho_a R/\rho_1 h)(V - U)^2\psi_n(z) = V_0^2 \qquad \text{(B-1)}$$

where z is given by Eq. (A-6). If $U > V + a$ we may, in accordance with Eqs. (3.9a) and (3.9b), write z in the form

$$z = \bar{\nu}\sqrt{[(U - V)/a]^2 - 1}\,e^{-i\pi/2}, \qquad \bar{\nu} = 2\pi R\cos\alpha/\lambda_1 \qquad \text{(B-2)}$$

where $\bar{\nu}$ is a dimensionless, axial wave number in the notation of Leonard and Hedgepeth. We require an expression for the imaginary part of ψ_n on the assumptions that $|z| \ll 1$ and $n > 0$ (since, for $n = 0$, V_0 has only a single minimum, and the choice between long and short wave length need not be made).

We first remark that ψ_n depends only on z^2 and $\ln z$; then, if (by hypothesis) the phase angle of V is small the phase of z (for $U > V + a$) will be approximately $-\pi/2$ [cf. Eq. (B-2)], and the imaginary part of ψ_n must arise through the logarithmic terms. Introducing the series expansion[18] for K_n in Eq. (A-8a), we obtain

$$\psi_n(z) = (1/n) + [4(-)^{n+1}/(n!)^2](z/2)^{2n}\ln z + O(z^2, z^{2n+2}\ln z) \qquad \text{(B-3)}$$

for the leading terms of interest. Substituting z from Eq. (B-2), the leading real and imaginary terms are given by

$$\psi_n = (1/n) + [2\pi i/(n!)^2](\bar{\nu}/2)^{2n}\{[(U - V)/a]^2 - 1\}^n \qquad n \geq 1, \quad U > V + a \qquad \text{(B-4)}$$

We proceed further on the assumption that $\rho_a R \ll n\rho_1 h$, so that V_0 serves as a first approximation to V [if this approximation were not justified the first approximation to V could be determined by substituting $\psi_n = n^{-1}$ in Eq. (B-1) and solving for V]; Eq. (B-1) then yields

$$V = V_0\{1 - (1/2)(\rho_a R/\rho_1 h)[(U - V_0)/V_0]^2\psi_n + O(\rho_a R/\rho_1 h)^2\} \qquad \text{(B-5)}$$

as the next approximation to V. The approximation to the damping ratio inferred from Eqs. (B-4) and (B-5) is

$$\delta = -[\pi\bar{\nu}^{2n}/2^{2n}(n!)^2](\rho_a R/\rho_1 h) \times [(U - V_0)/V_0]^2\{[(U - V_0)/a]^2 - 1\}^n \qquad n > 0, \quad \bar{\nu} \ll 1, \quad U > V_0 + a \qquad \text{(B-6)}$$

It is evident that the long wave length, negative damping factor given by Eq. (B-6) generally would be much smaller than the short wave-length factor of Eq. (4.13). We consider as a numerical example an isotropic shell of duralumin for which $h/R = 0.0025$, $M = 2$, and the properties of the air correspond to sea level. Fig. 7 yields a minimum Mach Number of 1.5 for instability, while Fig. 8 yields a negative damping factor of 0.08 at $M = 2$. The result of Eq. (B-6) cannot be maximized with respect to the parameters $\bar{\nu}$ and n without violating the approximations on which it is based (which, in itself, implies that maximum instability is not to be sought at long wave lengths), but if we set V_0 equal to its minimum value of $0.5a$ for the specified data and use the values $n = 2$ and $\bar{\nu} = 0.11$ [the smaller root of Eq. (17), reference 17] deduced by Leonard and Hedgepeth, we obtain $-\zeta = 1.9 \times 10^{-5}$. It seems unlikely that an instability as mild as that indicated by this last figure could occur in a real fluid.

References

[1] Miles, J. W., *On the Aerodynamic Instability of Thin Panels*, The Ramo-Wooldridge Corporation Report AM 5-2A, May 20,

1955; Journal of the Aeronautical Sciences, Vol. 23, No. 8, pp. 771–780, August, 1956.

[2] Miles, J. W., *Supersonic Flutter of a Cylindrical Shell: I—General Theory*, The Ramo-Wooldridge Corporation Report AM 5-2, August 19, 1955.

[3] Miles, J. W., *Supersonic Flutter of a Cylindrical Shell: II—Pressurization and Internal Fluid Effects*, The Ramo-Wooldridge Corporation Report AM 5-11, November 14, 1955.

[4] Miles, J. W., *Supersonic Flutter of a Cylindrical Shell: III—Aeolotropic Shells*, The Ramo-Wooldridge Corporation Report AM 5-12, December 2, 1955.

[5] Miles, J. W., *Supersonic Flutter of a Cylindrical Shell: IV—Effects of Nonuniform Steady Flow*, The Ramo-Wooldridge Corporation Report AM 5-16, December 7, 1955.

[6] Lord Rayleigh, *On the Instability of Jets*, Proc. Lond. Math. Soc., Vol. 10, p. 7, 1878; *Scientific Papers*, Vol. 1, p. 361, Cambridge University Press.

[7] Lord Rayleigh, *Theory of Sound*, Vol. 2, pp. 351–368; Dover Publications, New York, 1945.

[8] Reissner, Eric, *Nonlinear Effects in Vibrations of Cylindrical Shells*, The Ramo-Wooldridge Corporation Report AM 5-6, September 30, 1955.

[9] Lord Rayleigh, *op. cit.*, p. 76; Eq. (3.3) represents a generalization to three dimensions.

[10] *Ibid.*, p. 84.

[11] Lord Rayleigh, *Note on the Free Vibrations of an Infinitely Long Shell*, Proc. Roy. Soc. Lond., Vol. 45, pp. 443–448, 1889; *Scientific Papers*, Vol. 3, pp. 244–248, Cambridge University Press.

[12] Love, A. E. H., *The Mathematical Theory of Elasticity*, pp. 538–549; Dover Publications, New York, 1944.

[13] Timoshenko, S., *Theory of Elastic Stability*, Section 84; McGraw-Hill Book Co., New York, 1936.

[14] *Ibid.*, p. 476.

[15] *Ibid.*, p. 471.

[16] Lamb, H., *Hydrodynamics*, Section 267, p. 458; Dover Publications, New York, 1945.

[17] Leonard, R. W., and Hedgepeth, J. M., *On Panel Flutter and Divergence of Infinitely Long Unstiffened and Ring Stiffened Thin Walled Circular Cylinders*, NACA TN 3638, April, 1956.

[18] Watson, G. N., *Bessel Functions*, p. 80, Eq. 3.71(15); Cambridge University Press, 1945.

Travel Arrangements

Institute of the Aeronautical Sciences and The Royal Aeronautical Society Conference, London–Folkestone, September 1–16, 1957

Arrangements have been made with "The Travel Center of Manhasset" to accomplish all travel and hotel reservations for the delegates and their wives. This travel bureau handles all arrangements on a "personal" basis. The bureau has now obtained commitments from air lines, steamship companies, and hotels to assure the availability of accommodations. The air-line commitments include group arrangements on TWA and Pan American flights which will allow delegates to travel overseas together.

Special arrangements also have been made by the travel bureau with American Express, Thomas Cook & Son, and Ask Mr. Foster for preconvention and postconvention tours of Europe by the delegates—individually or in groups.

A travel brochure for the conference is being prepared and will be circulated to all members early this year. In the meantime, full travel information can be obtained and reservations made by addressing inquiries to:

IAS Conference Travel
2 East 64th Street
New York 21, N.Y.

An Authorized Binding for Journal of the Aeronautical Sciences

Arrangements have been made by the Institute of the Aeronautical Sciences for members and subscribers to have their Journals bound carefully and economically. Simply write for details to:

Publishers' Authorized Bindery Service

5809 West Division St. Chicago 51, Ill.

Tables and Curves for Deformations and Stresses in Circular Cylindrical Shells Under Localized Loadings†

JOSEPH KEMPNER,* JAMES SHENG,** AND FREDERICK V. POHLE***

Polytechnic Institute of Brooklyn

SUMMARY

The results of calculations of displacements, rotations, membrane stresses, and bending stresses corresponding to line loadings along generator segments of simply supported thin-walled circular cylindrical shells are presented in tables and curves. The computations are based upon a previously developed solution of the Donnell equations and are presented for radius-thickness ratios of 10 to 1,500 and radius-length ratios of 1/5 to 10. The data permit the determination of the displacements and stresses in the neighborhood of the applied loads. These loads (along generator segments) consist of a uniformly distributed radial load, symmetric with respect to a generator midpoint; a piecewise uniformly distributed radial load, antisymmetric with respect to the same point; and a symmetric uniformly distributed moment loading. Thus, the loads are statically equivalent to a concentrated radial force and to concentrated axial and circumferential bending moments applied at the midpoint of a generator.

Procedures are also described which facilitate the application of the present results to cylinders under arbitrary radial surface loads.

SYMBOLS

D = $Eh^3/[12(1-\nu^2)]$
E = elastic modulus
L = length of cylinder
M_x, M_φ = axial and circumferential internal moment resultants per unit length, respectively
$M_{x\varphi}$, $M_{\varphi x}$ = internal twisting moment resultants per unit length
M_x^*, M_φ^* = applied axial and circumferential moment resultants, respectively
P^* = applied inward radial load resultant
Q_x, Q_φ = axial and circumferential internal transverse shear resultants per unit length, respectively
a = mean radius of cylinder
h = wall thickness
u, v, w = ratios of the axial, circumferential, and inward radial displacements to the radius a
x = coordinate distance measured in axial direction divided by the radius a (origin at midpoint of loaded generator)
2δ = loaded length of generator symmetrically located about $x = 0$
ν = Poisson's ratio (taken as 0.3 in calculations)
σ_x, σ_φ, $\tau_{x\varphi}$ = axial, circumferential, and shear membrane stresses, respectively
σ_{xb}, $\sigma_{\varphi b}$ = maximum (extreme-fiber) axial and circumferential bending stresses, respectively, positive at inner surface of shell
φ = circumferential angular coordinate (origin on loaded generator)
, = comma under a symbol and followed by either x or φ denotes partial differentiation with respect to the indicated coordinate

Received December 21, 1955.

† The work reported on was sponsored by the Office of Ordnance Research, Department of the Army, under Contract No. Da-30-069-ORD-1263, Project No. TB2-001(999)ORD-TB-62.

The authors are indebted to Mrs. Elaine Godofsky, Drs. Frances and Louis Bauer, and the Reeves Instrument Corporation (contracted to the Bureau of Aeronautics on Project Cyclone) for their generous cooperation in the determination of the basic data required in this investigation, and to Julian Garvil of the PIBAL research staff for his assistance on the numerical calculations.

* Associate Professor of Aeronautical Engineering.

** Research Associate.

*** Associate Professor of Applied Mechanics.

INTRODUCTION

CIRCULAR CYLINDRICAL SHELLS are used extensively in all major industries such as the chemical, petroleum, electrical, and, more recently, nuclear reactor industries. They are also widely applied as structural components of submarines, airplanes, guided missiles, and rockets. In most applications, loads of a localized nature due to gravity and inertia effects or to thermal expansion of a connected piping system are transmitted to the shell walls. These loads generally consist of force and moment components. The attendant local stresses which must be combined with the basic stresses—e.g., due to internal pressure—can of themselves be significant and in many cases require careful consideration for the economical design of attachments and reinforcements.

Recently, an investigation of the deformations and stresses caused by localized radial forces and axial and circumferential bending moments applied to thin-walled circular cylinders of constant wall thickness was carried out for the Knolls Atomic Power Laboratory.[1–10] In this work, the loads were considered to be distributed along a segment of a generator, and the cylinder dimensions (radius-thickness and radius-length ratios) were assumed to be in a range such that the simple Donnell equations were applicable. A brief history of solutions of related problems, including a representative bibliography, can be found in references 2 and 8. Recent contributions to the solutions of such problems have also been made by P. P. Bijlaard.[11, 12] In this latter work, the loads were considered to be applied over a small rectangular area of the shell surface, and the equations used in the analysis differed somewhat from those of Donnell.

The purpose of the present paper is to present the results of calculations of displacement and stress quan-

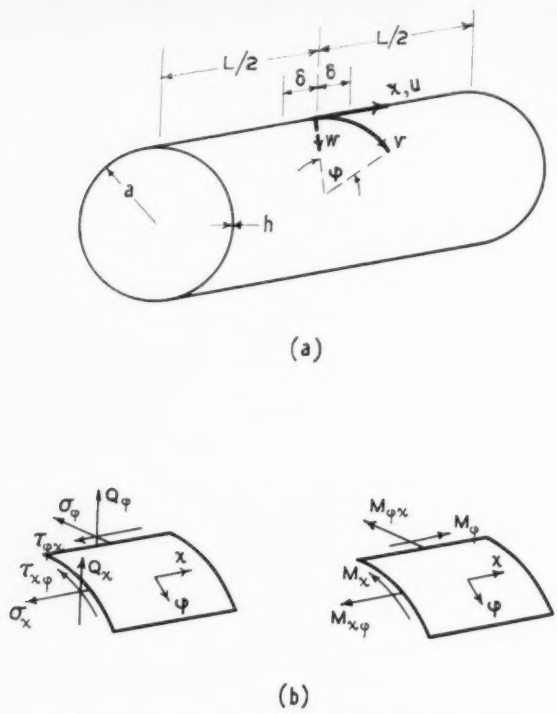

FIG. 1. Sign conventions for coordinates, displacements, membrane stresses, and internal moment and transverse shear resultants.

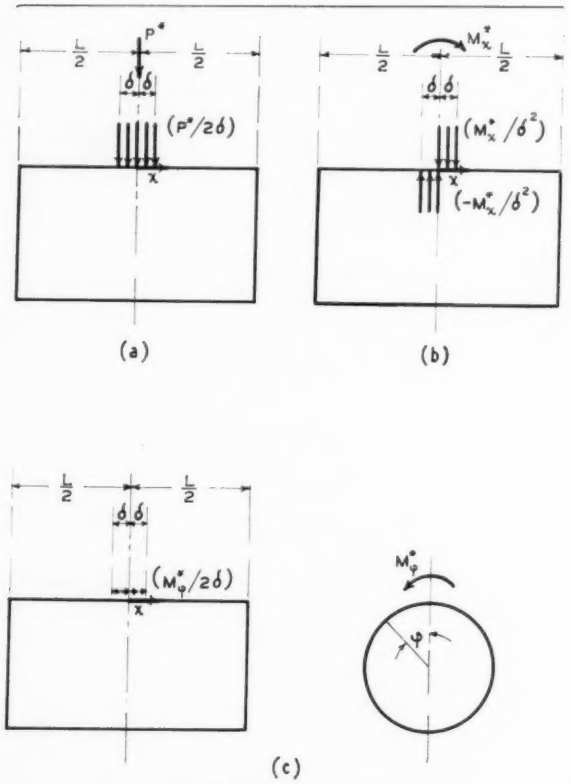

FIG. 2. Applied force and moment loadings.

tities caused by the action of localized radial forces and axial and circumferential moments applied as distributed line loads along a segment of a generator of a simply supported thin-walled cylinder. It is shown that the data presented can be utilized to approximate surface loadings of an arbitrary nature. Except for minor refinements indicated in reference 13, the method of calculation is that given in references 2, 3, 4, and 8. The results are presented in tables and curves in a form readily applied by the designer for the estimation of deflections, rotations, membrane stresses, and bending stresses at and in the neighborhood of the load resultants. The geometric cylinder parameters, radius-thickness and radius-length ratios, respectively, cover the ranges 10 to 1,500 and 1/5 to 10.

METHOD OF ANALYSIS

Solutions of the Donnell equations[14] were obtained in references 2 and 8 for distributed line loads whose resultants are a radial force P^*, an axial moment M_x^*, and a circumferential moment M_φ^* (see Figs. 1 and 2). The loads were applied along a length 2δ of the $\varphi = 0$ generator as indicated in Fig. 2, where φ is the circumferential angular coordinate. They consisted of a uniformly distributed radial load, symmetric with respect to the generator midpoint ($x = 0$) [see Fig. 2(a)]; a piecewise uniformly distributed radial load, antisymmetric with respect to the $x = 0$ plane [see Fig. 2(b)]; and a uniformly distributed moment loading [shown vectorially in Fig. 2(c)], symmetric with respect to $x = 0$.

The radial force, axial moment, and circumferential moment loadings, respectively, therefore correspond to a distributed symmetric radial load (P^* case), defined as

$$\left.\begin{array}{lll} (P^*/2\delta) & \text{when} & |x| \leq (\delta/a) \\ 0 & \text{when} & (L/2a) \geq |x| > (\delta/a) \end{array}\right\} \quad (1)$$

a distributed antisymmetric radial load (M_x^* case), given as

$$\left.\begin{array}{lll} (M_x^*/\delta^2) & \text{when} & 0 < x \leq (\delta/a) \\ -(M_x^*/\delta^2) & \text{when} & -(\delta/a) \leq x < 0 \\ 0 & \text{when} & (L/2a) \geq |x| > (\delta/a) \end{array}\right\} \quad (2)$$

and a distributed circumferential moment loading (M_φ^* case)

$$\left.\begin{array}{lll} (M_\varphi^*/2\delta) & \text{when} & |x| \leq (\delta/a) \\ 0 & \text{when} & (L/2a) \geq |x| > (\delta/a) \end{array}\right\} \quad (3)$$

in which L and a, respectively, are the length and mean radius of the cylinder, and x is the axial coordinate divided by a.

Formulas for stress and displacement quantities corresponding to the three loading cases are given in references 2, 8, and 13 for conditions of simple supports at the ends of the cylinder. These conditions imply that the radial and circumferential displacements as well as the axial membrane stresses and axial bending

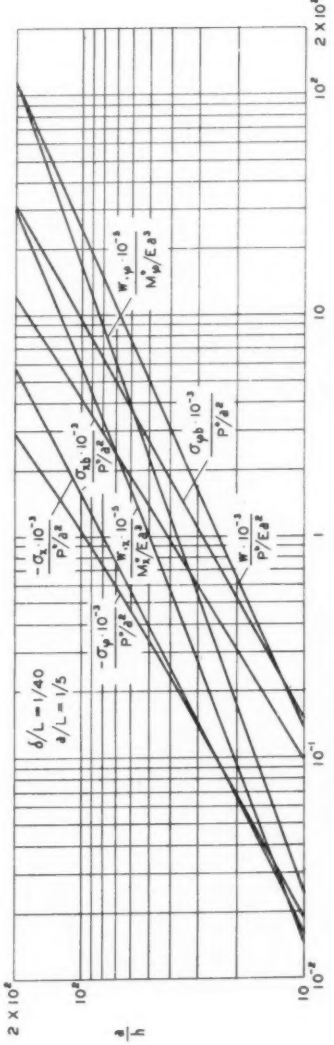

FIGURE 3 VARIATION OF STRESS AND DISPLACEMENT QUANTITIES WITH a/h AT x = 0, φ=0 FOR δ/L = 1/40 AND a/L = 1/5

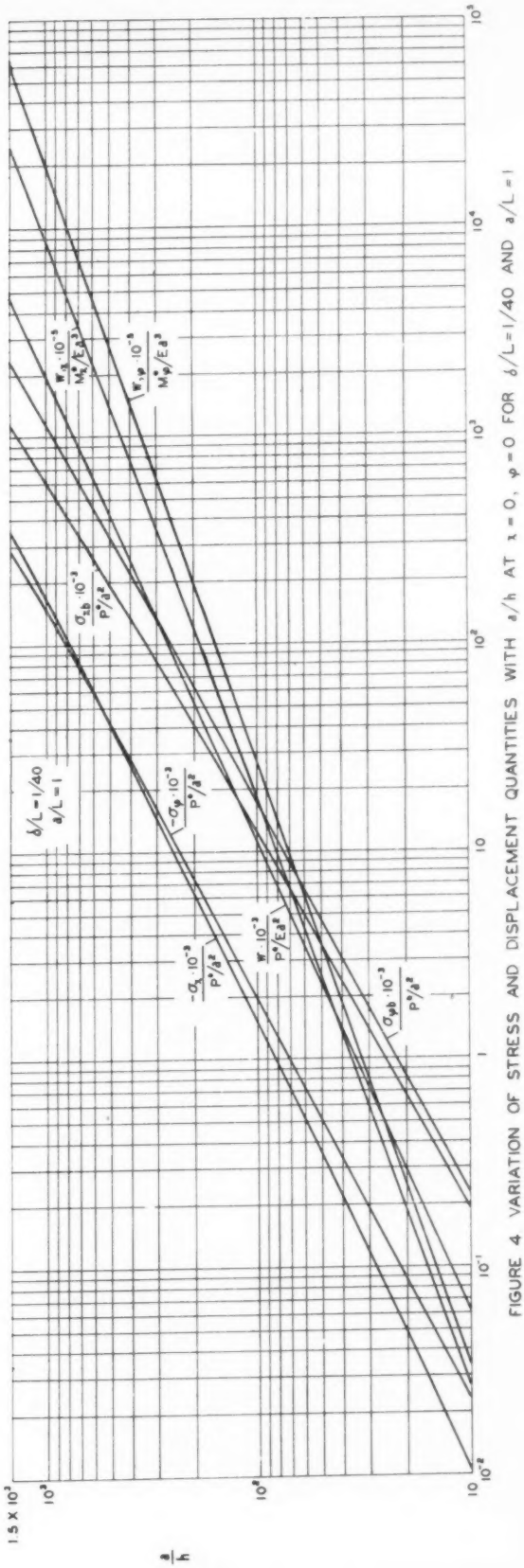

FIGURE 4 VARIATION OF STRESS AND DISPLACEMENT QUANTITIES WITH a/h AT x = 0, φ = 0 FOR δ/L=1/40 AND a/L = 1

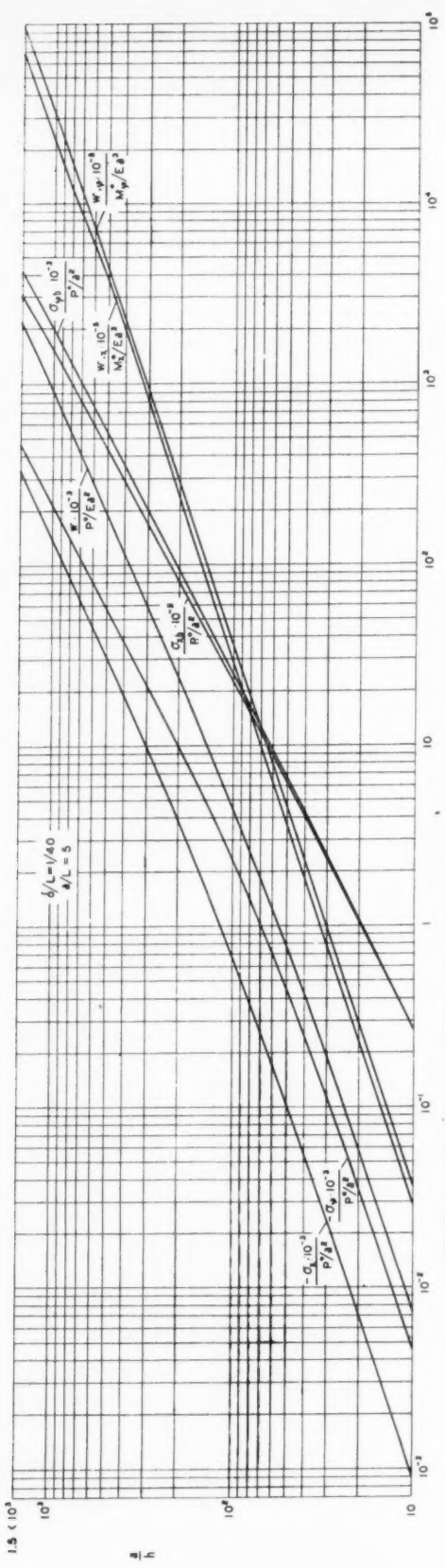

FIGURE 5. VARIATION OF STRESS AND DISPLACEMENT QUANTITIES WITH y/h AT $x = 0$, $\psi = 0$ FOR $\delta/L = 1/40$ AND $a/L = 5$

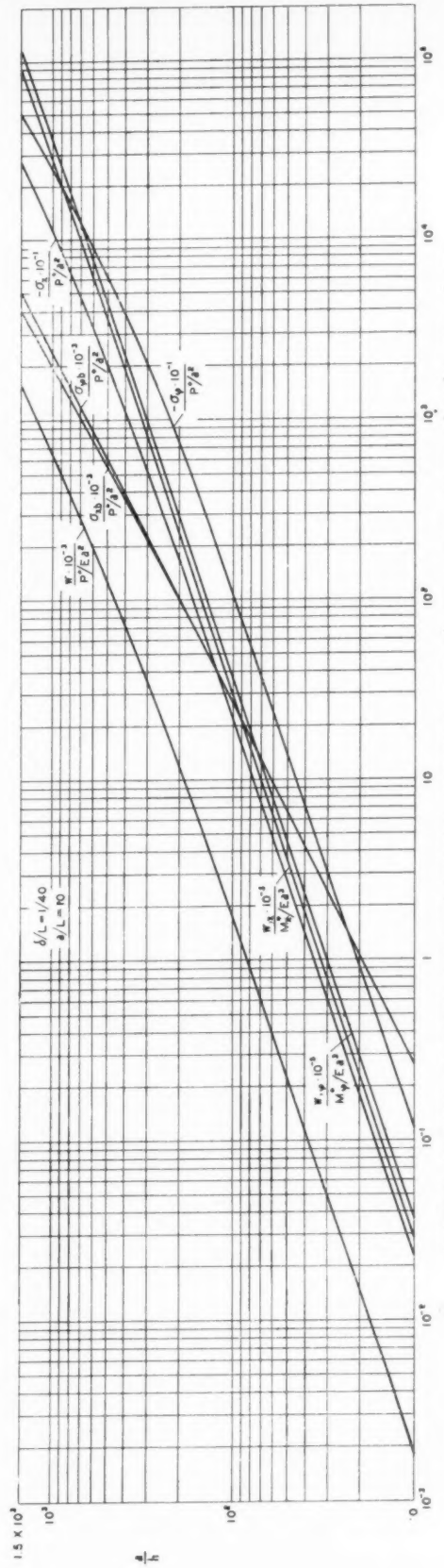

FIGURE 6 VARIATION OF STRESS AND DISPLACEMENT QUANTITIES WITH y/h AT $x = 0$, $\psi = 0$ FOR $\delta/L = 1/40$ AND $a/L = 10$

moment resultant vanish at $x = \pm(L/2a)$. Convenient methods for performing corresponding computations are presented in references 1, 3, 4, and 13, and discussions of conditions under which the results of solutions of Donnell's equations are applicable are given in references 6, 9, 10, 14, and 15.

Results and Applications

The formulas of references 2, 3, 8, and 13 were used to compute deflections w, rotations $w_{,x}$ and $w_{,\varphi}$, normal bending stresses σ_{xb} and $\sigma_{\varphi b}$, and normal membrane stresses σ_x and σ_φ for a wide range of geometric shell parameters (see Fig. 1). For each of the three loading cases characterized by Eqs. (1) to (3) (see also Fig. 2), the ratio of the loaded length to shell length $(2\delta/L)$ was fixed as $(1/20)$. Because of the large number of parameters involved in the analysis of the cylinders, it was deemed expedient to so limit the loaded length rather than any of the shell parameters. The small finite loaded length was chosen so as to bring out the salient effects of localized loadings on cylinders in a realistic manner; the use of truly concentrated loadings ($\delta = 0$) always introduces infinite bending stresses under the applied loads.[8] Moreover, it will be shown later that the present results can be used to analyze the effect of loadings other than those specifically treated.

Calculations were performed for values of the radius-length ratio (a/L) of 1/5, 1, 5, and 10. These values correspond to moderate to very short length cylinders, where the length of a cylinder in practical applications is considered to be the distance between adjacent reinforcing rings or bulkheads. Computations corresponding to $(a/L) = 1/5$ were performed for radius-thickness ratios (a/h) of 10, 20, 50, 100, and 200; and for $(a/L) = 1$, 5, and 10 for values of (a/h) of 10, 20, 50, 100, 200, 500, 800, 1,200, and 1,500. Thus, the range of (a/h) amply covers that usually encountered in shell applications with the exception of very thick-walled vessels. It may be noted that when $(a/L) = 1/5$, no calculations were performed for $(a/h) > 200$. The calculations were so limited, since for shells with $(a/L) < 1/4$, say, it is unlikely that very large (a/h) values would be permitted unless lateral supports, such as rings or bulkheads, were introduced. The resulting relatively short effective lengths permit the use of larger (a/L) values in the cylinder analysis.

Displacements and Stresses at $x = \varphi = 0$

The results of the calculations are presented in Figs. 3 to 6 and in Tables 2 to 21. Figs. 3 to 6 correspond to stress and displacement quantities computed at the location of the load resultants, that is, at $x = \varphi = 0$, (see Fig. 2). The nondimensional form for each quantity permits the corresponding load case to be readily identified. Thus, whenever P^* appears in the denominator, the data given correspond to the radial loading (P^*) case, etc.

The displacement quantities plotted may be considered as flexibility (reciprocal stiffness) quantities. Each is essentially the displacement or rotation under a load resultant in a direction corresponding to the resultant. These quantities should be quite useful when dealing with piping or similar problems in which the stiffness of the shell affects the amount of load introduced into the shell and external structure. The data show that, in the range of parameters considered, the flexibility in the circumferential direction is always greater than that in the axial direction. This result, of course, is influenced by the difference in the manner of loading in the M_φ^* case and M_x^* case.

The remaining data in Figs. 3 to 6 correspond to the axial and circumferential bending and membrane stresses at $x = \varphi = 0$ for the P^* case. Because the M_x^* loading is introduced as an antisymmetric radial load [see Eq. (2) and Fig. 2(b)], the deflections as well as normal bending and membrane stresses for this case are identically zero at $x = 0$; hence, these quantities are not indicated in Figs. 3 to 6. Similarly, since the M_φ^* loading is considered as a distributed moment along the $\varphi = 0$ generator [see Eq. (3) and Fig. 2(c)], the deflections and normal membrane stresses are identically zero at $\varphi = 0$, and the normal bending stresses can be obtained readily with the aid of Eq. (3) as follows. At $\varphi = 0$, the internal moment resultant M_φ is one-half of the applied distributed moment. Hence, from Eq. (3)

$$\left.\begin{aligned}(M_\varphi)_{\varphi=0} &= M_\varphi^*/4\delta \qquad \text{when } |x| \leq (\delta/a)\\ (M_\varphi)_{\varphi=0} &= 0 \qquad \text{when } (L/2a) \geq |x| > (\delta/a)\end{aligned}\right\} \tag{4}$$

Since maximum (extreme-fiber) bending stresses are simply $(6/h^2)$ times corresponding moment resultants (see, for example, p. 45 of reference 16), Eqs. (4) result in the following formulas for the inner surface circumferential bending stress at $\varphi = 0$:

$$\left.\begin{aligned}[\sigma_{\varphi b}/(M_\varphi^*/a^3)]_{\varphi=0} &= (3/2)\,(L/\delta)\,(a/h)^2\,(a/L)\\ &\qquad \text{when } |x| \leq (\delta/a)\\ [\sigma_{\varphi b}/(M_\varphi^*/a^3)]_{\varphi=0} &= 0\\ &\qquad \text{when } (L/2a) \geq |x| > (\delta/a)\end{aligned}\right\} \tag{5}$$

Furthermore, within the accuracy of the Donnell equations,

$$\left.\begin{aligned}M_x &= -(D/a)\,(w_{,xx} + \nu w_{,\varphi\varphi})\\ M_\varphi &= -(D/a)\,(w_{,\varphi\varphi} + \nu w_{,xx})\end{aligned}\right\} \tag{6}$$

Since w is identically zero at $\varphi = 0$, and hence, $(w_{,xx})_{\varphi=0} = 0$, Eqs. (6) yield $(M_x)_{\varphi=0} = \nu(M_\varphi)_{\varphi=0}$, and hence, the inner surface axial bending stress at $\varphi = 0$ is given by

$$[\sigma_{xb}/(M_\varphi^*/a^3)]_{\varphi=0} = \nu[\sigma_{\varphi b}/(M_\varphi^*/a^3)]_{\varphi=0} \tag{7}$$

Because the bending stresses given by Eqs. (5) and (7) are related in a simple manner to the various parameters involved, they are not plotted in Figs. 3 to 6. However, it may be noted that, since these stresses are simple power functions of (a/h), they would plot as straight lines in these Figures. It is seen that the

TABLE 1
Values of Coordinates Used in Calculations

$\delta/L = 1/40$

x or φ / a/L	$x_1 = \varphi_1$ $= (1/2)(\delta/a)$	$x_2 = \varphi_2$ $= (\delta/a)$	$x_3 = \varphi_3$ $= 2(\delta/a)$	$x_4 = \varphi_4$ $= (1/4)(L/a)$
1/5	0.0625	0.125	0.25	1.25
1	0.0125	0.025	0.05	0.25

TABLE 2
Variation of $w/(P^*/Ea^2)$ with (a/h) and x for $\varphi = 0$; $(\delta/L = 1/40)$

x / a/h	0	x_1	x_2	x_3	x_4
	$a/L = 1/5$				
10	1.39×10^{2}	1.37×10^{2}	1.31×10^{2}	1.16×10^{2}	4.87×10^{1}
20	6.55×10^{2}	6.44×10^{2}	6.11×10^{2}	5.28×10^{2}	2.29×10^{2}
50	5.06×10^{3}	4.95×10^{3}	4.65×10^{3}	3.98×10^{3}	1.79×10^{3}
100	2.36×10^{4}	2.31×10^{4}	2.17×10^{4}	1.86×10^{4}	8.50×10^{3}
200	1.11×10^{5}	1.08×10^{5}	1.02×10^{5}	8.80×10^{4}	9.74×10^{4}
	$a/L = 1$				
20	2.94×10^{2}	2.93×10^{2}	2.89×10^{2}	2.76×10^{2}	1.66×10^{2}
50	2.33×10^{3}	2.31×10^{3}	2.27×10^{3}	2.12×10^{3}	1.56×10^{2}
100	1.11×10^{4}	1.10×10^{4}	1.07×10^{4}	9.75×10^{3}	3.85×10^{3}
500	4.09×10^{5}	4.02×10^{5}	3.82×10^{5}	3.30×10^{5}	1.43×10^{5}
1500	4.74×10^{6}	4.64×10^{6}	4.35×10^{6}	3.72×10^{6}	1.69×10^{6}

TABLE 3
Variation of $\sigma_{xb}/(P^*/a^2)$ with (a/h) and x for $\varphi = 0$; $(\delta/L = 1/40)$

x / a/h	0	x_1	x_2	x_3	x_4
	$a/L = 1/5$				
10	9.64×10^{1}	8.95×10^{1}	5.85×10^{1}	1.25×10^{1}	2.46
20	3.10×10^{2}	2.87×10^{2}	1.47×10^{2}	2.20×10^{1}	9.35
50	1.37×10^{3}	1.28×10^{3}	7.25×10^{2}	8.80×10^{1}	5.10×10^{1}
100	4.07×10^{3}	3.92×10^{3}	2.21×10^{3}	4.54×10^{2}	1.74×10^{2}
200	1.21×10^{4}	1.21×10^{4}	7.08×10^{3}	2.13×10^{3}	3.11×10^{3}
	$a/L = 1$				
20	6.76×10^{2}	6.45×10^{2}	5.07×10^{2}	2.75×10^{2}	-1.47×10^{2}
50	3.56×10^{3}	3.37×10^{3}	2.52×10^{3}	1.12×10^{3}	1.38×10^{3}
100	1.23×10^{4}	1.15×10^{4}	8.17×10^{3}	2.86×10^{3}	1.38×10^{2}
500	1.94×10^{5}	1.79×10^{5}	1.09×10^{5}	1.41×10^{4}	5.84×10^{3}
1500	1.14×10^{6}	1.08×10^{6}	6.05×10^{5}	8.35×10^{4}	4.31×10^{4}

TABLE 4
Variation of $\sigma_{\varphi b}/(P^*/a^2)$ with (a/h) and x for $\varphi = 0$; $(\delta/L = 1/40)$

x / a/h	0	x_1	x_2	x_3	x_4
	$a/L = 1/5$				
10	1.50×10^{2}	1.42×10^{2}	1.09×10^{2}	5.63×10^{1}	1.07×10^{1}
20	5.27×10^{2}	4.99×10^{2}	3.73×10^{2}	1.80×10^{2}	3.68×10^{1}
50	2.72×10^{3}	2.58×10^{3}	1.87×10^{3}	8.46×10^{2}	1.84×10^{2}
100	9.26×10^{3}	8.80×10^{3}	6.28×10^{3}	2.81×10^{3}	6.17×10^{2}
200	3.13×10^{4}	2.99×10^{4}	2.12×10^{4}	9.46×10^{3}	1.50×10^{4}
	$a/L = 1$				
20	8.46×10^{2}	8.14×10^{2}	6.75×10^{2}	4.41×10^{2}	-5.00×10^{1}
50	4.75×10^{3}	4.55×10^{3}	3.69×10^{3}	2.25×10^{3}	1.82×10^{3}
100	1.73×10^{4}	1.65×10^{4}	1.31×10^{4}	7.47×10^{3}	1.32×10^{3}
500	3.30×10^{5}	3.12×10^{5}	2.33×10^{5}	1.12×10^{5}	2.30×10^{4}
1500	2.35×10^{6}	2.23×10^{6}	1.60×10^{6}	7.24×10^{5}	1.57×10^{5}

TABLE 5
Variation of $-\sigma_x/(P^*/a^2)$ with (a/h) and x for $\varphi = 0$; $(\delta/L = 1/40)$

x / a/h	0	x_1	x_2	x_3	x_4
	$a/L = 1/5$				
10	1.59×10^{1}	1.56×10^{1}	1.48×10^{1}	1.26×10^{1}	2.96
20	6.47×10^{1}	6.30×10^{1}	5.83×10^{1}	4.57×10^{1}	9.39
50	4.00×10^{2}	3.83×10^{2}	3.38×10^{2}	2.32×10^{2}	4.49×10^{1}
100	1.54×10^{3}	1.46×10^{3}	1.23×10^{3}	7.61×10^{2}	1.48×10^{2}
200	5.73×10^{3}	5.38×10^{3}	4.34×10^{3}	2.45×10^{3}	3.72×10^{3}
	$a/L = 1$				
20	4.93×10^{1}	4.92×10^{1}	4.87×10^{1}	4.70×10^{1}	2.89×10^{1}
50	3.53×10^{2}	3.51×10^{2}	3.44×10^{2}	3.23×10^{2}	4.02×10^{1}
100	1.51×10^{3}	1.49×10^{3}	1.45×10^{3}	1.32×10^{3}	4.01×10^{2}
500	4.05×10^{4}	3.94×10^{4}	3.65×10^{4}	2.86×10^{4}	5.87×10^{3}
1500	3.57×10^{5}	3.41×10^{5}	2.97×10^{5}	1.99×10^{5}	3.84×10^{4}

TABLE 6
Variation of $-\sigma_\varphi/(P^*/a^2)$ with (a/h) and x for $\varphi = 0$; $(\delta/L = 1/40)$

x / a/h	0	x_1	x_2	x_3	x_4
	$a/L = 1/5$				
10	1.84×10^{1}	1.75×10^{1}	1.46×10^{1}	7.56	-6.17×10^{-1}
20	6.70×10^{1}	6.16×10^{1}	4.65×10^{1}	1.33×10^{1}	-1.89
50	3.40×10^{2}	2.98×10^{2}	1.81×10^{2}	-1.69×10^{1}	-6.23
100	1.05×10^{3}	9.04×10^{2}	4.50×10^{2}	-1.68×10^{2}	-1.48×10^{1}
200	2.90×10^{3}	2.57×10^{3}	1.03×10^{3}	-5.90×10^{2}	1.08×10^{2}
	$a/L = 1$				
20	8.65×10^{1}	8.59×10^{1}	8.38×10^{1}	7.70×10^{1}	3.81×10^{1}
50	5.15×10^{2}	5.07×10^{2}	4.81×10^{2}	4.02×10^{2}	-4.63×10^{2}
100	1.98×10^{3}	1.92×10^{3}	1.76×10^{3}	1.29×10^{3}	-1.89×10^{2}
500	4.19×10^{4}	3.85×10^{4}	2.91×10^{4}	8.32×10^{3}	-1.18×10^{3}
1500	2.89×10^{5}	2.51×10^{5}	1.45×10^{5}	-2.49×10^{4}	-4.96×10^{3}

TABLE 7
Variation of $w/(P^*/Ea^2)$ with (a/h) and φ for $x = 0$; $(\delta/L = 1/40)$

φ / a/h	0	φ_1	φ_2	φ_3	φ_4
	$a/L = 1/5$				
10	1.39×10^{2}	1.35×10^{2}	1.25×10^{2}	9.90×10^{1}	-4.69×10^{1}
20	6.55×10^{2}	6.27×10^{2}	5.63×10^{2}	3.93×10^{2}	-2.20×10^{2}
50	5.06×10^{3}	4.70×10^{3}	3.93×10^{3}	2.10×10^{3}	-1.11×10^{3}
100	2.36×10^{4}	2.13×10^{4}	1.64×10^{4}	6.19×10^{3}	-1.92×10^{3}
200	1.11×10^{5}	9.51×10^{4}	6.58×10^{4}	1.22×10^{4}	5.08×10^{4}
	$a/L = 1$				
10	6.15×10^{1}	6.03×10^{1}	5.98×10^{1}	5.81×10^{1}	3.08×10^{1}
20	2.94×10^{2}	2.84×10^{2}	2.81×10^{2}	2.68×10^{2}	8.96×10^{1}
50	2.33×10^{3}	2.27×10^{3}	2.22×10^{3}	2.04×10^{3}	3.86×10^{1}
100	1.11×10^{4}	1.08×10^{4}	1.04×10^{4}	9.10×10^{3}	-2.05×10^{3}
200	5.27×10^{4}	5.12×10^{4}	4.81×10^{4}	3.91×10^{4}	-1.67×10^{4}
500	4.09×10^{5}	3.92×10^{5}	3.52×10^{5}	2.46×10^{5}	-1.38×10^{5}
800	1.17×10^{6}	1.11×10^{6}	9.60×10^{5}	5.96×10^{5}	-3.37×10^{5}
1200	2.89×10^{6}	2.69×10^{6}	2.26×10^{6}	1.23×10^{6}	-6.52×10^{5}
1500	4.74×10^{6}	4.38×10^{6}	3.59×10^{6}	1.78×10^{6}	-8.79×10^{5}

TABLE 8

Variation of $\sigma_{xb}/(P^*/a^2)$ with (a/h) and φ for $x = 0$; $(\delta/L = 1/40)$

a/h \ φ	0	φ_1	φ_2	φ_3	φ_4
	a/L = 1/5				
10	9.64×10^{1}	7.44×10^{1}	5.39×10^{1}	2.53×10^{1}	-5.79
20	3.10×10^{2}	2.23×10^{2}	1.45×10^{2}	4.36×10^{1}	-8.96
50	1.37×10^{3}	8.35×10^{2}	4.11×10^{2}	-4.44×10^{1}	-7.03
100	4.07×10^{3}	2.02×10^{3}	5.89×10^{2}	-5.43×10^{2}	2.33×10^{1}
200	1.21×10^{4}	4.40×10^{3}	-8.33×10^{1}	-1.99×10^{3}	-1.22×10^{3}
	a/L = 1				
10	1.90×10^{2}	1.67×10^{2}	1.46×10^{2}	1.13×10^{2}	2.36×10^{1}
20	6.76×10^{2}	5.85×10^{2}	5.01×10^{2}	3.72×10^{2}	3.40×10^{1}
50	3.56×10^{3}	2.99×10^{3}	2.47×10^{3}	1.68×10^{3}	-1.12×10^{2}
100	1.23×10^{4}	9.98×10^{3}	7.92×10^{3}	4.83×10^{3}	-8.32×10^{2}
200	4.11×10^{4}	3.21×10^{4}	2.40×10^{4}	1.22×10^{4}	-2.77×10^{3}
500	1.94×10^{5}	1.38×10^{5}	9.07×10^{4}	2.72×10^{4}	-5.60×10^{3}
800	4.19×10^{5}	2.79×10^{5}	1.63×10^{5}	2.13×10^{4}	-5.54×10^{3}
1200	8.03×10^{5}	4.96×10^{5}	2.51×10^{5}	-2.01×10^{4}	-4.59×10^{3}
1500	1.14×10^{6}	6.70×10^{5}	3.04×10^{5}	-7.26×10^{4}	-2.88×10^{3}

TABLE 9

Variation of $\sigma_{\varphi b}/(P^*/a^2)$ with (a/h) and φ for $x = 0$; $(\delta/L = 1/40)$

a/h \ φ	0	φ_1	φ_2	φ_3	φ_4
	a/L = 1/5				
10	1.50×10^{2}	9.02×10^{1}	5.45×10^{1}	1.71×10^{1}	-1.16×10^{1}
20	5.27×10^{2}	2.91×10^{2}	1.52×10^{2}	1.59×10^{1}	-2.21×10^{1}
50	2.72×10^{3}	1.27×10^{3}	4.63×10^{2}	-1.97×10^{2}	-2.30×10^{1}
100	9.26×10^{3}	3.56×10^{3}	6.75×10^{2}	-1.14×10^{3}	8.50×10^{1}
200	3.13×10^{4}	9.19×10^{3}	-5.45×10^{2}	-4.22×10^{3}	-2.69×10^{3}
	a/L = 1				
10	2.27×10^{2}	1.67×10^{2}	1.30×10^{2}	8.86×10^{1}	-2.80×10^{-1}
20	8.46×10^{2}	6.06×10^{2}	4.60×10^{2}	2.95×10^{2}	-3.96×10^{1}
50	4.75×10^{3}	3.26×10^{3}	2.34×10^{3}	1.33×10^{3}	-4.45×10^{2}
100	1.73×10^{4}	1.13×10^{4}	7.70×10^{3}	3.72×10^{3}	-1.81×10^{3}
200	6.21×10^{4}	3.83×10^{4}	2.40×10^{4}	8.72×10^{3}	-5.47×10^{3}
500	3.30×10^{5}	1.82×10^{5}	9.52×10^{4}	1.02×10^{4}	-1.38×10^{4}
800	7.67×10^{5}	3.91×10^{5}	1.77×10^{5}	-1.88×10^{4}	-1.71×10^{4}
1200	1.58×10^{6}	7.42×10^{5}	2.78×10^{5}	-1.07×10^{5}	-1.51×10^{4}
1500	2.35×10^{6}	1.05×10^{6}	3.40×10^{5}	-2.06×10^{5}	-8.20×10^{3}

TABLE 10

Variation of $-\sigma_z/(P^*/a^2)$ with (a/h) and φ for $x = 0$; $(\delta/L = 1/40)$

a/h \ φ	0	φ_1	φ_2	φ_3	φ_4
	a/L = 1/5				
10	1.59×10^{1}	1.55×10^{1}	1.45×10^{1}	1.14×10^{1}	-4.63
20	6.47×10^{1}	6.20×10^{1}	5.53×10^{1}	3.75×10^{1}	-1.75×10^{1}
50	4.00×10^{2}	3.69×10^{2}	2.97×10^{2}	1.35×10^{2}	-7.03×10^{1}
100	1.54×10^{3}	1.36×10^{3}	9.57×10^{2}	2.12×10^{2}	-1.68×10^{2}
200	5.73×10^{3}	4.72×10^{3}	2.70×10^{3}	-1.68×10^{2}	1.74×10^{3}
	a/L = 1				
10	1.04×10^{1}	1.03×10^{1}	1.02×10^{1}	9.99	5.21
20	4.94×10^{1}	4.82×10^{1}	4.78×10^{1}	4.61×10^{1}	1.65×10^{1}
50	3.53×10^{2}	3.46×10^{2}	3.40×10^{2}	3.17×10^{2}	2.00×10^{1}
100	1.51×10^{3}	1.48×10^{3}	1.43×10^{3}	1.27×10^{3}	-2.20×10^{2}
200	6.30×10^{3}	6.15×10^{3}	5.80×10^{3}	4.75×10^{3}	-1.73×10^{3}
500	4.05×10^{4}	3.88×10^{4}	3.46×10^{4}	2.34×10^{4}	-1.09×10^{4}
800	1.03×10^{5}	9.76×10^{4}	8.32×10^{4}	4.78×10^{4}	-2.30×10^{4}
1200	2.31×10^{5}	2.13×10^{5}	1.73×10^{5}	8.05×10^{4}	-4.15×10^{4}
1500	3.57×10^{5}	3.26×10^{5}	2.55×10^{5}	1.02×10^{5}	-5.65×10^{4}

TABLE 11

Variation of $-\sigma_\varphi/(P^*/a^2)$ with (a/h) and φ for $x = 0$; $(\delta/L = 1/40)$

a/h \ φ	0	φ_1	φ_2	φ_3	φ_4
	a/L = 1/5				
10	1.84×10^{1}	1.78×10^{1}	1.71×10^{1}	1.47×10^{1}	3.51×10^{-1}
20	6.70×10^{1}	6.52×10^{1}	6.05×10^{1}	4.66×10^{1}	-1.17
50	3.40×10^{2}	3.27×10^{2}	2.82×10^{2}	1.67×10^{2}	-1.23
100	1.05×10^{3}	9.74×10^{2}	7.70×10^{2}	3.15×10^{2}	-3.80
200	2.90×10^{3}	2.55×10^{3}	1.76×10^{3}	3.45×10^{2}	1.32×10^{3}
	a/L = 1				
10	2.32×10^{1}	2.26×10^{1}	2.25×10^{1}	2.24×10^{1}	1.78×10^{1}
20	8.65×10^{1}	8.14×10^{1}	8.11×10^{1}	7.99×10^{1}	5.47×10^{1}
50	5.15×10^{2}	4.90×10^{2}	4.86×10^{2}	4.69×10^{2}	2.06×10^{2}
100	1.98×10^{3}	1.90×10^{3}	1.86×10^{3}	1.74×10^{3}	4.05×10^{2}
200	7.52×10^{3}	7.27×10^{3}	7.03×10^{3}	6.21×10^{3}	3.79×10^{2}
500	4.19×10^{4}	4.07×10^{4}	3.78×10^{4}	2.91×10^{4}	-7.32×10^{2}
800	9.79×10^{4}	9.49×10^{4}	8.53×10^{4}	5.86×10^{4}	-1.04×10^{3}
1200	1.98×10^{5}	1.91×10^{5}	1.65×10^{5}	9.92×10^{4}	-7.94×10^{2}
1500	2.89×10^{5}	2.75×10^{5}	2.33×10^{5}	1.27×10^{5}	-7.63×10^{2}

TABLE 12

Variation of $w/(M_x^*/Ea^3)$ with (a/h) and x for $\varphi = 0$; $(\delta/L = 1/40)$

a/h \ x	0	x_1	x_2	x_3	x_4
	a/L = 1/5				
10	0	7.88×10^{1}	1.19×10^{2}	1.18×10^{2}	2.59×10^{1}
20	0	4.93×10^{2}	7.03×10^{2}	4.75×10^{2}	1.26×10^{2}
50	0	5.11×10^{3}	6.44×10^{3}	4.70×10^{3}	9.69×10^{2}
100	0	2.75×10^{4}	3.12×10^{4}	2.28×10^{4}	4.63×10^{3}
200	0	1.37×10^{5}	1.41×10^{5}	4.38×10^{4}	2.31×10^{4}
	a/L = 1				
20	0	2.28×10^{2}	3.91×10^{2}	5.68×10^{2}	4.81×10^{2}
50	0	1.56×10^{3}	4.94×10^{3}	6.67×10^{3}	3.08×10^{3}
100	0	2.04×10^{4}	3.28×10^{4}	5.96×10^{4}	1.10×10^{4}
500	0	1.54×10^{6}	2.18×10^{6}	1.89×10^{6}	3.92×10^{5}
1500	0	2.50×10^{7}	3.08×10^{7}	1.87×10^{7}	4.52×10^{6}

TABLE 13

Variation of $\sigma_{xb}/(M_x^*/a^3)$ with (a/h) and x for $\varphi = 0$; $(\delta/L = 1/40)$

a/h \ x	0	x_1	x_2	x_3	x_4
	a/L = 1/5				
10	0	7.74×10^{2}	6.06×10^{2}	1.30×10^{2}	4.63
20	0	2.94×10^{3}	2.17×10^{3}	2.58×10^{2}	1.65×10^{1}
50	0	1.61×10^{4}	1.03×10^{4}	-9.85×10^{1}	1.82×10^{1}
100	0	5.37×10^{4}	2.95×10^{4}	-1.53×10^{3}	1.40×10^{2}
200	0	1.64×10^{5}	7.88×10^{4}	4.31×10^{2}	5.50×10^{2}
	a/L = 1				
20	0	1.63×10^{4}	1.36×10^{4}	4.89×10^{3}	1.24×10^{2}
50	0	1.01×10^{5}	8.37×10^{4}	2.81×10^{4}	-1.29×10^{2}
100	0	4.00×10^{5}	3.26×10^{5}	9.79×10^{4}	3.44×10^{4}
500	0	9.20×10^{6}	6.77×10^{6}	8.05×10^{5}	5.15×10^{4}
1500	0	6.95×10^{7}	4.29×10^{7}	-2.39×10^{6}	-3.43×10^{5}

curves which are given in Figs. 3 to 6 approximate straight lines [particularly in the lower region of (a/h)], indicating that simple empirical formulas relating each of the quantities to a power of (a/h) could be obtained for the fixed values of (a/L).

Although all stress and displacement quantities thus increase monotonically with increasing (a/h), no such general observation can be made with respect to changes in (a/L). However, the data do show that within the ranges of (a/L) and (a/h) considered, the flexibility $w/(P^*/Ea^2)$ decreases with increasing (a/L) for fixed values of (a/h), while the flexibilities $w_{,\varphi} \div (M_\varphi^*/Ea^3)$ and $w_{,x}/(M_x^*/Ea^3)$ as well as the bending stresses increase as (a/L) increases. For $(a/h) \leq 200$, the radial flexibility is influenced much more strongly by changes in (a/L) than are the other flexibilities. The results also show that the bending stresses as well as the axial and circumferential flexibilities are relatively insensitive to changes in (a/L) when (a/L) goes from 5 to 10, particularly in the region $10 \leq (a/h) \leq 200$.

Figs. 3 to 6 also show that the circumferential bending stress is never less than the axial bending stress, and that the ratio of the former to the latter increases as (a/h) increases. On the other hand, the circumferential membrane stresses are larger than the axial membrane stresses for all (a/h) when $(a/L) = 5$ and 10, and less than the axial membrane stresses at the upper end of the (a/h) scale when $(a/L) = 1/5$ and 1. Furthermore, the membrane stresses are generally considerably smaller than the bending stresses, but nevertheless, they are not insignificant.

Displacements and Stresses Along Coordinate Axes

The quantities discussed above represent maximum values with respect to location in the cylinder, since they correspond to positions under the load resultants. Additional information on the behavior of cylindrical shells under localized loadings can be obtained from Tables 2 to 21. In these Tables, data for pertinent stresses and displacements are presented corresponding to distances along the axial and circumferential coordinate axes equal to one-half, one, and twice the half load-length δ (see Fig. 2) and to one-half the distance between the location of the load resultants and one end of the shell $(L/4)$. The corresponding nondimensional coordinates are tabulated in Table 2 for values of (a/L) equal to 1/5 and 1. For $(a/L) = 1/5$, data are presented for each of the three loading cases for $(a/h) = 10$, 20, 50, 100, and 200; for $(a/L) = 1$, similar results are presented corresponding to $(a/h) = 20$, 50, 100, 500, and 1,500. It should be noted that in view of the assumed simple supports at the cylinder ends, all radial displacements as well as normal and membrane stresses vanish at $x = (L/2a)$ for all loading cases.

Application of Results to Cylinders Under Arbitrary Loads

The practical utilization of the data presented in the Tables or curves is neither limited by the specific line loadings analyzed nor by the fact that in the calculations the half load-length δ was fixed as $L/40$. For example, if the load resultant in a given case is not at the center line of a generator, the present data can still be used because of the localized nature of the results. This is particularly true of the bending stresses, and these are usually the most significant quantities of interest. A particular example worked out in reference 1 for the P^* case showed that for a fixed $\delta = L/40$ the maximum bending stress decreased by only 7 per cent when the load was moved from the midpoint of a generator to a position equal to 80 per cent of the distance between this point and the end of the cylinder. With these observations in mind, it is not difficult to develop a procedure for applying the present numerical results to the approximate analysis of cylinders in cases for which the actual load-length is not equal to that considered herein.

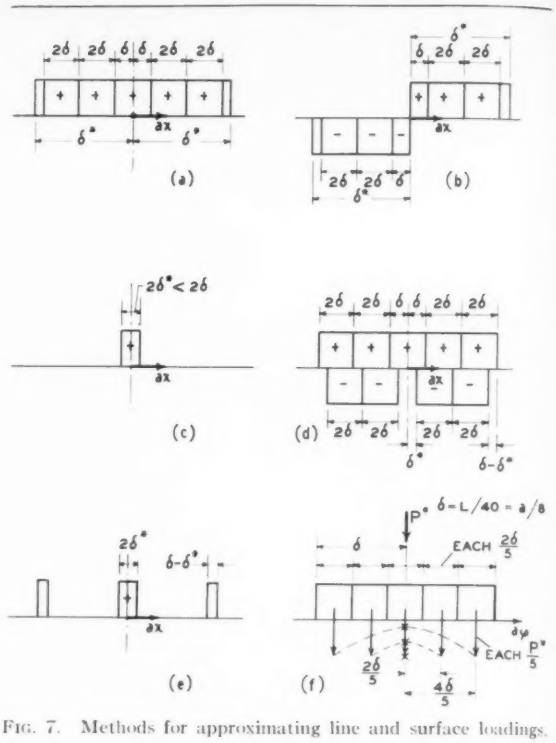

FIG. 7. Methods for approximating line and surface loadings.

If for P^* or M_φ^* loading cases [Figs. 2(a) and 2(c)] the actual load-length $2\delta^*$ is greater than $2\delta = L/20$, it need merely be subdivided symmetrically about the origin into an odd number of parts each of length $L/20$ [see Fig. 7(a)]. If, after this is done, remainders exist at the ends of the actual load-length they can either be neglected or approximated by lengths $L/20$, depending upon which procedure produces the better approximation to the actual load-length, or they can be accounted for with the use of a procedure described later. Thus, with the loading so subdivided, each segment of length $2\delta = L/20$ can be considered separately as though it acted symmetrically at the center of the cylinder, and hence, the results given in Figs. 3 to 6 and Tables 2 to 11 or 17 to 21 can be used. Of

TABLE 14

Variation of $\sigma_{\varphi b}/(M_x^*/a^2)$ with (a/h) and x for $\varphi = 0$; $(\delta/L = 1/40)$

x / a/h	0	x_1	x_2	x_3	x_4
			a/L = 1/5		
10	0	7.97×10^{2}	6.48×10^{2}	1.95×10^{2}	1.30×10^{1}
20	0	3.11×10^{3}	2.46×10^{3}	6.28×10^{2}	4.34×10^{1}
50	0	1.83×10^{4}	1.37×10^{4}	2.64×10^{3}	1.43×10^{2}
100	0	6.74×10^{4}	4.76×10^{4}	7.87×10^{3}	5.55×10^{2}
200	0	2.40×10^{5}	1.61×10^{5}	2.63×10^{4}	1.94×10^{3}
			a/L = 1		
20	0	1.63×10^{4}	1.37×10^{4}	5.04×10^{3}	4.43×10^{2}
50	0	1.02×10^{5}	8.49×10^{4}	3.03×10^{4}	2.43×10^{3}
100	0	4.05×10^{5}	3.35×10^{5}	1.14×10^{5}	4.19×10^{3}
500	0	9.73×10^{6}	7.70×10^{6}	1.96×10^{6}	1.36×10^{5}
1500	0	8.08×10^{7}	5.95×10^{7}	1.09×10^{7}	2.03×10^{5}

TABLE 15

Variation of $-\sigma_x/(M_x^*/a^2)$ with (a/h) and x for $\varphi = 0$; $(\delta/L = 1/40)$

x / a/h	0	x_1	x_2	x_3	x_4
			a/L = 1/5		
10	0	1.10×10^{1}	1.70×10^{1}	1.84×10^{1}	2.96
20	0	7.12×10^{1}	1.04×10^{2}	7.92×10^{1}	9.20
50	0	7.52×10^{2}	9.91×10^{2}	7.58×10^{2}	4.29×10^{1}
100	0	4.21×10^{3}	4.91×10^{3}	3.27×10^{3}	1.44×10^{2}
200	0	2.14×10^{4}	2.21×10^{4}	3.98×10^{3}	6.47×10^{2}
			a/L = 1		
20	0	3.03×10^{1}	5.24×10^{1}	7.81×10^{1}	7.99×10^{1}
50	0	2.25×10^{2}	6.79×10^{2}	9.52×10^{2}	6.06×10^{2}
100	0	2.79×10^{3}	4.79×10^{3}	8.32×10^{3}	2.09×10^{3}
500	0	2.19×10^{5}	3.21×10^{5}	3.06×10^{5}	2.90×10^{4}
1500	0	3.72×10^{6}	4.77×10^{6}	3.07×10^{6}	1.77×10^{5}

TABLE 16

Variation of $-\sigma_\varphi/(M_x^*/a^2)$ with (a/h) and x for $\varphi = 0$; $(\delta/L = 1/40)$

x / a/h	0	x_1	x_2	x_3	x_4
			a/L = 1/5		
10	0	$4.\times10^{1}$	6.04×10^{1}	4.88×10^{1}	-1.67
20	0	2.56×10^{2}	3.32×10^{2}	1.10×10^{2}	-2.53
50	0	2.35×10^{3}	2.54×10^{3}	9.79×10^{2}	-1.04×10^{1}
100	0	1.17×10^{4}	9.74×10^{3}	3.85×10^{3}	-5.40
200	0	4.56×10^{4}	2.96×10^{4}	-2.42×10^{4}	8.67×10^{2}
			a/L = 1		
20	0	1.35×10^{2}	2.29×10^{2}	3.24×10^{2}	2.12×10^{2}
50	0	8.13×10^{2}	2.77×10^{3}	3.55×10^{3}	5.56×10^{2}
100	0	1.14×10^{4}	1.89×10^{4}	3.20×10^{4}	-6.75×10^{2}
500	0	7.84×10^{5}	1.02×10^{6}	6.35×10^{5}	-6.70×10^{3}
1500	0	1.12×10^{7}	1.15×10^{7}	2.08×10^{6}	-6.43×10^{4}

TABLE 17

Variation of $w/(M_\varphi^*/Ea^2)$ with (a/h) and φ for $x = 0$; $(\delta/L = 1/40)$

φ / a/h	0	φ_1	φ_2	φ_3	φ_4
			a/L = 1/5		
10	0	1.15×10^{2}	1.80×10^{2}	2.34×10^{2}	2.02×10^{1}
20	0	8.00×10^{2}	1.20×10^{3}	1.44×10^{3}	-1.36×10^{2}
50	0	9.97×10^{3}	1.40×10^{4}	1.42×10^{4}	-2.80×10^{3}
100	0	6.52×10^{4}	8.48×10^{4}	7.32×10^{4}	-1.56×10^{4}
200	0	4.14×10^{5}	4.89×10^{5}	3.46×10^{5}	4.70×10^{5}
			a/L = 1		
20	0	2.64×10^{2}	4.46×10^{2}	6.85×10^{2}	8.68×10^{2}
50	0	3.70×10^{3}	6.13×10^{3}	9.04×10^{3}	7.49×10^{2}
100	0	2.69×10^{4}	4.36×10^{4}	6.16×10^{4}	2.94×10^{4}
500	0	2.50×10^{6}	3.75×10^{6}	4.49×10^{6}	-4.20×10^{5}
1500	0	5.12×10^{7}	7.05×10^{7}	6.90×10^{7}	-1.42×10^{7}

TABLE 18

Variation of $\sigma_{xb}/(M_\varphi^*/a^2)$ with (a/h) and φ for $x = 0$; $(\delta/L = 1/40)$

φ / a/h	0	φ_1	φ_2	φ_3	φ_4
			a/L = 1/5		
10	3.60×10^{2}	4.31×10^{2}	3.43×10^{2}	1.83×10^{2}	-9.11
20	1.44×10^{3}	1.38×10^{3}	1.12×10^{3}	5.67×10^{2}	-3.00×10^{1}
50	9.00×10^{3}	6.68×10^{3}	5.44×10^{3}	1.96×10^{3}	-7.02×10^{1}
100	3.60×10^{4}	2.75×10^{4}	1.75×10^{4}	2.73×10^{3}	-2.07×10^{2}
200	1.44×10^{5}	1.01×10^{5}	4.68×10^{4}	-3.54×10^{3}	2.67×10^{4}
			a/L = 1		
20	7.20×10^{3}	7.41×10^{3}	6.30×10^{3}	4.18×10^{3}	6.18×10^{2}
50	4.50×10^{4}	4.62×10^{4}	3.90×10^{4}	2.54×10^{4}	2.10×10^{3}
100	1.80×10^{5}	1.83×10^{5}	1.54×10^{5}	9.74×10^{4}	1.39×10^{3}
500	4.50×10^{6}	4.38×10^{6}	3.44×10^{6}	1.75×10^{6}	-9.37×10^{4}
1500	4.05×10^{7}	3.43×10^{7}	2.21×10^{7}	7.30×10^{6}	-2.91×10^{5}

TABLE 19

Variation of $\sigma_{\varphi b}/(M_\varphi^*/a^2)$ with (a/h) and φ for $x = 0$; $(\delta/L = 1/40)$

φ / a/h	0	φ_1	φ_2	φ_3	φ_4
			a/L = 1/5		
10	1.20×10^{3}	8.07×10^{2}	4.56×10^{2}	1.99×10^{2}	-1.77×10^{1}
20	4.80×10^{3}	2.88×10^{3}	1.69×10^{3}	6.74×10^{2}	-6.41×10^{1}
50	3.00×10^{4}	1.69×10^{4}	9.34×10^{3}	2.54×10^{3}	-2.45×10^{2}
100	1.20×10^{5}	6.48×10^{4}	3.09×10^{4}	4.00×10^{3}	-6.52×10^{2}
200	4.80×10^{5}	2.37×10^{5}	9.06×10^{4}	-3.66×10^{3}	4.93×10^{4}
			a/L = 1		
20	2.40×10^{4}	1.47×10^{4}	9.25×10^{3}	4.82×10^{3}	5.12×10^{2}
50	1.50×10^{5}	9.20×10^{4}	5.74×10^{4}	2.94×10^{4}	1.18×10^{3}
100	6.00×10^{5}	3.67×10^{5}	2.27×10^{5}	1.13×10^{5}	-2.67×10^{3}
500	1.50×10^{7}	8.94×10^{6}	5.26×10^{6}	2.11×10^{6}	-2.00×10^{5}
1500	1.35×10^{8}	7.64×10^{7}	4.01×10^{7}	9.59×10^{6}	-1.19×10^{6}

TABLE 20

Variation of $-\sigma_x/(M_\varphi^*/a^3)$ with (a/h) and φ for $x = 0$; $(\delta/L = 1/40)$

a/h \ φ	0	φ_1	φ_2	φ_3	φ_4
	a/L = 1/5				
10	0	1.47×10^{1}	2.26×10^{1}	2.74×10^{1}	3.29
20	0	8.29×10^{1}	1.29×10^{2}	1.48×10^{2}	-4.88
50	0	8.47×10^{2}	1.29×10^{3}	1.17×10^{3}	-7.65×10^{1}
100	0	5.21×10^{3}	6.88×10^{3}	4.50×10^{3}	-3.96×10^{2}
200	0	2.89×10^{4}	3.24×10^{4}	1.27×10^{4}	2.84×10^{4}
	a/L = 1				
20	0	7.02×10^{1}	1.16×10^{2}	1.60×10^{2}	1.62×10^{2}
50	0	7.82×10^{2}	1.24×10^{3}	1.58×10^{3}	1.26×10^{3}
100	0	4.64×10^{3}	7.21×10^{3}	8.91×10^{3}	4.54×10^{3}
500	0	2.60×10^{5}	4.04×10^{5}	4.62×10^{5}	-1.52×10^{4}
1500	0	4.28×10^{6}	6.32×10^{6}	5.34×10^{6}	-3.67×10^{5}

TABLE 21

Variation of $-\sigma_\varphi/(M_\varphi^*/a^3)$ with (a/h) and φ for $x = 0$; $(\delta/L = 1/40)$

a/h \ φ	0	φ_1	φ_2	φ_3	φ_4
	a/L = 1/5				
10	0	1.13×10^{1}	1.90×10^{1}	2.45×10^{1}	3.62
20	0	5.53×10^{1}	9.68×10^{1}	1.23×10^{2}	2.70×10^{-1}
50	0	4.22×10^{2}	8.01×10^{2}	8.75×10^{2}	-2.81
100	0	2.33×10^{3}	3.75×10^{3}	2.97×10^{3}	6.09
200	0	1.06×10^{4}	1.43×10^{4}	6.87×10^{3}	1.35×10^{4}
	a/L = 1				
20	0	6.48×10^{1}	1.14×10^{2}	1.68×10^{2}	1.55×10^{2}
50	0	6.95×10^{2}	1.19×10^{3}	1.62×10^{3}	1.22×10^{3}
100	0	3.49×10^{3}	6.68×10^{3}	8.76×10^{3}	4.40×10^{3}
500	0	1.73×10^{5}	3.03×10^{5}	3.84×10^{5}	8.44×10^{2}
1500	0	2.06×10^{6}	3.80×10^{6}	3.88×10^{6}	1.25×10^{4}

TABLE 22

Approximate Calculations Corresponding to a Uniformly Distributed Radial Load Over a Square Surface Area $2\delta \times 2\delta$ and to $x = \varphi = 0$

	DISPLACEMENTS AND STRESSES AT x = 0					
	δ/L = 1/40, a/L = 1/5, a/h = 100					
φ	$w\cdot10^{-4}/P^*/Ea^2$	$\sigma_{xb}\cdot10^{-3}/P^*/a^2$	$\sigma_{\varphi b}\cdot10^{-3}/P^*/a^2$	$-\sigma_x\cdot10^{-3}/P^*/a^2$	$-\sigma_\varphi\cdot10^{-3}/P^*/a^2$	Relative Contribution
0	2.36	4.07	9.26	1.54	1.05	1/5
(2/5)(δ/a)	2.20	2.38	4.45	1.42	1.00	2/5
(4/5)(δ/a)	1.85	1.10	1.65	1.12	0.86	2/5
Results	2.09	2.21	4.29	1.32	0.954	

TABLE 23

Comparison of Present Calculations With Those of Reference 11 for a Uniformly Distributed Radial Load Over a Square Surface Area $2\delta \times 2\delta$

			x = φ = 0, δ/L = 1/40, δ/a = 1/8, a/L = 1/5, a/h = 100				
a/L	δ/L	No. of Segments	$w\cdot10^{-4}/P^*/Ea^2$	$\sigma_{xb}\cdot10^{-3}/P^*/a^2$	$\sigma_{\varphi b}\cdot10^{-3}/P^*/a^2$	$-\sigma_x\cdot10^{-3}/P^*/a^2$	$-\sigma_\varphi\cdot10^{-3}/P^*/a^2$
1/3	1/24	(Ref. 11)	1.68	2.06	3.76	1.28	0.958
1/5	1/40	1[a]	2.36	4.07	9.26	1.54	1.05
"	"	3	2.11	2.36	4.67	1.34	0.959
"	"	5	2.09	2.21	4.29	1.32	0.954
"	"	9	2.09	2.15	4.13	1.32	0.952
1/8	1/64	(Ref. 11)	3.09	2.36	4.30	1.42	0.974
1/10	1/240	(Ref. 11)	7.14	2.40	4.60	1.55	0.962

[a] From figure 3 or tables 7 to 11

course appropriate recognition must be given to the symmetric or antisymmetric properties of the data with respect to the $x = 0$ and $\varphi = 0$ planes. The data obtained for a typical "unit" loading can then be plotted or tabulated in accordance with its actual relative position along the x axis. When this is done for each of the unit loadings, the principle of superposition can be applied to determine the results of the complete loading. Because tabulated data in x planes are given only for $x = 0$, for a thorough analysis, this procedure requires the estimation of the stresses in the $x\varphi$ surface from the data given along the coordinate axes.

The procedure described is not limited to uniformly distributed line loadings, since by choosing the load intensity of each unit loading in an appropriate manner, any arbitrary line loading can be approximated. Furthermore, in accordance with previous observations, the loading need not be located at the midpoint of a generator. Thus, general loading cases of the antisymmetric M_x^* type [Fig. 2(b)] are amenable to approximate analysis by this procedure. However, here it would seem sensible to make use of the tabulated results of the M_x^* case (Tables 12 to 16) in determining the contributions corresponding to the half unit load-lengths on the positive and negative sides of the x origin. The remaining portions of the actual load length would then be approximated by an even number of unit lengths $(L/20)$, and hence, the results of Tables 2 to 11 could be applied as described previously [see Fig. 7(b)].

If the actual load-length is less than $2\delta = L/20$ [see Fig. 7(c)], the above procedure must be modified. The actual loading can be replaced by symmetrical series of an odd number of positive and an even number of negative unit loadings, with the set of positive loads starting at the origin and the negative loads starting at distances equal to one-half the actual load-length [see Fig. 7(d)]. In this manner the net loading is equivalent to the actual loading plus two symmetrical loadings over lengths equal to one-half the difference between the unit and actual load-lengths [see Fig. (7e)]. These latter loadings can be made to appear at distances from the origin sufficient to eliminate their effect near the origin by choosing a suitable number of positive and negative unit loadings. In fact they may be transferred to positions quite close to the end supports of the cylinder. This procedure can be combined with the previous one for all load cases and may be particularly useful if it is necessary to choose small intervals when approximating variable load distributions.

The present results for line loadings along generators can also be applied to loadings distributed in the circumferential as well as axial directions (surface loads). The given loading must be subdivided into longitudinal slices, each of small finite circumferential width. The loading represented by each slice can then be approximated by a statically equivalent line load whose profile in the x direction approximates that of the slice. The effects of this equivalent load can then be determined as described previously. After each slice has been considered separately, the data obtained—e.g., stresses—can be plotted or tabulated rela-

tive to a fixed position on the cylinder circumference, and the final quantities required can be determined by superposition of the individual contributions. Such an analysis was carried out in order to obtain a comparison of the present results with those of reference 11. This reference presents results for $x = \varphi = 0$ corresponding to uniformly distributed radial loads over small rectangular surface areas of circular cylindrical shells. The basic differential equations used in the analysis differed somewhat from those of the present work. Table 1 of reference 11 contains the results of calculations for square loading areas with axial and circumferential half-lengths of extent $(\delta/a) = 1/8$, for $(a/h) = 15$, 50, 100, and 300, and for several values of (a/L). The present analysis was applied to the data corresponding to $(a/h) = 100$. For this case, results corresponding to $(a/L) = 1/3$, $1/8$, and $1/30$ are given in reference 11. To facilitate the numerical work, calculations were performed corresponding to $(a/L) = 1/5$. In this way, $(\delta/a) = 1/8$ corresponds to $(\delta/L) = 1/40$, for which data are given directly in the present tables and curves.

Table 22 and Fig. 7(f) illustrate the method of computation of displacements and stresses at $x = \varphi = 0$. The load-length in the circumferential direction was divided into five equal segments each of length $(2/5)\delta$. The dotted curves represent schematically displacement or stress distributions resulting from statically equivalent line loads replacing each segmental load. The crosses represent the values to be determined here. The last column of Table 22 lists the relative contribution of each segment when it is replaced by a statically equivalent line load of magnitude $(P^*/5)$ and when symmetry is taken into account [see Fig. 7(f)]. The remaining data were obtained for the indicated values of φ from curves plotted with the aid of Tables 7 to 11. Each final result was determined by multiplying the corresponding individual contributions by the factors representing the relative contributions and by adding the individual results so obtained. Thus, each row in the Table corresponds to the contributions of the corresponding segmental load to the displacement and stresses in the cylinder at $x = \varphi = 0$.

A comparison of the results of the present calculations with those of reference 11 is given in Table 23. In addition to the calculations just described, results corresponding to replacement of the surface load by one statically equivalent line load (one circumferential segment), and by 3 and 9 segmental loadings are also listed. The remaining data are from reference 11. It may be noted once again that w is the ratio of the inward radial displacement to the cylinder radius. With the exception of the bending stresses corresponding to the single line loading approximation, the data are in good agreement with those of reference 11. The exceptions indicated are to be expected, because of the concentrated nature of the approximating load. However, even the extremely brief calculation entailed in the use of three loading segments gives reasonable results. In view of the fact that the bending stresses are generally the most significant, these calculations suggest that the method of computation presented be used only for the determination of the bending stresses and that the data given in the earlier Tables and curves be used directly for approximating the remaining quantities.

Tables 1 to 21 can also be applied to problems involving interaction between a loading member and a cylinder, since the deflection data given represent influence coefficients for the cylinder. Such data, together with the principle of superposition applied in the manner described previously, can be used to determine the displacements and stresses caused by the interaction of the components involved.

References

[1] Hoff, N. J., Kempner, J., Nardo, S. V., and Pohle, F. V., *Deformations and Stresses in Circular Cylindrical Shells Caused by Pipe Attachments. Part I. Summary of the Investigation*, Knolls Atomic Power Laboratory, Schenectady, N.Y., Report No. KAPL - 921, November, 1953.

[2] Hoff, N. J., Kempner, J., and Pohle, F. V., *Deformations and Stresses in Circular Cylindrical Shells Caused by Pipe Attachments. Part II. Line Loads Acting Along Generatrices of Circular Cylindrical Shells*, Knolls Atomic Power Laboratory, Schenectady, N.Y., Report No. KAPL - 922, June, 1952.

[3] Pohle, Frederick V., *Deformations and Stresses in Circular Cylindrical Shells Caused by Pipe Attachments. Part III. Numerical Methods*, Knolls Atomic Power Laboratory, Schenectady, N.Y., Report No. KAPL - 923, November, 1952.

[4] Kempner, J., *Deformations and Stresses in Circular Cylindrical Shells Caused by Pipe Attachments. Part IV. Work Charts*, Knolls Atomic Power Laboratory, Schenectady, N. Y., Report No. KAPL - 924, February, 1953.

[5] Hoff, N. J., *Deformations and Stresses in Circular Cylindrical Shells Caused by Pipe Attachments. Part V. Local Effect of the Pipe*, Knolls Atomic Power Laboratory, Schenectady, N.Y., Report No. KAPL - 925, July, 1952.

[6] Kempner, J., *Deformations and Stresses in Circular Cylindrical Shells Caused by Pipe Attachments. Part VI. Derivation of Generalized Donnell-Type Equations for Circular Cylindrcial Shells with Application to Shells with Line Loads along Generatrices*, Knolls Atomic Power Laboratory, Schenectady, N.Y., Report No. KAPL - 926, June, 1953.

[7] Roche, M. T., *Deformations and Stresses in Circular Cylindrical Shells Caused by Pipe Attachments. Part VII. Work Charts for Off-Center Loading*, Knolls Atomic Power Laboratory, Schenectady, N.Y., Report No. KAPL - 1025, December, 1953.

[8] Hoff, N. J., Kempner, Joseph, and Pohle, Frederick V., *Line Load Applied Along Generators of Thin-Walled Circular Cylindrical Shells of Finite Length*, Q. Appl Math., Vol. XI, No. 4, pp. 411–425, January, 1954.

[9] Kempner, Joseph, *Remarks on Donnell's Equations*, J. Appl. Mech., Vol. 22, No. 1, pp. 117–118, March, 1955.

[10] Hoff, N. J., *The Accuracy of Donnell's Equations*, J. Appl. Mech., Vol. 22, No. 3, pp. 329–334, September, 1955.

[11] Bijlaard, P. P., *Stresses from Radial Loads in Cylindrical Pressure Vessels*, Welding J., Vol. 33, pp. 615s–623s, December, 1954.

[12] Bijlaard, P. P., *Stresses from Local Loadings in Cylindrical Pressure Vessels*, Trans. ASME, Vol. 77, No. 6, pp. 805–814, August, 1955.

[13] Kempner, Joseph, Sheng, James, and Pohle, Frederick V., *Tables and Curves for Deformations and Stresses in Circular Cylindrical Shells under Localized Loadings*, PIBAL Report No. 334, Polytechnic Institute of Brooklyn, October, 1955.

[14] Donnell, L. H., *Stability of Thin-Walled Tubes under Torsion*, NACA Report No. 479, 1933.

[15] Batdorf, S. B., *A Simplified Method of Elastic Stability Analysis for Thin Cylindrical Shells*, NACA Report, No. 874, 1947.

[16] Timoshenko, S., *Theory of Plates and Shells*; McGraw-Hill Book Co., Inc., New York 1940.

Dynamic Considerations Relating to the Behavior of Inertial Space-Stabilized Platforms

EDMUND GORCZYCKI*

Sperry Gyroscope Company

Introduction

Whenever the human element is present to close the multiloops in a moving vehicle such as an airplane, corrections are provided manually to steer the craft to its destination. This is especially true if the airplane is flying at subsonic speeds, since a navigator can determine by various means his present position and his course, taking into account natural effects such as winds and gusts. He has sufficient time to make computations to ascertain the course at any time to arrive at the touch-down point.

With the advent of unmanned aircraft, such as guided missiles, or manned aircraft at supersonic speeds, a requirement exists to derive basic information regarding aircraft altitude, rate of change of altitude, rate of travel at any time with respect to the earth, and many other time variables which a navigator has to compute in a subsonic aircraft. To meet this requirement, the inertial space-stabilized platform was conceived. Such a platform is supported within a housing which is rigidly attached to the body structure of the air frame.

The subsequent discussion presents the dynamics of an inertial space-stabilized platform in the presence of an arbitrary housing disturbance due to air-frame motion at an *isolated* point in inertial space. Air-frame translational motion with respect to the earth is not considered.

This paper avoids duplication of material regarding explanation of gyro operation in detail since it is very well described elsewhere in the literature†. The stress in this paper lies in the three-dimensional aspect of platform operation to determine the coupling effects which influence the platform motion. The basic factors which must be considered in stable platform design are discussed.

General

The inertial space stable platform is a device which has the capability of maintaining its vertical aligned with the direction of local gravity independent of air-frame rotational and translational maneuvers. To satisfy such a requirement, the device must behave as an integrator about each of three mutually perpendicular reference axes in inertial space. The reference axes are established by three integrating rate gyros whose input axes are mutually perpendicular. The input axis of one of the gyros is aligned perpendicular to the platform while the input axes of the remaining two gyros are located in the plane of the platform and arbitrarily oriented.

The gyros serve the function of detecting the platform disturbance and provide a reorientation of the inertial reference frame in accordance with prescribed command signal data. The output of the gyro is a rotation about the gyro output axis proportional to the time integral of the angular velocity about the gyro input axis. Application of a torque about the gyro output axis corresponds to an equivalent rate about the gyro input axis. This action results in a rotation of the input axis about the output axis to effect a change in reference coordinate.

Stabilization of the inertial space platform is accomplished by closing servo loops around the individual integrating rate gyros. Servo drive motors rotate the platform and its associated supporting gimbals in response to the electrical signals derived from the gyro rotation about its output axis. The motor drive is continued until the output signal from each gyro is nulled. When this null condition is satisfied, the platform is returned to the same space orientation that it had prior to the disturbance which upset it and the amount of platform disturbance is indicated on an electrical pickoff device mounted at each of the gimbal axes and the azimuth axis.

Analytical Development

The Newtonian law of motion for a rigid body is expressed generally in concise vector notation as follows:

$$m\ddot{\bar{r}}_{fs} = m[\ddot{\bar{r}}_{ms} + 2\bar{\omega} \times \dot{\bar{r}}_{ms} + \dot{\bar{\omega}} \times \bar{r} + \bar{\omega} \times (\bar{\omega} \times \bar{r})] \quad (1)$$

where

$\bar{r}$ = any directed distance referred to either fixed or moving space

$\bar{\omega}$ = angular velocity vector representing rotation of the rigid body about an axis of rotation passing through the body

$(\ )_{ms}$ = behavior of the directed distance with respect to moving space

Presented at the Instruments Session, Twenty-Fourth Annual Meeting, IAS, New York, January 23–26, 1956.

* Senior Engineer.

† See footnote, p. 138.

$(\ )_{fs}$ = corresponding behavior of the directed distance with respect to fixed space.

If a right-handed reference coordinate system is chosen as shown in the insert of Fig. 1, the components of acceleration of any moving point P in the platform with respect to fixed reference axes, X_I, Y_I, Z_I, are obtained from an expansion of Eq. (1) along these axes as follows:

$$(\ddot{r}_x)_{fs} = (\ddot{r}_x)_{ms} + 2[\omega_y(\dot{r}_z)_{ms} - \omega_z(\dot{r}_y)_{ms}] + r_z\dot{\omega}_y - r_y\dot{\omega}_z - r_x(\omega_y^2 + \omega_z^2) + r_y\omega_x\omega_y + r_z\omega_x\omega_z \quad (2)$$

$$(\ddot{r}_y)_{fs} = (\ddot{r}_y)_{ms} + 2[\omega_z(\dot{r}_x)_{ms} - \omega_x(\dot{r}_z)_{ms}] + r_x\dot{\omega}_z - r_z\dot{\omega}_x - r_y(\omega_x^2 + \omega_z^2) + r_z\omega_x\omega_y + r_z\omega_y\omega_z \quad (3)$$

$$(\ddot{r}_z)_{fs} = (\ddot{r}_z)_{ms} + 2[\omega_x(\dot{r}_y)_{ms} - \omega_y(\dot{r}_x)_{ms}] + r_y\dot{\omega}_x - r_x\dot{\omega}_y - r_z(\omega_x^2 + \omega_y^2) + r_x\omega_x\omega_z + r_y\omega_y\omega_z \quad (4)$$

Eqs. (2), (3), and (4) shall be used in the development of the force equations acting on a point mass m in the platform. Subsequently, these force components are used to derive the torque equations which are required in determining the motion of the platform.

Application of Newtonian Force Equations to a Pitch-on-the-Outside Stable Platform with Stationary Housing

Without sacrificing generality of exposition and mathematical development, regarding stable platforms, in general, the subsequent discussion will be directed toward the dynamic behavior of a pitch-on-the-outside stable platform whose configuration in rudimentary form is shown in Fig. 1. The reference X_I, Y_I, Z_I, axes in the insert of Fig. 1 are fixed in inertial space and are aligned initially with corresponding axes in the stable platform. It is assumed that the origin of the coordinate system lies along the azimuth axis at the centroid of the platform. The positive directions of the platform reference axes are the same as those of the initial airframe reference axes, when the gimbal angles are zero, that is,

X_I = positive toward the nose
Y_I = positive toward the right wing
Z_I = positive toward the bottom of the air frame

The subscript I designates reference to inertial space.

The platform is assumed to be oriented initially with its azimuth axis aligned with the fixed Z_I reference axis of Fig. 1 and the plane containing the X_I and Y_I reference axes passes perpendicularly through the centroid of the aximuth axis. The platform angular velocity of magnitude $\dot{G}_{I-p}$ is assumed not to be constant and the platform angular velocity vector is directed along the positive azimuth axis direction.

The accelerations of a typical particle P of mass m in the platform located at coordinates (X, Y, Z) shall be considered for the following conditions: Rotation of the platform about its azimuth axis is the only motion involved. The azimuth axis is assumed to lie along the reference Z_I axis and rotation is in the positive sense as shown in Fig. 1. Then, in addition to the rotation of the platform about its azimuth axis (Z_I axis), assume that the platform has an angular velocity $\dot{G}_{I-IG}$ about the inner gimbal axis (platform and housing X axis initially) and an angular velocity $\dot{G}_{I-OG}$ about the outer gimbal axis (platform and housing Y axis) in the indicated positive directions of Fig. 1.

The composite accelerations at point P (x, y, z) due to simultaneous rotations about the X_I, Y_I, and Z_I axes are derived from application of Eqs. (2), (3), and (4) and are given by:

$$(\ddot{r}_x)_{fs} = -(\dot{G}^2_{I-p} + \dot{G}^2_{I-OG})x + \ddot{G}_{I-OG}z - \ddot{G}_{I-p}y + \dot{G}_{I-IG}\dot{G}_{I-OG}y \quad (5)$$

$$(\ddot{r}_y)_{fs} = -(\dot{G}^2_{I-p} + \dot{G}^2_{I-IG})y - \ddot{G}_{I-IG}z + \ddot{G}_{I-p}x + \dot{G}_{I-IG}\dot{G}_{I-OG}x \quad (6)$$

$$(\ddot{r}_z)_{fs} = (2\dot{G}_{I-IG}\dot{G}_{I-p} - \ddot{G}_{I-OG})x + (\ddot{G}_{I-IG} + 2\dot{G}_{I-OG}\dot{G}_{I-p})y - (\dot{G}^2_{I-IG} + \dot{G}^2_{I-OG})z \quad (7)$$

Fig. 2 is drawn on the basis of Eqs. (5), (6), and (7).

Since point P is only a single point out of the multitude which comprise the rigid body (the platform), using Eqs. (5) and (7), and a double subscript notation for principal moments of inertia and products of inertia, the effective couple (T_{OG}) about axis OY_I is:

$$T_{OG} = I_{yy}\ddot{G}_{I-OG} - (I_{zz}\dot{G}_{I-p})\dot{G}_{I-IG} - I_{yz}\ddot{G}_{I-IG} - [(2I_{xy})\dot{G}_{I-OG}]\dot{G}_{I-p} - I_{yz}G_{I-p} - I_{xz}(\dot{G}^2_{I-p} - \dot{G}^2_{I-IG}) + I_{yz}\dot{G}_{I-IG}\dot{G}_{I-OG} \quad (8)$$

Similarly, using Eqs. (6) and (7), the effective couple (T_{IG}) about axis OX_I is:

$$T_{IG} = I_{xx}\ddot{G}_{I-IG} + (I_{zz}\dot{G}_{I-p})\dot{G}_{I-OG} - I_{xy}\ddot{G}_{I-OG} + [(2I_{xy})\dot{G}_{I-IG}]\dot{G}_{I-p} - I_{xz}\ddot{G}_{I-p} + I_{yz}(\dot{G}^2_{I-p} - \dot{G}^2_{I-OG}) - I_{xz}\dot{G}_{I-IG}\dot{G}_{I-OG} \quad (9)$$

Using Eqs. (5) and (6), the effective couple (T_p) about axis OZ_I due to motions of the platform about the inner and outer gimbal axes is:

$$T_p = I_{zz}\ddot{G}_{I-p} - I_{xz}\ddot{G}_{I-IG} - I_{yz}\ddot{G}_{I-OG} - I_{xy}(\dot{G}^2_{I-IG} - \dot{G}^2_{I-OG}) \quad (10)$$

Eqs. (8), (9), and (10) are represented diagrammatically in Fig. 3. It is seen from these equations that in a dynamically unbalanced stable platform, motions of the platform about the inner and outer gimbal axes manifest themselves as an effective torque about the platform azimuth axis. Similar dynamic results are obtained with respect to the inner and outer gimbal axes due to angular rotations about the azimuth axis.

If the stable platform housing is held stationary with respect to the established stationary set of reference axes, the outer gimbal axis is fixed in the Y_I direction. The aximuth axis of the stable platform has two degrees of freedom with respect to its supporting gimbals

due to its construction. Thus, if the outer gimbal axis is displaced by some angle G_{I-IG} with reference to the Z_I axis, the outer gimbal angular velocity $\dot{G}_{I-OG}$ will no longer be perpendicular to the azimuth axis. However, the entire preceding mathematical development is based on the fact that the angular velocity vectors lie along three mutually perpendicular fixed space axes in the plane of the platform (but not rotating with the platform). Thus, to validate the mathematics to encompass other situations, it is necessary to resolve the angular velocity $\dot{G}_{I-OG}$ and angular acceleration $\ddot{G}_{I-OG}$ vectors into two components. That is, one component of each of these vectors will be parallel to the azimuth axis and the other component perpendicular to the azimuth axis. The components $\dot{G}_{I-OG}$ sin G_{I-IG} and $\ddot{G}_{I-OG}$ sin G_{I-IG} parallel to the azimuth axis play no active role in the determination of platform motion about the platform inner and outer gimbal axes and do not affect azimuth motion. Thus, the effective components of outer gimbal angular velocity and angular acceleration are $\dot{G}_{I-OG}$ cos G_{I-IG} and $\ddot{G}_{I-OG}$ cos G_{I-IG}, respectively. Combined with the effects of gimbal inertias, these facts are used to derive Eqs. (13), (14), and (15), which represent torque equations relating to a pitch-on-the-outside stable platform with a stationary housing angularly displaced by an angle G_{I-IG} with respect to the stable platform.

The development, thus far, did not include the effect of the moments of inertia of the gimbals which support the platform. By reason of the gimbal construction and housing orientation within the air frame, the inner gimbal axis is always in the plane of the platform, regardless of the housing orientation in inertial space. Defining I_{IGF} as the moment of inertia of the inner gimbal frame about the inner gimbal axis plus associated gearing, electromechanical components, static balancing weights, and any other masses associated with the inner gimbal frame, the torque required to accelerate the inner gimbal frame by itself about the inner gimbal axis is expressed by

$$T_{IG} = I_{IGF}\,\ddot{G}_{I-IG} \tag{11}$$

Define I_{OGF} as the moment of inertia of the outer gimbal frame about the outer gimbal axis plus associated gearing, electromechanical components, static balancing weights, and any other masses associated with the outer gimbal frame.

The moment of inertia of the structure (exclusive of the platform) which it is desired to accelerate about the outer gimbal axis is not only I_{OGF} but also some function of gimbal displacement between inner and outer gimbals acting on I_{IGF}. Assuming that the platform housing is oriented such that the inner and outer gimbals are perpendicular to each other, the moment of inertia of the combined support structure mass about the outer gimbal axis is $I_{OGF} + I_{IGF}$. In general, the inner gimbal frame will be a shell-type ring. The moment of inertia of the inner gimbal ring about the outer gimbal axis is reduced from I_{IGF} when $G_{I-IG} = 0°$ to $I_{IGF}/2$ when $G_{I-IG} = 90°$. Based on this discussion, the torque required to accelerate the combined inner and outer gimbal frames by themselves about the outer gimbal axis is expressed by:

$$T_{OG} = \{I_{OGF} + I_{IGF} \cos^2 (G_{I-IG}/2)\}\,\ddot{G}_{I-OG} \tag{12}$$

Eqs. (8), (9), and (10) can now be modified to include the effects of gimbal inertias and housing tilt as follows:

$$\begin{aligned} T_{OG} = {} & \{I_{OGF} + I_{IGF} \cos^2 (G_{I-IG}/2)\} \times \\ & \ddot{G}_{I-OG} + I_{yy}(\ddot{G}_{I-OG} \cos G_{I-IG}) \cos G_{I-IG} - \\ & I_{xy}\ddot{G}_{I-IG} \cos G_{I-IG} - I_{yz}\ddot{G}_{I-p} \cos G_{I-IG} - \\ & (I_{zz}\dot{G}_{I-p})\dot{G}_{I-IG} \cos G_{I-IG} - [(2I_{xy})\dot{G}_{I-OG} \cos \\ & G_{I-IG}]\dot{G}_{I-p} \cos G_{I-IG} - I_{xz}(\dot{G}^2_{I-p} - \\ & \dot{G}^2_{I-IG}) \cos G_{I-IG} + I_{yz}\dot{G}_{I-IG}\dot{G}_{I-OG} \cos^2 G_{I-IG} \end{aligned} \tag{13}$$

$$\begin{aligned} T_{IG} = {} & (I_{IGF} + I_{xx})\ddot{G}_{I-IG} - I_{xyI}\ddot{G}_{I-OG} \cos G_{I-IG} - \\ & I_{xzI}\ddot{G}_{-p} + (I_{zz}\dot{G}_{I-p})\dot{G}_{I-OG} \cos G_{I-IG} + \\ & [(2I_{xy})\dot{G}_{I-IG}]\dot{G}_{I-p} + (\dot{G}^2_{I-p} - \dot{G}^2_{I-OG} \cos^2 \\ & G_{I-IG})I_{yz} - I_{xz}\dot{G}_{I-IG}\dot{G}_{I-OG} \cos G_{I-IG} \end{aligned} \tag{14}$$

$$\begin{aligned} T_p = {} & I_{zz}\ddot{G}_{I-p} - I_{xz}\ddot{G}_{I-IG} - I_{yz}\ddot{G}_{I-OG} \cos G_{I-IG} - \\ & (\dot{G}^2_{I-IG} - \dot{G}^2_{I-OG} \cos^2 G_{I-IG})I_{xy} \end{aligned} \tag{15}$$

Neglecting frictional effects, Eqs. (13), (14), and (15) are the differential equations of motion of the pitch-on-the-outside stable platform (including the effect of supporting gimbals) with a stationary housing. Simultaneous solution of these equations with proper initial conditions yields the results of platform rotation G_{I-OG} about the outer gimbal axis, G_{I-IG} about the inner gimbal axis, and G_{I-p} about the azimuth axis.

From the dynamics of a rigid body in inertial space, the rate of change of angular momentum about an axis of rotation of the system is equal to the torque arising from the impressed forces about the same axis. Thus, with respect to the torque equations (13), (14), and (15), each term on the right-hand side represents a rate of change of angular momentum. The bold linear vectors in Figs. 4, 5, and 6 show the angular momenta involved in arriving at the derived torques of Eqs. (13), (14), and (15) about the X_I, Y_I, Z_I axes, respectively, when the time rate of change of these angular momenta is taken for a platform with stationary housing. The thin-lined vectors in Figs. 4 and 5 represent the components of the bold-lined vectors which are projected along the X_I, Y_I, and Z_I axes assuming that the platform vertical is disturbed from the Z_I axis during platform stabilization by small angles ϵG_{I-OG} and ϵG_{I-IG} about the outer and inner gimbal axes, respectively.

The angular momenta of the gimbal frames about the X_I and Y_I axes, exclusive of the platform inertia, are $I_{IGF}\dot{G}_{I-IG}$ and $[I_{OGF} + I_{IGF} \cos^2 (G_{I-IG}/2)]$ [cos G_{I-IG}] $\dot{G}_{I-OG}$, respectively, and are directed in the same sense as the respective corresponding gimbal torques.

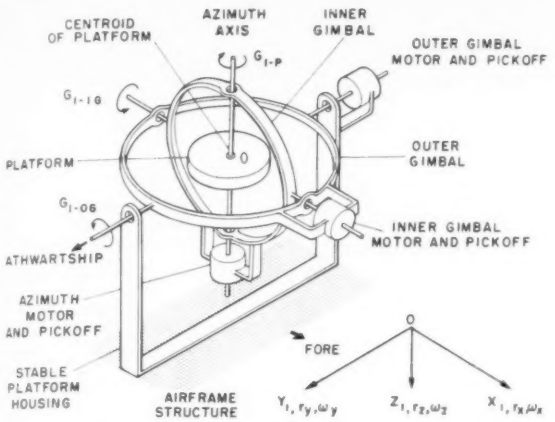

FIG. 1. The essential features of a pitch-on-the-outside stable platform. G_{I-IG} and G_{I-OG} are equal to zero—i.e., the housing, the inner gimbal, and the outer gimbal are mutually perpendicular to each other—and the centroid of the platform lies at the origin O of X_I, Y_I, Z_I references axes.

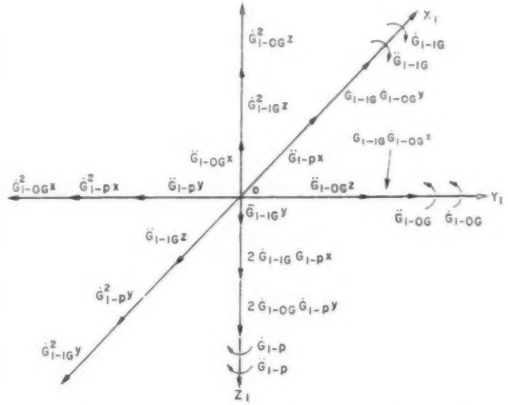

FIG. 2. Total accelerations on any mass point at P due to platform rotation about azimuth axis, inner gimbal axis, and outer gimbal axis (see Eqs. 5, 6, and 7).

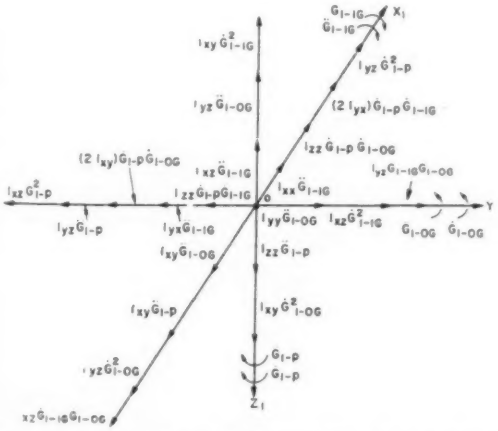

FIG 3. Torques influencing the motion of a platform with respect to inertial space—outer gimbal axis aligned with Y_I space axis. Effect of gimbal inertias neglected, platform housing assumed to be stationary (see Eqs. 8, 9, and 10).

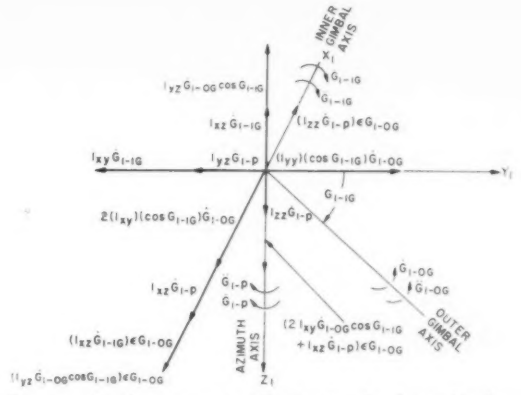

FIG. 4. Angular momenta effective in the determination of torque in the plane of the platform along the Y_I direction. (Effect of gimbal inertias neglected, platform housing assumed to be stationary.)

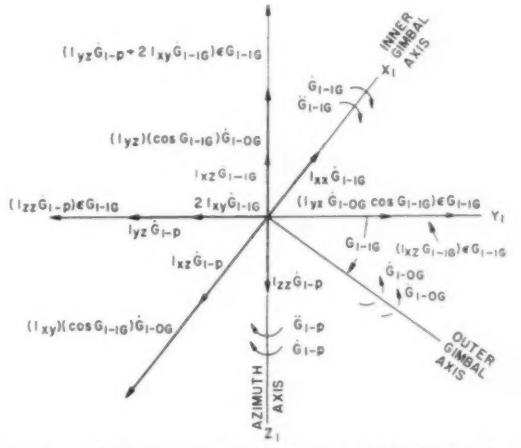

FIG. 5. Angular momenta effective in the determination of torque in the plane of the platform along the X_I direction. (Effect of gimbal inertias neglected, platform housing assumed to be stationary.)

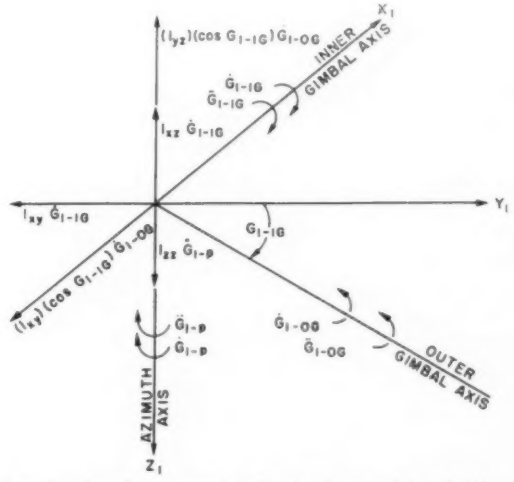

FIG. 6. Angular momenta effective in the determination of torque perpendicular to the plane of the platform along the Z_I direction (platform housing assumed to be stationary).

Effect on Platform Torque Equations Due to Rotating Housing

Thus far, the development considered only the effective torques acting on the platform whose housing is stationary. It is now desirable to investigate the effect on the platform torque Eqs. (13), (14), and (15) contributed by rotation of the platform housing in inertial space. From observation, it is apparent that the only rotation of the platform housing which will effect a physical rotation of reference axes fixed to the platform gimbals and aligned initially with the X_I, Y_I axes is a rotation about the inertial Z_I axis.

The rate of rotation of the housing about the Z_I axis in inertial space shall be designated as $\dot{G}_{Z_I-H}$ for which the quantitative expression

$$\dot{G}_{Z_I-H} = -p \sin G_{Y_I-H} \sec G_{X_I-H} + r \cos G_{Y_I-H} \sec G_{X_I-H} \quad (16)$$

may be derived.

The impressed torques T_{OG}, T_{IG}, and T_p of Eqs. (13), (14), and (15), respectively, give rise to the angular velocities $\dot{G}_{I-OG}$, $\dot{G}_{I-IG}$ and $\dot{G}_{I-p}$ about the platform outer, inner and azimuth axes when the housing is stationary. Acting upon the inertia constants of the platform, these angular velocities give rise to angular momenta along the X_I, Y_I, and Z_I axes.

In the process of platform stabilization against physical disturbances, the torques impressed on the platform act in such a direction as to counter the disturbance about the axis which is affected by the disturbance. If the stabilization of the vertical is not exactly perfect, the platform vertical will be displaced with respect to the true vertical by some small angles ϵG_{I-OG} and ϵG_{I-IG} about the outer and inner gimbals, respectively. As a result, components of angular momenta of the platform in Fig. 6 are transferred so that they align with the original angular momenta under consideration. Through physical constraint, the reference axes fixed to the platform gimbals are rotated at the rate $\dot{G}_{z_I-H}$ and cause the angular momenta along these axes to be rotated at the same rate. The rotation of these angular momenta gives rise to a rate of change of angular momenta (or torques) in the same sense as the angular rotation. Similarly, angular momenta of the platform in its gimbals contribute their rate of change to affect the torques which act on the platform. Fig. 7 shows these additional torques on the platform which arise from platform housing rotation. From Fig. 7, the following equations can be written directly.

$$\begin{aligned}\Delta T_{OG} = {} & [I_{zz}\dot{G}_{I-p}]\,[\epsilon G_{I-OG}]\,[\cos G_{I-IG}]\,[\dot{G}_{Z_I-H}] + \\ & [I_{IGF}\dot{G}_{I-IG}]\,[\dot{G}_{Z_I-H}] \cos G_{I-IG} - \\ & [I_{zz}\dot{G}_{I-IG}]\,[\epsilon G_{I-OG}]\,[\dot{G}_{Z_I-H}] \cos G_{I-IG} - \\ & [I_{zz}\dot{G}_{I-p}]\,[\dot{G}_{Z_I-H}] \cos G_{I-IG} - \\ & [2I_{zy}\dot{G}_{I-OG} \cos G_{I-IG}]\,[\dot{G}_{Z_I-H}] \cos G_{I-IG} - \\ & [I_{yz}\dot{G}_{I-OG} \cos G_{I-IG}][\epsilon G_{I-OG}][\dot{G}_{Z_I-H}] \cos G_{I-IG} \quad (17)\end{aligned}$$

$$\begin{aligned}\Delta T_{IG} = {} & [I_{zz}\dot{G}_{I-p}]\,[\epsilon G_{I-IG}][\dot{G}_{Z_I-H}] + [I_{yz}\dot{G}_{I-p}]\,[\dot{G}_{I_I-H}] + \\ & [2I_{zy}\dot{G}_{I-IG}]\,[\dot{G}_{Z_I-H}] - [I_{yz}\dot{G}_{I-OG} \cos G_{I-IG}] \times \\ & [\epsilon G_{I-IG}]\,[\dot{G}_{Z_I-H}] - [I_{zz}\dot{G}_{I-IG}]\,[\epsilon G_{I-IG}] \times \\ & [G_{Z_I-H}] - [I_{OGF} + I_{IGF} \cos^2 (G_{I-IG}/2)] \times \\ & [\dot{G}_{I-OG} \cos G_{I-IG}]\,[\dot{G}_{Z_I-H}] \quad (18)\end{aligned}$$

$$\Delta T_p = 0 \quad (19)$$

Eqs. (17) and (18) represent the additional torque components accrued along the outer and inner gimbal axes, respectively, due to platform housing rotation about the inertial Z_I axis at angular rate $\dot{G}_{Z_I-H}$. Eq. (19) indicates that no change in torque takes place about the platform azimuth axis due to platform housing rotation. Eqs. (17), (18), and (19) must be added algebraically to Eqs. (13), (14), and (15), respectively, to obtain the total dynamic behavior of the platform (including the effects of gimbal inertias) in the case of the rotating platform housing.

Fig. 8 is a block diagram representation of this summation of torques, showing the input torques at the platform about the platform outer, inner, and azimuth axes and the output platform angular accelerations and velocities. The expressions for the torques experienced at the platform are entirely general and any degree of simplification can be made upon them, depending upon platform design. For instance, by elimination of appropriate terms the platform may be transformed from a dynamically unsymmetrical one to a dynamically symmetrical one. Inclusion of the ΔT terms permits study of the effect of rotating housing compared to the case in which the housing is stationary.

The following development provides a transformation of rotational velocities about air-frame axes to equivalent rotations about inertial space axes. From this derivation, an expression is derived for the rotational rate $\dot{G}_{Z_I-H}$ which is required in Fig. 8.

Transformation of Rotational Velocities About Air-Frame Axes to Equivalent Rotations About Inertial Space Axes

Since the stable platform housing is rigidly attached to the air frame, its rotational velocity in inertial space is identical to the rotational velocity of the air frame. Air-frame angular velocities, and hence the platform housing, about air-frame body axes may be transformed into equivalent rotational velocities $\dot{G}_{X_I-H}$, $\dot{G}_{Y_I-H}$, and $\dot{G}_{Z_I-H}$ about the inertial space axes X_I, Y_I, and Z_I, respectively.

Air-frame angular velocity relationships based on the sequence of rotations yaw, roll, and pitch may be developed by matrix methods or by conventional methods of resolving rotational velocities represented by vectors. The magnitude of the rotational velocity vector is determined by the amount of rotational velocity, and its direction is obtained by means of the right-hand rule.

Referring to Fig. 9, the original orientation of the air-frame axes is represented by a mutually orthogonal

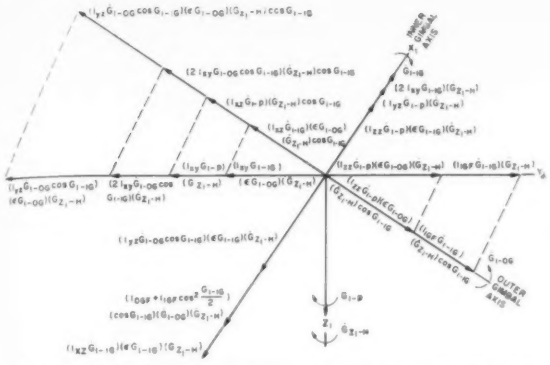

FIG. 7. Additional torque components accrued along the inner and outer gimbal axes due to platform housing rotation about the inertial Z_I axis (effect of gimbal inertias included).

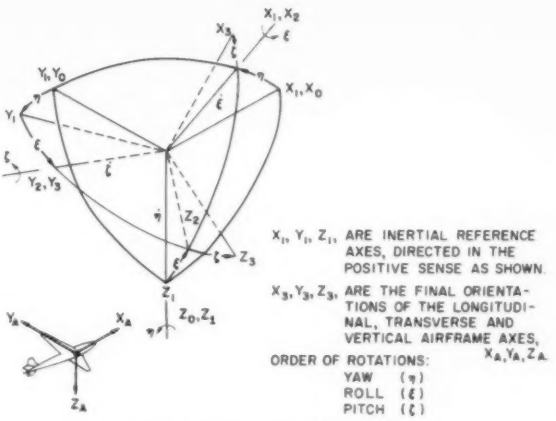
X_I, Y_I, Z_I ARE INERTIAL REFERENCE AXES, DIRECTED IN THE POSITIVE SENSE AS SHOWN.
X_3, Y_3, Z_3 ARE THE FINAL ORIENTATIONS OF THE LONGITUDINAL, TRANSVERSE AND VERTICAL AIRFRAME AXES, X_A, Y_A, Z_A.
ORDER OF ROTATIONS:
YAW (η)
ROLL (ξ)
PITCH (ζ)

FIG. 9. Euler orientation angles.

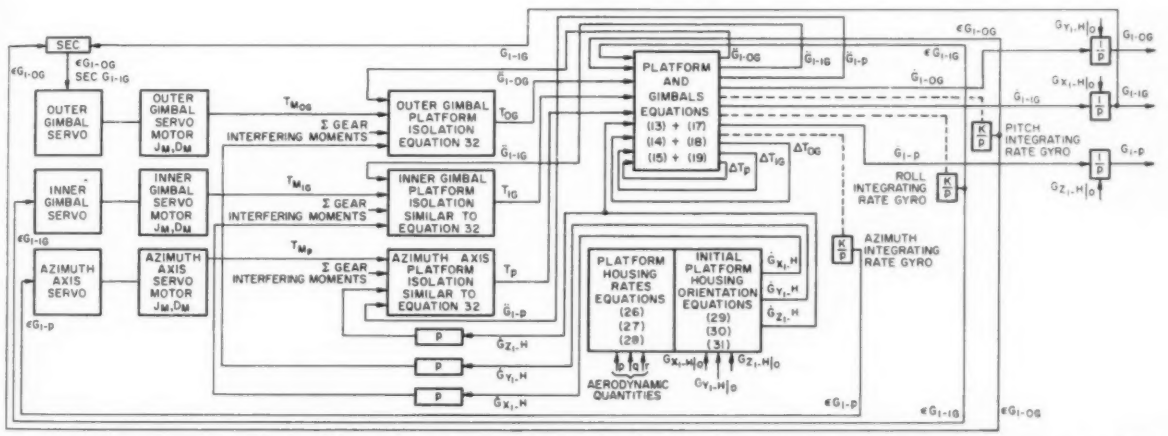
SEC
OUTER GIMBAL SERVO
OUTER GIMBAL SERVO MOTOR
INNER GIMBAL SERVO
INNER GIMBAL SERVO MOTOR
AZIMUTH AXIS SERVO
AZIMUTH AXIS SERVO MOTOR
Σ GEAR INTERFERING MOMENTS
OUTER GIMBAL PLATFORM ISOLATION EQUATION 32
INNER GIMBAL PLATFORM ISOLATION SIMILAR TO EQUATION 32
AZIMUTH AXIS PLATFORM ISOLATION SIMILAR TO EQUATION 32
PLATFORM AND GIMBALS EQUATIONS (13) + (17) (14) + (18) (15) + (19)
PLATFORM HOUSING RATES EQUATIONS (26) (27) (28)
INITIAL PLATFORM HOUSING ORIENTATION EQUATIONS (29) (30) (31)
AERODYNAMIC QUANTITIES
ROLL INTEGRATING RATE GYRO
AZIMUTH INTEGRATING RATE GYRO
PITCH INTEGRATING RATE GYRO

FIG. 8. Block diagram of gyro mounted stable platform. It is assumed that the input axis of the roll integrating rate gyro is initially aligned with the inner gimbal axis, and that the platform is initially erect.

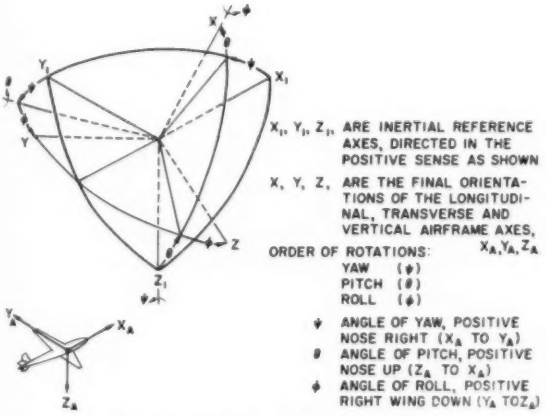
X_I, Y_I, Z_I, ARE INERTIAL REFERENCE AXES, DIRECTED IN THE POSITIVE SENSE AS SHOWN
X, Y, Z, ARE THE FINAL ORIENTATIONS OF THE LONGITUDINAL, TRANSVERSE AND VERTICAL AIRFRAME AXES, X_A, Y_A, Z_A
ORDER OF ROTATIONS:
YAW (ψ)
PITCH (θ)
ROLL (ϕ)
ψ ANGLE OF YAW, POSITIVE NOSE RIGHT (X_A TO Y_A)
θ ANGLE OF PITCH, POSITIVE NOSE UP (Z_A TO X_A)
ϕ ANGLE OF ROLL, POSITIVE RIGHT WING DOWN (Y_A TO Z_A)

FIG. 10. NACA orientation angles.

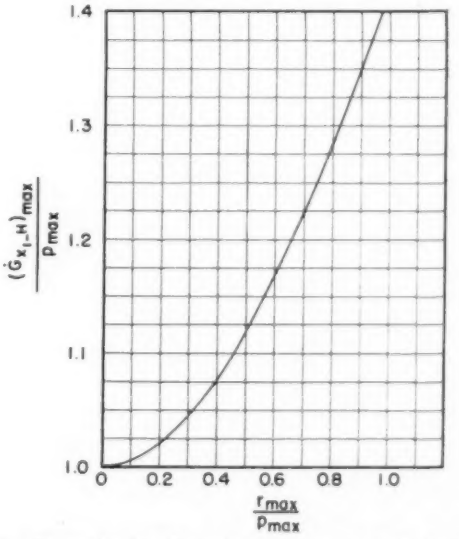

FIG. 11. Determination of maximum follow-up rates about the roll gimbal axis.

frame of axes with "0" subscript, i.e.—X_0, Y_0 and Z_0. The first sequence of rotation is a yaw maneuver at an angular velocity $\dot{\eta}$ about the Z_0 axis. This action displaces the air-frame axes from their original orientation into another axes orientation designated by the "1" subscript—i.e., X_1, Y_1, Z_1. At this time, the subscript "1" frame is rotated at an angular rate $\dot{\xi}$ about the X_1 axis. The roll maneuver rotates the Y_1, Z_1 axes into position Y_2, Z_2 while axis X_2 is still aligned with axis X_1. The final maneuver rotates the axes with subscript "2" into position with subscript "3" at an angular velocity $\dot{\zeta}$ about the Y_2 axis.

On the basis of Fig. 9 and the preceding discussion regarding air-frame motion, it may be shown that

$$p = \dot{\xi} \cos \zeta - \dot{\eta} \sin \zeta \cos \xi \tag{20}$$

$$q = \dot{\zeta} + \dot{\eta} \sin \xi \tag{21}$$

$$r = \dot{\xi} \sin \zeta + \dot{\eta} \cos \zeta \cos \xi \tag{22}$$

where p, q, and r are rotational rates about the air-frame roll, pitch, and yaw axes, respectively.

By physical reasoning, it can be deduced that for a pitch-on-the-outside stable platform, the sequence of rotations through which the platform housing must be rotated in order that each of the three angles about the three mutually perpendicular platform axes are independent of each other is yaw, roll, and pitch. Thus, the platform housing orientation is exactly the same as the air-frame orientation. Therefore,

$$\xi = G_{X_I - H} \tag{23}$$

$$\zeta = G_{Y_I - H} \tag{24}$$

$$\eta = G_{Z_I - H} \tag{25}$$

Substituting Eqs. (23), (24), and (25) into Eqs. (21), (21), and (22) and solving,

$$\dot{G}_{X_I - H} = p \cos G_{Y_I - H} + r \sin G_{Y_I - H} \tag{26}$$

$$\dot{G}_{Y_I - H} = p \tan G_{X_I - H} \sin G_{Y_I - H} + q - r \tan G_{X_I - H} \cos G_{Y_I - H} \tag{27}$$

$$\dot{G}_{Z_I - H} = -p \sin G_{Y_I - H} \sec G_{X_I - H} + r \cos G_{Y_I - H} \sec G_{X_I - H} \tag{28}$$

Eqs. (26), (27), and (28) are the required transformations of platform housing angular rates from air-frame body axes into equivalent rotational velocities about the inertial space axes X_I, Y_I, and Z_I, respectively.

Determination of Air-Frame Initial Angle Conditions

In order to specify a unique orientation of the air frame in space, it is necessary to relate the air-frame axes to reference axes. This is accomplished by means of a set of three air-frame orientation angles (ψ, θ, ϕ), called Euler angles, and a choice of the sequence of rotations which the air frame must follow by the amount of Euler angle corresponding to the air-frame axis with which it is associated. The choice of rotations recommended by the NACA is yaw ψ, pitch θ, and roll ϕ, as shown in Fig. 10. It is this sequence which had been chosen in what follows so that the amount of Euler pitch angle in space with respect to the reference coordinate system in the $X_I - Y_I$ plane is unaffected by either the Euler yaw angle or Euler roll angle.

By equating elements of the air-frame orientation matrix with corresponding elements of the platform orientation matrix, the following results are derived:

$$G_{X_I - H}\Big|_0 = \sin^{-1} (\cos \theta_0 \sin \phi_0) \tag{29}$$

$$G_{Y_I - H}\Big|_0 = \tan^{-1} (\tan \theta_0 \sec \phi_0) \tag{30}$$

$$G_{Z_I - H}\Big|_0 = \psi_0 - \tan^{-1} (\tan \phi_0 \sin \theta_0) \tag{31}$$

where the subscript "0" notation indicates air-frame and platform housing initial orientation angles with respect to the reference inertial axes X_I, Y_I, Z_I.

The advantage of deriving Eqs. (29), (30), and (31) in the sequence of rotations yaw, pitch, and roll is that this is the sequence generally applied in aerodynamic analyses.

If a perfectly stabilized and erect pitch-on-the-outside platform is considered, with no friction at the pivots, Eq. (29) represents the indicated angle between the inner and outer gimbals, Eq. (30) represents the indicated angle between the outer gimbal and housing, and Eq. (31) represents the angular rotation of the housing about the platform azimuth axis.

Stable Platform Isolation Consideration

Eqs. (13), (14), (15), (17), (18), and (19) show the relationships between the torques acting at the platform and its gimbals and the resultant motion that evolves from the presence of these torques. The driving torques originate in the motors at the gimbal and azimuth axes.

The motion of the platform gimbals with respect to inertial space can be related to the servo motor shaft torque, housing motion, interfering moments constituted by stiction and external loading. If a free body diagram is drawn for all the gears between the servo motor to the platform, it can be shown that

$$T_{OG} = T_{MOG} + [f \text{ (gear inertias, motor inertia, viscous motor damping ratio)}] (\ddot{G}_{Y_I - H}) - [g\text{(gear inertias and ratios, motor inertia, viscous motor damping)}] (\ddot{G}_{I - OG}) - \Sigma \text{ gear interfering moments} \tag{32}$$

Equations of similar form can be derived for T_{IG} and T_p.

The equations for T_{OG}, T_{IG}, and T_p in the form of Eq. (32) constitute dynamic transformations of the torques at the servo motors which drive the platform gimbals to maintain the verticality of the platform and to orient a set of reference axes in the plane of the platform.

Platform isolation, which is the relationship of platform motion to housing motion, ranges anywhere from perfect isolation in which no gyro is required for loop monitoring to the case in which the gyro-servo loop which is used in inertial space stabilization integrates

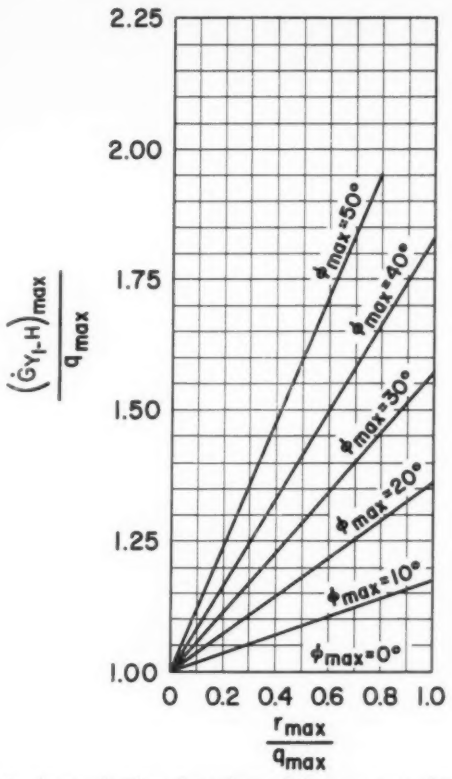

FIG. 12. Determination of maximum follow-up rates about the pitch gimbal axis.

with respect to the housing independent of housing motion. Perfect isolation is approached when the servo motor inertia, damping, and motor pinion gear inertia approach zero; the latter condition is approached when the gear ratio from motor to platform approaches infinity.

Normal platform stabilization design is a compromise condition between these extreme cases.

STABLE PLATFORM GIMBAL SERVOS

It can be shown from the application of servo techniques to the design of the platform gimbal servos that the desired transfer function of platform displacement from the motor shaft at the outer gimbal to the platform itself is of the form:

$$G_{I-OG}(p)/\epsilon(p) = K(1 + p\tau_1)/p(1 + p\tau_2)(1 + p\tau_3) \quad (33)$$

Similar equations apply to the inner gimbal axis and platform azimuth axis.

Based on preceding discussion, the error signal which drives the outer gimbal servo must be altered by the secant of the roll angle in order to project it in line with the outer gimbal axis. This transformation is shown in Fig. 8.

In order to arrive at a transfer function of the form of Eq. (33) the following must be assumed:

(a) The servo system is linear. (b) The gimbal loading reflected to the motor is constant. (c) Platform angular disturbance occurs about the gimbal axis under consideration. Rotations about the other two platform axes are zero. (d) The orientation of the housing and platform is such that all the indicated gimbal angles are zero initially. (e) The platform housing is nonrotating.

In general, the design parameters in Eq. (33) are obtained on the basis of relative magnitudes of the constants, practicability of obtaining these magnitudes with undue difficulty, and stability and performance within the bandwith of frequencies in which the servos must respond. The servos must have the capability of tracking the maximum platform rates determined from the prescribed maximum rotational rates of the air frame about its body axes. Assuming that the maximum rotational rates p_{max}, q_{max}, r_{max} about the air-frame body axes and the maximum bank angle ϕ_{max}, of the air frame are specified, the maximum gimbal rates about the inner gimbal axis, outer gimbal axis, and platform axis can be determined from Figs. 11, 12, 12a, and 13. Figs. 12 and 12a are related in the sense that in order to arrive at the maximum pitch gimbal rate it is necessary to divide the ordinate in Fig. 12 by the ordinate in Fig. 12a for a corresponding value of ϕ_{max}.

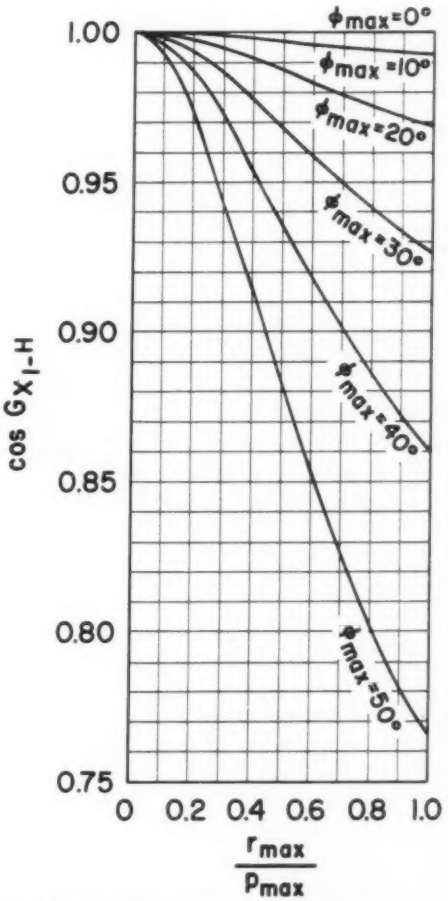

FIG. 12a. Determination of maximum follow-up rates about the pitch gimbal axis.

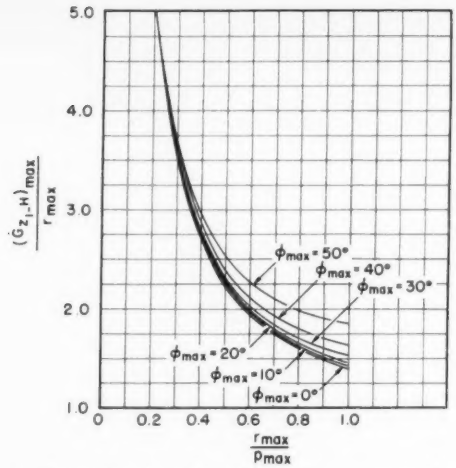

FIG. 13. Determination of maximum follow-up rates about the azimuth axis.

Overdesign of the platform servo may be avoided by designing the servo to follow up accurately to some percentage of the values derived from Figs. 11, 12, 12a, and 13 and permitting the platform vertical to lag behind its true position as long as the gyro reference is not lost. In a zero velocity error servo, the vertical will arrive at its true position in time.

THE INTEGRATING RATE GYRO

Expressions have been derived for the dynamic motion of the platform with respect to inertial space and for the motion of the platform housing with respect to inertial space. Both of these motions are "open-loop" unless a device is placed into the system to derive the relative difference between these two motions. Such a device is the integrating rate gyro. Three of these gyros are mounted on the platform to detect platform disturbance about their respective input axes which are mutually perpendicular.

The integrating rate gyro is a single degree of freedom gyro immersed in a viscous medium. The gyro output angular displacement is the resultant time integral of the angular rates of the gyro about its input axis. The input axis of the gyro lies along the perpendicular to the gyro spin axis and the output axis. The output which is the integral to which reference was made is detected using a microsyn pickoff. Fig. 14 shows a working sketch of such a gyro unit. Draper, Wrigley, and Grohe have presented a comprehensive account of the mechanism of the integrating rate gyro.*

On the basis of the dynamics of the gyro, the gyro transfer function is expressed by $K/[p(1 + \tau_g p)]$.

* *The Floating Integrating Gyro and Its Application to Geometrical Stabilization Problems on Moving Bases*, Aeronautical Engineering Review, Vol. 15, No. 6, pp. 46–62, June, 1956.

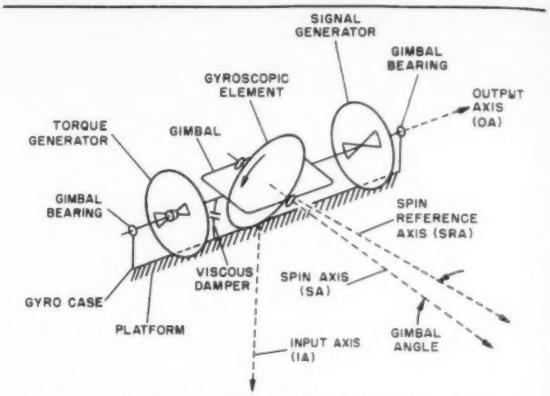

FIG. 14. Schematic diagram of the integrating rate gyro.

However, the time constant τ_g in $(1 + \tau_g p)$ term usually is adjusted in design so that its effect is small within the working range of frequencies.

In Fig. 8, it is assumed that the input axis of the roll integrating rate gyro is initially aligned with the inner gimbal axis. In general, the input axes of the roll and pitch integrating rate gyros are arbitrarily oriented so that a resolver is required to transform the platform rates in the direction of the gimbal axes as projected in the plane of the platform.

OUTPUTS

The outputs of a typical system as described in this paper are high accuracy indications of air-frame attitude and rates with respect to an inertial space-stabilized reference.

CONCLUSIONS

A mathematical development has been presented which describes the behavior of a stable platform which is under the influence of air-frame disturbances in isolated space. The method enumerates the factors which must be considered in stable platform design.

The presentation allows one to develop a deeper insight into inertial platform operation by considering its dynamics; it permits coupling effects between axes in the platform to be investigated fully; it establishes design goals for the azimuth and gimbal follow-up servos based on air-frame performance limits; it shows how the transformation of air-frame quantities to platform quantities is effected. These are a few of the many significant benefits derived from an analysis of the type which has been presented.

To extend the development described in this paper, it would be desirable to determine the effects of translation of the air frame with respect to the earth. Other areas of interest lie in determining the effect of temporary power interruption during an air-frame maneuver and investigating various methods of establishing a platform vertical.

The Calculation of Thermoelastic Beam Deflections by the Principle of Virtual Work†

BRUNO A. BOLEY*

Columbia University

SUMMARY

An approximate formula for the calculations of the deflections of heated beams is studied in this paper. This formula is analogous to the familiar equation $v = \int (MM_D/EI)dx$ of strength of materials. The accuracy of the formula, from the standpoint of a more rigorous thermoelastic solution, is assessed with particular reference to rectangular beams under arbitrary temperature distributions.

INTRODUCTION

THE CALCULATION of the deflections of beams is very often most conveniently carried out with the aid of the principle of virtual displacements. The deflection v at any point in the beam is then usually obtained from the formula

$$v(x) = \int_0^L \frac{M(x_0)M_D(x_0, x)}{EI}\, dx_0 \qquad (1)$$

which is easily derived from that principle. In this formula the beam is assumed to extend from $x = 0$ to $x = L$; its cross section has a (principal) moment of inertia I about an axis perpendicular to the direction of v, and its material a Young's modulus E. $M(x_0)$ is the bending moment at any point $x = x_0$, and $M_D(x_0, x)$ is the bending moment caused at $x = x_0$ by a dummy system of loads constructed so that it does work if and only if the deflection v occurs at x; the magnitude of the dummy loads is such that this work is numerically equal to v.

The principle of virtual work is, of course, of general validity, and holds regardless of whether the beam deflection is due to heating or to actual applied forces. It is therefore desirable to see whether a simple formula, analogous to Eq. (1), cannot be derived from it for the calculation of thermal deflections of beams, and, further, whether its range of validity is as wide as that of Eq. (1). The purpose of the present paper is the establishment of such a formula.

The derivation of an equation of the form of Eq. (1), for the deflection of a beam subjected to an arbitrary temperature distribution, is an easy matter, provided the assumption that sections plane before heating remain plane after heating is accepted and that principal axes are employed; it takes the form

$$v(x) = \int_0^L \frac{M_T(x)M_D(x_0, x)}{EI}\, dx_0 \qquad (2)$$

The quantity M_T is defined by

$$M_T(x) = \int_A\int \alpha ET(x, y, z)y\, dy\, dz \qquad (2a)$$

where the integration extends over the entire cross-sectional area A, and where the y and z axes are principal axes of the cross section, the y axis extending in the same direction as the deflection v. The coefficient of thermal expansion is denoted by α. The derivation of Eq. (2) must be examined now from a more rigorous standpoint so as to determine its accuracy and range of validity.

GENERAL FORMULA FOR DEFLECTIONS OF DETERMINATE BEAMS

Let the stresses due to the dummy load system be denoted by the subscript D, and let the strains due to the actual (thermal) loading be denoted by the subscript T. Then the work done by the dummy system, as defined above, will be

$$\delta = \int\int\int (\sigma_{xD}\epsilon_{xT} + \sigma_{yD}\epsilon_{yT} + \sigma_{zD}\epsilon_{zT} + \tau_{zyD}\gamma_{zyT} + \tau_{xzD}\gamma_{xzT} + \tau_{yxD}\gamma_{yxT})\, dx\, dy\, dz \qquad (3)$$

if the deformations are taken to be those caused by the actual loadings. The limits of integration must be chosen so as to cover the entire structure. The symbols σ and ϵ denote the normal stresses and strains in the directions indicated by the subscript, and similarly for the shear stresses and strains τ and γ.

Consider now a statically determinate beam, under an arbitrary temperature distribution and under no applied loads; then the reactions will all be zero and the thermal stresses will satisfy equilibrium conditions of the type

$$\int_A\int \sigma_{xT}\, dy\, dz = \int_A\int \sigma_{xT}y\, dy\, dz = \int_A\int \tau_{xyT}dy\, dz = 0 \qquad (4)$$

The determination of the total deflection δ is usually most conveniently carried out by first calculating separately the deflections v and w along the principal direc-

Received February 24, 1956.

† This work was carried out as part of a project sponsored by the U.S. Air Force, and was in part described in the report of reference 1.

* Associate Professor of Civil Engineering, Institute of Flight Structures.

tions y and z, respectively, of the cross section, and then superimposing them according to the formula $\delta = (v^2 + w^2)^{1/2}$. In what follows, only the deflection v will be considered, but it is clear that the analysis presented can be applied to w with only a change in nomenclature. For the present case, then, one may write the stress components due to a dummy load passing through the shear center and, therefore, causing no twist, as follows:

$$\left.\begin{aligned} \sigma_{xD} &= M_D\, y/I; \qquad \tau_{xzD} = -(\partial\varphi/\partial y)/I; \\ \tau_{yxD} &= [(\partial\varphi/\partial z)/I] - [y^2/(2I)]\,(d\,M_D/dx_0); \\ \sigma_{yD} &= \sigma_{zD} = \tau_{yzD} = 0 \end{aligned}\right\} \quad (5)$$

where the function φ must be determined from the Saint Venant theory of flexure (reference 2). Substitution into Eq. (3) gives

$$v(x) = (1/EI)\int_0^L \int_A\int \{[\alpha\, ET - \nu(\sigma_{yT} + \sigma_{zT})]y\, M_D(x_0, x) - (1+\nu)y^2(dM_D/dx_0)\,\tau_{xyT} + 2(1+\nu)\,[(\partial\varphi/\partial z)\,\tau_{xyT} - (\partial\varphi/\partial y)\tau_{xzT}]\}dx_0\,dy\,dz \quad (6)$$

provided that use is made of Eq. (4) and Hooke's law

$$E\epsilon_{xT} = \sigma_{xT} - \nu(\sigma_{yT} + \sigma_{zT}) + \alpha ET \quad (7)$$

The first term on the right-hand side of Eq. (6) is identical with the right-hand side of Eq. (2); it is shown below, for the special case of a rectangular section under a two-dimensional temperature distribution, that this term is usually much larger than all the others and that use of Eq. (2) may therefore be considered permissible in practice.

Deflections of Rectangular Beams

The shear stresses in a simply supported rectangular bar of depth $2c$ are

$$\left.\begin{aligned} \tau_{yzD} &= [(c^2 - y^2)/2I]\,(dM_D/dx_0) \\ \tau_{xzD} &= 0 \end{aligned}\right\} \quad (8)$$

Then

$$(\partial\varphi/\partial y) = 0; \qquad (\partial\varphi/\partial z) = (c^2/2)\,(dM_D/dx_0) \quad (8a)$$

Substitution into Eq. (6) gives

$$v(x) = (1/EI)\int_0^L \int_A\int [(\alpha ET - \nu\sigma_{yT})\, yM_D - (1+\nu)y^2\tau_{xyT}(dM_D/dx_0)]dx_0dy\,dz \quad (8b)$$

provided that use is made of the last of Eqs. (4). The last term of Eq. (8b) may be simplified as follows:

$$\int_0^L \int_A\int y^2\tau_{xyT}(dM_D/dx_0)\,dx_0dy\,dz = \int_0^L \int_A\int y^2\left[\frac{\partial(M_D\tau_{xyT})}{\partial x_0} - M_D\,\frac{\partial\tau_{xyT}}{\partial\, x_0}\right]dx_0\,dy\,dz = \int_A\int y^2(M_D\tau_{xyT})\,\Big|_{x_0=0}^{x_0=L}\,dy\,dz + \int_0^L\int_A\int M_D\,y^2 \times \frac{\partial\sigma_{yT}}{\partial y}\,dx_0dy\,dz \quad (9)$$

where use has been made of the equilibrium equation

$$(\partial\tau_{xyT}/\partial x) + (\partial\sigma_{yT}/\partial y) = 0 \quad (9a)$$

All surfaces are, however, free of tractions; then τ_{xyT} is zero when $x_0 = 0, L$ and, therefore,

$$v(x) = (1/EI)\int_0^L \int_A\int \left[\alpha ETy - \nu\sigma_{yT}y - (1+\nu)y^2\,\frac{\partial\sigma_{yT}}{\partial y}\right]M_D\,dx_0dy\,dz \quad (9b)$$

For the present case σ_y must vanish at $y = \pm c$; then integration by parts gives

$$\int_{-c}^{c} y^2\,\frac{\partial\sigma_{yT}}{\partial y}\,dy = (y^2\sigma_{yT})\,\Big|_{y=-c}^{y=c} - 2\int_{-c}^{c} y\;\sigma_{yT}dy \quad (9c)$$

where the first term of the right-hand side is zero. Substitution of Eq. (9c) into Eq. (9b) finally gives the deflection as

$$v(x) = \frac{1}{EI}\int_0^L \int_A\int [\alpha ET + (2+\nu)\sigma_{xT}]M_Dy \times dx_0dy\,dz \quad (10)$$

Comparison of Eqs. (10) and (2) shows that the only term omitted in the latter equation is that proportional to the quantity

$$b\int_0^L \int_{-c}^{c} \sigma_{yT}M_D\; y\; dx_0dy$$

where b is the width of the beam in the z direction. Reference 3 gives, for a statically determinate rectangular beam subjected to an arbitrary two-dimensional temperature distribution, the following result:

$$\begin{aligned} \sigma_{yT}/\alpha E = \Big\{ & -y\int_{-c}^{y} T''dy + \int_{-c}^{y} T''y\,dy + \\ & (c/4)\int_{-c}^{c} T''\,dy\,[1 + 2(y/c) + (y/c)^2] - \\ & (1/4)\int_{-c}^{c} T''y\,dy[2 + 3\,(y/c) - (y/c)^3]\Big\} + \\ & \Big\{(y^3/6)\int_{-c}^{y} T''''\,dy - (y^2/2)\int_{-c}^{y} T''''\,y\,dy + \\ & (y/2)\int_{-c}^{y} T''''\,y^2\,dy - (1/6)\int_{-c}^{y} T''''\,y^3\,dy - \\ & (c^3/24)\int_{-c}^{c} T''''\,dy[(y/c)^2 + 2(y/c)^3 + 2(y/c)^4] + \\ & (c^2/40)\int_{-c}^{c} T''''\,y\,dy \times \\ & [4\,(y/c) + 10\,(y/c)^2 + 7(y/c)^3 - (y/c)^5] - \\ & (c/8)\int_{-c}^{c} T''''\,y^2\,dy\,[1 + 2(y/c) + (y/c)^2] + \\ & (1/24)\int_{-c}^{c} T''''\,y^3\,dy\,[2 + 3(y/c) - (y/c)^3]\Big\} + \\ & \{\text{terms containing only sixth and higher derivatives of } T\} \end{aligned} \quad (11)$$

where primes indicate differentiation with respect to x. Inspection of Eq. (11) shows that, for temperature distributions which are either constant along the span or vary linearly with x, the stress σ_{yT} is zero; Eq. (2) is therefore exact in these cases. For other temperature distributions Eq. (2) will be in error, but if the variation of T along the span is sufficiently smooth the higher derivatives of T with respect to x will be small, the term $(2 + \nu)\sigma_{yT}$ will be small compared with αET, and therefore Eq. (2) will provide a good approximation. This qualitative discussion may be made more specific with the aid of the following example.

Let the deflection in the y-direction due to a temperature distribution of the form

$$T = T_0(x/L)^n(y/c)^m \tag{12}$$

be calculated at the center ($x = L/2$) of a simply supported beam. Then the moment M_D is

$$M_D(x_0, x) = \begin{cases} x_0[1 - (x/L)] & \text{for } 0 \leq x_0 \leq x \\ -x[(x_0/L) - 1] & \text{for } x \leq x_0 \leq L \end{cases} \tag{13}$$

and the deflection may be written in the form

$$I\, v(L/2)/\alpha T_0 b\, c^2 L^2 = v_0 + (c/L)^2\, v_1 + (c/L)^4\, v_2 + \ldots . \tag{14}$$

Here v_0 is the contribution of the term αET in Eq. (10) and, therefore, comprises the entire deflection as calculated from the approximate Eq. (2). The succeeding terms are the required correction due to the σ_{yT} term; v_1 results from the first bracket of Eq. (11), v_2 from the second, and so forth. It may be seen from Eq. (14) that the shallower the beam the better the approximation provided by v_0. Numerical calculations were carried out for a beam four times as long as it is deep— i.e., with $(c/L) = (1/8)$, which represents a comparatively short beam and therefore provides an upper limit to the error to be expected in practice. The results are collected in Table 1; the maximum error encountered in the range of exponents considered is only about 2.8 per cent of the correct value. It is therefore reasonable to conclude that Eq. (2) will be adequate for most practical calculations.

The above developments have been limited to statically determinate beams, but the conclusion just stated is easily extended to indeterminate beams as well. In fact, the additional deflections occurring in this case, due to the various redundant loads, may be calculated separately from Eq. (1) and then superimposed on those just obtained from Eq. (2).*

TABLE 1

Per Cent Error Introduced by the Use of Eq. (2) in Place of Eq. (10)

n	$m = 1$	$m = 3$	$m = 5$
0	0%	0%	0%
1	0	0	0
2	0.003	−0.5	−0.4
3	0.000	−1.1	−0.9
4	−0.02	−1.9	−1.5
5	−0.06	−2.8	−2.2

It is of interest to note that the accuracy of Eq. (1) may also be examined in a manner entirely analogous to that just employed here for Eq. (2), by using the results of reference 4 in place of those of reference 3. It is shown in reference 4 that an expansion of the same form as Eq. (11) may be written for the stresses due to any type of distributed loadings on a rectangular beam.

In conclusion, it should be remarked that in the analysis presented above the effect of inertia was tacitly neglected. The error thus incurred was examined in reference 6, and was found to be small in usual engineering applications.

REFERENCES

[1] Boley, Bruno A., and Mechanic, Harold, *Thermoelastic Stresses and Deflections in Beam-Columns*, WADC Tech. Rep. 54-425, March, 1954.

[2] Timoshenko, S., and Goodier, J. N., *Theory of Elasticity*, Second Ed., McGraw-Hill Book Co., New York, 1951.

[3] Boley, Bruno A., *The Determination of Temperature, Stresses, and Deflections in Two-Dimensional Thermoelastic Problems*, Journal of the Aeronautical Sciences, Vol. 23, No. 1, pp. 67–75, January, 1956.

[4] Boley, Bruno A., and Tolins, Irwin S., *Stresses and Deflections of Rectangular Beams*, Journal of Applied Mechanics, Vol. 23, No. 3, pp. 339–342, September, 1956.

[5] Boley, Bruno A., and Moore, Roland H., *Note on the Calculation of Deflections of Indeterminate Structures*, Journal of the Aeronautical Sciences, Vol. 17, No. 8, pp. 526–527, August, 1950. See also Vol. 18, No. 4, p. 285, April, 1951.

[6] Boley, Bruno A., *Thermally Induced Vibrations of Beams*, Journal of the Aeronautical Sciences, Vol. 23, No. 2, pp. 179–181, February, 1956.

* Note that in the calculation of the thermal deflections of statically indeterminate beams the simplification discussed in reference 5 can still be employed; in other words, it is permissible to disregard entirely all redundant quantities (and therefore to treat the beam as a determinate one) in the calculation of the stresses due to the dummy loads.

Change of Address

Since the Post Office Department does not as a rule forward magazines to forwarding addresses, it is important that the Institute be notified of changes in address 30 days in advance of publishing date to ensure receipt of every issue of the JOURNAL and REVIEW.

Notices should be printed legibly and sent directly to:

Institute of the Aeronautical Sciences, Inc.
2 East 64th Street, New York 21, N.Y.

Optimum Thickness and Lift Distribution for a Fuselage in the Presence of a Prescribed Wing System

M. E. GRAHAM*

Douglas Aircraft Company, Inc,

SUMMARY

A drag formula of Hayes is utilized to obtain a generalized supersonic "area rule" expressed in terms of sources, lift, and side-force singularities. Simple examples of optimum fuselage source distributions and optimum fuselage lift distributions are presented.

DISCUSSION

THE RULE, in supersonic flow, for the optimization of a fuselage-thickness distribution in the presence of a prescribed wing-thickness distribution has been described by various authors—e.g., Ward[1] and Jones.[2] It is interesting to see how easily this rule is derived in terms of singularity distributions from the drag formula developed by Hayes,[3] and how, from Hayes' formula, the generalization of the rule to include lift and side-force as well as source distributions is immediately evident. Such a generalization, in terms of area distributions and forces, has already been presented by Lomax and Heaslet.[4] However, the subject seems of sufficient interest to be reconsidered from a slightly different viewpoint. Since the drag formula of Hayes, which is valid within linear theory, is expressed in terms of singularities, it seems natural to determine optimum configurations in terms of singularities and then later obtain the geometry of the configuration. (The analysis presented here appears also in a slightly different form and in somewhat more detail in reference 5.)

For midwing monoplanes, the rule in its usual form (without forces) is adequate to prescribe the optimum fuselage-thickness distribution. However, for configurations such as high-wing monoplanes and ring wings, the thickness distributions and the lift and side-force distributions do not act independently in producing drag. Thus, in general, the optimization of the fuselage-thickness distribution is affected by the lift and side-force distributions on the wing as well as by the wing thickness. In addition, there is the possibility of optimizing the fuselage lift distribution.

This generalized rule prescribes what lineal distribution of sources, lift, and side force should be used to represent a fuselage in order to minimize the wave drag of the fuselage in combination with a given wing (the wing being represented by a spatial distribution of singularities). Furthermore, if no net lift or side force is carried on the fuselage, the minimum pressure drag (wave plus vortex drag) is achieved. (No net lift or side force on the fuselage means that the fuselage singularities, which are distributed along a streamwise line, will produce zero rather than infinite vortex drag.)

Although the actual geometry of the wing-body combination has not been obtained, the fuselage produced by these singularities is cambered and has essentially circular cross sections. Distortions of the fuselage cross sections, which are considered by Lomax and Heaslet,[4] have not been included in this analysis. Within slender body theory the rate of change of the fuselage cross-sectional area is proportional to the strength of the fuselage source distribution.

A wing fuselage combination may be represented by disposing singularities along a streamwise line, say the ξ-axis, to form the fuselage, and by distributing singularities in a region of space to form the wing system. The wave drag of the combination is, according to Hayes,[3]

$$D_{w+f} = \frac{1}{2\pi}\int_0^{2\pi} \frac{-q}{2\pi}\iint \frac{\partial}{\partial\xi_1}\left[f_s(\xi_1) - \frac{\beta\sin\theta}{2q} f_l(\xi_1) - \frac{\beta\cos\theta}{2q} f_h(\xi_1) + W_s(\xi_1,\theta) - \frac{\beta\sin\theta}{2q} W_l(\xi_1,\theta) - \frac{\beta\cos\theta}{2q} W_h(\xi_1,\theta)\right] \frac{\partial}{\partial\xi_2}\left[f_s(\xi_2) - \frac{\beta\sin\theta}{2q} f_l(\xi_2) - \frac{\beta\cos\theta}{2q} f_h(\xi_2) + W_s(\xi_2,\theta) - \frac{\beta\sin\theta}{2q} W_l(\xi_2,\theta) - \frac{\beta\cos\theta}{2q} W_h(\xi_2,\theta)\right] \ln|\xi_1 - \xi_2|\, d\xi_1 d\xi_2 d\theta \quad (1)$$

where the inner integrations extend over all the singularities. The subscripts s, l, h denote sources, lifting elements, and side-force elements. $f_i(\xi)$, where $i = s$, l, or h, are the fuselage singularity distributions. $W_i(\xi, \theta)$ are "equivalent" lineal distributions formed for each radial angle θ, measured from the horizontal, by transferring the spatial wing singularities w_s, w_l and w_h along Mach planes to the ξ-axis.

This equation (discussed in detail in reference 6) was derived from linear theory by considering the momentum flux at a distant control surface enclosing the spatial distribution of sources, lifting elements, and side-force elements. It gives the drag of a spatial distribu-

Received April 13, 1956.

* Aerodynamicist, Santa Monica Division.

tion of singularities in terms of the drag of an equivalent "lineal" distribution.

It is important to note that, since the fuselage singularity distributions f_s, f_l and f_h are actually lineal, they do not depend upon θ. After interchanging the order of the θ and ξ integrations, it can be seen that the fuselage singularities interfere only with certain averages of the wing singularity distributions. To illustrate this, consider a wing-fuselage combination formed only from sources. The wave drag becomes (omitting the subscript s)

$$D_{w+f} = \frac{-q}{2\pi}\int\int\Bigg\{\frac{\partial}{\partial\xi_1}f(\xi_1)\,\frac{\partial}{\partial\xi_2}f(\xi_2) + \frac{\partial}{\partial\xi_1}f(\xi_1)\,\frac{\partial}{\partial\xi_2}\,\frac{1}{2\pi}\int_0^{2\pi}W(\xi_2,\theta)d\theta + \frac{\partial}{\partial\xi_2}f(\xi_2)\,\frac{\partial}{\partial\xi_1}\,\frac{1}{2\pi}\int_0^{2\pi}W(\xi_1,\theta)\,d\theta\Bigg\}\times \ln|\xi_1-\xi_2|\,d\xi_1d\xi_2 + \frac{1}{2\pi}\int_0^{2\pi}\frac{-q}{2\pi}\int\int\frac{\partial}{\partial\xi_1}\times W(\xi_1,\theta)\frac{\partial}{\partial\xi_2}W(\xi_2,\theta)\ln|\xi_1-\xi_2|\,d\xi_1d\xi_2d\theta \quad (2)$$

Now the fuselage sources interfere only with the average $\bar{w}$ of the wing sources where $\bar{w} = 1/2\pi\int_0^{2\pi} W(\xi,\theta)d\theta$. If $\bar{w}$, which is a lineal distribution, is combined with f, then the first two terms can be rearranged to form $D_{\bar{w}+f}$, the drag of the combined fuselage and average wing distributions, and $D_{\bar{w}}$, the drag of the average wing distributions.

$$D_{\bar{w}+f} = (-q/2\pi)\iint(\partial/\partial\xi_1)\,[f(\xi_1)+\bar{w}(\xi_1)]\,(\partial/\partial\xi_2)\times[f(\xi_2)+\bar{w}(\xi_2)]\ln|\xi_1-\xi_2|\,d\xi_1d\xi_2$$

$$D_{\bar{w}} = (-q/2\pi)\iint(\partial/\partial\xi_1)\bar{w}(\xi_1)\,(\partial/\partial\xi_2)\bar{w}(\xi_2)\times\ln|\xi_1-\xi_2|\,d\xi_1d\xi_2$$

The final term of Eq. (2) is just the drag D_w of the wing alone. The drag of the wing fuselage combination thus becomes

$$D_{w+f} = D_{w+f} - D_{\bar{w}} + D_w \quad (3)$$

If the wing system is fixed, then only the first term of Eq. (3) can be minimized. Thus, the fuselage source distribution $f = (f+\bar{w}) - \bar{w}$ is an optimum if $(f+\bar{w})$ is an optimum source distribution.

If lift and side-force elements as well as sources are included, the derivation is analogous to that above, and Eq. (3) still results. However, in the equations for D_{w+f} and $D_{\bar{w}}$, f is replaced by $\sum_{i=s,\,l,\,h}\gamma_i(\theta)\,f_i(\xi)$ and $\bar{w}$ by $\sum_{i=s,\,l,\,h}\gamma_i(\theta)\bar{w}_i(\xi)$—where $\gamma_s(\theta) = 1$, $\gamma_l(\theta) = -\left(\frac{\beta}{2q}\right)\sin\theta$, and $\gamma_h(\theta) = -(\beta/2q)\cos\theta$—and the drag expressions are each averaged over θ. Note that $\bar{w}$ now consists of lift and side-force elements $\bar{w}_l$ and $\bar{w}_h$ as well as sources $\bar{w}_s$. Each of these $\bar{w}_i$ can depend upon all of the different types of wing singularities w_s, w_l, w_h. (See Example 1.) The definition of $\bar{w}_i$ is

$$\bar{w}_i = \frac{\int_0^{2\pi}\gamma_i(\theta)\sum_{j=s,\,l,\,h}\gamma_j(\theta)W_j(\xi,\theta)d\theta}{\int_0^{2\pi}\gamma_i^2(\theta)\,d\theta} \quad (4)$$

(The optimum strengths of the three lowest ordered multipoles of Lomax and Heaslet[4] correspond to the negatives of these $\bar{w}_i$.)

The generalized area rule thus states that the optimum fuselage singularity distributions are obtained if $(f+\bar{w})$ consists of the optimum source distribution $(f_s+\bar{w}_s)$, the optimum lift distribution $(f_l+\bar{w}_l)$, and the optimum side-force distribution $(f_h+\bar{w}_h)$. [$(f+\bar{w})$ can be separated in this way since a source and a lifting element (or two other unlike singularities) lying on the same streamwise line have no interference drag.] For certain important cases $(f+\bar{w})_{opt}$ is already known.

Example 1—Optimum Fuselage Source Distribution

Consider the problem of optimizing the fuselage source distribution f_s in the presence of a given wing distribution of sources, lift, and side force. Let the fixed wing volume be V_w, and require the fuselage to have the fixed volume V_f. The lineal source distribution $f_s + \bar{w}_s$ can be pictured as producing a fictitious body of revolution of fixed volume

$$V = \int_{-\infty}^{+\infty}d\xi\int_{-\infty}^{\xi}[f_s(\xi_1)+\bar{w}_s(\xi_1)]d\xi_1$$

(It is sufficient, though perhaps not necessary, to assume slender body theory in order to say that $V_f + V_w$ is the physical volume produced by the wing and fuselage sources. This is discussed, in part, in reference 7. It is not the purpose of this paper to make distinctions between the use of slender body theory and linear theory to determine the geometrical configuration produced by the singularities.)

If the wing and fuselage lie in the same horizontal plane, it can be shown that the wing lift distribution does not contribute to $\bar{w}_s(\xi)$. Presumably such a wing carries no side-force distribution, so $\bar{w}_s(\xi)$ depends only on the wing sources. Then $V = V_f + V_w$. This is the case of the midwing monoplane for which drag due to thickness is independent of drag due to lift. It is to this case that the usual supersonic rule for optimizing the fuselage-thickness distribution applies.

However, in general, $\bar{w}_s(\xi)$ does depend also upon the wing lift and side-force distributions. Then $V = V_f + V_w + V_p$ where V_p is a "pseudo volume" dependent upon the forces on the wing. A lifting high-wing monoplane or a ring wing with an outwardly directed normal force distribution each contribute a negative pseudo volume. (For a discussion of pseudo volumes, see, for example, reference 8.)

If the length c_f of the fuselage is specified, and if the fuselage extends at least over the mean lineal wing distributions (i.e., the wing system lies within the double Mach cone defined by the fuselage), then the fictitious body produced by $f_s + \bar{w}_s$ has the length c_f. Thus,

under the constraint of fixed length and fixed total volume, $(f_s + \bar{w}_s)_{opt}$ is a source distribution obtained by Sears[9] and Haack.[10] (In a practical case, other constraints, such as minimum admissible cross-sectional area for the fuselage, might be necessary.)

Example 2—Optimum Fuselage Lift Distribution

If the net lift, L_f, carried on the fuselage and L_w carried on the wing are fixed, then the lineal lift distribution $f_l + \bar{w}_l$ produces a fixed lift $L = \int_{-\infty}^{+\infty} (f_l + \bar{w}_l)d\xi = L_f + L_w$. If the fuselage has a specified length c_f extending at least over the mean lineal wing distributions, then the lineal distribution $f_l + \bar{w}_l$ also has the length c_f. Thus, under the constraint of fixed length and fixed total lift, the optimum distribution for $f_l(\xi) + \bar{w}_l(\xi)$ is elliptic.[11] (Again, in a practical case it is likely that additional constraints, such as limiting the magnitude of the local angles of attack of the fuselage, would be necessary.)

If no net lift is carried on the fuselage ($L_f = 0$), then the fuselage produces no vortex drag. Eq. (3) then applies to wave plus vortex drag, if the term D_w is interpreted as the wave plus the vortex drag of the wing.

It is interesting to note that Hayes' equation provides a certain equivalence between lift distributions and source distributions. The lift distribution $f_l(\xi) + \bar{w}_l(\xi)$ can be converted into a source distribution which would produce the same wave drag. This source distribution represents a fictitious body of revolution with a base area proportional to the total lift. The optimum elliptic lift distribution mentioned above converts (within slender body theory) into a Kármán ogive.

REFERENCES

[1] Ward, G. N., *The Drag of Source Distributions in Linearized Supersonic Flow*, The College of Aeronautics, Cranfield, Report No. 88, February, 1955.

[2] Jones, R. T., *Theory of Wing-Body Drag at Supersonic Speeds*, NACA RM A53H18a, September, 1953.

[3] Hayes, Wallace D., *Linearized Supersonic Flow*, North American Aviation, Inc., Los Angeles, Report No. A.L. 222, June, 1947.

[4] Lomax, Harvard, and Heaslet, Max. A., *Recent Developments in the Theory of Wing-Body Wave Drag*, presented at 24th Annual Meeting of the Institute of the Aeronautical Sciences, New York, January 23–26, 1956. (Preprint No. 617).

[5] Graham, M. E., *Application of Drag Reduction Methods to Supersonic Biplanes*, Douglas Aircraft Company Report No. SM-19258, September, 1955.

[6] Graham, E. W., Lagerstrom, P. A., Licher, R. M., and Beane, B. J., *A Theoretical Investigation of the Drag of Generalized Aircraft Configurations in Supersonic Flow*, Douglas Aircraft Company Report No. SM-19181, July, 1955.

[7] Bleviss, Z. O., *Some Integrated Volume Properties in Linearized Flow and Their Connection with Drag Reduction at Supersonic Speeds*, Douglas Aircraft Company Report No. SM-19469, February, 1956.

[8] Graham, E. W., *Examples of Wave Drag Calculation by Application of Fourier Analysis about a Streamwise Axis*, Douglas Aircraft Company Report No. SM-19529, January 1956.

[9] Sears, W. R., *On Projectiles of Minimum Wave Drag*, Quarterly of Applied Mathematics, Vol. IV, No. 4, January, 1947.

[10] Haack, W., *Geschossformen Kleinsten Wellenwiderstandes* Bericht 139 der Lilienthal-Gesellschaft für Luftfahrt, 1941. Also available as Translation CGD-253, Goodyear Aircraft Corp., or Translation No. A9-T-3, Brown University, 1948.

[11] Jones, R. T., *Theoretical Determination of the Minimum Drag of Airfoils at Supersonic Speeds*, Journal of the Aeronautical Sciences, Vol. 19, No. 12, December, 1952.

A Two-Dimensional Approximation to the Unsteady Aerodynamics of Rotary Wings

(*Continued from page 92*)

REFERENCES

[1] Daughaday, H., and Kline, J., *An Approach to the Determination of Higher Harmonic Rotor Blade Stresses*, Proceedings 9th Annual Forum, American Helicopter Society, Washington, D.C., May 14–17, 1953.

[2] Isaacs, R., *Airfoil Theory for Flows of Variable Velocity*, Journal of the Aeronautical Sciences, Vol. 12, No. 1, pp. 113–117, January, 1945.

[3] Isaacs, R., *Airfoil Theory for Rotary Wing Aircraft*, Journal of the Aeronautical Sciences, Vol. 13, No. 4, p. 218, April, 1946.

[4] Greenberg, J. M., *Airfoil in Sinusoidal Motion in a Pulsating Stream*, NACA TN 1326, June, 1947.

[5] Chang, T. T., *A Flutter Theory for a Flexible Helicopter Rotor Blade in Vertical Flight*, Cornell Aeronautical Laboratory Report SB-862-S-1, July, 1954.

[6] Daughaday, H., and Kline, J., *An Investigation of the Effect of Virtual Delta-Three Angle and Blade Flexibility on Rotor Blade Flutter*, Cornell Aeronautical Laboratory Report SB-862-S-2, August, 1954.

[7] Theodorsen, T., and Regier, A. A., *Effect of the Lift Coefficient on Propeller Flutter*, NACA ACR L5F30, July, 1954.

[8] Brooks, G. W., and Baker, J. E., *Classified Report*, NACA RM L53D24, June, 1953.

[9] Schwarz, L., *Berechnung derdruchverteilung siner harmonisch sich verformenden tragfiache in ebener strömung Luftfahrtforschung*, Band 17, Lfg, pp. 379–386, December, 1940.

[10] Bierens De Haan, *Nouvelles tables d'integrales definies*, Stechert and Co., 1939.

[11] Söhngen, H., *Mathematische zeitschrift*, Band 45, pp. 245–264, 1939.

[12] Theodorsen, T., *General Theory of Aerodynamic Instability and the Mechanism of Flutter*, NACA TR 496, 1949.

[13] Smilg, B., and Wasserman, L., *Application of Three-Dimensional Flutter Theory to Aircraft Structures*, AFTR 4798, July, 1942.

[14] Loewy, R. G., *Tables of Two-Dimensional Oscillating Airfoil Coefficients for Rotary Wings*, Cornell Aeronautical Laboratory Report No. 77.

[15] Runyan, H. L., *Single-Degree-of-Freedom Flutter Calculations for a Wing in Subsonic Potential Flow and Comparison With an Experiment*, NACA TN 2396, July, 1951.

[16] Flax, A. H., and Goland, L., *Dynamic Effects in Rotor Blade Bending*, Journal of the Aeronautical Sciences, Vol. 18, No. 12, p. 813, December, 1951.

Readers' Forum

BRIEF REPORTS of investigations in the aeronautical sciences and discussions of papers published in the JOURNAL are presented in this special department. Entries must be restricted to a maximum of 1,300 words or the equivalent of one JOURNAL page including formulas and illustrations. Publication is completed as soon as possible after receipt of the material. The Editorial Committee does not hold itself responsible for the opinions expressed by the correspondents.

Contents

Vibration of Clamped Parallelogrammic Isotropic Flat Plates ..... M. HASEGAWA 145

A Useful Method for Integrating the Time-Dependent, Viscous Equations of Motion ..... L. FILLER, H. F. LUDLOFF, AND P. TREUENFELS 147

Approximate Trajectories of High-Drag Bodies ..... GEORGE S. CAMPBELL 147

Discussion of the Influence of Confining Surfaces Upon the Boundary Layer in a Channel ..... RALPH BURTON 149

Location of Mach Discs and Diamonds in Supersonic Air Jets ..... DONALD E. WILCOX, ALEXANDER WEIR, JR., J. A. NICHOLLS, AND ROGER DUNLAP 150

Effect of Thermal Resistance of Joints Upon Thermal Stresses ..... B. E. GATEWOOD 152

Total Creep Under Varying Loads ..... WILLIAM PRAGER 153

Second Approximation to the Laminar Boundary-Layer Flow Over a Flat Plate ..... ISAO IMAI 155

Three-Dimensional Vortex Pattern Behind a Circular Cylinder ..... FRANCIS R. HAMA 156

Subsonic Boundary-Layer Transition Caused by Single Roughness Elements ..... J. LEITH POTTER 158

An Approximate Method Applied to the Solution of the Problem of Vibrating Rectangular Plates ..... MILOMIR M. STANIŠIĆ 159

Vibration of Clamped Parallelogrammic Isotropic Flat Plates

M. Hasegawa
Shimane University, Matsue, Japan

September 6, 1956

VIBRATION of rectangular plates was discussed by W. Ritz,[1] S. Iguchi,[2] D. Young,[3] and M. V. Barton,[4] and vibration of skew cantilever plates was discussed by M. V. Barton.[4] Vibration of clamped rhombic plate was discussed by the author.[5] In this paper, we shall calculate the smallest frequency of the vibration of clamped parallelogrammic isotropic plates by the Ritz method.

Let the oblique coordinates axes (x, y) be taken in the middle plane of the plate of uniform thin thickness in such a way that the origin coincides with the center of the plate and the axes are parallel to the sides. Let us denote the lengths of side, thickness, the density, Young's modulus, and Poisson's ratio of the plate by $2a$, $2b$, h, ρ, E and ν, respectively. Let the angle between coordinates axes be denoted by α. If w is the transverse displacement of a point on the middle plane and t the time, the differential equation for w is

$$(D/\sin^4\alpha)\,[(\partial^4 w/\partial x^4) - 4\cos\alpha(\partial^4 w/\partial x^3\partial y) + 2(1 + 2\cos^2\alpha)\,(\partial^4 w/\partial x^2\partial y^2) - 4\cos\alpha\,(\partial^4 w/\partial x\partial y^3)] + \rho h(\partial^2 w/\partial t^2) = 0 \quad (1)$$

where $$D = Eh^3/12(1 - \nu^2)$$

The boundary conditions are

$$w = 0 \quad \text{and} \quad \partial w/\partial n = 0 \qquad \text{at} \quad x = \pm a \quad \text{and} \quad y = \pm b \quad (2)$$

where $\partial/\partial n$ denotes differentiation along the normal.

As the problem is so complicated, we shall use the Ritz method. According to this method, the mode of vibration is assumed. If we assume the following mode,

$$w = W(x, y)\cos\rho t \quad (3)$$

Eq. (1) is transformed into

$$(\partial^4 W/\partial x^4) - 4m(\partial^4 W/\partial x^3\partial y) + 2(1 + 2m^2)\,(\partial^4 W/\partial x^2\partial y^2) - 4m(\partial^4 W/\partial x\partial y^3) + (\partial^4 W/\partial y^4) - K'W = 0 \quad (4)$$

with the boundary conditions

$$W = 0 \quad \text{and} \quad \partial W/\partial n = 0 \qquad \text{at} \quad x = \pm a \quad \text{and} \quad y = \pm b \quad (5)$$

in which $m = \cos\alpha$ and

$$K' = (\rho h\,\rho^2\sin^4\alpha)/D \quad (6)$$

In order to apply the Ritz method, we consider the following integral:

$$2U = \frac{D}{\sin^4\alpha}\int_{-a}^{a} dx \int_{-b}^{b}\Big[(\Delta W)^2 - 4\cos\alpha\,\frac{\partial^2 W}{\partial x\partial y}\,\Delta W + 4\cos^2\alpha(\partial^2 W/\partial x\,\partial y)^2 + 2(1 - \nu)\sin^2\alpha\{(\partial^2 W/\partial x\partial y)^2 - (\partial^2 W/\partial x^2)(\partial^2 W/\partial y^2)\} - K'W^2\Big]\,dy \quad (7)$$

We assume for the expression of W which satisfies the boundary conditions of Eq. (5) that

$$W = (a^2 - x^2)^2 (b^2 - y^2)^2 (a_{00} + a_{11}xy + a_{20}x^2 + a_{02}y^2 + a_{31}x^3y + a_{13}xy^3 + a_{22}x^2y^2) \quad (8)$$

in which a_{00}, a_{11}, . . . and a_{22} are arbitrary constants and Eq. (8) is introduced into U.

Since the constants are to be determined so as to make U a minimum by the Ritz method, we must have

$$\partial U/\partial a_{00} = 0; \quad \partial U/\partial a_{11} = 0; \quad \partial U/\partial a_{20} = 0; \quad \partial U/\partial a_{02} = 0; \quad \partial U/\partial a_{22} = 0; \quad \partial U/\partial a_{31} = 0; \quad \partial U/\partial a_{13} = 0 \quad (9)$$

These equations are linear in the A's and are found to be

$$\left.\begin{aligned} &B_{100}A_{00} + B_{111}A_{11} + B_{120}A_{20} + B_{102}A_{02} + B_{131}A_{31} + B_{113}A_{13} + B_{122}A_{22} = 0 \\ &\cdots\cdots\cdots\cdots\cdots\cdots\cdots\cdots\cdots\cdots\cdots\cdots\cdots\cdots\cdots\cdots\cdots\cdots \\ &B_{700}A_{00} + B_{711}A_{11} + B_{720}A_{20} + B_{702}A_{02} + B_{731}A_{31} + B_{713}A_{13} + B_{722}A_{22} = 0 \end{aligned}\right\} \quad (10)$$

where

$$A_{ij} = a^{1+i}b^{1+j}a_{ij}, \quad k = \frac{b}{a}, \quad K = K'a^4 = \frac{\rho h a^4 p^2 \sin^4 \alpha}{D}$$

$$B_{100} = \frac{1 + k^4}{1{,}575} + \frac{4k^2(1 + 2m^2)}{11{,}025} - \frac{2Kk^4}{99{,}225}, \quad B_{111} = B_{200} = \frac{2m(k^3 + k)}{11{,}025}$$

$$B_{120} = B_{300} = \frac{k^4}{11{,}025} + \frac{1}{17{,}325} - \frac{2Kk^4}{1{,}091{,}475}, \quad B_{102} = B_{400}$$

$$B_{131} = B_{500} = 2m\left(\frac{k^3}{33{,}075} + \frac{k}{40{,}425}\right), \quad B_{211} = \frac{k^4 + 1}{24{,}255} + \frac{4k^2(1 + 2m^2)}{99{,}225} - \frac{2Kk^4}{12{,}006{,}225}$$

$$B_{122} = B_{302} = B_{420} = B_{700} = \frac{k^4 + 1}{121{,}275} - \frac{2Kk^4}{12{,}006{,}225}, \quad B_{113} = B_{600}$$

$$B_{220} = B_{311} = -2m\left(\frac{k^3}{33{,}075} + \frac{k}{121{,}275}\right), \quad B_{222} = B_{711} = \frac{2m(k^3 + k)}{363{,}825}$$

$$B_{231} = B_{511} = \frac{k^4}{72{,}765} + \frac{1}{105{,}105} + \frac{8k^2(1 + 2m^2)}{1{,}091{,}475} - \frac{2Kk^4}{52{,}026{,}975}, \quad B_{202} = B_{411}$$

$$B_{320} = \frac{k^4}{3{,}675} + \frac{1}{75{,}075} + \frac{4k^2(1 + 2m^2)}{121{,}275} - \frac{2Kk^4}{4{,}729{,}725}, \quad B_{213} = B_{611} \quad (11)$$

$$B_{331} = B_{520} = 2m\left(\frac{k^3}{121{,}275} + \frac{k}{525{,}525}\right), \quad B_{313} = B_{620} = -2m\left(\frac{k^3}{121{,}275} + \frac{k}{363{,}825}\right)$$

$$B_{322} = B_{720} = \frac{k^4}{40{,}425} + \frac{1}{525{,}525} - \frac{2Kk^4}{52{,}026{,}975}, \quad B_{413} = B_{602}$$

$$B_{431} = \frac{13k^4}{800{,}415} + \frac{1}{315{,}315} + \frac{68k^2(1 + 2m^2)}{14{,}189{,}175} - \frac{2Kk^4}{156{,}080{,}925}, \quad B_{431} = B_{502}$$

$$B_{513} = B_{631} = \frac{k^4 + 1}{315{,}315} + \frac{16k^2(1 + 2m^2)}{12{,}006{,}225} - \frac{2Kk^4}{225{,}450{,}225}, \quad B_{422} = B_{702}$$

$$B_{522} = B_{731} = -2m\left(\frac{k^3}{1{,}334{,}025} + \frac{k}{1{,}576{,}575}\right), \quad B_{622} = B_{713}$$

$$B_{613} = \frac{k^4}{315{,}315} + \frac{13}{800{,}415} + \frac{68k^2(1 + 2m^2)}{14{,}189{,}175} - \frac{2Kk^4}{156{,}080{,}925}$$

$$B_{722} = \frac{k^4 + 1}{175{,}175} + \frac{4k^2(1 + 2m^2)}{1{,}334{,}025} - \frac{2Kk^4}{225{,}450{,}225}$$

The coefficients B_{102}, B_{113}, B_{202}, B_{213}, B_{402}, B_{413}, B_{422}, B_{431}, and B_{622} are obtained, respectively, by interchanging the numerators of the first two terms of each of the following coefficients: B_{120}, B_{131}, B_{220}, B_{231}, B_{320}, B_{331}, B_{322}, B_{313}, and B_{522}. For instance, we have

$$B_{102} = (1/11{,}025) + (k^4/17{,}325) - (2Kk^4/1{,}091{,}475)$$

If we eliminate A_{00}, A_{11} . . . . . from Eqs. (10), we have the determinantal equation. This equation determines the values of K—i.e., the frequencies of vibrations. The smallest roots of the determinantal equation are calculated for several values of α and k and are shown in Table 1.

TABLE 1

k	1	1	1	1	1
α	55°	60°	70°	75°	90°
K	72.991	74.930	78.209	79.356	80.955
k	2	2	2	2	2
α	55°	60°	70°	75°	90°
K	36.293	36.592	37.173	37.460	37.770

The exact value of K for the square plate is 80.9348 which is obtained by Prof. S. Tomotika.[6] We shall report the more accurate values in a subsequent paper.

REFERENCES

[1] Ritz, W., *Theorie der Transversalschwingungen eines quadratischen Platten mit freien Randern*, Ann. der Physik, Vol. 28, p. 737, 1909.

[2] Iguchi, S., *Die Eigenwertsprobleme für die elastische rechteckige Platte*, Memoirs of the Faculty of Engineering, Hokkaido Imperial University, Vol. 4, p. 305, 1938.

[3] Young, D., *Vibration of Rectangular Plates by the Ritz Method*, J. Appl. Mech., Trans. ASME, Vol. 72, p. 448, 1950.

[4] Barton, M. V., *Vibration of Rectangular and Skew Cantilever Plates*, J. Appl. Mech., Trans. ASME, Vol. 73, p. 129, 1951.

[5] Hasegawa, M., *On the Vibration of Clamped Rhombic Isotropic Plates I*, Bulletin of the Shimane University, Vol. 6, p. 21, 1956.

[6] Tomotika, S., *On the Transverse Vibration of a Square Plate with Four Clamped Edges*, Report of the Aeronautical Research Institute, Tokyo Imperial University, Vol. X, p. 301, 1935.

A Useful Method for Integrating the Time-Dependent, Viscous Equations of Motion*

L. Filler, H. F. Ludloff, and P. Treuenfels
New York University, New York
September 4, 1956

As a preliminary to numerical integration of the three time-dependent, viscous equations of motion, it is instructive to study the "Burgers equation," which contains both characteristic features of the motion of a real fluid—viz., the nonlinear as well as the viscosity effects. The most interesting difference procedure to be used for integrating this parabolic differential equation (as well as the true equations of motion) is an implicit scheme, in which the *time steps* may be taken *arbitrarily large*. We have carried out an analysis of stability and of convergence of iterations before carrying out the numerical integration and comparing it with an analytic solution which we had derived before.

An analytic solution of

$$u_t + u \cdot u_x = \nu \cdot u_{xx}$$

is $$u(x, t) = A + B \cdot \tanh[(AB \cdot t - B \cdot x)/2\nu]$$

This curve varies with x between 1 and 0 if we set $A = B = 1/2$. As t increases, it is displaced parallel to itself without deformation. The slope, always negative, reaches the extremum $-B^2/\nu$, which can be made arbitrarily large for proper ν. Therefore, it may be considered a propagating shock in a viscous medium.

Using an implicit scheme, the difference equation is

$$\frac{u_{j,\,k+1} - u_{j,\,k}}{\Delta t} + u \cdot \frac{u_{j+1,\,k+1} - u_{j-1,\,k+1}}{2 \cdot \Delta x} - \nu \frac{u_{j+1,\,k+1} - 2u_{j,\,k+1} + u_{j-1,\,k+1}}{(\Delta x)^2} = 0 \quad (1)$$

Here j indicates the space point and k the time cycle. Using von Neumann's error analysis, it is easily seen that the *stability condition* is satisfied *for all values* of $\Delta t/\Delta x$ and $\nu/\Delta x$.

In order to solve the implicit difference equation [Eq. (1)], the iteration procedure, indicated below, has been employed. It appears appropriate to use here also von Neumann's Fourier analysis to derive a *criterion for the convergence* of the iteration procedure. We use superscripts to designate the number of iterations carried out in a time cycle. It is best to collect the two linear terms at lattice point j, $k+1$, in iteration cycle $n+1$, while all other terms are kept in iteration cycle n. Then

$$u^{n+1}_{j,\,k+1} = \frac{u_{j,\,k} - u \cdot (\Delta t/2\Delta x)\,(u^{n}_{j+1,\,k+1} - u^{n}_{j-1,\,k+1}) + (\nu/\Delta x) \cdot (\Delta t/\Delta x)\,(u^{n}_{j+1,\,k+1} + u^{n}_{j-1,\,k+1})}{1 + (2\nu/\Delta x) \cdot (\Delta t/\Delta x)}$$

We substitute $$u^{n}_{j,\,k+1} = \bar{u}_{j,\,k+1} + \delta^{n}_{j,\,k+1}$$

where $\bar{u}_{j,\,k+1}$ is the exact solution of Eq. (1) and $\delta^{n}_{j,\,k+1}$ the iteration error committed up to the nth iteration of the $(k+1)$th time cycle. Furthermore, note that $u_{j,\,k} = \bar{u}_{j,\,k}$ without error since iterations in kth cycle were carried to completion. Then

$$\delta^{n+1}_{j,\,k+1} = \frac{-u \cdot (\Delta t/2\Delta x)\,(\delta^{n}_{j+1,\,k+1} - \delta^{n}_{j-1,\,k+1}) + (\nu/\Delta x) \cdot (\Delta t/\Delta x)\,(\delta^{n}_{j+1,\,k+1} + \delta^{n}_{j-1,\,k+1})}{1 + (2\nu/\Delta x)/(\Delta t/\Delta x)}$$

After introducing $\delta_{j,\,k+1} = e^{ij\beta\Delta x} \cdot e^{b\,n}$, we obtain *for convergence*

$$|e^{b}| = \left| \frac{-u \cdot (\Delta t/\Delta x)\,(i \sin \beta\Delta x) + (2\nu/\Delta x) \cdot (\Delta t/\Delta x) \cdot \cos \beta\Delta x}{1 + (2\nu/\Delta x) \cdot (\Delta t/\Delta x)} \right| \leq 1$$

Thus,

$$|e^{b}|^2 = C_1^2 + (C_2^2 - C_1^2) \cdot \sin^2(\beta \cdot \Delta x) \leq 1$$

where

$$C_1 = \frac{(2\nu/\Delta x) \cdot (\Delta t/\Delta x)}{1 + (2\nu/\Delta x) \cdot (\Delta t/\Delta x)}\,; \quad C_2 = \frac{u \cdot (\Delta t/\Delta x)}{1 + (2\nu/\Delta x) \cdot (\Delta t/\Delta x)}$$

If $u \leq 2\nu/\Delta x$, then $C_2 \leq C_1$, and $|e^{b}|_{max}^2 = C_1^2 \leq 1$ is satisfied for *any values* of $\Delta t/\Delta x$. If $u > 2\nu/\Delta x$, then $C_2 > C_1$, and $|e^{b}|_{max}^2 = C_2^2 \leq 1$ yields

$$\Delta t/\Delta x \leq 1/[u - (2\nu/\Delta x)]$$

This convergence criterion has been checked for the values of $\Delta t/\Delta x$ and $\nu/\Delta x$, indicated by crosses in Fig. 1 (where $A = B = 1/2$), and checked perfectly with difference calculations carried out in the N.Y.U. thesis of L. Goldberg, divergence of iterations resulting in increasing oscillations. Also, the numerical shock curve advanced in agreement with the analytical curve, although for approx. $\Delta t/\Delta x > 2$, gradually changes of shape occur—an indication that the solution of the difference equation gradually deviates from that of the differential equation with increasing mesh width.

Analogous considerations have been carried out for the system of the three viscous equations of motion. For this purpose, new concepts have to be introduced which will be explained elsewhere.

* Investigation sponsored by ONR and ORS.

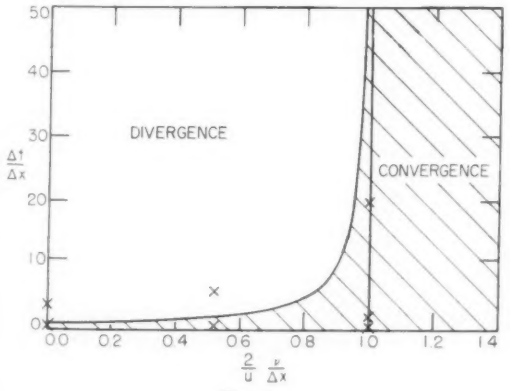

FIG. 1.

Approximate Trajectories of High-Drag Bodies

George S. Campbell
Research Engineer, Hughes Aircraft Company, Culver City, Calif.
September 10, 1956

Introduction

This note presents charts for the rapid determination of approximate trajectories of high-drag bodies. Such a prob-

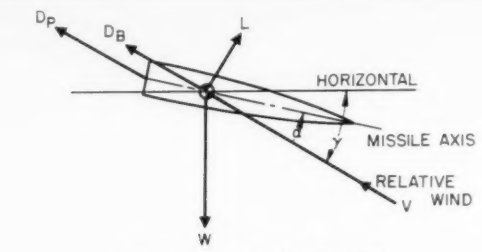

FIG. 1. Forces acting on body.

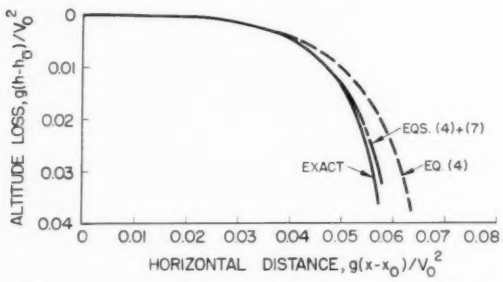

FIG. 2. Comparison of exact and approximate trajectories for $50g$ initial deceleration, $\gamma_0 = 0$.

lem might arise, for example, in the retrieval of a missile by parachute deployment. The forces acting on such a vehicle are illustrated in Fig. 1, in which D_P represents the drag of a parachute or similar device. Within the accuracy of this analysis, the actual source of the drag is immaterial, and so only the total drag D is considered. Furthermore, the lift acting on the missile is neglected.

ANALYSIS

The tangential and normal force equations are

$$m\dot{V} = -D + W \sin \gamma \tag{1a}$$

$$mV\dot{\gamma} = W \cos \gamma \tag{1b}$$

Although these equations are relatively simple, it is necessary to make further assumptions before a closed-form solution may be obtained. A useful simplification results if $W \sin \gamma$ is replaced by W, which is the asymptotic value of the weight term. The physical justification of this approximation depends on the assumption of a high-drag body—i.e., $D \gg W$, initially. The approximate solution obtained in this manner may be regarded as the first step of an iterative procedure.

First Approximation

The differential equations for the first approximation to the solution of Eq. (1) are

$$\dot{V}_1 + KV_1^2 = g \tag{2a}$$

$$V_1\dot{\gamma}_1 = g \cos \gamma_1 \tag{2b}$$

Time histories of velocity and flight-path angle are obtained by a simple integration of Eq. (2) so that

$$\left.\begin{aligned} V_1/V_0 &= B \operatorname{ctnh} u \\ \gamma_1 &= 2 \tan^{-1}(C\xi) - (\pi/2) \end{aligned}\right\} \tag{3}$$

The variables u and ξ are related to the time t by the equations

$$u = A + BKV_0t$$

$$\xi = \cosh u$$

and the nondimensional constants A, B, and C depend on the initial deceleration and flight-path angle:

$$A = \tanh^{-1} B$$

$$B = 1/\sqrt{1 - (\dot{V}_0/g)}$$

$$C = \tan[(\gamma_0/2) + (\pi/4)]/\cosh A$$

Altitude loss and horizontal distance from an initial position are obtained by integrating the proper components of the resultant velocity; therefore,

$$\left.\begin{aligned} &K(h_1 - h_0) = \\ &\frac{1}{(C^2+1)}\left[\frac{(C^2-1)}{2}\log\frac{\xi^2-1}{\xi_0^2-1} + \log\frac{(C\xi)^2+1}{(C\xi_0)^2+1}\right] \\ &K(x - x_0) = [2/(C^2+1)] \times \\ &[\tan^{-1}(C\xi) - \tan^{-1}(C\xi_0) - C\operatorname{ctnh}^{-1}\xi + C\operatorname{ctnh}^{-1}\xi_0] \end{aligned}\right\} \tag{4}$$

Second Approximation

In many cases, the trajectories calculated from Eqs. (3) and (4) may be of sufficient accuracy for engineering use. However, if more accurate results are required, the following correction procedure may be used. The main source of error in the first approximation is the use of a constant weight term in the drag equation, which results in predicted velocities that are too large. The difference, ΔV, between the true velocity and the first approximation may be obtained from the linear differential equation

$$(d/dt)(\Delta V) + 2KV_1(\Delta V) = g(\sin \gamma_1 - 1) \tag{5}$$

in which V_1 and γ_1 are given by Eq. (3). This relation is derived by subtracting Eq. (2a) from Eq. (1a) and linearizing the resultant expression. The solution of Eq. (5) is

$$\frac{\Delta V}{V_0} = \frac{B}{\sinh^2 u}\left[\frac{\sqrt{C^2+1}}{C^2}\log \frac{C^2 + \cosh^2 u + 2\sqrt{C^2+1}\cosh u \sinh u + (C^2+1)\sinh^2 u}{C^2 + \cosh^2 A + 2\sqrt{C^2+1}\cosh A \sinh A + (C^2+1)\sinh^2 A} - \frac{\sqrt{C^2+1}}{C^2}\log\frac{1 + C^2\cosh^2 u}{1 + C^2\cosh^2 A} - \frac{2}{C^2}\log\frac{\cosh u + \sinh u}{\cosh A + \sinh A}\right] \tag{6}$$

where the approximate value for B has been used:

$$B^2 \simeq g/KV_0^2$$

The increments in the horizontal and vertical positions due to the velocity correction, ΔV, are readily calculated by graphical integration:

$$\left.\begin{aligned} \Delta h &= \int_0^t (\Delta V) \sin \gamma_1 \, dt \\ \Delta x &= \int_0^t (\Delta V) \cos \gamma_1 \, dt \end{aligned}\right\} \tag{7}$$

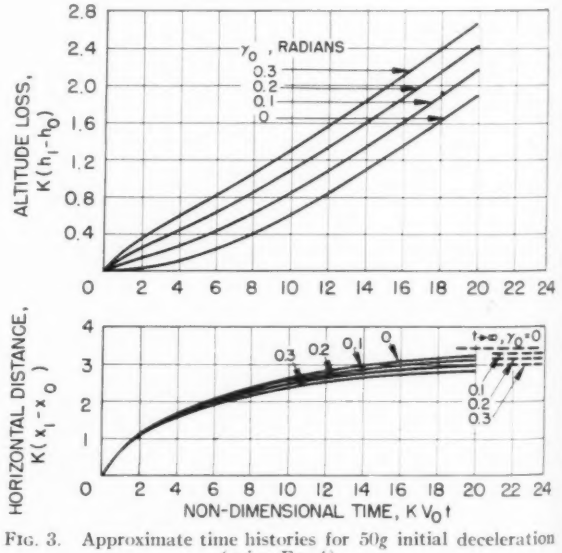

FIG. 3. Approximate time histories for $50g$ initial deceleration (using Eq. 4).

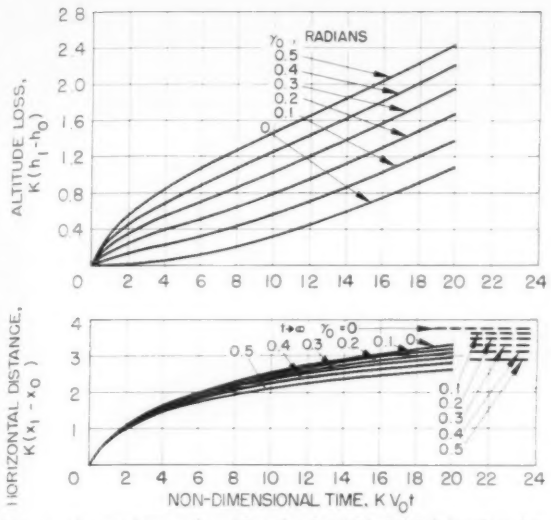

FIG. 4. Approximate time histories for 100g initial deceleration (using Eq. 4).

RESULTS

In Fig. 2, comparison is made between the approximate trajectories obtained from Eqs. (4) and (7) and an exact solution of Eq. (1) obtained by the Kutta-Runge method. The body has an initial deceleration of 50g and zero flight-path inclination. Use of the simplest approximation, Eq. (4), is justified when a position error of the order of 10 per cent can be tolerated. It is expected that the error introduced by using Eq. (4) might be considerably smaller than 10 per cent for larger values of the initial deceleration or nonzero (but positive) flight-path inclinations. Addition of the velocity correction term, Eq. (7), brings the approximate trajectory into much better agreement with the exact, step-by-step result.

In order to facilitate rapid estimation of the trajectory of a high-drag body, time histories are presented in Figs. 3 and 4 for 50 and 100g initial decelerations. The approximate equations [Eqs. (4)] were used for these calculations, and so the initial deceleration is related to the initial drag as follows:

$$\dot{V}_0/g = 1 - (KV_0^2/g)$$

$$K/g = \rho C_D S/2W$$

Variations in density or drag coefficient may, if necessary, be taken into account by allowing K to have a stepwise variation with time.

Discussion of the Influence of Confining Surfaces Upon the Boundary Layer in a Channel

Ralph Burton
Assistant Professor, University of Missouri, Columbia, Mo.
September 10, 1956

THE BOUNDARY LAYER in a narrow channel does not behave exactly like that on, say, an isolated airfoil. Interactions between the boundary layer, the free stream, and the confining walls of a channel are now well understood in the case of supersonic flow. However, the subsonic case, especially where applicable to the passages of turbomachines, seems to lie in a blind spot. The ideas presented below have been discussed with several other workers in the field of fluid mechanics and have been deemed by them to be of sufficient interest for presentation in this Forum.

Let us begin with the simple, divergent channel or diffuser—one of the basic systems of fluid mechanics. It is well known that diffusers are inefficient when the divergence angle is too great. In fact, it can be shown that, for a two-dimensional diffuser with large divergence angle, the efficiency can actually be improved by insertion of a plate along the center streamline (see Fig. 1). This improvement in efficiency results even though *more friction surface* has been added. The usual explanation of the influence of divergence angle on efficiency is well put in the following quotation: "As the angle of flare increases beyond the optimum value, however, the adverse pressure gradient associated with the deceleration of the fluid becomes big enough to cause a rapid thickening of the boundary layer and separation from the wall."*

Let us assume that the Reynolds Number is high and that the boundary layers are consequently thin. Under these conditions, the reduction of flare by the insertion of a plate does not in any way affect the pressure distribution along the original diffuser walls. The adverse pressure gradients are unchanged. Something other than the change of pressure distribution has altered or prevented separation.

Turning to another phenomenon, let us take note of the separation and reattachment near the nose of a thin-plate airfoil at small angles of attack. Free-streamline solutions of classical wake theory do not account for this reattachment. In discussing this, Prof. A. H. Shapiro suggested in conversation (1952) that the phenomenon is probably related to that of jet mixing. It

* Hunsaker and Rightmire, *Engineering Applications of Fluid Mechanics*, p. 349; McGraw-Hill Book Company, Inc., New York, 1947.

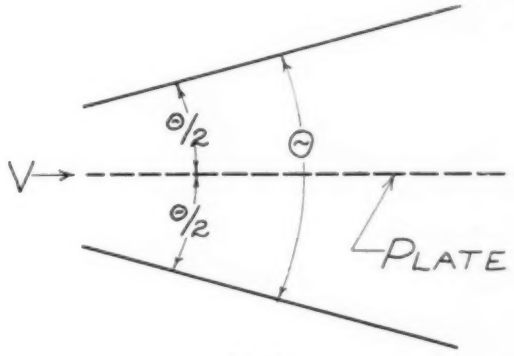

FIG. 1.

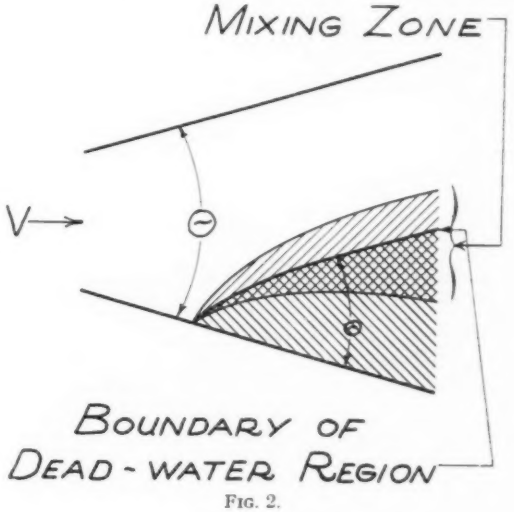

FIG. 2.

is well known that, for two-dimensional, turbulent mixing between a jet and a dead region, the mixing zone grows linearly with a divergence angle of about 15° (this should be taken only as a rule of thumb). Now, if we calculate the free-streamline pattern for a plate airfoil with separation, we find the dead-water region to be roughly wedge shaped with its edge at the point of separation. If the wedge angle is greater than the angle of turbulent mixing, separation will be unaffected. If it is less, presumably the mixing will knit the free-stream flow back to the surface. An analytical solution, estimating the losses on an airfoil with frictionless surface but with this kind of separation and reattachment, would be most welcome. This would, undoubtedly, be difficult to obtain. However, in the case of the channel, even the crudest of investigations yields much useful information.

Taking account of the above-mentioned phenomenon of reattachment, let us return again to the diffuser. Let us say that separation has taken place and that the dead-water region satisfies the condition of constant pressure. Some distance past the separation point the streamlines will have become parallel. The angle bounding the dead region will be the angle of divergence of the diffuser (see Fig. 2).

If this angle is greater than the angle of mixing, reattachment will not take place. If it is less, separation will not take place. Whether or not this last conclusion is true, the angle of separation undoubtedly influences the behavior of the boundary layer; and, where separation has not taken place, the *virtual angle of separation* offers to be a factor of considerable influence. By *virtual angle of separation* is meant the angle at which the separated flow would leave the surface *if* separation took place at a given point. Any explanation of the behavior of the boundary layer must be in terms of factors within the boundary layer or in the immediately adjacent portions of the free stream. Confining surfaces some distance away cannot in themselves influence the boundary layer. They do, however, determine the virtual angle of separation which is a factor within the boundary layer itself. This angle is a point function, variable along the surface. Its influence should be of importance even after actual separation has occurred, especially when the dimensions of the separated region are small.

From these observations it appears that, in any study of the boundary layer in a channel, one should take cognizance of this angle as well as the surface velocity distribution and aspect ratio (this last factor influences secondary flow). Conversely, if two surfaces have the same pattern of velocity variation and of virtual-separation-angle variation, one would expect similar boundary-layer behavior, irrespective of the actual geometry. This last statement can be taken as a specification of the conditions for quasi-similitude. Once it becomes established that this angle does truly account for the influence of confining walls, it should be possible to generalize experimental measurements from a few typical channels to a variety of others. For example, it should be possible to predict, confidently, the behavior of a mixed-flow impeller from studies of a stationary channel modeled upon the factors mentioned above.

Two reservations should enter into the evaluation of the ideas presented above. First, the validity of virtual separation in explaining boundary-layer behavior need not necessarily depend upon the mechanisms proposed here. Secondly, when one attempts to compute the angle of separation, he may find, say, that at the separation point it is initially zero, gradually growing to a finite value. In an effort to bypass such local effects, the author has had some success in restricting the analysis to overall mass movements of the fluid rather than to local conditions. For example, in dealing with the velocity recovery on the surface of a vane in a turning cascade, the width of the separated zone in the plane of trailing edges and the distance of this line from the separation point were used to compute the angle. This procedure reduces the virtual-separation concept to nothing more than a yardstick for comparison purposes. As such, however, it still promises to be useful in the study of narrow turbomachine passages.

One cannot but feel that there is some more exact concept lying behind that which has been discussed here. Now that the need has been made apparent it may soon be forthcoming.

Location of Mach Discs and Diamonds in Supersonic Air Jets†

Donald E. Wilcox,* Alexander Weir, Jr.,** J. A. Nicholls,*** and Roger Dunlap****

Aircraft Propulsion Laboratory, University of Michigan, Ann Arbor, Mich.

September 17, 1956

Symbols

A_t = throat area of nozzle
A_e = exit area of nozzle
D_d = diameter of Mach disc
D_e = exit diameter of nozzle
Ma_e = exit Mach Number computed from Eq. (1)
P_a = atmospheric pressure
P_e = exhaust pressure
P_0 = upstream stagnation pressure
x = distance from nozzle exit to oblique shock-wave intersection point or distance from nozzle exit to Mach disc location
γ = ratio of heat capacities, assumed to be 1.4

Introduction

The complicated shock and rarefaction patterns existing in supersonic jets have long been of fundamental interest in the study of fluid dynamics. It is well known that an overexpanded nozzle (exit pressure less than receiver pressure) leads to oblique shock waves at the exit of the nozzle which intersect and give the familiar "diamond" pattern. If the degree of overexpansion is great enough, this pattern is modified so as to terminate the oblique shocks with a normal shock—or the so-called Mach disc configuration. On the other hand, a sufficiently underexpanded nozzle will lead to a similar Mach disc because of the focusing of compression waves from the jet boundary. At extreme degrees of underexpansion, the oblique shocks and their reflection from the Mach disc are markedly curved, and the configuration is appropriately termed a shock bottle.

Numerous investigators[1–4] have devoted effort to experimental and analytical studies of these phenomena. However, most of these investigations have been restricted to sonic nozzles and relatively low-pressure ratios (stagnation pressure to receiver pressure). Kelber and Jarvis[5] have utilized the method of characteristics to analyze the flow from a nozzle operating

† This research was sponsored by the Office of Ordnance Research, U.S. Army. Discussions of this experimental program with Profs. T. C. Adamson, R. B. Morrison, and H. E. Bailey of the Aeronautical Engineering Department are gratefully acknowledged.

* Research Assistant, Engineering Research Institute.
** Lecturer in Chemical Engineering and Associate Research Engineer, Engineering Research Institute.
*** Instructor in Aeronautical Engineering.
**** Assistant in Research, Engineering Research Institute

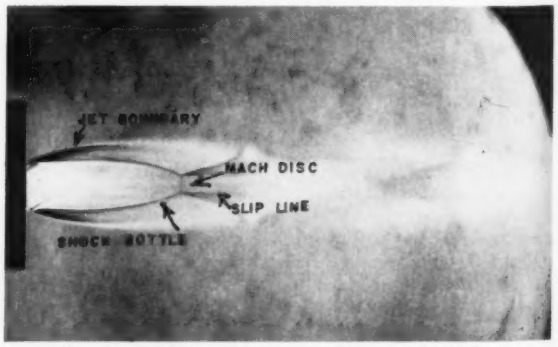

Fig. 1. Schlieren photograph of supersonic air jet.

under extremely high pressures. Such a technique fails to indicate the presence of a Mach disc so that the phenomenological considerations for locating the disc are in question. Weir[6, 7] has reported information on the variation of disc location with pressure ratio for airflow through two-dimensional slits.

The influential parameters in determining the Mach disc location in a supersonic jet would appear to be the ratio of driving pressure to receiver pressure, the nozzle exit Mach Number, and the nozzle divergence angle. Information of this type is meager and limited in the range of variation. Accordingly, the initial portion of this research contract was devoted to a systematic experimental investigation of the effect of these variables. These results have been used as an aid to the theoretical study which is still in progress. This paper is devoted solely to the experimental results.

Experimental Apparatus and Procedure

Air was obtained from a 2,000-psia storage system with a total volume of 170 cu.ft. The air used thus had a very low absolute humidity owing to the high storage pressure. The air leaving the storage system passed through two dome-control valves in parallel, through the test nozzle, and then discharged into the atmosphere. The pressure upstream of the test nozzle was maintained constant by the dome-control valves, which were operated by adjusting nitrogen pressure above the diaphragm. Any pressure desired from 0 to 600 psig could be maintained by this system.

In order to investigate quantitatively the influence of nozzle geometry, four axially symmetric nozzles with rounded inlets, throat diameters of 0.250 in., and conical diverging angles of 10°, 15°, 20°, and 30° (total angle) were designed to be connected to the 1-in. pipe downstream of the control valves. The Mach Number at the exit was 3.5 in all cases, as computed by the isentropic flow relation

$$\frac{A_t}{A_e} = Ma_e\left[\frac{(\gamma+1)/2}{1+[(\gamma-1)/2]\,Ma_e^2}\right]^{(\gamma+1)/2(\gamma-1)} \qquad (1)$$

Schlieren photographs were obtained of the flow issuing from these nozzles at upstream stagnation pressures from 55 to 615 psia in 50-psi increments. A conventional schlieren system with a 6-in. field of view was used, the pictures being recorded on 8- by 10-in. film.

In order to investigate the influence of the exit Mach Number on the flow, the above-mentioned nozzles were modified. After each series of runs at one Mach Number, the nozzle was shortened until the exit diameter agreed with that given by the area ratio required for the next Mach Number. The Mach Numbers tested were 3.5, 3.0, 2.5, and 2.0.

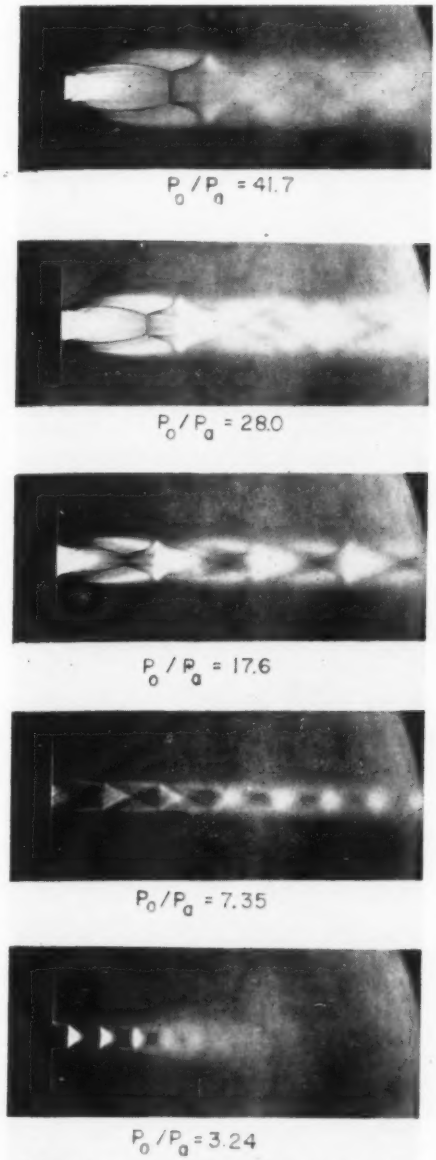

Fig. 2. Effect of pressure ratio on flow pattern. Exit Mach Number = 2.0. Divergence angle = 10°.

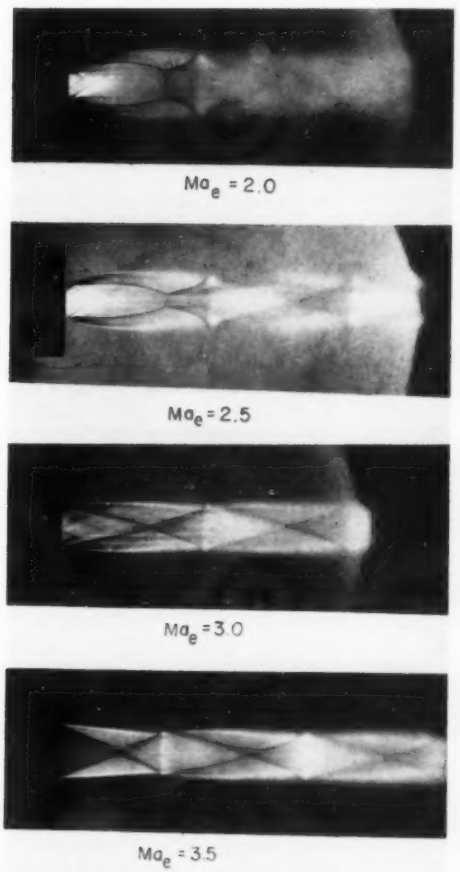

Fig. 3. Effect of exit Mach Number on flow pattern. Pressure ratio = 41.7. Divergence angle = 10°.

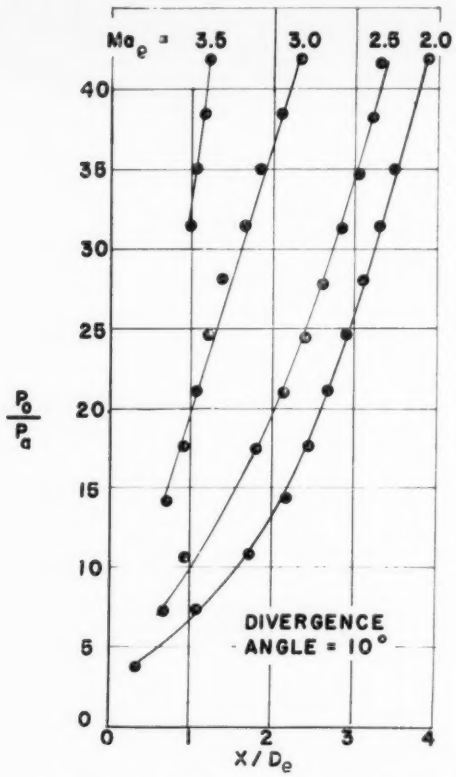

FIG. 4. Variation of shock-wave intersection location with stagnation pressure—10° nozzle.

RESULTS

A schlieren photograph of the flow issuing from a supersonic nozzle is presented in Fig. 1. The jet boundaries as indicated by the optical technique and the curved shock waves extending from the nozzle exit to the normal shock wave are clearly visible. Less visible are the weak oblique shock waves in the region between the nozzle exit and the Mach disc which are due to imperfections in the nozzle.

In Fig. 2, a series of schlieren photographs showing the influence of the pressure ratio on the flow pattern in the axially symmetric jet is presented. Fig. 3 presents four photographs of the flow issuing from nozzles with the same divergence angle (10°) and pressure ratio ($P_0/P_a = 42$) but at exit Mach Numbers of 2, 2.5, 3, and 3.5.

Measurements of the distance of the Mach disc or shock-wave intersection point from the nozzle exit (x) were made from the schlieren negatives. Fig. 4 presents the results of these measurements in graphic form for the 10° nozzle. The plots for all the angles are very similar. The ratio (x/D_e) is plotted versus pressure ratio (P_0/P_a) for the 10° divergent angle nozzle in Fig. 4, with exit Mach Number as a parameter.

DISCUSSION

As mentioned, the exit Mach Numbers presented were computed assuming isentropic flow. It is realized that there is some departure from isentropy in the nozzle, as evidenced by the schlieren photographs.

Figure 4 indicates that the exit Mach Number, in addition to the pressure ratio, is a most influential variable in determining the Mach diamond or disc location. The effect of the divergence angle of the nozzle is relatively small over most of the pressure range.

REFERENCES

[1] Ladenburg, R., Van Voorhis, C. C., and Winckler, J., *Interferometric Studies of Faster than Sound Phenomena, Part II. Analysis of Supersonic Air Jet*, Physical Review, Vol. 76, July–September, 1949.

[2] Pack, D. C., *A Note on Prandtl's Formula for the Wave Length of a Supersonic Gas Jet*, Quart. J. Mech. and Appl. Math., Vol. 3, 4, 1950–51.

[3] Hartmann, J., and Lazarus, F., *The Air Jet with a Velocity Exceeding that of Sound*, London Philosophical Magazine, Seventh Series, Vol. 31, January–June, 1941.

[4] Kawamura, R., *Shock Waves in Axially Symmetric Supersonic Jets*, NACA Translation, Tokyo University, Institute of Science and Technology, Report v. 6, No. 3, June, 1952.

[5] Kelber, C. N., and Jarvis, S., Jr., *An Analysis of the Gas Flow from a Very High Pressure Nozzle*, Pitman-Dunn Laboratories, Frankford Arsenal Report No. R-1107, ASTIA AD 9477, December, 1952.

[6] Weir, A., Jr., *Progress Report on Thesis*, University of Michigan, Chemical and Metallurgical Engineering Department, December, 1952.

[7] Weir, A., Jr., Ph.D. Thesis, *Two and Three-Dimensional Flow of Air Through Square-Edged Sonic Orifices*, University of Michigan, February, 1954.

Effect of Thermal Resistance of Joints Upon Thermal Stresses

B. E. Gatewood
Research Coordinator and Research Professor, Air Force Institute of Technology, Wright-Patterson AFB, Ohio

September 24, 1956

RECENTLY, Griffith and Miltonberger[1] have considered the effect of the thermal resistance of a skin-stringer joint upon the thermal stresses produced by a constant heat source on the skin [Fig. 1(b)]. By dividing the cross section of the joint [Fig. 1(b)] into 15 sections and using an electronic differential analyzer, they calculated the thermal stresses for several values of the parameters for heat transfer to the skin, heat transfer across the joint, and skin geometry. Also, Schuh[2] has solved numerically the equivalent problem [Fig. 1(a)] for no joint thermal resistance and has constructed curves for the maximum stresses in the web against the skin heat-transfer parameter $q = L(h/kh_s)^{1/2}$, where h is skin heat-transfer coefficient (B.t.u./hour ft.^{2} F.), k is coefficient of thermal conductivity (B.t.u./hour ft. F.), and L and h_s are defined in Fig. 1(a).

The results given in references 1 and 2 indicate that it may be possible to obtain an approximate analytical solution for the thermal stresses in the multiweb beam or skin-stringer element

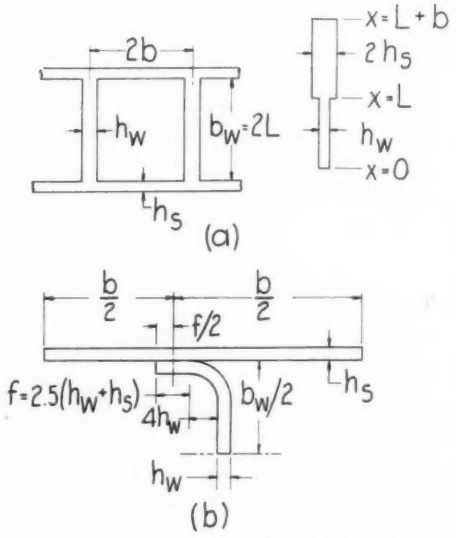

FIG. 1. Structural element for multiweb beam.

(Fig. 1) for any value of the parameter q and for any value of the joint thermal resistance.[3] If the skin is assumed to have a uniform temperature from a constant heat source (this neglects the effect of the web on the skin but is approximately correct for the skin[2] heavier than the web), then the skin temperature is

$$T_s/T_{as} = 1 - e^{-B_h t}, \qquad B_h = h/\rho_s h_s (c_p)_s \tag{1}$$

where t is time, ρ_s is skin density, $(c_p)_s$ is specific heat, and T_{as} is adiabatic skin temperature.

From Carslaw and Jaeger,[4] the heat-conduction equation for the stringer or web is

$$\partial T/\partial t = (k/\rho c_p)\,(\partial^2 T/\partial x^2) \tag{2}$$

If there is no heat loss at $x = 0$ and if h_j is the thermal conductance across the joint from the skin to the stringer, then the initial and boundary conditions on the stringer or web are

$$\left.\begin{aligned} T = 0 \quad &\text{at} \quad t = 0, \qquad \partial T/\partial x = 0 \quad \text{at} \quad x = 0 \\ \partial T/\partial x = (h_j/k_b)\,[T_{as}(1 - e^{-B_h t}) - T] \quad &\text{at} \quad x = L \end{aligned}\right\} \tag{3}$$

The solution of Eq. (2) with the conditions of Eq. (3) is

$$\left.\begin{aligned} T/T_{as} &= 1 - C_1 \exp(-q^2 W t/t_1)\cos(qx/L) + \sum_{n=0}^{\infty} a_n \exp(-p_n^2 W t/t_1)\cos(p_n x/L) \\ q^2 &= h\rho_b (c_p)_b L^2/k_b \rho_s (c_p)_s h_s, \qquad W = k_b t_1/\rho_b (c_p)_b L^2, \qquad m_j = h_j L/k_b \\ C_1 &= m_j/(m_j \cos q - q \sin q), \qquad p_n = m_j \cot p_n \\ a_n &= -2q^2 \sin p_n/[(q^2 - p_n^2)\,(p_n + \sin p_n \cos p_n)] \end{aligned}\right\} \tag{4}$$

If there is no resistance at the joint or if the skin and web are integral structure, then $m_j = \infty$, and the expressions simplify to

$$\left.\begin{aligned} C_1 &= \sec q, \qquad p_r = (2n+1)\pi/2 \\ a_n &= 2(-1)^n q^2/[p_n(p_n^2 - q^2)] \end{aligned}\right\} \tag{5}$$

For the case of no bowing of the structure (symmetrical temperature distribution or external bending restraint) the thermal stress in the web is[5]

$$f = -\alpha E T(x) + (1/A)\int_0^L \alpha E T(x) b(x)\,dx \tag{6}$$

where $b(x)$ is the width of the web or stringer and A is the total area of the skin and web. Fig. 2 shows the maximum thermal stresses in the web ($x = 0$) against the parameter q for several values of the joint thermal conductance parameter m_j. The curves are drawn for a skin and web combination of the same material with $\phi = A_s/A_w = 5.0$, where A_s is the skin area and A_w is the web area.

It should be noted that Fig. 2 can be drawn for different values of the parameter ϕ. Schuh's curves[2] for $m_j = \infty$ show some variation with ϕ and also a small variation with the ratio h_s/h_w. The assumption used to obtain Eq. (1) loses this latter ratio h_s/h_w. However, for $2h_s/h_w$ varying from 1 to 7.5, the curve for $m_j = \infty$ in Fig. 2 varies at most by 15 per cent from Schuh's curves, with practically no variation for $q > 5$. Fig. 2 also shows that the thermal resistance has little effect on the maximum stresses for $q > 5$ so the Schuh's results for $m_j = \infty$ could be used directly.

The calculations in reference 1 were made for three values of the parameter q (approximately 1.55, 5.0, 15.5), several values of m_j including $m_j = 0$ and ∞, three values of ϕ in the range of 3 to 12, and $h_s/h_w = 2.0$. Note that the parameter ϕ for the case of reference 2 [see Fig. 1(b)] is different at $m_j = 0$ and $m_j = \infty$ (the flat flange of the web should be included in the web area for $m_j = 0$ but not for $m_j = \infty$). If the proper ϕ is used and if the web length L is taken to include the curved portion of the web (but not the length f) in Fig. 1(b), then the results for $m_j = \infty$ in reference 1 check Schuh's results.[2] The results[1] for $m_j = 0$ check the value $\phi/(1 + \phi)$, and m_j shows little effect on the maximum stress for the cases of $q = 5.0$ and 15.5. For $q = 1.55$, the variation of the stress with m_j is similar to Fig. 2. For one case in which ϕ is approximately 5.0 at $m_j = 0$ and 8.0 at $m_j = \infty$, the results check Fig. 2 for $0 \le m_j \le 1.0$ but change to the $\phi = 8$ curve at $m_j = \infty$.

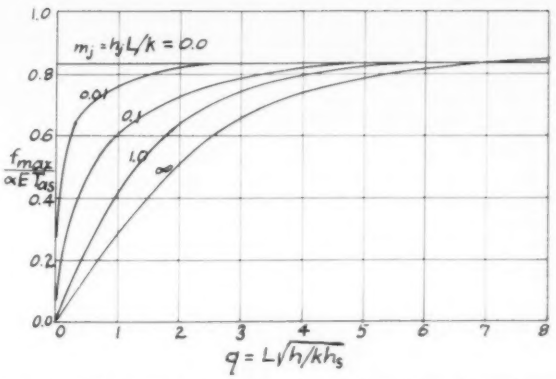

FIG. 2. Maximum web stresses for various joint thermal resistances ($\phi = 5$).

It should be noted that in many cases the variation in the maximum stress produced by the ϕ and h_s/h_w parameters may be no larger than the variation produced by the m_j parameter. From references 6 and 7, the range of h_j for 75ST-6 plates face to face is approximately: (1) 50–100 B.t.u./hour ft.^{2} F. for asbestos or cement bond, (2) 225–500 for zinc chromate primer or as received or as riveted, (3) 500–1,300 for finished surface, and (4) 700–1,300 for aluminum foil sandwich.

REFERENCES

[1] Griffith, G. E., and Miltonberger, Georgine H., *Some Effects of Joint Conductivity on the Temperatures and Thermal Stresses in Aerodynamically Heated Skin-Stiffener Combinations*, NACA TN 3699, June, 1956.

[2] Schuh, H., *Transient Temperature Distributions and Thermal Stresses in a Skin-Shear Web Configuration at High-Speed Flight for a Wide Range of Parameters*, Journal of the Aeronautical Sciences, Vol. 22, No. 12, pp. 829–836, December, 1955.

[3] Gatewood, B. E., *Effect of Thermal Resistance of Joints upon Thermal Stresses*, USAF Institute of Technology Technical Report 56–6, ASTIA No. AD-106014, May, 1956.

[4] Carslaw, H. S., and Jaeger, J. C., *Conduction of Heat in Solids*; Oxford University Press, 1947.

[5] Gatewood, B. E., *Approximate Procedures for Transient Thermal Stresses in Missile Structures*, Presented at the 24th Annual Meeting, Institute of the Aeronautical Sciences, January, 1956, Preprint No. 578.

[6] Barzelay, M. E., Tong, K. N., and Hollo, George, *Thermal Conductance of Contacts in Aircraft Joints*, NACA TN 3167, March, 1954.

[7] Barzelay, M. E., Tong, K. N., and Hollo, George, Effect of Pressure on Thermal Conductance of Contact Joints, NACA TN 3295, May, 1955.

Total Creep Under Varying Loads*

William Prager
Chairman, Physical Sciences Council, Brown University, Providence, R.I.

October 3, 1956

INTRODUCTION

IN A SHELL or guided missile that is designed for a single use, the development of appreciable creep deformations during the useful life need not impair proper functioning. In comparison with such creep strains of the order of several per cent, elastic strains may often be neglected. The analysis may then be based on a relation between the stress and the rate of creep strain. When the load intensity varies with time, an estimate of the total creep developing during the lifetime of the structure can be obtained as follows. Dividing the lifetime into a sufficiently large number of short periods, determine the creep defor-

* The results presented in this paper were obtained in the course of research sponsored by the Ballistic Research Laboratories of Aberdeen Proving Ground under Contract DA-19-020-ORD-798.

mation that would occur during each of these periods if the loads were maintained at their mean values for the considered period. To find the desired total creep deformation, superimpose the creep deformations obtained for the various periods. Since the relation between stress and rate of creep strain is nonlinear, this process, as a rule, requires the solution of as many nonlinear boundary-value problems as there are periods to be considered. It is the purpose of the present note to show that under certain conditions only a single nonlinear boundary-value problem needs to be solved.

Relation Between Stress and Rate of Creep Strain

As Hoff[1] has pointed out, the present writer's discussion of the mathematical structure of stress-strain laws in the work-hardening range[2] is readily applied to the relations between stress and rate of creep strain.

With reference to rectangular Cartesian coordinates x_i (i = 1, 2, 3), let σ_{ij} denote the stress tensor and ϵ_{ij} the strain-rate tensor. Since the material is treated as incompressible,

$$\epsilon_{kk} = 0 \tag{1}$$

where the repeated letter subscript indicates summation in the customary manner.

The stress deviation s_{ij} is defined by

$$s_{ij} = \sigma_{ij} - (1/3)\sigma_{kk}\delta_{ij} \tag{2}$$

where δ_{ij} is the Kronecker delta. A complete set of independent invariants of the stress deviation is given by

$$\left.\begin{aligned} J_1 &= s_{kk} \\ J_2 &= (1/2)s_{kj}s_{jk} \\ J_3 &= (1/3)s_{ij}s_{jk}s_{ki} \end{aligned}\right\} \tag{3}$$

The first of these vanishes by the definition of s_{ij}. Any invariant of the stress deviation can therefore be written as a function of J_2 and J_3. The deviation t_{ij} of the square of the stress deviation is given by

$$t_{ij} = s_{ik}s_{kj} - (2/3)J_2\delta_{ij} \tag{4}$$

For simple tension in the x_1-direction, the relation between the tensile stress σ_{11} and the corresponding creep rate ϵ_{11} is generally given in the form

$$\epsilon_{11} = c\sigma_{11}^{\,n} \tag{5}$$

where c and n are constants. For an incompressible isotropic material, the most general relation between the tensors of stress and creep strain that reduces to Eq. (5) in simple tension has the form†

$$\epsilon_{ij} = f(J_2, J_3)[g(J_2, J_3)s_{ij} + h(J_2, J_3)t_{ij}] \tag{6}$$

In Eq. (6) each of the functions f, g, and h is homogeneous in the components of the stress deviation, the orders of the products fg and fh being $n - 1$ and $n - 2$, respectively. Note that the creep laws suggested by Odqvist[3] and Bailey[4] are special cases of Eq. (6).

Boundary-Value Problem

Consider a body that consists of a material with the creep behavior defined by Eq. (6). Denote the volume occupied by the body by V and let its surface S consist of the parts S_V and S_T.

Starting with the stress-free, undeformed state, let the velocities v_i of the points of S_V be required to vanish at all times, while the points of S_T are subjected to given surface tractions of the form $T_i(x, t) = T_i^*(x)\phi(t)$, where x stands for the coordinates of a generic point and t denotes the time.

We will show that the stresses, velocities, and displacements throughout the body then have the forms

$$\sigma_{ij}(x, t) = \sigma_{ij}^*(x)\phi(t) \tag{7}$$

$$v_i(x, t) = v_i^*(x)\psi(t) \tag{8}$$

$$u_i(x, t) = u_i^*(x)\chi(t) \tag{9}$$

† For a proof of this statement see reference 2.

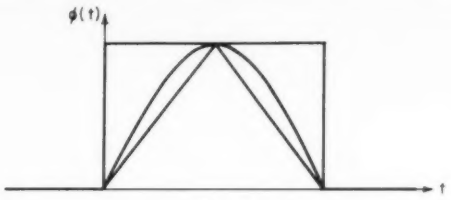

Fig. 1.

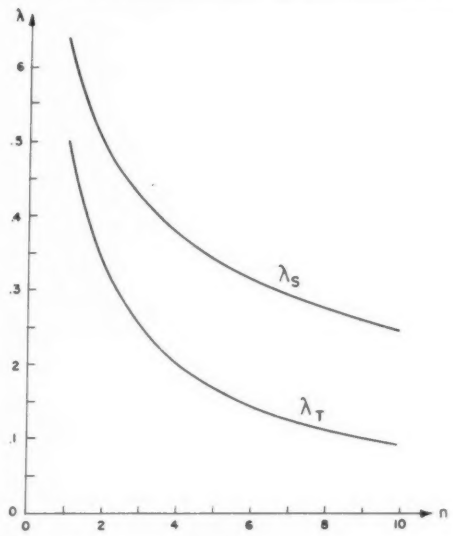

Fig. 2.

where $$\psi = \phi^n \quad \text{and} \quad \chi = \int_0^t \psi\, dt \tag{10}$$

To prove this, we need the fundamental equations of the problem. These are (a) the equation of equilibrium, $\sigma_{ij,j} = 0$, where the comma subscript followed by the subscript j denotes differentiation with respect to x_j; (b) the definition of the strain rate in terms of the velocity, $\epsilon_{ij} = (v_{i,j} + v_{j,i})/2$; (c) the condition of incompressibility, Eq. (2); (d) the relation, Eq. (6), between strain rate and stress; (e) the boundary condition on stress, $\sigma_{ij}n_j = T_i$ on S_T, where n_j is the unit vector along the exterior normal of S_T; and (f) the boundary condition on velocity, $v_i = 0$ on S_V.

With the exception of the stress-strain law of Eq. (6), each of these fundamental equations involves, in a linear and homogeneous manner, either only the dynamic variables σ_{ij} and T_i or only the kinematic variables v_i and ϵ_{ij}. Accordingly, the functions $\phi(t)$ and $\psi(t)$ will drop out when Eqs. (7) and (8) are substituted into these equations. The stress-strain law of Eq. (6), on the other hand, is linear in the components of the strain rate but homogeneous of the order n in the components of the stress. This law therefore furnishes the first relation of Eq. (10) between ϕ and ψ. The second relation of Eq. (10) then follows from Eqs. (8) and (9) and the fact that $v_i = \partial u_i/\partial t$.

Analyzing stresses and strains in incompressible, work-hardening plastic solids, Ilyushin[5] pointed out that, under stress boundary conditions, the proportionality between stresses and loads, familiar from linear elastic solids, subsisted when the secant shear modulus was proportional to a power of the octahedral shearing stress—i.e., a power of J_2. Aside from the substitution of "rate of creep strain" for "strain," the result established above is a natural extension of Ilyushin's result.

To illustrate the effect of the exponent n in the stress-strain law of Eq. (5) for some typical variations of the load intensity with time, consider the rectangular, sinusoidal, and triangular

pulses shown in Fig. 1. These pulses have the same duration and the same peak value. The total creep deformations produced by the sinusoidal or triangular pulse can be obtained by applying correction factors λ_S or λ_T to the total creep deformation produced by the rectangular pulse. Fig. 2 shows these correction factors versus the exponent n in the stress-strain law of Eq. (5). For $n = 1$, these correction factors are the ratios between the average load intensities of the sinusoidal or triangular pulses and that of the rectangular pulse. The sharp decrease of the correction factors with increasing n is due to the fact that the relative contribution of loads below the peak intensity to the total creep deformation is small for large values of n.

References

[1] Hoff, N. J., *Approximate Analysis of Structures in the Presence of Moderately Large Creep Deformations*, Quart. Appl. Math., Vol. 12, pp. 49–55, 1954.

[2] Prager, W., *Strain-Hardening Under Combined Stresses*, J. Appl. Phys., Vol. 16, pp. 837–840, 1945; see also Handelman, G. H., Lin, C. C., and Prager, W., *On the Mechanical Behavior of Metals in the Strain-Hardening Range*, Quart. Appl. Math., Vol. 4, pp. 397–407, 1947.

[3] Odqvist, F. K. G., *Creep Stresses in a Rotating Disc*, Proc. 4th International Congress of Applied Mechanics, Cambridge, England, 1934, pp. 228, 229.

[4] Bailey, R. W., *The Utilization of Creep Test Data in Engineering Design*, J. Institution of Mechanical Engineers, Vol. 131, pp. 248–269, 1935.

[5] Ilyushin, A. A., *The Theory of Small Elastic-Plastic Deformations* (Russian with English summary), Prikladnaia Matematika i Mekhanika, Vol. 9, pp. 207–218, 1945.

Second Approximation to the Laminar Boundary-Layer Flow Over a Flat Plate†

Isao Imai*

Visiting Research Professor, Institute for Fluid Dynamics and Applied Mathematics, University of Maryland, College Park, Md.

October 8, 1956

IT IS WELL KNOWN that the boundary-layer theory is the first approximation of the asymptotic solution of the Navier-Stokes differential equations for large Reynolds Numbers. Alden[1] was the first to consider the second approximation for the case of a semi-infinite flat plate—i.e., the Blasius flow. He obtained the second approximation to the stream function and discussed the pressure and velocity distributions as well as the local skin friction on the plate. The second-order correction to the local skin friction turned out to be proportional to $x^{-3/2}$, x being the distance from the leading edge, so that the total drag could not be calculated by integration of the local skin friction. Kuo[2] has overcome this difficulty by use of the Lighthill technique. Actually, he considered a more difficult problem of a finite flat plate instead of a semi-infinite plate. However, it should be noted that Kuo's second approximation is lower in degree of approximation than Alden's because the basic equations for his second approximation are nothing other than the usual boundary-layer equations; the difference from the first approximation lies only in adopting the pressure distribution as calculated from the displacement thickness of the boundary layer. Alden's equations for the second approximation is, of course, different from the usual boundary-layer equations.

Unfortunately, Alden's result contains the serious defect that the vorticity tends to zero as a negative power of the distance from the plate, although it should decay *exponentially*. This latter requirement can easily be inferred on the basis of the Oseen equations, which are certainly valid outside the boundary layer.

In this paper, a second approximation to the Blasius flow which is free from the above-mentioned difficulty will be given. Also, the total skin friction acting on the portion of the plate of length x from the leading edge is calculated by use of the theorem of momentum, thus avoiding the difficulty of nonintegrable singularity at the leading edge. The procedure employed is similar to that employed in the investigation of the asymptotic behavior of viscous fluid flow past a finite body.[3]

Recently, Bell[4] raised a question about the validity of Alden's scheme of solution of the Navier-Stokes equations in terms of an expansion in inverse powers of the local Reynolds Number, which has been suggested by von Kármán.[5] Bell concluded that Alden's scheme could not lead to a solution because at the fourth approximation it unavoidably violates the condition at the outer edge of the boundary layer. The author believes that this difficulty is intimately related to the above-mentioned slow decay of vorticity as a function of the distance from the plate in Alden's solution. Also, it is believed that the original von Kármán scheme of successive approximation can be successfully followed if appropriate consideration is given to the behavior of vorticity distribution in the boundary layer as shown below.

Let a viscous incompressible fluid of kinematic viscosity ν be flowing with velocity U in the positive direction of the x-axis and a semi-infinite flat plate be placed along the positive x-axis with its leading edge at the origin.

In terms of the parabolic coordinates ξ, η defined by

$$Uz/\nu = \zeta^2 \tag{1}$$

where

$$z = x + iy, \qquad \zeta = \xi + i\eta \tag{2}$$

the Navier-Stokes equations can be expressed in the form

$$\begin{aligned}(\xi^2 + \eta^2)\Delta\Delta\Psi - 4[\xi(\partial/\partial\xi) + \eta(\partial/\partial\eta) - 1]\Delta\Psi = \\ -(1/\nu)\{2[\xi(\partial\Psi/\partial\eta) - \eta(\partial\Psi/\partial\xi)]\Delta\Psi + \\ (\xi^2 + \eta^2)[(\partial\Psi/\partial\xi)(\partial/\partial\eta) - (\partial\Psi/\partial\eta)(\partial/\partial\xi)]\Delta\Psi\}\end{aligned} \tag{3}$$

where $\Delta \equiv (\partial^2/\partial\xi^2) + (\partial^2/\partial\eta^2)$, and Ψ is the stream function such that the velocity components are given by

$$u = \partial\Psi/\partial y, \qquad v = -\partial\Psi/\partial x \tag{4}$$

It will be assumed that Ψ can be expressed in the form

$$\Psi = \nu\{\xi F(\eta) + \psi_0 + \psi_1 + \ldots\} \tag{5}$$

as $\xi \to \infty$, where $\psi_n = 0(\xi^{-n})$ and $\log \xi$ is considered to be $0(1)$. (Alden tacitly assumed that even-order terms $\psi_0, \psi_2, \ldots$ are absent from the asymptotic expression.) The boundary conditions are that on the plate

$$\eta = 0, \qquad u = v = 0 \tag{6}$$

and, as the edge of the boundary layer is approached, the vorticity should vanish exponentially,

$$\omega = -(\Psi_{xx} + \Psi_{yy}) \to 0 \text{ exponentially as } \eta \to \infty \tag{7}$$

since the boundary layer goes over smoothly to the outside irrotational main flow. [This latter condition has been ignored in Alden's and Bell's work in favor of the more intuitive condition of smooth joining to the uniform flow: $u \to U$, $v \to 0$ as $\eta \to \infty$. It should be borne in mind that the expansion in the form of Eq. (5) is only valid for the boundary layer where $\eta = 0(1)$ but not for the main flow where ξ and η are of the same order of magnitude.] In our case, it is also required that

the flow is symmetrical with respect to the x-axis (8)

Substituting Eq. (5) into Eq. (3) and comparing terms of the same order of magnitude, we can set up a system of equations for $F, \psi_0, \psi_1, \ldots$. As should be expected from the outset, F is found to be the Blasius function such that

$$\left.\begin{aligned} F''' + FF'' &= 0 \\ F(0) = F'(0) &= 0, \qquad F''(0) = \alpha \\ F &\to 2(\eta - \beta) \quad \text{as} \quad \eta \to \infty \\ \alpha &= 1.32824, \qquad \beta = 0.8604 \end{aligned}\right\} \tag{9}$$

By considering the conditions of Eqs. (6), (7), and (8), it is found that

$$\psi_0 \equiv 0 \tag{10}$$

$$\psi_1 = [G(\eta)/\xi] + (1/\xi)[C_1 - (A/2)\log\xi](\eta F' - F) \tag{11}$$

† This investigation was carried out under Contract Nonr-595(08) of the Office of Naval Research, whose support is gratefully acknowledged.

* On leave of absence from the University of Tokyo, Japan.

where

$$\left.\begin{aligned} G(\eta) &= (\eta F' - F)\int_0^\eta (F'H/F^2F'')\,d\eta - \\ &\qquad F'\int_0^\eta [(\eta F' - F)H/F^2F'']d\eta \\ H(\eta) &= \int_0^\eta \{(\eta F' - F)^2 - 4\beta^2\}F\,d\eta + \\ &\qquad (A/2)\,[FF'' - (1/2)F'^2] \\ A &= \int_0^\infty \{(\eta F' - F)^2 - 4\beta^2\}F\,d\eta = -3.3190 \\ G(\infty) &= -2.2073 \end{aligned}\right\} \quad (12)$$

and C_1 is an arbitrary constant.

Next, by use of the technique developed in the previous paper,[3] the irrotational flow induced by the vorticity distribution in the boundary layer can be calculated. The result is that the stream function can be expressed as the imaginary part of an analytic function (complex velocity potential) $f(\zeta)$:

$$\Psi = \mathrm{Im}\, f(\zeta) \quad (13)$$

where

$$f(\zeta) = \nu\{\zeta^2 - 2i\beta\zeta + i(C/\zeta) - i\beta A[(\log \zeta/i)/\zeta] + 0(1/\zeta^2)\} \quad (14)$$

with

$$C = 2\beta C_1 + G(\infty) \quad (15)$$

The local skin friction can be calculated as

$$\tau_0 = -\mu\omega(0) = (1/4)\,(\rho U^2\alpha/R^{1/2}) \times \{1 + (1/R)\,[C_1 - (A/2)\log R^{1/2}]\} \quad (16)$$

where $R = Ux/\nu$. The first term is the well-known Blasius formula. It is obvious that the "total skin friction" cannot be calculated by the formula

$$D = 2\int_0^x \tau_0\,dx$$

in view of the singularity at $x = 0$ of the term $R^{-3/2} = 0(x^{-3/2})$. This difficulty can be avoided by considering the balance of momentum of the fluid contained in a large circle of radius x with center at the origin. For this purpose it is only necessary to know the behavior of the flow on that circle, which is exactly (to the order required) given by Eq. (14) (in the main flow) and by Eq. (5) (in the boundary layer). This procedure has also been used in the previous paper.[3] The result is

$$\left.\begin{aligned} C_f &= (\alpha/R^{1/2}) + (\pi\beta^2/R) + (\alpha/R^{3/2})\{(A/2) \times (1 + \log R^{1/2}) - C_1\} + 0(1/R^2) \\ &= (1.328/R^{1/2}) + (2.326/R) - (1.328/R^{3/2}) \times \{1.659(1 + \log R^{1/2}) + C_1\} + 0(1/R^2) \end{aligned}\right\} \quad (17)$$

where $C_f = D/[(1/2)\rho U^2 \cdot 2x]$ is the total skin-friction coefficient.

It is interesting to note that the lowest order correction to the Blasius formula is $\pi\beta^2/R$, although an intuitive argument based on the formula for the local skin friction [Eq. (16)] would suggest it to be of order $0(R^{-3/2})$. Also, it is remarkable that for the calculation of the correction term it is only necessary to know the Blasius solution if the momentum theorem is used instead of the integration of the local skin friction. Further, it may be interesting to compare the result with Kuo's formula for the total skin-friction coefficient of a finite plate:[2]

$$C_f = (1.328/R^{1/2}) + (4.12/R) \quad (18)$$

Finally, it should be mentioned that the constant C_1 appearing in Eqs. (11), (15), (16), and (17) remains undetermined in the above analysis. It seems to the author that this, as well as other constants which would appear in the higher order approximations $\psi_2, \psi_3, \ldots$, could only be determined by taking into account the flow condition near the leading edge, which can be investigated on the basis of the Stokes-type approximations, as done by Carrier and Lin.[6] In fact, it can be shown that for small R

$$C_f = (b/R^{1/2}) - (\pi b^2/256)R + 0(R^{5/2}) \quad (19)$$

where b is an undetermined constant. If one tentatively adopts the condition that C_f and dC_f/dx, and hence total and local skin friction, should be continuous at $R = 1$, C_1 and b can be determined as follows:

$$C_1 = 0.0164, \qquad b = 1.454$$

Thus, the constant b characterizing the friction near the leading edge is about 10 per cent higher than the Blasius value α, contrary to Carrier and Lin's conclusion that $b = \alpha$.

References

[1] Alden, H. L., *Second Approximation to the Laminar Boundary Layer Flow over a Flat Plate*, J. Math. & Phys., Vol. 27, No. 2, pp. 91–104, July, 1948.

[2] Kuo, Y. H., *On the Flow of an Incompressible Viscous Fluid past a Flat Plate at Moderate Reynolds Numbers*, J. Math. & Phys., Vol. 32, No. 2, pp. 83–100, July, 1953.

[3] Imai, I., *On the Asymptotic Behaviour of Viscous Fluid Flow at a Great Distance from a Cylindrical Body, with Special Reference to Filon's Paradox*, Proc. Roy. Soc. London A, Vol. 208, pp. 487–516, 1951.

[4] Bell, S., *Studies of Boundary Layer Slip Solutions and Alden's Method for Boundary Layer Correction*, University of California Institute of Engineering Research Tech. Report, No. 20-106, December, 1955.

[5] von Kármán, Th., *The Engineer Grapples with Nonlinear Problems*, Bull. Am. Math. Soc., Vol. 46, pp. 615–683 (especially 655–659), 1940.

[6] Carrier, G. F., and Lin, C. C., *On the Nature of the Boundary Layer near the Leading Edge of a Flat Plate*, Quart. Appl. Math., Vol. 6, No. 1, pp. 63–68, April, 1948.

Three-Dimensional Vortex Pattern Behind a Circular Cylinder*

Francis R. Hama

Assistant Research Professor, Institute for Fluid Dynamics and Applied Mathematics, University of Maryland, College Park, Md.

October 15, 1956

DEVELOPMENT OF THE WAKE behind circular cylinders is investigated in detail by Roshko by means of a hot-wire anemometer.[1] The Reynolds Number range of periodic vortex shedding is divided into the following three subranges:

Stable range	$40 < U_1 d/\nu < 150$
Transition range	$150 < U_1 d/\nu < 300$
Irregular range	$300 < U_1 d/\nu$

where U_1 is the velocity of the incoming flow, d the cylinder diameter, and ν the kinematic viscosity. Whereas regular laminar vortex streets are formed in the stable range and no turbulent motion develops, turbulence is initiated by laminar-turbulent transition in the free shear layer separated from the cylinder. This transition begins to appear in the transition range.

On the other hand, the present writer[2] has investigated the flow phenomena associated with transition especially behind a trip wire attached to a flat plate, finding that a two-dimensional discrete vortex imbedded in shear flows has a strong tendency to form three-dimensional vortex loops and that the formation and development of the three-dimensional vortex loop are directly responsible to the creation of a turbulence spot.

In order to examine whether or not the same principle should apply to the transition behind a circular cylinder also, the three-dimensional vortex pattern behind a circular cylinder is observed in a towing tank, 2 ft. wide, 2 ft. deep, and 12 ft. long. The circular cylinder is a 1/4-in. outside diameter brass tube, approximately 20 in. long, and is submerged horizontally at the mid-depth of the water. Red dye is very slowly leaked through a row of small holes separated approximately 1/24 in. and aligned parallel to the cylinder axis, the diameter of the holes being 1/32 in. The row of holes is located approximately 120° measured from the forward stagnation point so that only one side of the vortex streets is observed from above the plane of the vortex street.

Result of the observation is presented typically in Figs. 1–3. Fig. 1 is taken at the lowest Reynolds Number among the pictures and stable range. The vortices are shed regularly without showing much three dimensionality except for a slight long-wave de-

* This research was supported by the U.S. Air Force through the Office of Scientific Research, ARDC, under Contract AF 18(600)-1014.

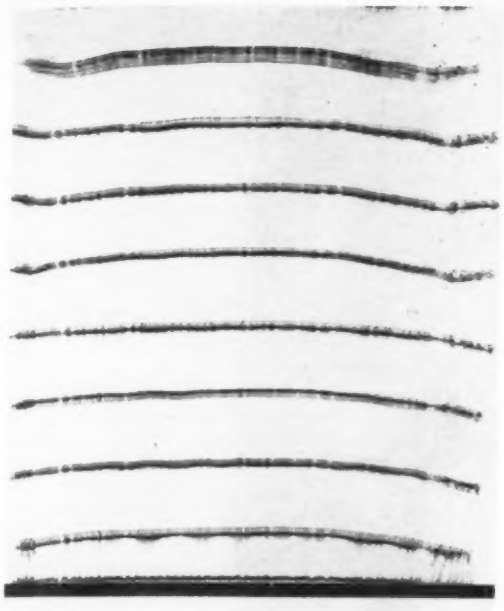

FIG. 1. Vortices behind a circular cylinder ($U_1 d/\nu = 117$).

formation which is rather attributable to persistent large-scale disturbance in still water. Although lower Reynolds Numbers than this could not be obtained in our towing tank, an appreciable long-wave three dimensionality at low Reynolds Numbers occurs only when the observation is made after a relatively short waiting period between consecutive runs evidently due to persisting large-scale disturbances; otherwise reasonably good two dimensionality such as Fig. 1 is consistently obtained. We fear that the long-wave three dimensionality at very low Reynolds Numbers such as 80 reported by Roshko is due to the lack of uniformity of the wind-tunnel flow.

When the Reynolds Number is increased slightly larger than 150, a three dimensionality—i.e., the transverse waviness—begins to appear fairly randomly and quite hesitantly. At the Reynolds Number of around 200, the three dimensionality appears violently as shown in Fig. 2. As the Reynolds Number is furthermore increased, the three dimensionality appears more regularly and periodically in the longitudinal as well as transverse directions. The transverse wave length seems to decrease as the Reynolds Number increases. In this transition range, however, the three dimensionality does not develop further but only rotates around the original vortex axis. Consequently, the local transition from laminar to turbulent motion does not seem to occur in the shear-flow region. Nevertheless, a hot-wire trace should indicate somewhat of irregularity as observed by Roshko because of the three-dimensional deformation. The transition occurs far downstream of the circular cylinder due perhaps to the interactions between consecutive deformed vortex lines and the two vortex streets and to the side effect. In wind-tunnel experiments, moreover, the flow turbulence would promote these interactions.

Flow phenomena in the irregular range, in which the Reynolds Number exceeds approximately 300, look much the same as those behind a trip wire on a flat plate. In this Reynolds Number range, the vortex line shed by the circular cylinder becomes wavy almost immediately, develops further apparently in the shear layer, and breaks down into turbulent motion—a typical picture being Fig. 3.

The appearance of the three dimensionality and its important role in the creation of the local transition into turbulent motion are thus confirmed in the wake behind a circular cylinder also. These processes are therefore considered to be the guiding principle of transition phenomena not only in boundary layers and jet boundaries as reported elsewhere[2] but in wakes as well.

In connection with the above observation, it may be of interest to mention the destabilization effect of a thin flat plate mounted behind a cylinder in the center plane of the wake. This interference device is also investigated by Roshko,[1] and the effectiveness in stopping the periodic shedding is attributed to the interruption of the communication of the two free vortex layers. It is true that the separation plate interrupts the communication, which occurs always three dimensionally, and stops a large-scale periodic shedding. This constitutes, however, only one side of the effectiveness. The other and important side of the story is

FIG. 2. Vortices behind a circular cylinder ($U_1 d/\nu = 190$).

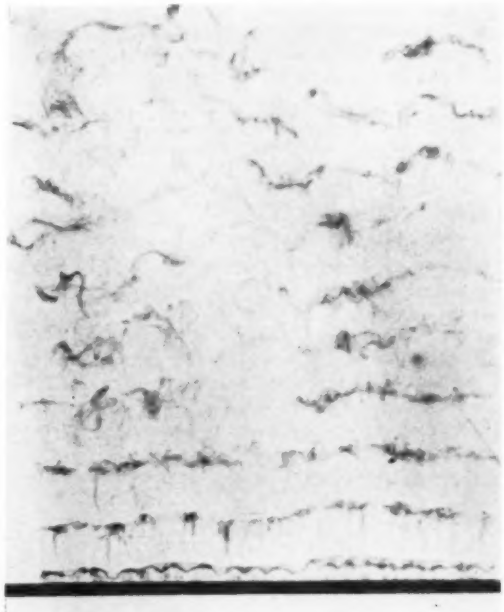

FIG. 3. Vortices behind a circular cylinder ($U_1 d/\nu = 313$).

that, because of the shear layers along the flat plate, the formation of the three-dimensional transverse waviness and the breakdown into turbulent motion are promoted and that therefore, when the flow leaves the combined system of cylinder and plate, periodic vortices are entirely destroyed, and no periodic shedding is experienced. One other feature of the effect of the separation plate should also be mentioned—that is, that the separation plate stabilizes the periodic vortices at low Reynolds Numbers. As a result, the stable range is extended to approximately 320 with a tested length of the plate, whereas the transition range is extremely squeezed, and an entirely turbulent wake is observed at 335.

References

[1] Roshko, Anatol, *On the Development of Turbulent Wakes from Vortex Streets*, NACA Rep. 1191, 1955 (supersedes NACA TN 2913, 1953).

[2] Hama, F. R., Long, J. D., and Hegarty, J. C., *On Transition from Laminar to Turbulent Flow*, J. Appl. Phys. (in press).

Subsonic Boundary-Layer Transition Caused by Single Roughness Elements

J. Leith Potter
Gas Dynamics Facility, ARO, Inc., Tullahoma, Tenn.
October 15, 1956

THE GENERALLY ACCEPTED VIEW of boundary-layer transition is that the Tollmien-Schlichting oscillations precede and control transition if free-stream turbulence is somewhat less than 0.1 per cent, while the Taylor theory, based on the concept of momentary separation, is only valid for free-stream turbulence greater than about 0.2 per cent (c.f., Dryden[1]). Thus, all of the more recent theoretical work on laminar boundary-layer instability has been directed toward the improvement and extension of the Tollmien-Schlichting theory. However, there is a part of the transition problem that seems ideally suited for an attack patterned after Taylor's method—namely, transition caused by roughness. This note presents results for the case of single roughness elements on flat plates in subsonic, low-turbulence streams.

The present subject has been considered by Dryden,[2] who summarized a great amount of experimental data and discussed several intuitively plausible parameters for correlating data. Most of the experimental information used by Dryden was taken from Tani and Hama,[3] and some newer data have been published by Klebanoff, Schubauer, and Tidstrom.[4] The work to be described assumed model configurations and flow conditions typified by these references.

In 1936, Taylor[5] published a theoretical discussion of the relation between scale of turbulence and the critical resistance of spheres. For isotropic stream turbulence produced by grids in subsonic wind tunnels, he was able to demonstrate that the Pohlhausen parameter, $\sqrt{\lambda'^2}$, written for turbulent motion, could be considered to attain some constant value defining transition. This led him to the formulation of satisfactory parameters describing boundary-layer transition on smooth plates and spheres. Considerable supplemental information was available to aid Taylor's study of transition due to isotropic turbulence produced by grids, but the published data on transition produced by roughness do not include similar details of the flow. It has been necessary to cover these gaps by numerous assumptions which are now described.

The form of the Pohlhausen parameter to be used is

$$\sqrt{\lambda'^2} = -(\delta^2/\mu U')\,(\partial p'/\partial x) \tag{1}$$

where

δ = boundary-layer thickness at x
μ = dynamic viscosity
U' = free-stream velocity
p' = fluctuating pressure caused by oscillations in boundary layer
x = distance from leading edge of plate

It is evident that ability to evaluate the fluctuating pressure gradient due to oscillations or unsteadiness in the laminar boundary layer represents the main obstacle to calculation of the value of the Pohlhausen parameter defining transition. An intuitive approach will be shown.

Assume that

$$\partial p'/\partial x \propto \rho u'^2/s \tag{2}$$

u' = fluctuating component of velocity
ρ = mass density
s = an unknown characteristic length

and $\propto$ means "proportional to."

Now it is stipulated that this derivation is restricted to cases where transition is predominantly influenced by the roughness element—i.e., we neglect free-stream turbulence and any other disturbing factors. Thus, we assume

$$u'^2 \propto U'^2 f_1(x_t/x_k,\ k/\delta_k) \tag{3}$$

where

U' = free-stream velocity
x_t = location of transition
x_k = location of roughness element ($x_k < x_t$)
k = height of roughness element
δ_k = boundary-layer thickness corresponding to x_k

The terms in parentheses in Eq. (3) represent the location and size of the roughness element. The length, x_t, is used with x_t because Eq. (1) must be evaluated at the location of transition.

To complete Eq. (2), the length, s, must be considered. It seems reasonable that the length between successive vortices shed by the roughness element should be important in regard to the fluctuating pressure gradients. If this length is taken as s, then u' and s should be so related that we may rewrite Eq. (3) as

$$u'^2/s \propto (U'^2/k)\, f_2(x_t/x_k,\ k/\delta_k) \tag{4}$$

Eq. (4) may be substituted into Eq. (2) showing that the result of these assumptions is

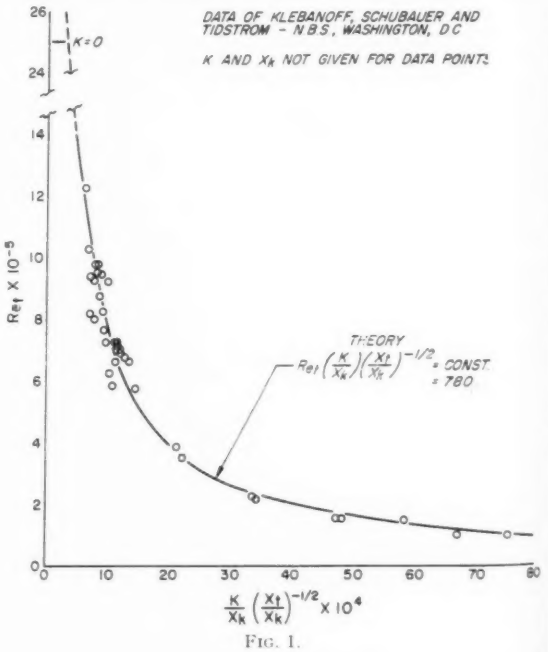

FIG. 1.

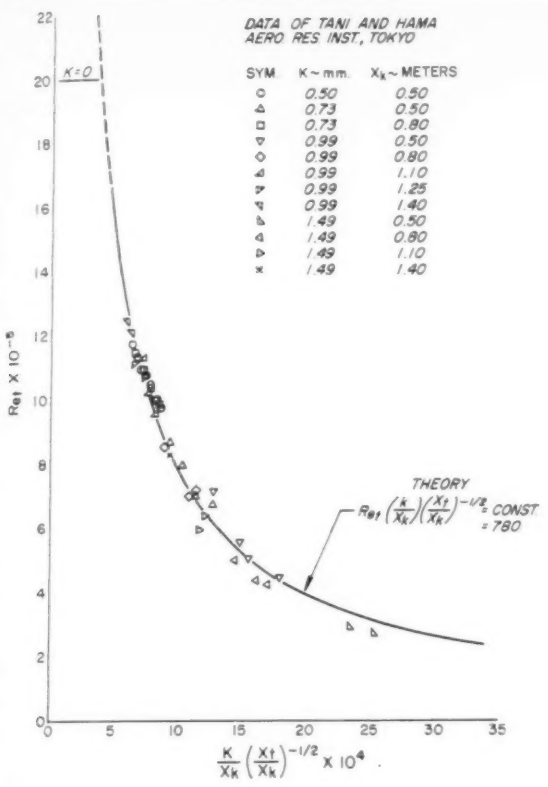

FIG. 2.

$$\partial p'/\partial x \propto (\rho U'^2/k)\, f_2(x_t/x_k,\ k/\delta_k) \tag{5}$$

Substituting the above result in Eq. (1) yields the expression

$$\sqrt{\lambda'^2} \propto (\delta^2/\mu U')\,(\rho U'^2/k)\, f_2(x_t/x_k,\ k/\delta_k) \tag{6}$$

Now δ is to be evaluated at x_t and δ_k at x_k, so Eq. (6) becomes

$$\sqrt{\lambda'^2} \propto (x_t/k)\, f_2\,[x_t/x_k,\ k(U/\nu x_k)^{1/2}] \tag{7}$$

To complete the right side of Eq. (7) and find if the result is indeed a constant at transition, it is necessary to determine the functions inside brackets. Inspection of published data,[3, 4] first for x_t/x_k = const., indicates that

$$(x_t/k)\, f_2[k(U/\nu x_k)^{1/2}] \cong (x_t/k)\,[k(U/\nu x_k)^{1/2}]^2$$

This may be rewritten as

$$Re_t(k/x_k) \cong \text{const.} \quad \text{when } x_t/x_k = \text{const.}$$

where $Re_t = Ux_t/\nu$

ν = kinematic viscosity

Having obtained this information, it is easy to establish $f_2(x_t/x_k)$ and complete the parameter. We find that

$$\sqrt{\lambda'^2} \propto Re_t(k/x_k)\,(x_t/x_k)^{-1/2} \tag{8}$$

or

$$Re_t(k/x_k)\,(x_t/x_k)^{-1/2} = \text{const.} \tag{9}$$

for single roughness elements on flat plates in low-speed streams.

The validity of this derivation cannot be checked without detailed experimental measurements. However, the result expressed by Eq. (9) is readily verified by available data as demonstrated by Figs. 1 and 2. From these figures, it is found that the constant of Eq. (9) is approximately 780 for both sets of data. Here it should be noted that the data points have been read from small figures in the referenced publications, so it is possible that small and probably consistent errors may be present. These might make a slight change in the value of the constant, though this is unlikely in view of the experimental scatter. The points plotted are for the condition $x_k < x_t < x_{t0}$ where x_{t0} corresponds to $k = 0$, the case of no roughness. Eq. (9) does not predict when $x_t \leq x_k$, nor does it tell when $x_t = x_{t0}$. These are the limiting cases not considered in the analysis, and Eq. (9) probably becomes less accurate as the bounds are approached. However, references 2 and 4 contain information permitting the approximate prediction of these limits, and they should be estimated before using Eq. (9) for engineering calculations.

REFERENCES

[1] Dryden, H. L., "Recent Advances in the Mechanics of Boundary Layer Flow," *Advances in Applied Mechanics*, Edited by R. von Mises and T. von Kármán, Vol. I, pp. 8–16; Academic Press, Inc., New York, 1948.

[2] Dryden, H. L., *Review of Published Data on the Effect of Roughness on Transition from Laminar to Turbulent Flow*, Journal of the Aeronautical Sciences, Vol. 20, No. 7, pp. 477–482, July, 1953.

[3] Tani, I., and Hama, F. R., *Some Experiments on the Effect of Single Roughness Elements on Boundary-Layer Transition*, Readers' Forum, Journal of the Aeronautical Sciences, Vol. 20, No. 4, pp. 289, 290, April, 1953.

[4] Klebanoff, P. S., Schubauer, G. B., and Tidstrom, K. D., *Measurements of the Effect of Two-Dimensional and Three-Dimensional Roughness Elements on Boundary-Layer Transition*, Readers' Forum, Journal of the Aeronautical Sciences, Vol. 22, No. 11, pp. 803, 804, November, 1955.

[5] Taylor, G. I., *Statistical Theory of Turbulence, V—Effect of Turbulence on Boundary Layer*, Proc. Royal Society (London), Series A, Vol. 156, pp. 307–317, 1936.

An Approximate Method Applied to the Solution of the Problem of Vibrating Rectangular Plates

Milomir M. Stanišić

Associate Professor of Mechanics, Engineering Sciences, Purdue University, Lafayette, Ind.

October 1, 1956

SUMMARY

Ordinary product solution and Galerkin method are used in order to find the natural frequency of a rectangular plate subjected to the following boundary conditions: (a) all edges fixed, and (b) two adjacent edges fixed and the other two edges free. The plates here considered are assumed to obey the classical small deflection theory, and the influence of rotatory inertia and shear forces are neglected in the solution. Results are tabulated.

SYMBOLS

x, y	= rectangular coordinates
a, b	= lateral dimensions of plate, in. (See Fig. 1)
$w(x, y, t)$	= transversal deflection of the plate, in.
h	= thickness of plate, in.
D	= $Eh^3/12(1-\nu^2)$ = bending stiffness of a plate, lb.-in.
ν	= Poisson's ratio
ρ	= mass density of plate material, lbs. sec.^{2} in.$^{-4}$
ω	= angular frequency of conservative system, rad. sec.$^{-1}$
Ω	= angular frequency of the nonconservative system, rad. sec.$^{-1}$
λ	= $(\rho h/D)\,\omega_m$ = value defined by Eq. (11)
Λ	= $\lambda a^2 b$ = eigenvalue of the problem

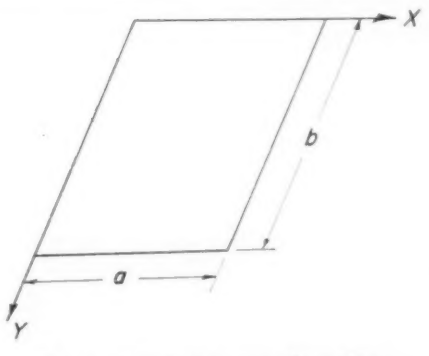

FIG. 1. Coordinate system of the plate.

m, n; r, s; p, q; i, j; u, v = positive integers

A_{rs} = coefficient used in series representation of deflection

$\phi(x, y)$ = a function of x and y alone

X_r = a function of x alone

Y_s = a function of y alone

$\Psi(t)$ = time-depending function

η_v = characteristic function of the vibrating beam

k = damping coefficient

α = coefficient defined by Eq. (10)

$\delta_{p,q}$ = Kronecker delta

Derivatives with respect to x and y are indicated by subscript x, xx, . . . y, yy, and, with respect to time, by t, tt . . . .

Solution of the Problem

According to the classical two-dimensional theory of flexural motion of a vibrating plate, assuming that the damping forces are proportional to the velocity, neglecting rotatory inertia and shear forces, the motion of the plate is governed by the following partial differential equation:

$$\Delta^4 w(x, y, t) + (\rho h/D) w_{tt}(x, y, t) = -(k/D) w_t(x, y, t) \quad (1)$$

Using an ordinary product solution, such as

$$w(x, y, t) = \sum_{m=0}^{n} \phi_m(x, y)\Psi(t) \quad (2)$$

the homogeneous equation

$$\nabla^4 w(x, y, t) + (\rho h/D) w_{tt}(x, y, t) = 0 \quad (3)$$

becomes

$$\nabla^4 \phi_m(x, y) - \lambda \phi_m(x, y) = 0 \quad (4)$$

Then

$$\nabla^4 \phi_m(x, y) = (\rho h/D) \omega_m{}^2 \varphi_m(x, y) \quad (5)$$

Hence, Eqs. (1), (2), and (5) lead to

$$\Psi_{m,tt}(t) + (k/\rho h)\, \Psi_{m,t}(t) + \omega_m{}^2 \Psi_m(t) = 0 \quad (6)$$

the solution of which is

$$\Psi_m(t) = A_m e^{-\alpha t} \cos(\Omega_m t + \beta_m) \quad (7)$$

Eqs. (6) and (7) show that

$$2\alpha - (k/\rho h) = 0 \quad (8)$$

$$\Omega_m{}^2 - \alpha^2 + (k/\rho h)\alpha - \omega_m{}^2 = 0 \quad (9)$$

Therefore,

$$\alpha = k/2\rho h \quad (10)$$

$$\Omega_m = [\omega_m{}^2 - (k/2\rho h)^2]^{1/2} \quad (11)$$

Hence the solution is determined as soon as the angular frequency of vibration of the conservative system ω_m is found. In other words, the eigenvalue of Eq. (4) must be determined.

A most convenient method is that of Galerkin. Using

$$\phi(x, y) = \sum_{r=1}^{i} \sum_{s=1}^{j} A_{rs} X_r Y_s \quad (12)$$

where X and Y are of the form

$$\eta_v(\xi) = \cosh \mu_v(\xi/l) - \cos \mu_v(\xi/l) - \gamma_v[\sinh \mu_v(\xi/l) - \sin \mu_v(\xi/l)] \quad (13)$$

the Galerkin form of the stated problem becomes

$$\sum_{r=1}^{i} \sum_{s=1}^{j} A_{rs} \int_0^a \int_0^b [\nabla^4(X_r Y_s) - \lambda(X_r Y_s)] X_p Y_q dx dy = 0 \quad (14)$$

Table 1

The Eigenfrequencies, $\Lambda^{1/2}$, of the Plate for Different Shape Ratios and $k = 0$

Type of Plate Support	b/a	Mode Numbers 1	2	3
All edges fixed	1.0	36.11	73.73	108.85
	1.5	33.18	51.31	81.30
	2.0	34.86	54.20	90.75
	2.5	37.48	44.14	99.97
	3.0	40.26	44.95	108.66
Two adjacent edges fixed and the two other edges free	1.0	4.98	21.04	22.78

Two cases will be considered in this paper—namely, (a) a plate with all edges fixed, and (b) a plate with two adjacent edges fixed and the other two edges free. The characteristic functions, Eq. (13), are orthonormal and satisfy the boundary conditions—namely,

$$\text{(a)} \quad \eta_v(0) = \eta_{v,\xi}(0) = \eta_v(l) = \eta_{v,\xi}(l) = 0 \quad (15)$$

$$\text{(b)} \quad \eta_v(0) = \eta_{v,\xi}(0) = \eta_{v,\xi\xi}(l) = \eta_{v,\xi\xi\xi}(l) = 0 \quad (16)$$

Then Eqs. (13) and (15) lead to

$$\left.\begin{aligned} &\cosh \mu_v \cos \mu_v - 1 = 0 \\ &\gamma_v = (\cosh \mu_v - \cos \mu_v)/(\sinh \mu_v - \sin \mu_v) \end{aligned}\right\} \quad (17)$$

while Eqs. (13) and (16) lead to

$$\left.\begin{aligned} &\cosh \mu_v \cos \mu_v + 1 = 0 \\ &\gamma_v = (\cosh \mu_v + \cos \mu_v)/(\sinh \mu_v + \sin \mu_v) \end{aligned}\right\} \quad (18)$$

With the abbreviated notations

$$l \int_0^l \eta_u(\xi)\, \eta_{v,\xi\xi}(\xi)\, d\xi = H_{u,v}$$

$$\int_0^l \eta_u(\xi)\eta_v(\xi) d\xi = l\delta_u{}^v$$

and, since the characteristic functions are orthonormal, it follows that

$$\sum_{r=1}^{i} \sum_{s=1}^{j} A_{rs}\, (E_{pq}^{(rs)} - \Lambda \delta_{pq}^{(rs)}) = 0 \quad (19)$$

where

$$\delta_{pq}^{(rs)} = \begin{cases} 1 \text{ for } p = r \text{ and } q = s \\ 0 \text{ for either } p \neq r \text{ or } q \neq s \end{cases}$$

$$E_{pq}^{(rs)} = (b/a)\mu_r{}^4 + (a/b)^3 \mu_s{}^4 + 2H_{rr}H_{ss} \text{ for } p = r \text{ and } q = s$$

$$E_{pq}^{(rs)} = 2(a/b)H_{pr}H_{qs} \text{ for either } p \neq r \text{ or } q \neq s$$

Finally, since

$$\lambda = \rho h \omega_m{}^2/D$$

or

$$\omega_m{}^2 = \Lambda D/\rho h a^3 b$$

then

$$\Omega_m = [(\Lambda D/\rho h a^3 b) - (k/2\rho h)^2]^{1/2}$$

The results for μ_r and γ_v are given in any standard reference of vibration.

The coefficients $Ev_{pq}{}^{(rs)}$ can easily be determined for various shape ratios and for each boundary condition. Using only two terms in the series representation, the eigenfrequencies, $\Lambda^{1/2}$, for each case under consideration and for $k = 0$ are shown in Table 1. The results show that the mode number is irregular with increasing shape ratio.

ent Shape

umbers—
3
3 108.85
1 81.30
0 90.75
4 99.97
5 108.66

4 22.78

ely, (a) a
cent edges
functions,
nditions—

(15)

0 (16)

(17)

(18)

it follows

(19)

$q = s$

erence of

r various
only two
$A^{1/2}$, for
Table I.
with in-